UNIVERSITY of TASMANIA

Pyrite Trace Element Geochemistry of black shales of the "Boring Billion" period (1800-800 Ma): Implications for Evolution of the Atmospheric oxygen and Complex Life

Indrani Mukherjee

Bachelor of Science (Hons.) and Master of Science in Geology

University of Delhi, India

Submitted in fulfilment of the requirements for the degree of

Doctor of Philosophy

University of Tasmania

September 2017

Statements and Declarations

Declaration of originality

This thesis contains no material which has been accepted for a degree or diploma by the University or any other institution, except by way of background information and duly acknowledged in the thesis, and to the best of my knowledge and belief no material previously published or written by another person except where due acknowledgement is made in the text of the thesis, nor does the thesis contain any material that infringes copyright.

Signed: Dated: 28th September, 2017

Authority of access

This thesis may be made available for loan and limited copying and communication in accordance with the Copyright Act 1968.

Signed: Dated: 28th September, 2017

Statement regarding published work contained in this thesis

The publishers of the papers comprising Chapters 2, 3, 4, 6 hold the copyright for that content and access to the material should be sought from the respective journals. The remaining non-published content of the thesis may be made available for loan and limited copying and communication in accordance with the Copyright Act 1968.

Signed: Dated: 28th September, 2017

Statements and Declarations

Statement of Co-Authorship

The following people and institutions contributed to the publication of work undertaken as part of this thesis:

Candidate = Indrani Mukherjee, Centre of Excellence in Ore Deposits (CODES), University of Tasmania (UTAS)
Author 1= Professor Ross Large, Primary Supervisor, CODES, UTAS
Author 2= Dr. Jaqueline Halpin, Supervisor, Institute for Marine and Antarctica Studies, UTAS
Author 3= Dr. Sebastien Meffre, Supervisor, CODES, UTAS
Author 4= Professor Leonid Danyushevsky, CODES, UTAS
Author 5= Dr. Ross Corkrey, Tasmanian Institute of Agricultural Research, UTAS
Author 6= Professor Mihir Deb, Indian National Science Academy, India
Author 7= Dr. Stuart Bull, CODES, UTAS
Author 8= Dr. Daniel Gregory, University of California, Riverside, U.S.A
Author 9= Dr. Janaína Ávila, The Australian National University, Canberra
Author 10= Professor Trevor Ireland, The Australian National University, Canberra
Author 11= Dr. Aleksandr S. Stepanov, CODES, UTAS
Author 12= Dr. Ivan Belousov, CODES, UTAS

Proportion of work undertaken

Paper 1, < Pyrite trace element chemistry of the Velkerri Formation, Roper Group, McArthur Basin: Evidence for atmospheric oxygenation during the Boring Billion>:

Located in chapter 2 (Published in Precambrian Research)

Candidate was the primary author and with author 1 contributed to the conception and design of the research project and drafted significant parts of the paper.

Candidate contributed approximately 80% to the planning, execution and preparation of the work for the paper and contributed to the analysis and interpretation of the research data. Author 1, contributed to the interpretation of the work by critically revising the paper.

Paper 2, < Application of pyrite trace element chemistry to exploration for SEDEX style Zn-Pb deposits, McArthur Basin, Northern Territory, Australia >:

Located in chapter 3 (Published in Ore Geology Reviews)

Candidate was the primary author and with author 1 contributed to the conception and design of the research project and drafted significant parts of the paper.

Candidate contributed approximately 80% to the planning, execution and preparation of the work for the paper and contributed to the analysis and interpretation of the research data. Author 1, contributed to the interpretation of the work by critically revising the paper.

Paper 3, < Pyrite trace element and sulphur isotope geochemistry of Paleo-Mesoproterozoic black shales from the McArthur Basin, Northern Australia >:

Located in chapter 4 (Under review in Geochimica et Cosmochimica Acta)

Candidate was the primary author and with author 1 contributed to the conception and design of the research project and drafted significant parts of the paper.

Candidate contributed 75% to the planning, execution and preparation of the research paper including contributing to the analysis and interpretation of the research data.

Authors 7, 8, 9, 10 and 11 contributed to the interpretation of the work by critically revising the paper. Author 5 helped with statistical interpretation of the data.

Paper 4, < Sedimentary Pyrites of Bijaigarh Shales, Vindhyan Basin, India: Textures, Trace Element Chemistry and their Implications >:

Located in chapter 5 (Yet to be submitted in Journal of Asian Earth Sciences)

Candidate was the primary author and with author 1 and 6 contributed to the conception and design of the research project and drafted significant parts of the paper.

Candidate contributed 75% to the planning, execution and preparation of the research paper including contributing to the analysis and interpretation of the research data. Authors 1, 2, 3, 6, 12 contributed to the interpretation of the work by critically revising the paper.

Paper 5, < The Boring Billion, a slingshot for Complex Life on Earth >:

Located in chapter 6 (Published in Scientific Reports)

Candidate was the primary author and with author 1 and 6 contributed to the conception and design of the research project and drafted significant parts of the paper.

Candidate contributed 90% to the planning, execution and preparation of the research paper including contributing to the analysis and interpretation of the research data. Authors 1, 4 and 5 contributed to the interpretation of the work by critically revising the paper. Author 5 helped with statistical treatment and interpretation of the data.

We the undersigned agree with the above stated "proportion of work undertaken" for each of the above published (or submitted) peer-reviewed manuscripts contributing to this thesis:

Signed: _

Professor Ross Large

Primary Supervisor

School of Physical Sciences

University of Tasmania

Date: 25/9/17

Signed: _

Professor Leonid Danyushevsky

Head of Discipline, Earth Sciences

School of Physical Sciences

University of Tasmania

Date: 25/9/17

Acknowledgements

First and foremost, I would like to thank Prof. (my primary supervisor, Professor Ross Large) for accepting me as his PhD student in 2014 and his invaluable guidance, patience, support and encouragement ever since. I am particularly grateful to him for my research topic "Boring Billion". Reluctant, to begin with, I gradually became fascinated (and still am!) with my research topic. He is the best supervisor one can have and my PhD journey has been absolutely fantastic because of him. Thank you to both my co-supervisors (Dr. Jaqueline Halpin and Dr. Sebastien Meffre) for all their help. As a leading female geoscientist, Jacqui inspires me and Sebastien, with his intellect. I owe gratitude to Professor Leonid Danyushevsky (and his fabulous team) for being incredibly helpful to me throughout the course of my PhD and providing me with the excellent analytical facility that has been a critical part of my PhD. Many thanks to Prof. Mihir Deb who sparked my interest in Geology in the first place. He has been a wonderful mentor and a fantastic teacher ever since I have known him. Thanks to Dr. Corkrey for collaborating with us and helping me cope with statistical jargons. Thanks to both previous and current Graduate Research Coordinators (Prof. Jocelyn McPhie and Prof. Anya Reading) for the management of my candidature.

Thanks to Jane Higgins and Deborah Macklin for being absolute angels at all times but especially when it came to dealing with administrative issues (not that we had many). I would also like to thank Al (Alexander Cuison) for making countless laser mounts for me and for putting up with my repetitive and mundane descriptions of how the black shales need to be mounted.

Thank you to my dear parents for believing in me despite my non-traditional lifestyle that I am now happily accustomed to. Thanks to Marley Large and Gloria Pullen for helping me out at the very start of my journey. Together we have truly had some of the most amazing times involving laughter and tears. Thanks to Chris Large for being so very supportive and understanding, especially towards the end of the PhD when my stress counts went soaring high. Not to forget his encouraging words every time I doubted myself. I would like to thank Daniel Gregory and Selina Wu for their support and generous hearts. I sincerely acknowledge Jacob Mulder's help at various points in my PhD especially during "technologically challenged" times. Thanks to all my friends here and back in India for granting me a life outside my PhD. And lastly, thanks to whoever invented caffeine as the PhD would not be the same experience without copious cups of coffees. Below are some quotes that inspired me during the course of my PhD.

- "Take it easy", Ross Large (Distinguished Professor, UTAS). I am not sure if he meant it.

- "Your work demonstrates some purpose", Dima Kamanetsky at the Graduate Research Poster presentation, 2015.

- By Paul Olin

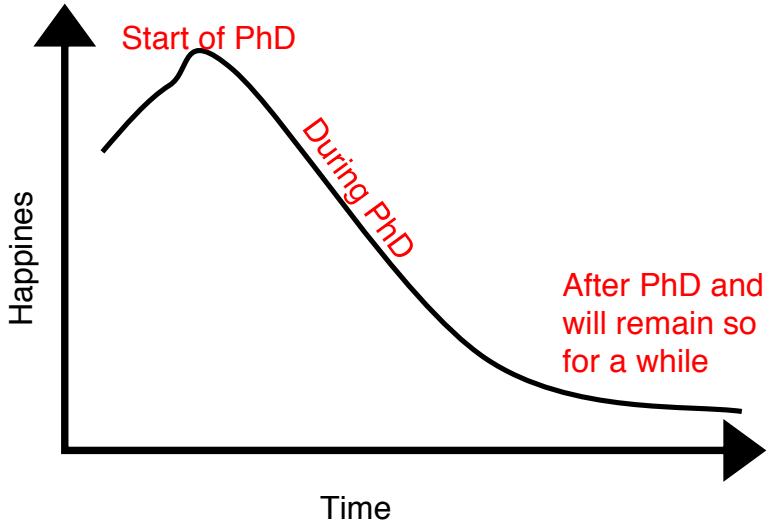

- "The trace element spectra of pyrites in sediments have been the subject of innumerable investigations with a view to using these as environmental indicators. Unfortunately, it is a common PhD topic suggestion and students are advised to steer well clear of accepting this subject for their PhD studies", David Rickard, 2012.

- "Accept it, you will hate it (PhD)", Togatus magazine, UTAS

- "Are you sure you want to do this?", Mukherjees'

Table of contents

List of Figures

List of Tables

List of Appendices

Abstract

This study focused on a particular time span in Earth's history known as the "Boring Billion" i.e., 1800-800 million years ago (Ma). This period has been referred to as a period of environmental stasis (geological and biological) that prohibited complex microscopic life forms to evolve into their macroscopic counterparts. Apart from absence of major biological evolutionary events, the period also lacks certain types of major ore deposits specifically, volcanic-hosted massive sulfides, orogenic gold deposits, Banded Iron Formations (BIFs), Mn oxide deposits and phosphorites. Major glaciation events, mineral species evolution (Hg, Be, B) and evidence for modern style plate tectonics are also lacking. Several studies in the past have applied different geochemical techniques such as, C, S, Cr, Sr, Fe, Tl, Zn and Mo isotopes and redox sensitive trace element (Mo, U, Se etc.) enrichments in marine sediments towards understanding the above-mentioned characteristics of this time span. Outcomes of previous research point toward this geo-biological stasis having been caused primarily by lack of adequate oxygen in the atmosphere and ocean in the Proterozoic, which resulted in a billion-year delay in biologic evolution.

Even though previous research suggests stasis during the "Boring Billion", primarily based on geochemical proxies, there appears to be a discord between geochemical signatures and paleo-biological observations in the rock record. Such as, certain key evolutionary breakthroughs including the evolution of the first complex eukaryotic cell and its cell organelles occurred during the "Boring Billion", including the first major diversification of eukaryotes and appearance of metaphytes. Also, the two major oxygenation events in Earth's history either pre-date or post-date major evolution events, for instance the Great Oxidation Event 1 at ~2.3 Ga (GOE 1) pre-dates the appearance of the first eukaryotic cell (~1.5 Ga) and the second great xidation event GOE 2 (~560 Ma) post-dates the rise of metazoans (~750 Ma). The discord exists mainly due to sole emphasis on the availability of oxygen in the atmosphere and the ocean (and their effect on evolution) by past researchers despite the fact that primitive organisms have known to require very small amounts of oxygen. Also, apart from oxygen, the role of bio-essential elements (Se, Ni, Mo, Zn, Mo etc.) and other toxic elements (W, Pb, As) have not been taken in to consideration even though they play a vital role in an organism's life both in terms of scarcity and abundance. These roles include forming enzymes or protein molecules that aid in basic cellular level functions and cater to nutritional requirements for growth and sustenance. Variations in trace element availability through the "Boring Billion" is therefore critical to our understanding and was addressed in this thesis.

This study investigated the importance of bio-essential trace element availability in the Proterozoic oceans using a novel technique, i.e., analysing bio-essential trace element concentrations and sulfur isotopic compositions in sedimentary pyrite in Proterozoic black shales using Laser Ablation-

Inductively Coupled Plasma- Mass Spectrometry (LA-ICP-MS) and Sensitive High Resolution Ion Microprobe- Stable Isotope (SHRIMP-SI) respectively, to further our understanding of the "Boring Billion". Considering high resolution temporal bio-essential trace elements trends are currently scarce in the literature, this study resolved the issue by systematic sampling of Proterozoic black shales from the McArthur and Mt Isa basins in northern Australia and Vindhyan Basin in central India. That was followed by pyrite LA-ICP-MS (~2000 analyses) to measure trace element concentrations of Se, Mo, Ni, Co, Bi, Cu, Zn, Mo, Pb, As, Tl, Cd, Ag, Au not only to reflect on their availability but also to infer paleo-redox structure of the Proterozoic oceans and atmosphere and its effect on biologic evolution. Additionally, pyrites used for LA-ICP-MS analyses were also analysed for sulfur isotope compositions using SHRIMP-SI to provide a more robust indicator of ocean redox conditions in the Proterozoic. Also, some black shales are known to host some of the world's largest Zn-Pb SEDEX style ore deposits, such as the Barney Creek Formation hosting the McArthur River deposit. This study also explored the possibility of using trace element concentrations in pyrite as mineralization vectors to McArthur River style Zn-Pb deposits in sedimentary basins.

There are four main conclusions from this PhD research discussed in separate chapters in the thesis. First, the pyrite LA-ICP-MS technique adopted for the study to measure trace element concentrations was proven to be a sensitive tool, that incorporated petrography and allowed better analytical detection limits than whole rock method, which was critical. Particularly in the Proterozoic where trace element signatures in the rock record are suppressed, the sensitivity of the technique, unlike the whole rock method, allowed robust trace element trends to be recognised. Second, this research demonstrates how redox sensitive trace element concentrations in sedimentary pyrite and their ratios can be effectively used as proxies for tracking nutrient-productivity cycles and atmospheric oxygenation through the "Boring Billion" period. Elements like Se, Zn, Ni, Co, Mo and Bi and their ratios (Se/Co, Ni/Co, Zn/Co, Mo/Co, Se/Bi, Ni/Bi, Mo/Bi, Zn/Bi) are particularly robust indicators. The research concludes that whilst certain trace elements show an increase in their concentrations in pyrite in response to rise in atmospheric oxygen such as Se, Zn, Ni and Mo, some elements show a decrease (Co, Bi) as the latter is relatively more readily adsorbed onto Fe-Mn hydroxides and oxides owing to their ionic forms. Therefore, an increase in elements like Se, Mo, Zn coupled with a decrease in Bi and Co is a more robust indicator of any proposed oxygenation event. Also, pyrite-sulfur isotope compositions obtained using SHRIMP-SI provide useful insights regarding ocean oxygenation. We suggest that an increase in mean pyrite sulfur isotope compositions ($\delta^{34}S_{VCDT}$ values) for black shales depositing under open ocean conditions is possibly indicative of progressive ocean oxygenation and a simultaneous decrease in areal extent of anoxia making it a more efficient reducing system. This causes the pyrites to exhibit heavy $\delta^{34}S_{VCDT}$ values. Third, variation in trace element concentrations in sedimentary pyrites from varying proximity to an ore body (in this case McArthur River deposit) are excellent mineralization vectors. Results demonstrate that elements like Mo, Ni, Co showed a consistent decrease in concentrations and Zn, Tl, Pb showed an increase, moving closer to mineralization. This was further used to construct pyrite vector diagrams that would aid in exploration for more Zn-Pb deposits (McArthur River style) in the McArthur Basin. Another important finding was that black shales

affected by mineralization events and hydrothermal activity should not be used to infer paleo-seawater chemistry as the trace element chemistry becomes altered significantly due to both mineralization and hydrothermal fluid activity. Therefore, for black shales known to host mineral deposits, caution during sampling is recommended; sampling black shales farthest from a mineralized zone is most preferable. Fourth, the thesis provides a novel and fresh perspective on the "Boring Billion" and highlights evidence against the current consensus on the significance of this time span. Findings from this study, for the first time, point towards a fluctuating trace element availability unlike the low and flat trends suggested by previous studies. This study observes both periods of low (1800-1400 Ma) and relatively high (1400-800 Ma) TE availability during the Proterozoic. Also, unlike previous research, I propose low trace element availability as a major driving force for evolution. The study concludes that periods of low nutrient TE caused an evolutionary pressure, and were essential triggers promoting biological innovations such as the emergence of the first complex cell (eukaryote) and periods of high TE promoted rapid diversification of eukaryotes.

Chapter 1

Introduction

1.0 Overview

The term "Boring Billion" has been referred to as the period spanning from 1.8 to 0.8 Ga in Earth's dynamic history. It covers the late part of Paleoproterozoic (Statherian), Mesoproterozoic and early Neoproterozoic (Tonian) (Fig. 1.1). The period is sometimes referred to as one of the "dullest periods" in Earth's history due to low carbon isotope values of marine carbonates from the Bangemall Group of northwestern Australia (Buick et al., 1995). The $\delta^{13}C$ isotope values from marine carbonates of the Mesoproterozoic rocks of the Bangemall Group showed very little variation with a mean value of – 0.5 ‰. (Buick et al, 1995). The values are much lower than values from rocks deposited in a similar environmental setting in the Neoproterozoic. It has been inferred that the organic carbon burial, redox state of the hydrosphere and atmosphere were fairly constant during the Mesoproterozoic. Brasier and Lindsay (1998) also noted a stable temporal $\delta^{13}C$ trend between 2.0-1.0 Ga, and recognised this period as a billion years of environmental stasis. These workers suggested that the prime cause of the stasis was suppressed tectonic activity (low lying cratons, lower levels of crustal activities and low weathering rates) that led to a decreased P (critical nutrient) supply to the ocean. Consequently, decreased nutrient supply had a major implication on biological evolution.

These two landmark papers drew the attention of researchers and the period of stasis became more recognisable through different geochemical approaches. Canfield (1998) added a new dimension to the Proterozoic ocean when he first described the Mesoproterozoic sulphidic deep ocean. The study argued that the "Great Oxidation Event 1" (GOE 1) between 2.3-2.2 Ga (Holland, 1994; Lyons et al., 2014) was not enough to foster deep ocean oxygenation. However, the O_2 concentration was enough to facilitate oxidative weathering that increased sulphate input into the ocean. This sulphate was reduced to hydrogen sulphide and converted to iron sulphides, particularly pyrite, by sulfur-using microbes via anoxygenic photosynthesis (a consequence of the sulphidic ocean) for their sustenance and proliferation (Kerr, 2005). Anoxygenic photosynthesis, unlike oxygenic photosynthesis, is a phototropic process, where a variety of reduced compounds such as H_2S, Fe^{2+} and other organic compounds are used as electron donors instead of water (Abelson, 2009). That is because it is easy to extract an electron from sulfur instead of a water molecule, making it a more favourable mechanism. Hence this mode of sulfur-based photosynthesis, which does not release oxygen, had the sulfur recycled and contained in the system. Furthermore, when these sulfur-using organisms died, they consumed any remaining oxygen by their decomposition. Hence all available iron was used up in precipitating pyrite hindering formation of BIF (Canfield, 1998). A transient increase in seawater sulphate concentration into the ocean (owing to GOE 1), anoxygenic photosynthesis

carried out by sulfur-loving microorganisms, and presence of sulfidic black shales along with a striking absence of BIF, underpinned Canfield's contention. Using the sulfur isotope record in non-hydrothermal sedimentary sulphides, Canfield (1998) suggested a transition from a Fe-rich ocean to a sulphidic ocean is recorded in the form of a small fractionation between sea-water sulphate and sulphide before 2.20-2.30 Ga and a relatively large fractionation (4 - 46 ‰) after 2.20-2.30 Ga (Fig. 1.2). The small fractionation (before 2.20-2.30 Ga) was attributed to limited availability of sulphate and vice-versa.

The sulphidic ocean possibly caused rapid drawdown of essential trace elements strongly affecting their bioavailability and hence prohibited or delayed eukaryotic evolution (Anbar and Knoll, 2002). The suggestion was that all the bio-essential trace elements (Mo, Fe, Se, V and Mn) required for N_2 fixation, were being scavenged by the H_2S-rich waters. This prohibited nitrogen from being bioavailable to photosynthetic eukaryotes as they are morphologically incapable of fixing nitrogen, unlike autotrophic bacteria. A N-limited environment could have been one of the reasons eukaryotic evolution was impeded. Molybdenum isotope signatures of euxinic sediments such as black shales of the Roper Group and Tawallah Group of the McArthur Basin, Australia, reflected a remarkable transition from Mn hydroxides and related sediments (f_{ox})/ euxinic sediments (f_{eux}) being < 0.4 in the Middle Proterozoic compared to ~3 today (Arnold et al, 2004). Low abundance of authigenic molybdenum in sulphidic black shales in the Proterozoic compared to the modern inventory, also suggested an expansion of sulphidic conditions during the Boring Billion period (Fig. 1.3) (Scott et al, 2008).

Other studies, including U abundance in sulfidic black shales, redox sensitive trace elements in sedimentary pyrite and Banded Iron Formations (BIF), Cr isotopes in iron formations and shales, Fe speciation, and N isotopes, all point towards low concentrations of oxygen in Proterozoic ocean and atmosphere (Arnold et al., 2004; Scott et al., 2008; Konhauser et al., 2011; Planavsky et al., 2013; Partin et al., 2013; Large et al., 2014; Planavsky et al., 2014; Lyons et al., 2014; Ader et al., 2014). Current consensus is that a lack of oxygen in the atmosphere and the oceans stalled evolution of the eukaryotes (Fig. 1.4).

Plate tectonics provides additional information for stasis as the Boring Billion was believed to mark a period of tectonic quiescence (Brasier and Lindsay, 1998). Geological and paleomagnetic evidence indicates that Columbia (amalgamated during 2.0-1.7 with collisional orogenesis at 1.95-1.85 Ga) remained intact despite several break-up attempts, indicated in the form of large coeval dyke swarms (Roberts, 2013) suggesting a period of suppressed tectonic activity during the Boring Billion. One could also attribute tectonic quiescence to lid tectonics as it is suggested that modern-style plate tectonics was not operative until the late Neoproterozoic (Piper et al., 2013). Lid tectonics is characterised by an absence (or only intermittent expression) of three key features of plate tectonics i.e., differential mobility,

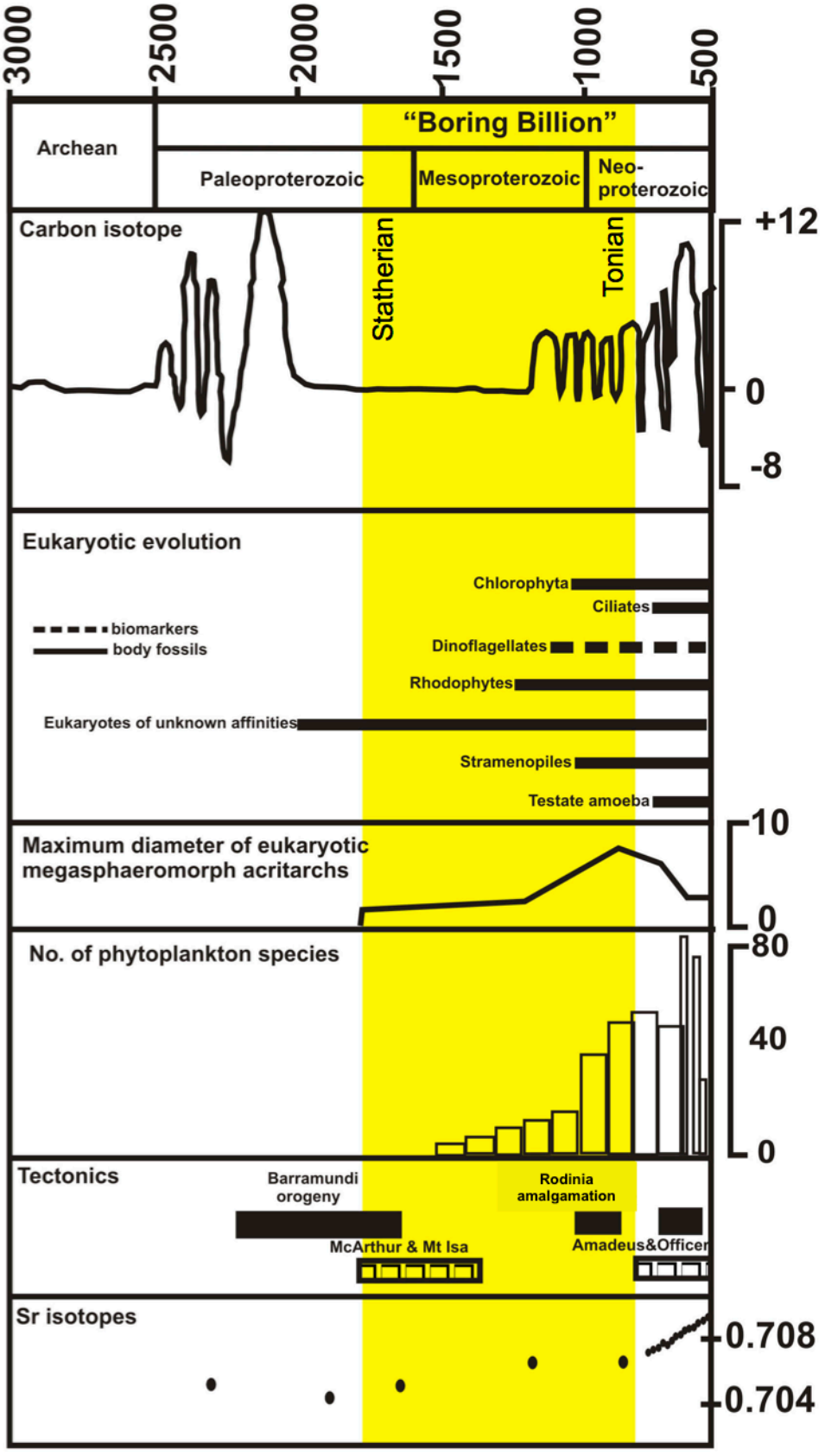

Fig. 1.1 Schematic representation of the biological, geochemical and tectonic activities during the boring billion period (Based on data compilation by Brasier et al, 1998)

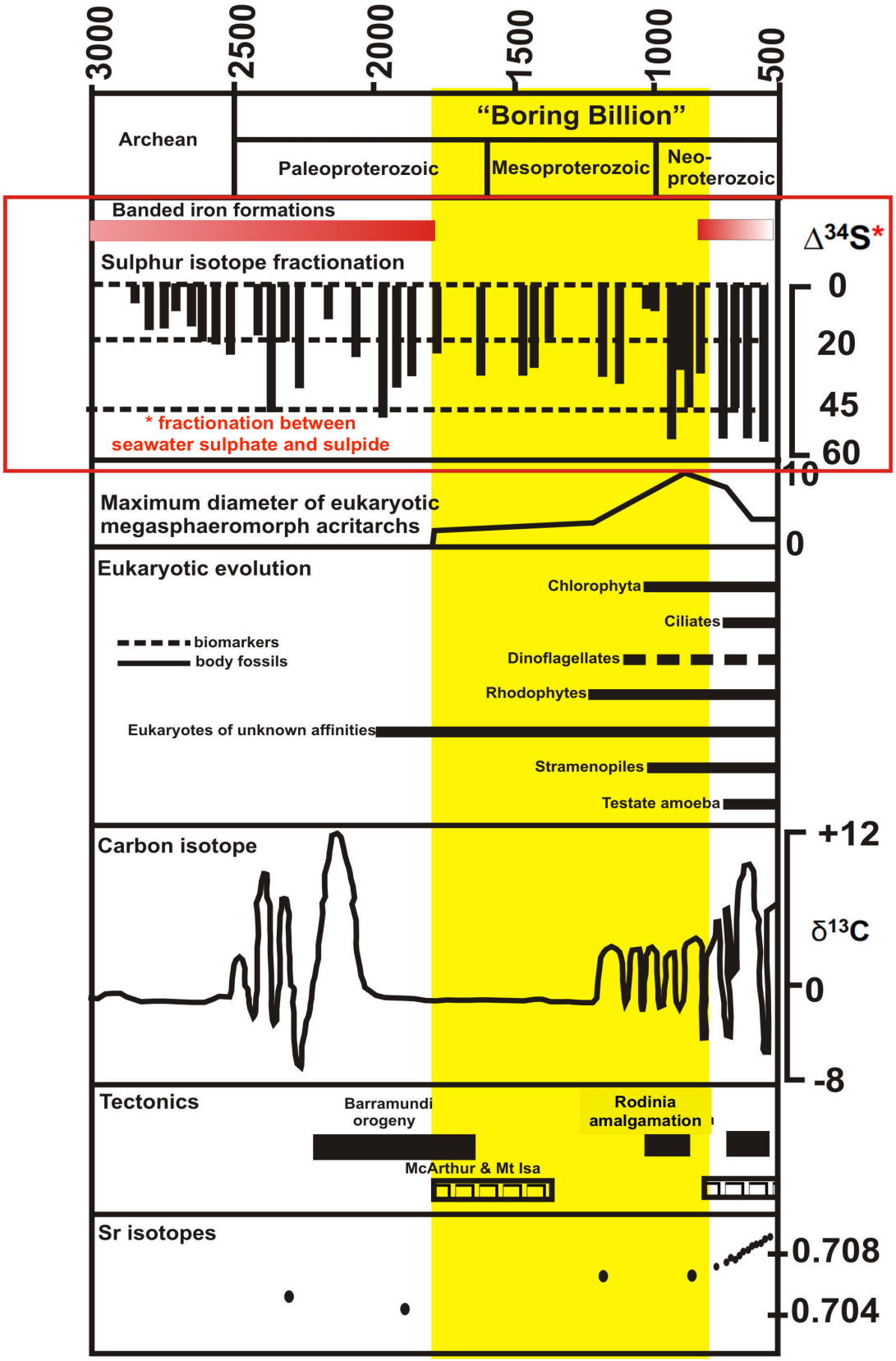

Fig. 1.2 Schematic representation of the biological, geochemical and tectonic activities during the boring billion period (Anbar and Knoll, 2002) *sulfur isotope fractionation b/w sea water sulphate and sedimentary pyrite from Canfield (1998)

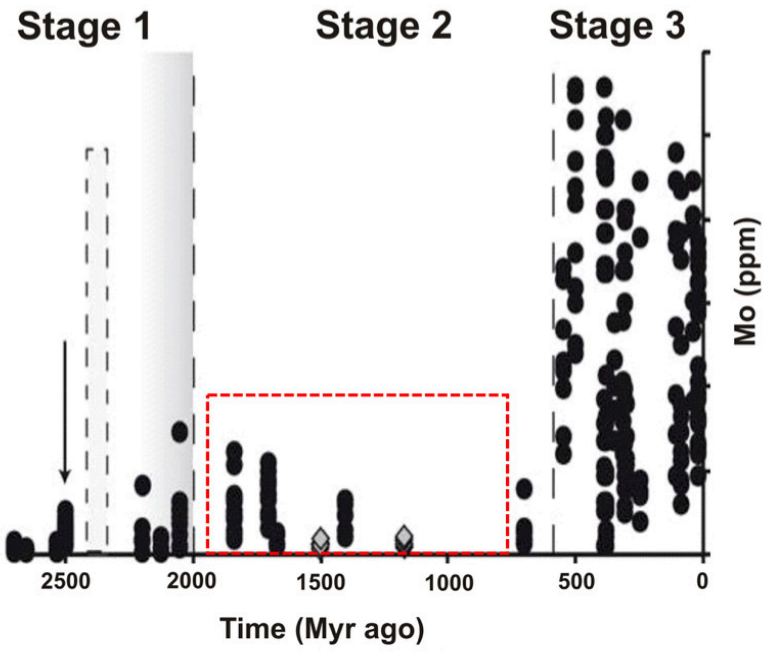

Fig. 1.3 Molybdenum abundance in black shales (black circles represent euxinic shales; grey diamonds represent non-euxinic organic rich shales (Scott el, 2008) Red square represents the Boring Billion

processes resulting from subduction and continent collision/break-up (Piper, 2013). It is generally viewed as whole lithosphere motion rather than lithospheric plates, over the mantle. It involves stagnant lid convection where an elastic shell forms as a result of conductive cooling of the lithosphere. Lid tectonics is currently operative in one-plate planets such Mars, Venus, Mercury etc. (Piper, 2013).

Since the evolution of the Earth's biosphere, atmosphere and hydrosphere are critically dependant on plate movements, suppressed or enhanced plate motion may have played an important role in evolution (Roberts, 2013). Previous studies have highlighted the role of tectonic activity in allowing high rates of organic C burial, due to increased continental margin lengths and opening of anoxic basins during periods of rifting (Bartley et al. 2000). Orogenesis, normally associated with high siliciclastic burial rates, may also result in changes in C burial rates, and therefore changes in C isotope signatures in the rock record. This however, does not rule out the effect of expanding biogenic ecosystems for instance; cyanobacteria ecosystems on C isotope signatures. Enhanced tectonic activity also promotes erosion/ weathering, causing P from sedimentary and igneous rocks to go into solution (riverine flux). Increased P subsequently stimulates and sustains primary productivity, which also affects the C isotope signatures (Brasier and Lindsay, 1998).

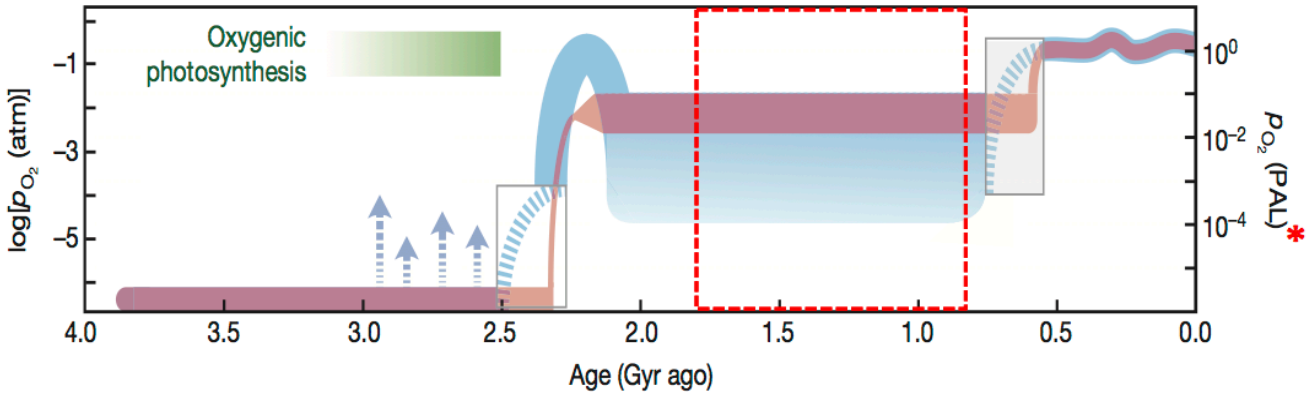

Fig. 1.4 Evolution of oxygen in atmosphere through time (Lyons et al., 2014); *PAL: Present atmospheric level; red rectangle represents the Boring Billion

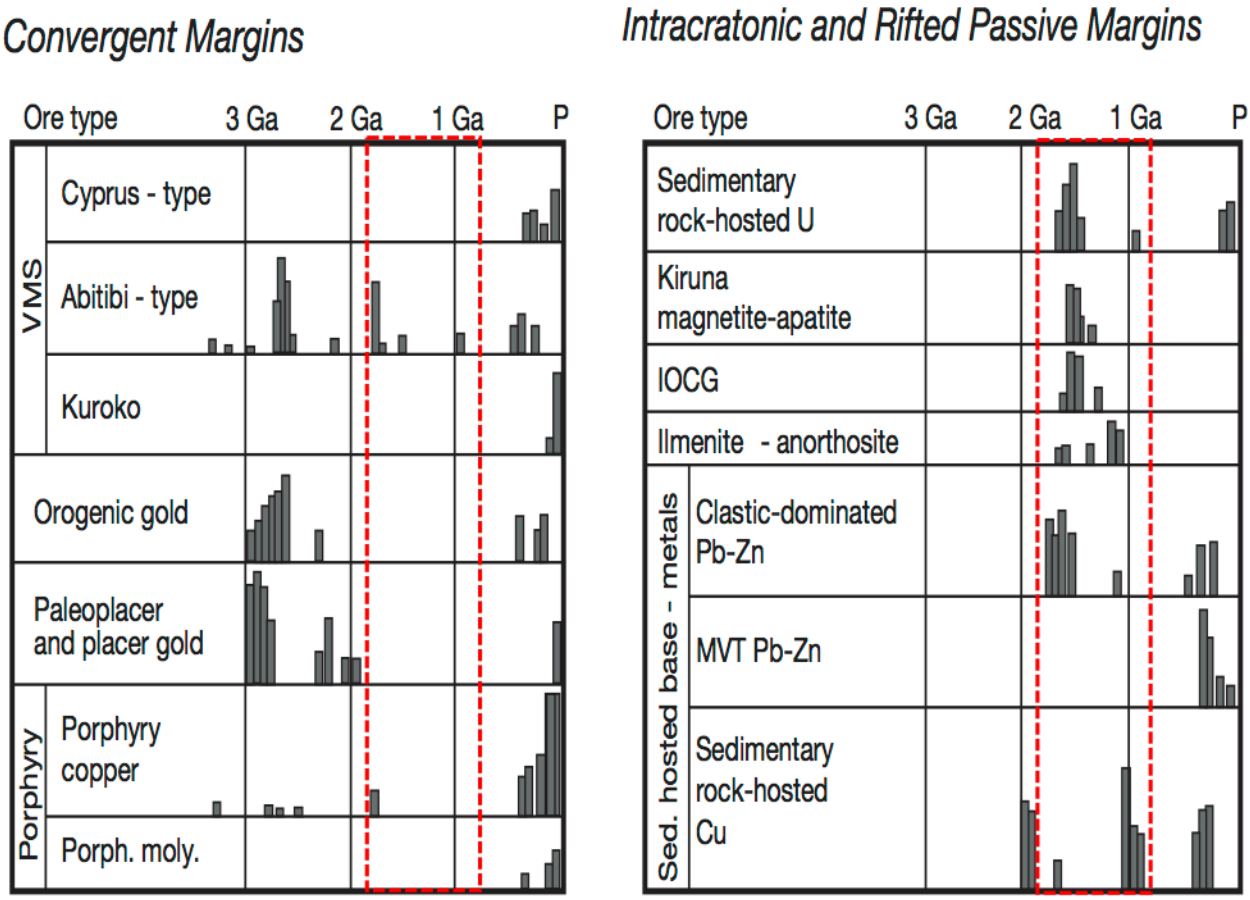

Fig. 1.5 Ore deposits through time (Goldfarb, 2010); red rectangle represents the Boring Billion

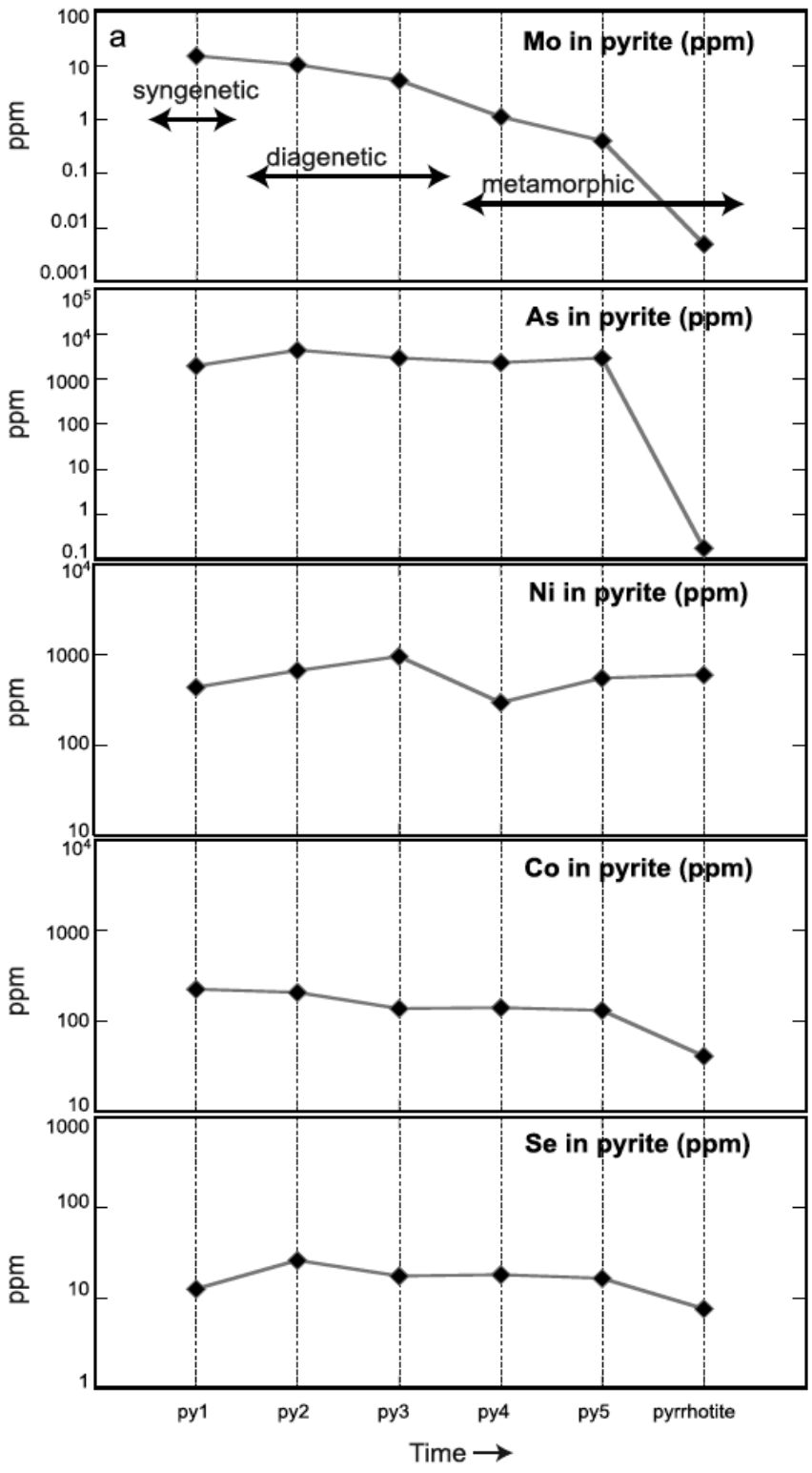

Fig. 1.6 Variation in trace element concentration in different pyrite types (Large et al., 2014); py1= syngenetic to early diagenetic pyrite; py2= early diagenetic pyrite; py3= late diagenetic pyrite; py4= metamorphic pyrite; py5= late metamorphic pyrite; pyrrhotite= late metamorphic pyrite replacing pyrite

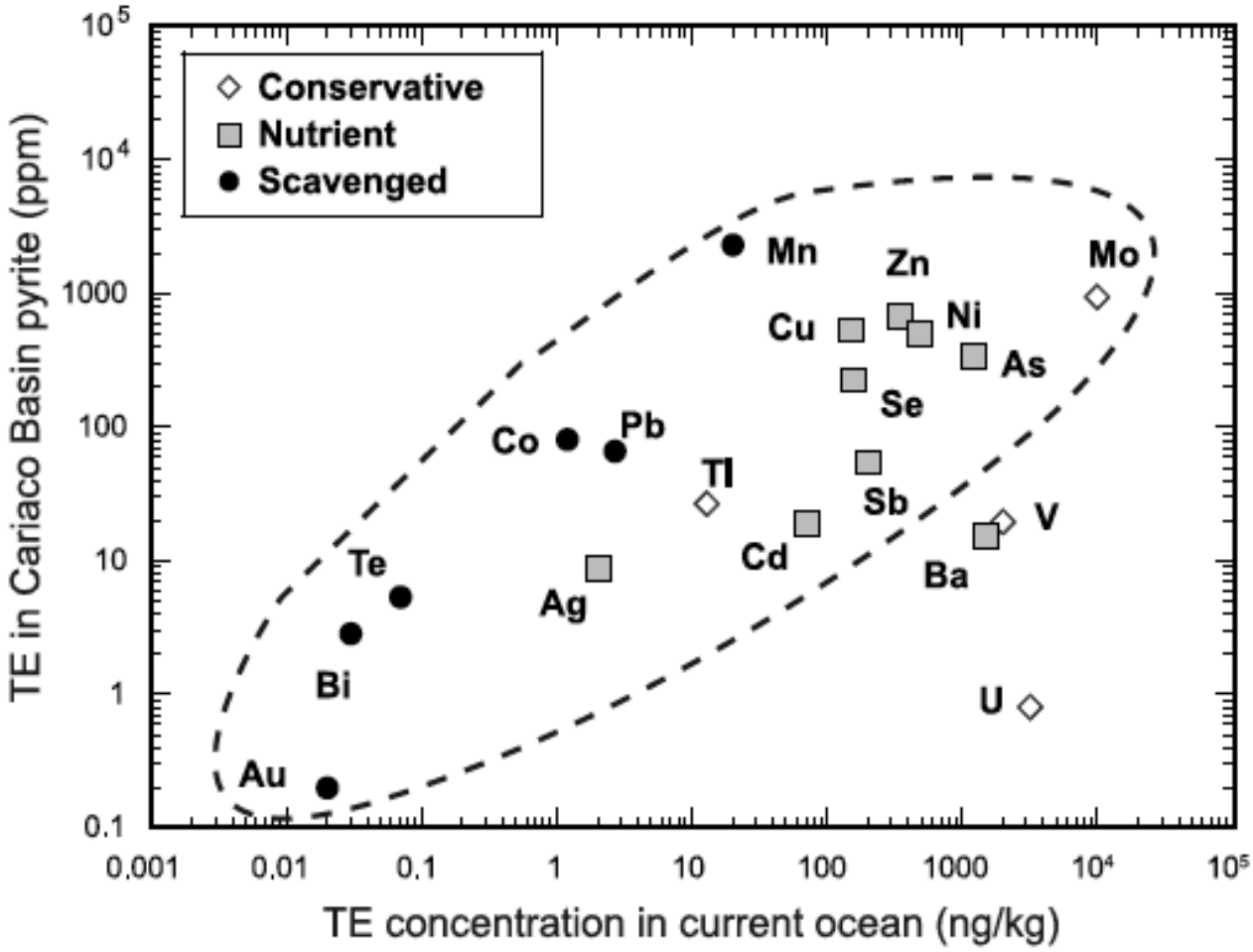

Fig. 1.7 Positive correlation between modern day trace element concentrations in the ocean and Cariaco Basin sedimentary pyrites (Large et al., 2014)

The temporal distribution of various types of ore deposits has been related to physio-chemical changes associated with the evolution of the Earth (Goldfarb et al., 2010). It has been observed that certain deposit types exhibit a secular pattern of occurrence depending on events like supercontinental cycles, juvenile crustal growth and periods of cratonisation and orogenesis (Goldfarb et al, 2010).

Ore deposit types such as VMS, orogenic gold, paleoplacers and paleoplacer Au, porphyry deposits (Cu/Mo/Au), sedimentary Cu and MVT type deposits are strikingly absent in the Boring Billion (Fig. 1.5). A lack of banded iron formations, marine manganese deposits, major evaporites and phosphorites is also noteworthy. However, their presence is noted in the geologic record both before 1.8 and after 0.8 Ga (Holland, 2006).

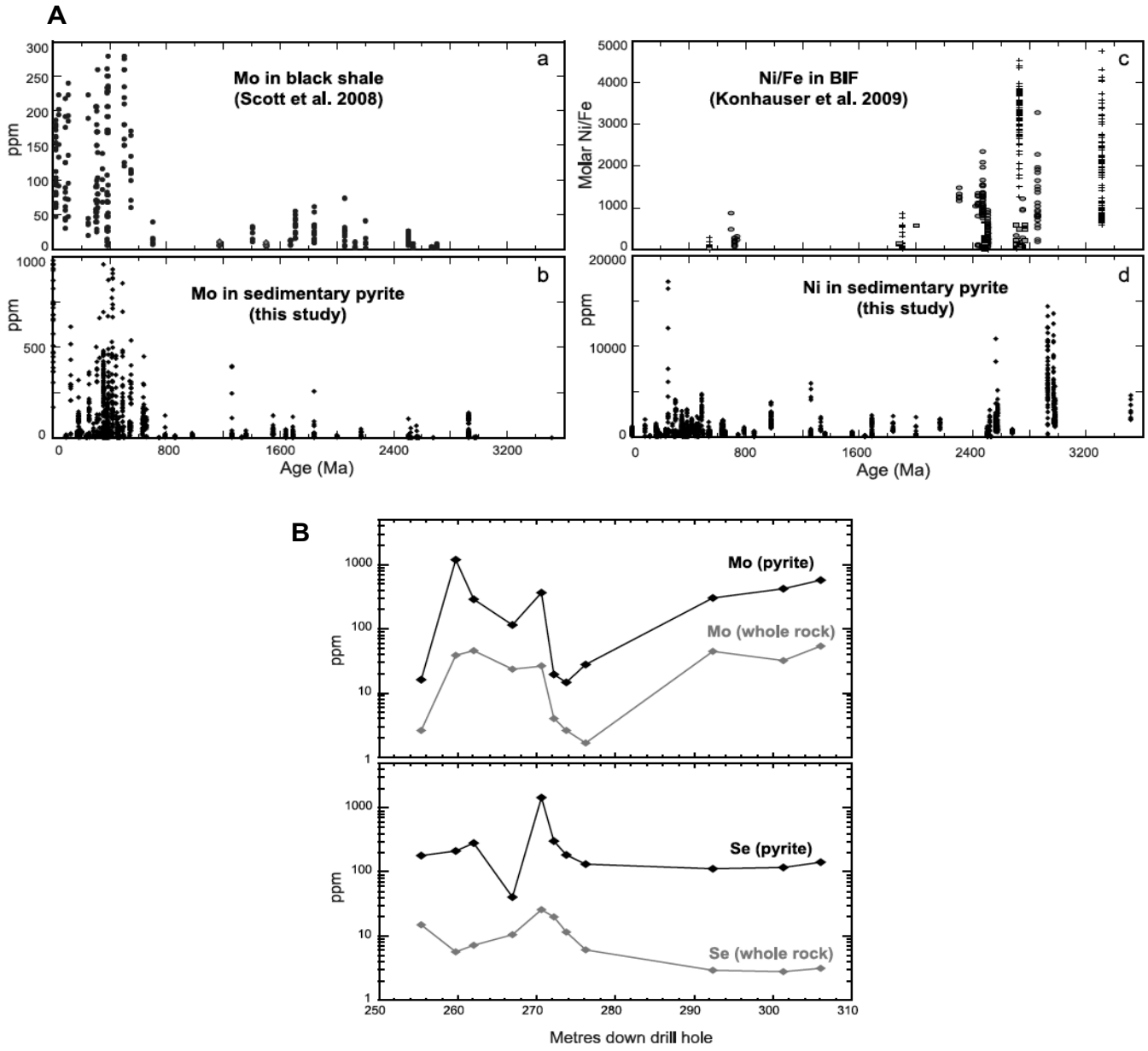

Fig. 1.8 A) Comparison of published data obtained using conventional whole rock technique with pyrite-LA-ICP-MS data from Large et al. (2014); B) Down hole comparison of whole rock analyses of black shales vs LA-ICP-MS sedimentary pyrite analyses.

From a mineralogists' point of view, the time span marks a delay in mineral evolution of certain elements. For instance, mercury mineral diversity was noted after the first rise of oxygen in the atmosphere i.e., GOE 1 (Hazen, 2012). However, lack of sufficient oxygen and a sulphidic ocean may have hindered mineral diversity as mercury atoms readily reacted with the sulfur to form cinnabar, which is very insoluble. It was not until 600 Ma, when oceans became oxygenated, that the population of mercury minerals rapidly increased. Other minerals showing similar trends are Be and B species (Hazen, 2012).

1.1 Gaps in our knowledge

Detailed literature review has revealed gaps in our knowledge concerning the Boring Billion. Firstly, even though a period of biological stasis was proposed for the Boring Billion we observe some critical evolutionary breakthroughs in this period. These include: the appearance of eukaryotes (including cell organelles) via endosymbiosis, multicellularity and the origin of sexual reproduction (Butterfield, 2015; Knoll, 2014; Katz, 2012; Porter, 2004), and the evolution of precursors of metazoans (Urmetazoa) (Muller, 2001; Wray et al., 1996).

After GOE 1, an important transition from prokaryotes to eukaryotes occurred at ~1.9 Ga (Anbar and Knoll, 2002; Butterfield, 2015). Further at 1.4 Ga, a two-stage diversification of eukaryotes is recognised, where key biological innovations are observed (Javaux et al., 2001; 2004; 2017). These include morphological complexities, e.g., cytoskeleton and membrane system etc. This was followed by another major diversification (1.2-0.75 Ga) that occurred within the subgroup with the appearance of red algae.

Current understanding is that a rise in atmospheric O_2 and ocean oxygenation (deep + surface) causes an increase in the complexity of multi-cellular life forms (Planavsky et al., 2014). Interestingly, we observe the first major diversification of eukaryotes (Crown group), appearance of metaphytes and metazoans (Knoll, 2014; Erwin et al., 2011) before the second Great Oxidation Event (GOE 2; Canfield, 2005), indicating that oxygen may not have been the only driver of these developments. Experiments also support low oxygen requirements of modern analogues of primitive metazoans (Danovaro et al., 2010).

Supressed or minimal tectonic activity during the Boring Billion is stated as one of the causes of the stasis (Brasier and Lindsay, 1998). However, extensive orogenesis occurred during the Late Paleoproterozoic, as evidenced by the widespread Svecofennian, Hudsonian, and Barramundi orogenies along with amalgamation of Laurentia between 1910 and 1630 Ma (Hoffman, 1988). Major collisional belts e.g., Grenvillian orogeny, also formed during the Boring Billion, along with two supercontinents (Columbia and Rodinia) (Roberts, 2013). Rifting of the Columbian supercontinent between 1450 Ma-1380 Ma (cf.

Pisarevsky et al., 2014) resulted in the deposition of huge sedimentary sequences, and the transformation from Columbia to Rodinia brought about major environmental changes at ~1300 Ma (Roberts, 2013). The onset of arc formation and arc-continent collisions at the margins of Laurentia began ca. 1300 Ma, marking the beginnings of Rodinia. The protracted assembly event ultimately resulted in continent–continent collision and the uplift of a global chain of mountain belts over the interval 1160–1050 Ma (Dalziel, 1991; Hoffman, 1991). Therefore, tectonic quiescence, which is one of the main explanations for the stasis, is doubtful.

Although several major deposit-types are absent in this period, we do observe clustering of clastic-dominated Pb-Zn & sediment-hosted U deposits in the early part of the Boring Billion, and MVT Pb-Zn deposits in its later part (Goldfarb et al, 2010). Also, Kiruna magnetite-apatite, IOCG, and ilmenite-anorthosite deposits occur in the early to middle part of the Boring Billion (Fig. 5). Sedimentary rock-hosted Pb-Zn deposits have a complex secular distribution in close association with the oxygenation of Earth (Leach et al., 2010). Clastic-dominated Pb-Zn ores forming within passive margins, back-arc regions, and continental rifts, first become significant in the geologic record between 2.0 to 1.6 Ga (Fig. 5). Their emergence correlates with significant near-surface Earth changes owing to GOE 1, which include increased sulfate availability, enhanced Pb and Zn mobility in the surface environment, formation of sulfate-bearing evaporates and red beds, abundance of sulfate-reducing bacteria, and the development of important redox gradients.

Most bio-geochemical studies undertaken to understand the "Boring Billion" center around the availability of oxygen and its effects on life. Any one element (e.g. O) cannot account for the course of biologic evolution (Kobayashi & Ponnamperuma., 1985). A suite of bio-essential elements including H, C, N, O, P, S, Cl, Na, Mg, K, Ca, Fe, Al, Si (macro elements) and V, Cr, Mn, Co, Ni, Cu, Zn, Mo, B, F, As, Se (trace elements) are required for all kinds of life forms (Kobayashi & Ponnamperuma, 1985). With the possible exception of Fe, major elements are not limiting in nature, unlike trace elements, which are scarce by definition. Thus, knowledge of nutrient trace element variability in the ocean is an essential aspect in understanding biologic evolution. This aspect has yet to be fully explored, and is the main focus of this dissertation.

1.2 PhD research questions

The PhD research aims to answer the following questions:

1. How can we use trace element concentrations in sedimentary pyrite, and sulfur isotope compositions of sedimentary pyrite in black shales, to infer paleo-atmospheric ocean redox structure and nutrient-productivity cycles in the Boring Billion period?

2. Does hydrothermal alteration affect sedimentary pyrite chemistry, and can this be used as a mineralisation vector?

3. How do trace element concentrations in pyrite reflect their availability in the oceans during the "Boring Billion"? If so, what are the possible factors controlling their availability in the oceans?

4. What are the possible implications of trace element availability in the oceans on biologic evolution during the Boring Billion?

1.3 Method

Systematic sampling of Proterozoic black shales was undertaken for this study. Four black shale formations from the McArthur Basin were sampled (Corcoran Formation, Velkerri Formation, Barney Creek Formation, Wollogorang Formation), along with the Riversleigh Siltstone from the Mt Isa Basin, Australia, and the Bijaigarh Shale from the Vindhyan Basin in central India. Drill core samples were collected for all black shale formations studied except the Bijaigarh Shale, in which case we used samples from mine adits. A total of ~2000 pyrite analyses were carried out as part of this study, using Laser Ablation-Inductively Coupled Plasma-Mass Spectrometry (LA-ICP-MS). Sulfur isotope analysis of the same sedimentary pyrites was undertaken using Sensitive High Resolution Ion Microprobe-Stable Isotope (SHRIMP-SI). Details of instrumentation (LA-ICP-MS and SHRIMP-SI) are described in subsequent chapters. Below is the rationale behind using sedimentary pyrite for trace element and sulfur isotope analyses using LA-ICP-MS and SHRIMP-SI respectively and proof of concept.

1.3.1 Pyrite LA-ICP-MS

Certain redox-sensitive trace elements (Mo, U, Cr, V, Zn) in black shales have been used previously as paleo-redox indicators of the water column (Algeo et al., 2006; Tribovillard et al., 2006; Algeo et al., 2009; Algeo et al., 2012; Meyer et al., 2008; Gordon et al., 2009; Sahoo et al., 2012; Sahoo et al., 2016). Futhermore, the same elements have been used to track atmospheric oxygenation through time (Scott et al., 2008; Partin et al., 2013; Lyons et al., 2014). The present study focuses on using a technique where trace element concentrations in sedimentary pyrite, determined using LA-ICP-MS, provide useful first order (semi-quantitative) insights on trace element availability in the ocean (Large et al., 2014). The premise on which the technique is based is that enhanced oxidative weathering on land causes an increase in the supply of redox-sensitive trace elements in the riverine flux (dominant source) to the ocean (Bertine et al., 1973; Taylor et al., 1995; Scott et al., 2008; Sahoo et al., 2012; Crowe et al., 2013). These redox-sensitive trace elements, on encountering the redox-boundary, become readily adsorbed by sedimentary pyrites in anoxic black shales forming in bottom waters and pore waters (Huerta-Diaz and Morse, 1992; Morse and Arakaki, 1993, Rickard et al., 2012; Gregory et al., 2014; Large et al., 2014; Gregory et al., 2015a, 2015b, 2016; Steadman et al., 2015). The validity of the technique has been the subject of several publications (Gregory et al., 2014; Large et al., 2014; Gregory et al., 2015a; Gregory et al., 2015b, Steadman et al., 2015; Gregory et al., 2016), which includes the proof of concept paper (Large et al., 2014). These extensive studies have shown that redox sensitive trace element concentrations in sedimentary pyrites act as an indirect first order proxies for atmospheric oxygenation events.

The proof of concept paper (Large et al., 2014) outlined four major lines of evidence towards validating the technique. First, both syngenetic and early-diagenetic pyrite record seawater trace element chemistry as they form in the water column and in pore waters in the seafloor muds, respectively (Huerta-Diaz and Morse, 1992). Pore waters in sediments where early-diagenetic pyrites form typically contain 60-85 % seawater within the first few centimeters, and over 40 % in the top 100-200 m (Large et al., 2014). Due to this, trace element content in early-diagenetic pyrites may vary from their syngenetic counterparts. However, the variation is only 1.4 to 6 times compared to 2 to 4 orders of magnitude noted in pyrite analyses through time (Large et al., 2014). Second, the importance of textural screening prior to LA-ICP-MS analyses was emphasized. Large et al. (2014) demonstrated that trace element content gradually decreases with increasing diagenetic and metamorphic influence (Fig 1.6). Also, in any given sample it was found that trace element concentration was invariant to the size of framboids. Third, modern day sedimentary pyrite analyses from the Cariaco Basin on the Venezuela Shelf were compared with modern day trace element concentrations in seawater. A positive correlation was noted between both datasets where the trace elements in the Cariaco Basin pyrites were enriched 5-8 orders of magnitude relative

to seawater (Fig. 1.7) (Large et al., 2014). Fourth, trace element concentrations in pyrite (particularly, Mo) were compared with trace elements measured via conventional whole rock method in black shales and Banded Iron Formations. Strikingly similar trends were observed, with trace elements being 10-100 times enriched in pyrite compared to whole rock (Fig. 1.8a, 8b). All these lines of evidence confirm that trace elements in marine sedimentary pyrites can be used to track past changes in ocean trace element concentrations in a first order sense.

1.3.2 Pyrite-SHRIMP-SI

Bulk rock sulfur (^{32}S and ^{34}S) isotope compositions of the McArthur Basin sediments have been previously studied by various researchers to gain an understanding of biogeochemical cycles of sulfur (Donnelly and Jackson, 1988; Canfield, 1998; Shen et al., 2002; Shen et al., 2003; Kah et al., 2004; Lyons et al., 2006; Johnston et al., 2008). Additional information on depositional environment, microbial activity and connectivity to the global ocean can be obtained using isotopes such as ^{33}S and ^{36}S (Johnston et al., 2008). Sulfur isotopic compositions of the McArthur Basin sediments have also been reported previously in order to understand changes in seawater sulphate concentration and the sulphate reservoir, biogeochemical sulfur isotope fractionation patterns, global oxidative sulfur cycling and redox stratification of the Proterozoic oceans (Shen et al., 2002; Kah et al., 2004; Johnston et al., 2008; Luo et al., 2015). The present study carried out sulfur isotope analyses of sedimentary pyrites, in combination with trace element concentrations, to provide additional insight into changes in biogeochemical processes operative during the deposition of the black shale formations.

1.3.3 Advantages of sedimentary pyrite trace element and sulfur isotope compositions

There are several advantages of using sedimentary pyrite to understand trace element concentrations (using LA-ICP-MS) and sulfur isotope compositions (using SHRIMP-SI) as previously highlighted in Gregory et al. (2014), Large et al. (2014), Gregory et al. (2015a), Gregory et al. (2015b), Steadman et al. (2015), Gregory et al. (2016).

Both techniques (LA-ICP-MS and SHRIMP-SI) are highly sensitive and allow better detection limits than whole rock (particularly for elements like Se and Mo when using LA-ICP-MS). Secondly, both techniques analyze one mineral, pyrite, avoiding the problem of variation in composition and isotope ratios of different minerals in the shales. Many TEs, such as Mo, are partitioned between minerals in the shale (Tribovillard et al., 2006), and thus variation in mineral composition affects the bulk rock analyses. Thirdly and most importantly, the effects of diagenesis, metamorphism and hydrothermal activity, which affect trace element concentrations and sulfur isotopic compositions, can easily be detected by textural study

of the pyrite before analyses. In the case of trace elements, Large et al. (2009) demonstrated that the process of recrystallization (due to diagenesis or metamorphism), releases most trace elements to form trace elements-poor subhedral to euhedral forms of pyrite. Hydrothermal pyrites, on the other hand, may be enriched or depleted in trace elements depending on the conditions of formation (temperature, salinity and proximity to vents). The concentrations in metamorphic and hydrothermal pyrites therefore do not reflect primary first order trace element concentrations of the global ocean (Large et al., 2014).

1.4 Thesis structure

The thesis comprises five manuscripts systematically prepared in accordance with the PhD research questions, including technique validation for pyrite LA-ICP-MS analysis.

Paper 1 objectives: The primary objective of the first manuscript was to understand trace element concentrations in sedimentary pyrites in the Velkerri Formation and Corcoran Formation in the Roper Group of the McArthur Basin. It also compared pyrite LA-ICP-MS and bulk rock techniques to highlight advantages of the pyrite-LA-ICP-MS technique, and validated the use of trace element concentrations to infer paleo redox conditions. The first manuscript focussed on research question 1.

Paper 2 objectives: The objective of the second manuscript was to investigate the possibility of using pyrite chemostratigraphy as an exploration tool for mineralization because certain black shales in the Boring Billion period, selected for interpreting paleo-redox conditions, are also known to host world class-Zn-Pb SEDEX style mineralization. Trace element concentrations in sedimentary pyrites from increasing distance from an ore body were analysed to observe systematic variations (if any) and to evaluate whether they could be used as pathfinders (vectors) in mineral exploration. This has implications for sampling potentially mineralised black shales for paleo-redox interpretations. The second manuscript focussed on research question 2.

Paper 3 objectives: The objective of the third manuscript was to combine two complementary techniques (pyrite-LA-ICP-MS and pyrite-SHRIMP-SI) in order to use both trace element concentrations and sulfur isotopic compositions of sedimentary pyrite to provide insights into biogeochemical processes operative in the McArthur Basin in Northern Australia during the "Boring Billion". The primary aim was to test if we could use trace elements and their ratios as atmospheric oxygenation proxies, and sulfur isotopic compositions as an ocean oxygenation proxy. Statistical tests to verify results of the pyrite analyses owing to their variability were also undertaken. The third manuscript focussed on research questions 1 and 3.

Paper 4 objectives: The fourth manuscript applied the pyrite LA-ICP-MS technique to a black shale formation (Bijaigarh Shale) in the Vindhyan Basin, India. A detailed pyrite textural study was combined with trace element concentrations to infer Mesoproterozoic (~1210 Ma) atmospheric redox conditions in the Vindhyan Basin. The fourth manuscript focussed on research question 1.

Paper 5 objectives: The fifth manuscript, combined data from previous manuscripts and new pyrite analyses from a black shale formation (Riversleigh Siltstone) in the Mt. Isa Basin to obtain trace element trends for an overall understanding of the Boring Billion. The main aim was to discuss the role of atmospheric oxygenation and nutrient-productivity cycles in the oceans, and its profound effect on evolution of Earth's first complex organisms. The fifth manuscript focussed on research question 4.

Synthesis: Major findings of these papers were summasrised along with potential future research lines that were identified over the course of this thesis.

1.5 References

Abelson, J., 2009. The birth of oxygen. Scientific Insights into the Evolution of the Universe and of Life Pontifical Academy of Sciences, Acta 20.

Ader, M., Sansjofre, P., Halverson, G.P., Busigny, V., Trindade, R.I.F., Kunzmann, M., Nogueira, A.C.R., 2014. Ocean redox structure across the Late Neoproterozoic Oxygenation Event: A nitrogen isotope perspective. Earth and Planetary Science Letters 396, 1–13

Algeo, T.J., Lyons, T.W., 2006. Mo–total organic carbon covariation in modern anoxic marine environments: Implications for analysis of paleoredox and paleohydrographic conditions. Paleoceanography 21, 1- 23.
Algeo, T.J., Rowe, H., 2012. Paleoceanographic applications of trace-metal concentration data. Chemical Geology 324, 6–18.

Algeo, T.J., Tribovillard, N., 2009. Environmental analysis of paleoceanographic systems based on molybdenum-uranium covariation. Chemical Geology 268, 211–225.

Anbar, A.D. & Knoll, A.H., 2002 Proterozoic ocean chemistry and evolution: a bioinorganic bridge? Science 297, 1137–1142

Arnold, G.L., Anbar, A.D., Barling, J., Lyons, T.W., 2004. Molybdenum isotope evidence for widespread anoxia in Mid-Proterozoic ocean. Science 304, 87-90.

Bartley, J.K., Semikhatov, M.A., Kaufman, A.J., Knoll, A.H., Pope, M.C., Jacobsen, S.B., 2001. Global events across the Mesoproterozoic–Neoproterozoic boundary: C and Sr isotopic evidence from Siberia. Precambrian Research 111, 165–202

Bertine, K.K., Koide, M., and Goldberg, E.D., 1996. Comparative marine chemistries of some trivalent metals-bismuth, rhodium and rare Earth elements. Mar. Chem. 53, 89–100.

Brasier, M.D., Lindsay, J.F., 1998. A billion years of environ- mental stability and the emergence of eukaryotes: new data from northern Australia. Geology 26, 555–558.

Buick, R., Des Marais, D.J., Knoll, A.H., 1995. Stable isotopic compositions of carbonates from the Mesoproterozoic Bangemall Group, northwestern Australia. Chem. Geol. 123, 153–171.

Butterfield, N.J., 2015. Early evolution of the Eukaryota: Palaeontology 58, 5–17.

Canfield, D.E., 1998. A new model for Proterozoic ocean chemistry: Nature 396, 450–453.

Canfield D. E., 2005. The early history of atmospheric oxygen: homage to Robert M. Garrels. Annu. Rev. Earth Planet. Sci. 33, 1–36.

Chen, J., Walter, M.R., Logan, G.A., Hinman, M.C. and Summons, R.E., 2003. The Paleoproterozoic McArthur River (HYC) Pb/Zn/Ag deposit of northern Australia: organic geochemistry and ore genesis. Earth and Planetary Science Letters 210, 467-479.

Crowe, S.A., Døssing, L.N., Beukes, N.J., Bau, M., Kruger, S.J., Frei, R., Canfield, D.E., 2013. Atmospheric oxygenation three billion years ago. Nature 501, 535–538.

Dalziel, I.W.D., 1991. Pacific margins of Laurentia and East Antarctica–Australia as a conjugate rift pair: evidence and implications for an Eocambrian supercontinent. Geology 19, 598–601.

Danovaro, R., Dell'Anno, A., Pusceddu, A., Gambi, C., Heiner, I., and Reinhardt Møbjerg, K., 2010. The first metazoa living in permanently anoxic conditions: BioMed Central Biology, 8:30. doi: 10.1186/1741-7007-8-30.

Donnelly, T.H. and Jackson, M.J., 1988. Sedimentology and geochemistry of a mid-Proterozoic lacustrine unit from northern Australia. Sedimentary Geology 58, 145–169.

Erwin, D.H., Laflamme, M., Tweedt, S.M., Sperling, E.A., Pisani, D., and Peterson, K.J., 2011, The Cambrian conundrum: early divergence and later ecological success in the early history of animals: Science, 334, 1091–1097.

Farquhar, J., Wu, N-P., Canfield, D.E., and Oduro, H., 2010. Connections between sulfur cycle evolution, sulfur isotopes, sediments, and base metal sulfide deposits: Econ Geol, 105, 509–533.

Goldfarb, R.J., Bradley, D., Leach, D.L., 2010. Secular Variation in Economic Geology. Econ Geol. 105, 459-465.

Gordon, G.W., Lyons, T.W., Arnold, G.L., Roe, J., Sageman, B.B., Anbar, A.D., 2009. When do black shales tell

molybdenum isotope tales? Geology 37, 535–538.

Gregory, D.D., Large, R.R., Bath, A.B., Steadman, J.A., Wu, S., Danyushevsky, L., Bull, S.W., Holden, P., and Ireland, T.R., 2016, Trace Element Content of Pyrite from the Kapai Slate, St. Ives Gold District, Western Australia: Economic Geology 111 (6), 1297-1320.

Gregory, D.D., Large, R.R., Halpin, J.A., Steadman, J.A., Hickman, A.H., Ireland, T.R., and Holden, P., 2015, The chemical conditions of the late Archean Hamersley basin inferred from whole rock and pyrite geochemistry with Δ 33 S and δ 34 S isotope analyses: Geochimica et Cosmochimica Acta 149, 223-250.

Gregory, D., Meffre, S., and Large, R., 2014. Comparison of metal enrichment in pyrite framboids from a metal-enriched and metal-poor estuary: American Mineralogist 99 (4), 633-644.

Gregory, D.D., Large, R.R., Halpin, J.A., Lounejeva Baturina, E., Lyons, T.W., Wu, S., Sack, P.J., Chappaz, A., Maslennikov, V.V., Bull, S.W., Danyushevsky, L., 2015a. Trace element content of sedimentary pyrite in black shales. Econ. Geol. 110, 1389–1410.

Hazen Robert, 2012. The story of Earth. Penguin books. pp.320

Hoffman, P.F., 1988. United plates of America, the birth of a craton; early Proterozoic assembly and growth of Laurentia. Annu. Rev. Earth Pl. Sci. 16, 543–603.

Hoffman, P.F., 1991. Did the breakout of Laurentia turn Gondwanaland inside-out? Science 252, 1409–1412.

Holland H.D., 1994. Early Proterozoic atmospheric change. Early Life on Earth, ed. Bengston S (Columbia Univ Press, New York), pp 237–244.

Holland. H.D., 2006. The oxygenation of the atmosphere and oceans Phil. Trans. R. Soc. 361.

Huerta-Diaz, M.A., Morse, J.W., 1992. Pyritization of trace metals in anoxic marine sediments. Geochim. Cosmochim. Acta 56, 2681–2702

Javaux E.J., Knoll, A.H., Walter, M.R., 2001. Morphological and ecological complexity in early eukaryotic ecosystems. Nature 412, 66–69.

Javaux, E., Knoll, A.H., and Walter, M.R., 2003. Recognizing and interpreting the fossils of early eukaryotes: Origins of Life and Evolution of the Biosphere 33, 75–94.

Javaux, E., Knoll, A.H., Walter, M.R., 2004. TEM evidence for eukaryotic diversity in mid-Proterozoic oceans. Geobiology 2, 121–132.

Johnston, D.T., Farquhar, J., Summons, R.E., Shen, Y., Kaufman, A.J., Masterson, A.L., Canfield, D.E., 2008. Sulfur isotope biogeochemistry of the Proterozoic McArthur Basin. Geochim. Cosmochim. Acta 72, 4278–4290.

Kah, L.C., Lyons, T.W., Frank, T.D., 2004. Low marine sulphate and protracted oxygenation of the Proterozoic bio- sphere. Nature 431, 834–838.

Katz, L.A., 2012. Origin and diversification of eukaryotes: Annual Review of Microbiology 66, 411–427.

Kerr, R.A., 2005. The story of O2. Science 308, 1730-1732.

Knoll, A.H., 2014. Paleobiological perspectives on early eukaryotic evolution: Cold Spring Harbor Perspectives in Biology, doi:10.1101/cshperspect.a01612.

Kobayashi, K., and Ponnamperuma, C., 1985. Trace elements in chemical evolution, I. Origins of Life and Evolution of the Biosphere 16(1), 41-55.

Konhauser, K.O., Pecoits, E., Lalonde, S.V., Papineau, D., Nisbet, E.G., Barley, M.E., Arndt, N.T., Zahnle, K., and Kamber, B.S., 2009. Oceanic nickel depletion and a methanogen famine before the Great Oxidation Event. Nature 458, 750–753.

Large, R.R., Danyushevsky, L., Hollit, C., Maslennikov, V., Meffre, S., Gilbert, S., Bull, S., Scott, R., Emsbo, P., Thomas, H., Singh, B., Foster, J., 2009. Gold and trace element zonation in pyrite using a laser imaging technique: Implications for the timing of gold in orogenic and carlin-style sediment-hosted deposits. Econ. Geol. 104, 635–668.

Large, R.R., Halpin, J.A., Danyushevsky, L.V., Maslennikov, V.V., Bull, S.W., Long, J.A., Gregory, D.D., Lounejeva, E., Lyons, T.W., Sack, P.J., McGoldrick, P. and Calver, C.R., 2014. Trace element content of sedimentary pyrite

as a new proxy for deep-time ocean- atmosphere evolution. Earth and Planetary Science Letters 389, 209-220.

Leach, D.L., Bradley, D.C., Huston, D., Pisarevsky, S.A., Taylor, R.D., and Gardoll, S.J., 2010. Sediment-hosted lead-zinc deposits in Earth history: Econ Geol, 105, 593–625.

Lenton, T.M., Boyle, R.A., Poulton, S.W., Shileds-Zhou, G.A., Butterfield, N.J., 2014. Co-evolution of eukaryotes and ocean oxygenation in the Neoproterozoic era. Nature Geoscience 7, 257–265.

Lindsay, J.F. and Brasier, M.D., 2000. A carbon isotope reference curve for ca. 1700-1575 Ma, McArthur and Mount Isa Basins, northern Australia. Precambrian Research, 99 (3-4), 271-308.

Luo, G., Ono, S., Huang, J., Algeo, T.J., Li, C., Zhou, L., Robinson, A., Lyons, T.W., and Xie, S., 2015. Decline in oceanic sulphate levels during the early Mesoproterozoic. Precambrian Research 258, 36-47.

Lyons T.W., Gellatly A.M., Goldrick P.J. and Kah L.C., 2006. Proterozoic sedimentary exhalative (SEDEX) deposits and links to evolving global ocean chemistry. Geol. Soc. Am. Mem. 198, 169–184.

Lyons, T.W., Reinhard, C.T., Planavsky, N.J., 2014. The rise of oxygen in Earth's early ocean and atmosphere. Nature 506, 307-315.

Meert, J.G., 2014. Strange attractors, spiritual interlopers and lonely wanderers: The search for pre-Pangean supercontinents. Precambrian Research 5, 155-166.

Meyer K.M., Kump L.R., 2008. Oceanic euxinia in Earth history: Causes and consequences. Annu. Rev. Earth Planet. Sci. 36, 251–88.

Muller, W.E.G., 2001. How was metazoan threshold crossed: the hypothetical Urmetazoa: Comparative Biochemistry and Physiology-Part A 129, 433-460.

Nielsen C., 2008. Six major steps in animal evolution: are we derived sponge larvae? Evolution and Development 10, 241–57.

Ochiai, E.I., 1978a, The evolution of the environment and its influence on the evolution of life: Origins Life, v. 9, p. 81-91; Ochiai, E.I., 1978b, Principles in the selection of inorganic elements by organisms

-Application to molybdenum enzymes: BioSystems, v. 10, p. 329-337.

Partin, C.A., Bekker, A., Planavsky, N.J., Scott, C.T., Gill, B.C., Li, C., Podkovyrov, V., Maslov, A., Konhauser, K.O., Lalonde, S.V., Love, G.D., Poulton, S.W., Lyons, T.W., 2013. Large-scale fluctuations in Precambrian atmospheric and oceanic oxygen levels from the record of U in shales. Earth Planet. Sci. Lett. 369–370.

Piper, J.S.A., 2013. A planetary perspective on Earth evolution: Lid Tectonics before Plate Tectonics. Tectonophysics 589, 44-56.

Pisarevsky, S.A., Elming, S-Å., Pesonen, L.J., and Li, Z-X., 2014. Mesoproterozoic paleogeography: supercontinent and beyond Precambrian Res., 244, 207-225

Planavsky, N.J., McGoldrick, P., Scott, C.T., Li, C., Reinhard, C.T., Kelly, A.E., Chu, X., Bekker, A., Love, G.D., and Lyons, T.W., 2011. Widespread iron-rich conditions in the mid-Proterozoic ocean. Nature 447, 448–451.

Planavsky, N.J., Reinhard, C.T., Wang, X., Thomson, D., McGoldrick, P., Rainbird, R.H., Johnson, T., Fischer, W.W., Lyons, T.W., 2014. Low Mid-Proterozoic atmospheric oxygen levels and the delayed rise of animals. Science, 346, 635-638.

Planavsky, N.J., Reinhard, C.T., Wang, X., Thomson, D., McGoldrick, P., Rainbird, R.H., Johnson, T., Fischer, W.W., and Lyons, T.W., 2014. Low Mid-Proterozoic atmospheric oxygen levels and the delayed rise of animals: Science 346, 635-638.

Porter, S.M., 2004. The fossil record of early eukaryotic diversification: Paleontological Society Papers 10, 35-50.

Rickard, D., 2012. Sulfidic sediments and sedimentary rocks. In: Van Loon, A.J. (Ed.), Developments in Sedimentology. Elsevier, p. 801.

Roberts, N.M.W., 2013. The boring billion? – Lid tectonics, continental growth and environmental change associated with the Columbia supercontinent. Geoscience Frontiers 4, 681-691.

Sahoo, S. K., Planavsky, N. J., Jiang, G., Kendall, B., Owens, J. D., Wang, X., Shi, X., Anbar, A. D. and Lyons, T. W., 2016. Oceanic oxygenation events in the anoxic Ediacaran ocean. Geobiology 14, 457–468.

Sahoo, S.K., Planavsky, N.J., Kendall, B., Wang, X., Shi, X., Scott, C., Anbar, A.D., Lyons, T.W., Jiang, G., 2012. Ocean oxygenation in the wake of the Marinoan glaciation. Nature 489, 546–549.

Scott, C., Lyons, T.W., Bekker, A., Shen, Y., Poulton, S.W., Chu, X., Anbar, A.D., 2008. Tracing the stepwise oxygenation of the Proterozoic ocean. Nature 452, 456–459.

Shen Y., Canfield D.E. and Knoll A.H., 2002 Middle Proterozoic ocean chemistry: evidence from the McArthur Basin, northern Australia. Am. J. Sci. 302(2), 81–109.

Shen, Y., Knoll, A.H., Walter, M.R., 2003. Evidence for low sulphate and anoxia in a mid-Proterozoic marine basin. Nature 423, 632–635.

Steadman, J.A., Large, R.R., Meffre, S., Olin, P.H., Danyushevsky, L.V., Gregory, D.G., Belousov, I., Lounejeva, E., Ireland, T.R., and Holden, P. 2015. 'Synsedimentary to early diagenetic gold in black shale-hosted pyrite nodules at the Golden Mile Deposit, Kalgoorlie, Western Australia', Economic Geology 110 (5), 1157-1191.

Taylor, S.R., Mclennan, S.M., 1995. The geochemical evolution of the continental crust. Rev. Geophys. 33, 241–265.

Tribovillard, N., Algeo, T.J., Lyons, T., Riboulleau, A., 2006. Trace metals as paleoredox and paleoproductivity proxies: an update. Chem. Geol. 232, 12–32.

Wray, G.A., Levinton, J.S. and Shapiro, L.H., 1996. Molecular evidence for deep Precambrian divergences among metazoan phyla: Science, 568-573.

Chapter 2

Pyrite trace element chemistry of the Velkerri Formation, Roper Group, McArthur Basin: Evidence for atmospheric oxygenation during the Boring Billion

(Mukherjee, I., and Large, R., 2016. Precambrian Research 281, 13-26)

Indrani Mukherjee and Ross R. Large
Centre of Excellence in Ore Deposits (CODES), University of Tasmania

2.0 Abstract

The trace element content of sedimentary pyrite in black shales of varying ages has recently been used to construct secular trends of trace element variation in the ocean. The approach also has potential to be used as a proxy for estimating evolution of the redox state of the ocean/atmosphere system through time. Here, we apply a combination of whole-rock chemostratigraphy and laser ablation-inductively coupled plasma-mass spectrometer (LA-ICP-MS) analyses of marine pyrite to the carbonaceous mudstones of the Mesoproterozoic (~1400 Ma) Velkerri Formation, and underlying Corcoran Formation, Roper Group, McArthur Basin to interpret and compare basin water conditions and basinal trace element chemistry at the time of sedimentation. Our results suggest that the black shales of the Velkerri Formation deposited under different geochemical conditions in comparison to the underlying Corcoran Formation. This proportionate difference is manifested in the form of high total organic carbon (TOC) contents coupled with an increase of trace elements such as P, Mo, Cd, Se, Ni, Se/Co, Ni/Co in the mudstones of Upper Velkerri Formation in comparison to Lower Velkerri and underlying Corcoran Formation. Cobalt on the other hand, exhibits an opposite trend compared to other redox sensitive trace elements (Mo, Se) due to its unique redox chemistry, particularly the cationic nature of its soluble species making Se/Co a useful proxy for redox conditions of the atmosphere. This progressive increment in trace elements (P, Mo, Cd, Se, Ni, Se/Co, Ni/Co) up-stratigraphy from Corcoran Formation to Lower Velkerri Formation to Upper Velkerri is herein attributed to an increase in nutrient trace element supply into the marine reservoir, possibly in response to tectonic activity and an increase in oxygen in the atmosphere. This increased nutrient supply subsequently promoted an increase in primary productivity as indicated by high TOC contents in the Upper Velkerri Formation. This positive change in nutrient supply also coincides with an increased supply of sulphate to the ocean (modelled paleo-seawater [SO_4^{2-}]) as evidenced by

previous sulfur isotope studies and development of morphological complexity in eukaryotes based on paleontological observations of previous workers. The totality of evidence from this study and previous studies, suggest that there was a possible oxygenation event around ~1400 Ma. This is in contrast with the general notion that Mesoproterozoic oxygen levels were low and devoid of significant fluctuations.

2.1 Introduction

The Velkerri Formation of the Roper Group (McArthur Basin) in Northern Australia has drawn attention of various branches of geoscience. It is believed to host the world's oldest live oil (Sweet andJackson, 1986) and is a prime target for hydrocarbons because of its potential to be an excellent source rock (Warren et al., 1998; Silverman et al., 2007). Considering the potential for generating hydrocarbons, sedimentological studies of the Formation have been carried out in order to understand the depositional environment, in relation to tectonics and geologic setting (Jackson and Raiswell, 1991; Abbott and Sweet, 2000). Detailed geochemical and isotopic studies of the Velkerri Formation have also been undertaken to elucidate the redox state of the Mesoproterozoic ocean and atmosphere (Canfield, 1998; Shen et al., 2003; Scott et al., 2008; Johnston et al., 2008; Kendall et al., 2009; Planavsky et al., 2011, 2014). Large spheroidal acritarchs (Tappania plana) and other microfossils that are believed to exhibit morphological complexity and possess an eukaryotic origin, are found in this part of the Roper Group stratigraphy (Javaux et al., 2003). Biomarkers of both prokaryotic and eukaryotic origins (steranes) have also been discovered in the Velkerri suite of rocks (Jackson et al., 1986; Crick et al., 1988). Recently, Large et al. (2014) used the trace element content in sedimentary pyrite to understand ocean trace element chemistry and proposed the selenium (Se) content in pyrite as a potential proxy for atmospheric oxygenation through time. Furthermore, it has been established that Se in the sedimentary rock record could be used as an independent tool to assess selenium cycles to understand atmospheric redox state (Stüeken et al., 2015). Using the above-mentioned approach, Large et al. (2014) suggested, that during the Proterozoic, oxygen in the atmosphere gradually declined after 1800 Ma before increasing towards the end of the Boring Billion (1800 Ma). This decline also coincides with the decrease in other bio-essential trace elements that possibly thwarted biologic evolution (Anbar and Knoll, 2002). In contrast to this suggestion, other studies (Canfield, 2005; Scott et al., 2008; Planavsky et al., 2014; Lyons et al., 2014) propose low and stable oxygen levels to be the cause of a hiatus in biologic evolution. This paper presents, for the first time, whole rock and pyrite chemostratigraphy of the Velkerri Formation and the underlying Corcoran Formation in order to provide a new perspective on the geochemical environment of the Mesoproterozoic ocean and redox state of the atmosphere around 1400 Ma and compare it with outcomes of various geochemical proxies. An attempt is also made to understand relationships/ correlations (if any) between trace elements in pyrite and bio-geologic processes operative during the deposition of the Velkerri Formation.

2.2.1 Stratigraphic and geologic context

The Roper Group rocks in the McArthur Basin represent the youngest and final episode of sedimentation in the Paleo to Mesoproterozoic history of the McArthur Basin (Fig. 2.1). The Roper Group was deposited on a siliciclastic ramp, which developed in response to sea level fluctuations and episodic flexural tectonics, within an intracratonic basin referred to as the Roper Superbasin by Abbott and Sweet (2000). The Roper Group is subdivided into two subgroups (Fig. 2.2), Collara and Maiwok (Abbott and Sweet, 2000). This subdivision was introduced to differentiate between tidal/platform sandstone-dominated and mudstone dominated sequences. The Velkerri Formation, in the Maiwok Subgroup, is overlain by Moroak Sandstone and underlain by Bessie Creek Sandstone, and is dominantly composed of black carbonaceous mudstones with minor grey siltstones and very fine-grained sandstones including calcite nodules, pyritic stringers and glauconitic siltstones (Fig. 2.3; Abbott and Sweet, 2000). The formation is 330–880 m thick, with the latter thickness being attained in the Beetaloo Sub-basin in the south (Fig. 2.4; Ahmad et al., 2013) and is spread over ~80,000 square kilometres (Abbott and Sweet, 2000). The formation is essentially unmetamorphosed and is relatively undeformed. Thermal maturity of the organic matter present in the Velkerri Formation suggests it was subjected to a maximum depth of ~2.5 km

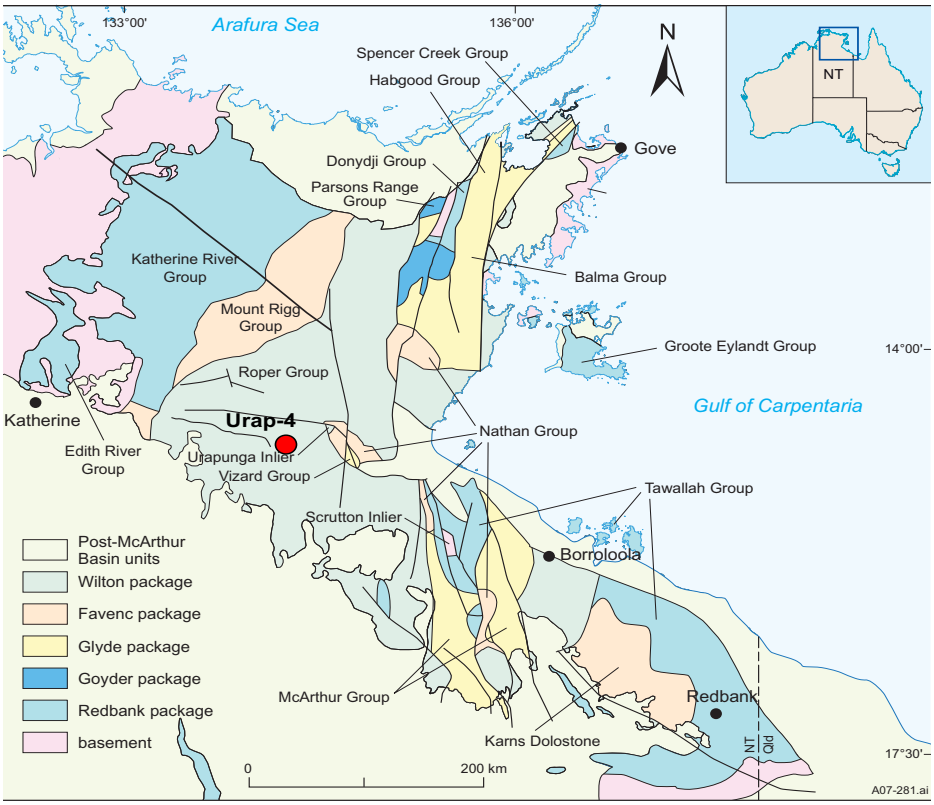

Fig 2.1. Geological map of the McArthur Basin, Northern Australia showing the spatial locations of the Roper Group, McArthur Group and drill hole undertaken for the study; Red solid circle: Urapunga 4 (figure adapted from Ahmad et al., 2013).

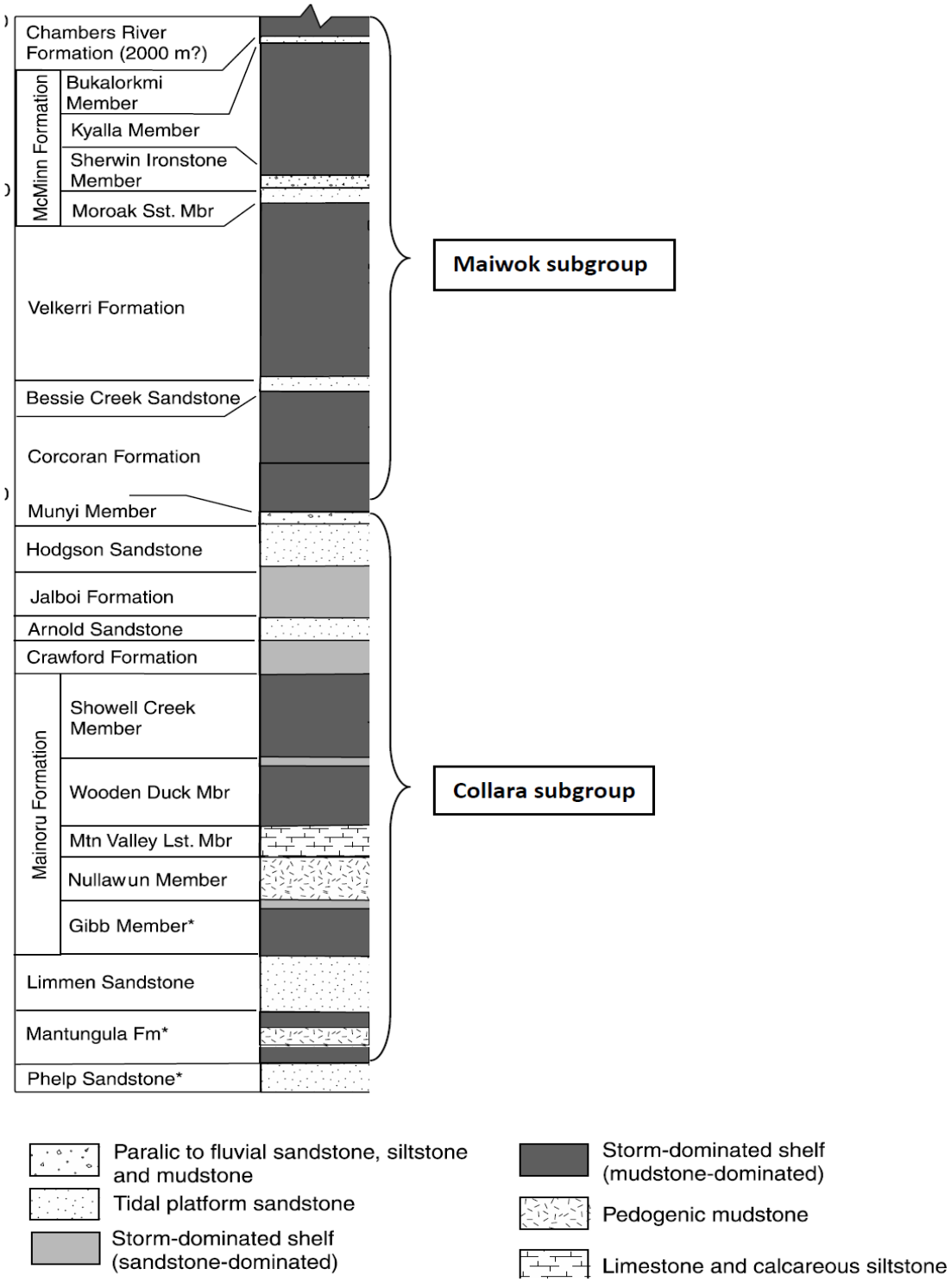

Fig 2.2 Stratigraphy of the Roper Group, McArthur Basin (modified from Abbott et al, 2001); Lithostratigraphic nomenclature is from Dunn (1963) and Sweet et al. (1999).

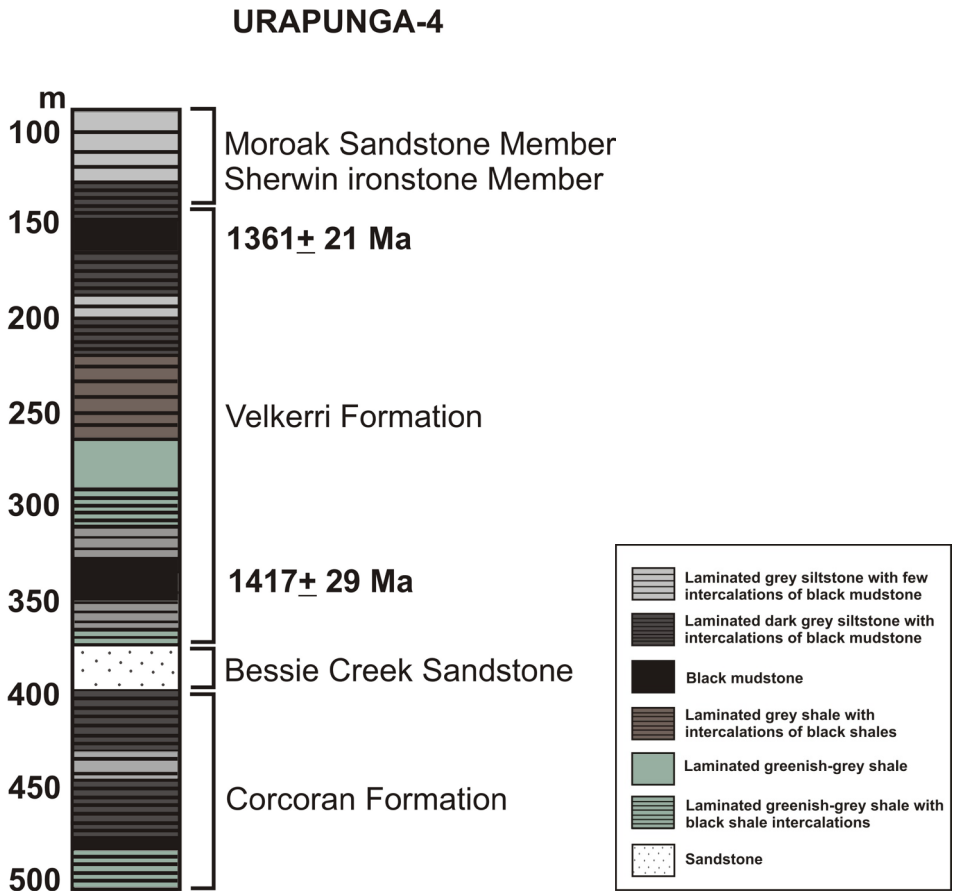

Fig 2.3. Simplified log of drill hole Urapunga-4 (type section for the Velkerri Formation); Depositional ages of the Upper and Lower Velkerri Formation from Kendall et al., 2009.

and temperatures ranging from ~75 ºC to 150 ºC, classifying it as marginally matured. However, certain portions are highly mature as a result of dolerite sill intrusions in the strata (Crick et al., 1988; George and Ahmed, 2002). Also, to the south in the Beetaloo sub-basin, the Velkerri Formation is gas prone and burial depths are >4 km in many places. Kendall et al. (2009) attempted to constrain the depositional age of the Velkerri Formation using Re-Os dating and obtained 1361 ± 21 Ma for the Upper Velkerri Formation and 1417 ± 29 Ma for the Lower Velkerri Formation (Fig. 2.3). These ages are in agreement with the maximum age constraint (1492 ± 4 Ma: U–Pb SHRIMP zircon date) obtained from a tuff in the Wooden Duck Member of the Mainoru Formation that underlies the Velkerri Formation (Fig. 2.2).

2.2.2 Palaeo-environment of Roper Group

Abbott and Sweet (2000) conducted a detailed study of the Roper Group rocks (particularly Middle Roper Group) in terms of sequence stratigraphy (Fig. 2.2). Their study concluded that the Roper Group

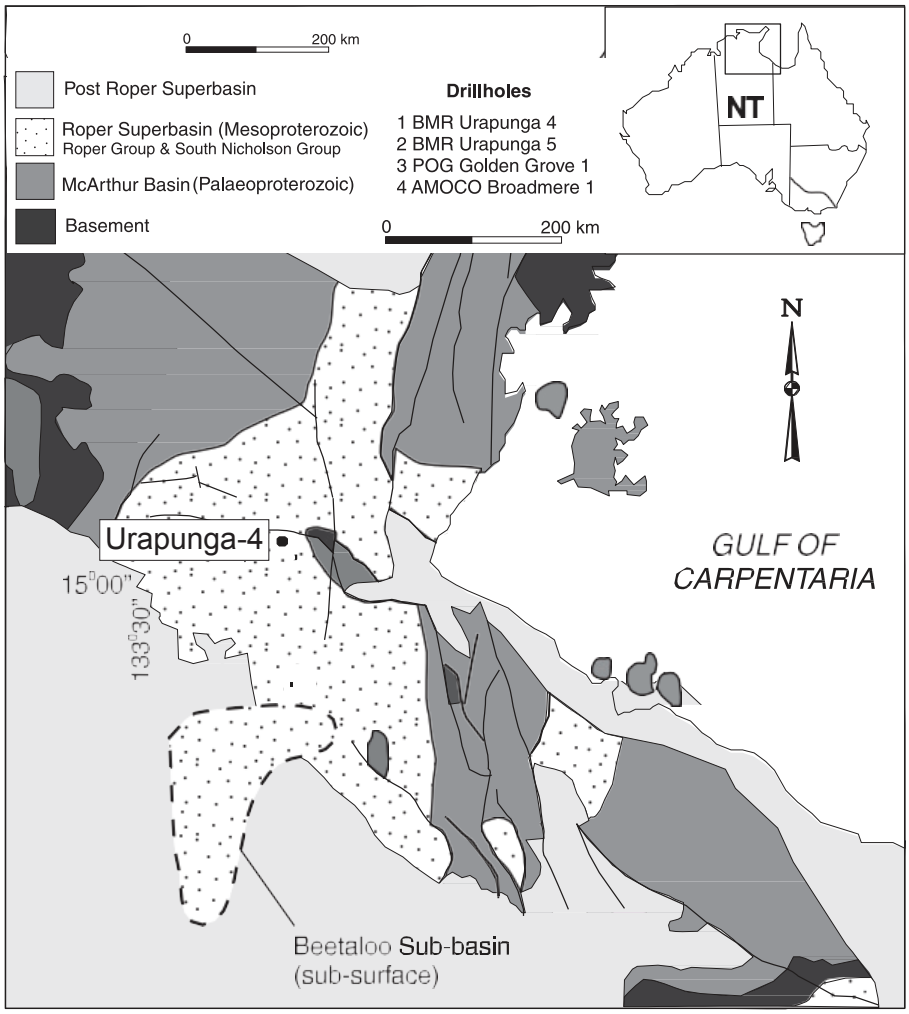

Fig 2.4. Geological map of the McArthur Basin showing the sub-surface extension of the Betaloo sub-basin (modified after Abbott and Sweet, 2000)

sequences are highly asymmetric and coarsening upward, attributed to flexural tectonics operative during sedimentation in the intra-cratonic basin. Regressive successions such as basinal black shales, distal to proximal storm-dominated shelf facies and tidal-platform sandstone dominate over poorly represented transgressive successions such as paralic red-bed intervals including ooidal ironstones. Although a wide range of depositional environments is interpreted for the Roper Group sequence, i.e., from basinal, distal to proximal storm dominated shelf, tidal platformal to terrestrial/paralic environments, a marine setting is most preferred. Six third-order depositional sequences were observed that imparted a cyclical pattern with alternating mudstones and sandstones units. Black mudstones of the Velkerri Formation belong to the Veloak sequence

constrained by the Bessie Creek Sandstone below and Moroak Sandstone above representing one of these cyclic units. Mudstones of Corcoran Formation belong to the Corbess sequence constrained by the Hodgson Sandstone below and Bessie Creek Sandstone above representing another cyclic unit. The

Velkerri Formation is dominantly composed of parallel-laminated grey to black mudstone (with TOC ranging from 0–8.68%; Crick et al., 1988) and minor glauconitic siltstone deposited in a low energy offshore environment (Abbott and Sweet, 2000) as a result of hemipelagic sedimentation under anoxic conditions

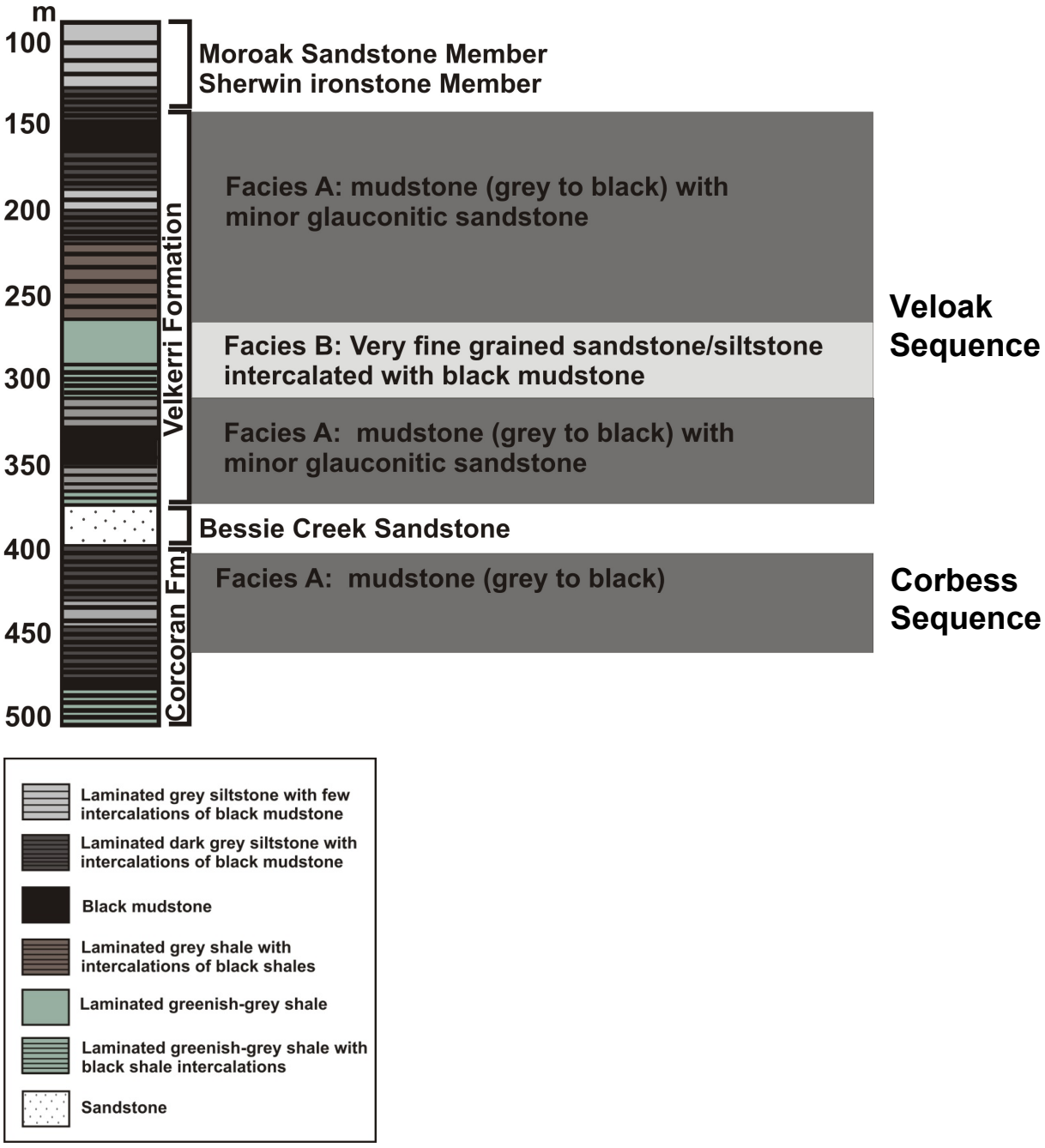

Fig 2.5. Simplified log of drill hole Urapunga-4 along with facies description incorporated from Abbott et al., 2000.

with cyanobacterial and algal biotic communities as the source for the organic matter (Crick et al., 1988). Also, grey siltstone/ sandstone intercalated with black shales that represent a minor component of the Velkerri Formation, formed from suspension of storm-derived sediments along with black mud. Abbott and Sweet (2000) classified parallel-laminated black mudstone in the Velkerri Formation as Facies A and termed the grey siltstone/sandstone with black shale intercalations that forms a minor component, as Facies B1. Facies A also comprises 50% of Corcoran Formation (Fig. 2.5). Both facies A and B represent distal shelf environments with the latter representing occasionally storm-dominated, distal shelf.

2.2.3 Tectonics

The highly asymmetric, coarsening-upward, cyclic nature of Roper sequences indicate that the siliciclastic ramp setting was in close proximity to a tectonically active hinterland (cf. Harris and Eriksson, 1990). Moreover, the above features, which are characteristic of the Roper sequences, are also observed in a foreland basin for instance the Appalachian Basin (Grotzinger and McCormick, 1988; Ettensohn, 1994). However, these features are not restricted to foreland basins as they have been noticed in extensional settings as well (Embry and Podruski, 1989; Jackson et al., 1990). The orogen responsible for the Roper Group episodic sedimentation is speculated. Gorter and Grey (2012) suggest a southeast provenance, possibly from the Helen Spring High on the basis of facies variation and provenance. However, the 1580–1480 Ma Isan orogeny and the Anmatjira Uplift that possibly occurred between 1500 and 1400 Ma has also been suggested on the basis of their timing (Abbott and Sweet, 2000). Nevertheless, Abbott and Sweet (2000) suggested that flexural loading in response to these orogenic activities operative around that time possibly resulted in third order sedimentary cyclicity.

2.3 Method

2.3.1 Drill hole details, sampling and analytical method

Samples for the study were obtained from BMR Urapunga-4 drillhole, provided by Geoscience Australia drill core repository in Canberra, Australia. BMR Urapunga 4 (Latitude: 141° 32′ 17″ S; Longitude: 134° 17′ 29″ E) is one of the three fully cored holes drilled as part of contract drilling program in 1985, in order to obtain a complete section of the Roper Group in the Roper Bar area (Sweet and Jackson, 1986). It intersected the McMinn Formation, a full section of Velkerri Formation and terminated with Corcoran Formation. This drill hole was chosen for sampling because it represents the type section of the Velkerri Formation and the ~330 m thick package of rocks (mainly laminated black mudstone/siltstone) are unmetamorphosed and undeformed with the exception of parts affected by doleritic sill intrusion (Crick

et al., 1988; Crick, 1992; Summons et al., 1994; George and Ahmed, 2002). Black shales from Urapunga-4 were sampled systematically down the drill hole approximately every 10 meters from depths mentioned in Table 2.1. Samples were collected with regard to sedimentary facies variations, such that both facies A and B were represented. Drill core samples collected were analysed for major, trace elements, total sulfur, total carbon and total organic carbon. A portion of each sample was crushed using the hydraulic rock crusher and an automated agate mill was used to prepare powders of the samples for whole rock analyses. Major element analyses using X-ray Fluorescence (XRF) were undertaken at CODES, University of Tasmania, trace elements were analysed using ICP-MS at ALS, Brisbane and total sulfur (TS), total carbon (TC) and total organic carbon (TOC) were analysed at CODES, University of Tasmania using Element Analyser (Table 2.1). In order to compare bulk rock chemistry (whole rock data) with pyrite chemistry (pyrite LA-ICP-MS data), laser mounts (~2 cm) from the same intervals as whole rock analyses, were prepared for sedimentary pyrite analyses using LA-ICP-MS at CODES, University of Tasmania (Table 2.2). A New wave Research UP-213 Nd:YAG laser microprobe coupled to an Agilent 7500a ICP-MS was used to conduct laser based analyses on the samples. The laser instrument was set up for a background analysis of 30 s to allow better detection limits to be assessed followed by 40–60 s of signal acquisition in counts per second (cps) with ~3.5 J/cm2 laser influence and 5 Hz laser repetition rate. Samples were run along with reference materials, STGL2b2, GSD-1G and Peruvian pyrite crystal, every 1.5 h (~after analyses of two samples). STDGL2b2 is an inhouse standard used for primary calibration for quantifying siderophile and chalcophile elements (Danyushevsky et al., 2011), GSD- 1G (USGS reference material; Jochum et al., 2005) was used to quantify lithophile elements and sulfur was quantified using a massive pyrite with stoichiometric Fe and S (46.5% Fe, 53.5% S). The mode of analyses was spot, i.e., approximately 10 pyrite spot analyses and 5 black shale matrix spot analyses were conducted on each laser mount. 10–35 μ laser spot sizes were used for pyrite analyses and 35–105 l laser spot sizes were used for standards. Due to the fine-grained nature of the sedimentary pyrites, matrix material of the black shales was analysed for trace elements, in order to negate effects of matrix contamination during laser ablation of fine-grained pyrite. Sedimentary pyrites of URAP-4 were analysed for a range of trace elements as shown in Table 2.2. Raw LA-ICP-MS generated-data, in counts per seconds were converted into parts per million (ppm) using CODES in-house data reduction template (TEO Template 8.10).

Table 2.1: Whole rock analyses of black shales of the Velkerri Formation from Urapunga-4; TS=Total sulfur; TOC=Total organic carbon

Formation	Sample interval	Mn	Co	Ni	Cu	Zn	As	Se	Mo	Ag	Cd	V	U	P	TOC (%)	TS (%)
Upper Velkerri	105.7	156	44	61.1	143.5	31	8.4	3	2.35	0.18	0.03	100	2.6	2300	2.42	1.87
Upper Velkerri	115.2	141	36.4	42.2	77.6	31	4.4	2	1.75	0.14	0.02	100	2.9	1710	2.17	0.84
Upper Velkerri	126.3	83	53.1	183	90.4	68	61.2	11	5.84	0.43	0.15	203	4.2	2220	1.99	3.17
Upper Velkerri	140.1	52	17.7	93.4	54.3	225	23.5	2	37.3	0.42	3.35	198	10.9	710	6.02	3.75
Upper Velkerri	172.4	66	43.6	107	165.5	144	22	3	29.2	0.84	0.62	183	6.7	2970	6.52	2.40
Upper Velkerri	183.4	177	28.2	66.4	205	230	10.3	4	12	0.67	1.06	274	7.2	5470	3.09	1.28
Upper Velkerri	193.9	173	48.2	66.2	168.5	187	8.7	3	16.7	0.62	0.66	262	6.7	3870	3.22	0.05
Upper Velkerri	204.4	102	31	20.6	38.5	49	7.8	1	6.21	0.09	0.06	73	3.1	130	2.76	1.95
Upper Velkerri	216.9	2260	43.2	102	295	929	22.5	6	29	0.45	5.14	321	9.8	4050	4.61	0.02
Upper Velkerri	227	96	19.4	11.5	23.1	46	1.7	1	0.37	0.03	0.05	60	1.9	120	0.11	0.02
Lower Velkerri	249.7	84	23.2	11.2	25.3	50	1.4	1	0.4	0.01	<0.02	75	2.1	120	0.22	0.02
Lower Velkerri	260	107	19.5	10.5	27.5	57	1.6	1	0.33	0.01	<0.02	69	1.9	170	0.05	0.02
Lower Velkerri	294.5	145	22	14.1	30.1	48	1.4	1	0.33	0.02	<0.02	50	3.2	150	0.12	0.03
Lower Velkerri	305.5	150	13.4	16.1	23.9	33	3	1	0.35	0.04	<0.02	69	2.6	170	0.10	0.07
Lower Velkerri	316.8	105	27.3	21.9	36.7	47	9.1	1	5.84	0.13	0.07	78	2.9	140	1.25	0.06
Lower Velkerri	339.6	185	20.2	24.8	31.6	22	2.8	2	0.56	0.11	<0.02	86	3.3	190	0.44	0.34
Lower Velkerri	350.9	133	12.1	30.1	62.3	92	5.8	2	2.68	0.14	0.22	101	4	230	1.32	1.68
Lower Velkerri	360.6	114	28.2	44.6	88.8	30	12.4	3	9.09	0.35	0.06	130	5.5	330	2.27	0.04
Corcoran	407.4	151	25.3	12.9	33.7	27	1.3	2	0.32	0.07	<0.02	69	3.4	190	0.11	0.04
Corcoran	417.3	230	41.1	19.8	34.1	39	2.2	1	0.24	0.09	<0.02	66	2.7	190	0.04	0.03
Corcoran	430.7	166	25.6	33.3	58.2	22	6.9	2	0.52	0.14	<0.02	78	3.4	310	0.24	0.88
Corcoran	441.2	108	53.1	33.6	68.1	20	6.7	2	0.58	0.12	<0.02	77	3.7	190	0.32	0.41
Corcoran	451.2	98	31.2	26.3	46.2	17	6.5	2	1.09	0.12	<0.02	87	3.5	190	0.33	0.97
Corcoran	465.6	99	36.5	30.5	83.8	24	7.1	2	0.73	0.15	<0.02	95	3.7	210	0.33	0.81
Corcoran	489.4	226	35.4	34.6	26.7	83	19.5	1	0.91	0.13	<0.02	80	3	220	0.02	0.07
Corcoran	505.8	171	34.6	26.8	1.8	74	1.5	1	0.2	0.05	<0.02	80	3	190	0.02	0.01

Table 2.2: LA-ICP-MS mean analyses of pyrites in black shales of the Velkerri Formation from Urapunga-4

Formation	Sample interval	Mn	Co	Ni	Cu	Zn	As	Se	Mo	Ag	Cd	V	U
Upper Velkerri	105.7	175.45	261.29	280.11	96.01	29.49	233.58	16.85	13.11	1.87	0.81	158.61	1.59
Upper Velkerri	115.7	823.76	1.74	112.88	98.98	31.39	85.27	9.52	7.24	0.33	0.24	61.21	1.74
Upper Velkerri	126.3	498.14	56.15	281.19	48.27	48.89	42.83	14.23	42.22	3.79	0.55	262.79	3.51
Upper Velkerri	140.1	19.14	41.85	718.90	112.97	137.40	7685.23	88.77	40.85	3.19	2.66	388.58	59.57
Upper Velkerri	151.2	280.35	63.97	718.04	66.50	1951.61	897.65	36.19	30.70	6.03	30.27	300.07	6.65
Upper Velkerri	161.8	188.88	197.41	2063.17	264.58	1400.59	642.48	39.94	794.28	15.03	18.70	349.83	20.70
Upper Velkerri	172.4	566.15	34.13	244.84	51.58	717.20	11042.64	14.60	10.07	2.67	5.25	133.45	4.72
Upper Velkerri	183.4	986.01	119.37	640.45	149.58	33.20	8584.38	61.53	3.80	9.80	0.28	142.98	4.29
Upper Velkerri	193.9	240.61	149.20	477.24	408.23	271.73	525.68	11.30	60.06	6.45	0.63	757.35	9.89
Upper Velkerri	216.9	67.70	290.25	440.31	205.40	365.85	699.59	16.90	25.46	3.53	2.92	409.43	6.98
Lower Velkerri	260	188.14	359.02	210.49	2.30	122.83	935.83	9.76	0.67	3.59	1.44	104.25	1.43
Lower Velkerri	316.8	1026.31	76.84	442.30	45.27	10.27	4516.33	35.85	0.56	5.65	0.30	171.62	6.37
Lower Velkerri	374.4	1.17	7.75	5.80	5.64	0.93	407.10	4.87	0.44	0.05	0.26	0.00	0.00
Corcoran	417.3	24.07	6856.90	1048.75	129.57	8.88	966.83	163.35	0.60	3.52	0.03	22.52	1.07
Corcoran	430.7	1519.88	483.84	1319.84	1366.67	510.22	315.46	19.71	5.65	10.61	3.85	58.51	9.29
Corcoran	441.3	269.34	192.30	204.32	282.25	82.87	89.91	6.74	1.64	1.21	0.97	104.56	3.24
Corcoran	452.1	1126.42	323.27	1046.41	1128.02	420.58	304.49	11.01	8.08	8.04	2.53	106.08	9.91
Corcoran	465.6	152.00	766.78	431.24	142.86	87.14	1114.13	43.49	0.77	1.51	0.02	40.08	18.22
Corcoran	474.5	1186.81	455.73	822.16	273.16	326.87	443.25	25.02	32.41	3.63	3.22	188.61	7.89

*Mean of TEs in pyrite analyses except U, V analyses in matrix shale

2.4 Results

2.4.1 Textural study

Prior to laser-based analysis, polished mounts through the carbonaceous mudstone section were studied under reflected light in order to select samples that contain early-formed sedimentary pyrite suitable for the study. A detailed textural study was conducted not only to ensure suitability of the pyrites for analyses but also to note the textural variability of pyrite in the samples through the different facies of the formation. A variety of textures were observed in the pyritic shales of URAP-4

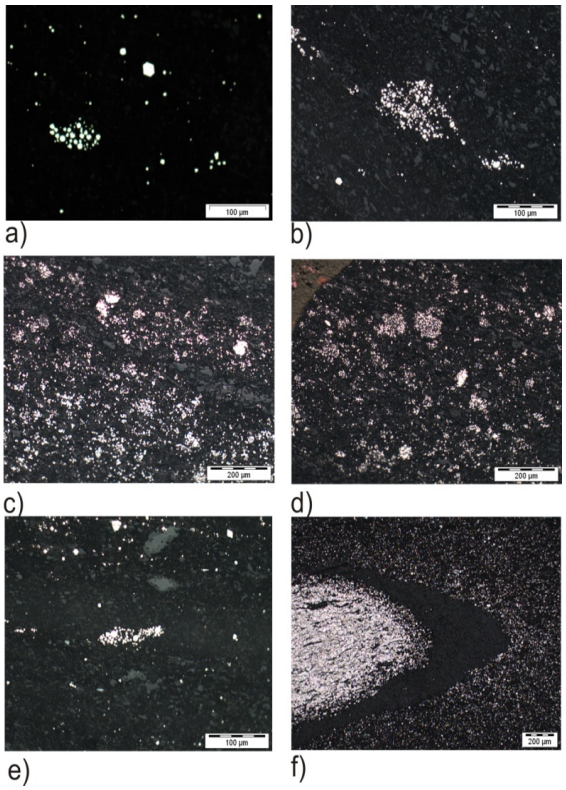

Fig 2.6. Sedimentary-diagenetic pyrite textures observed in Urapunga-4; a) & b) cluster of individual crystals of pyrite; c) & d) fine grained pyrite disseminated in the black shale matrix; e) & f) micro-macro nodules of pyrite

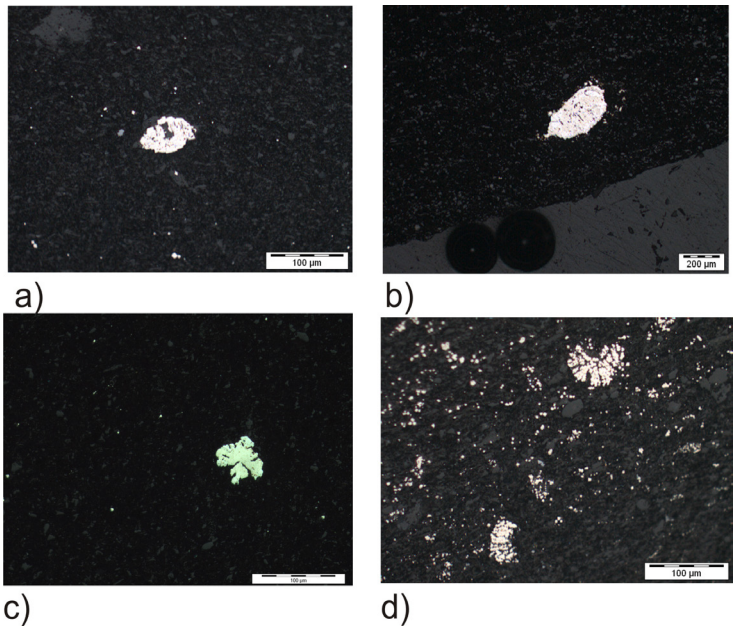

Fig 2.7. Recrystallised pyritic textures observed in Urapunga-4; a) & b) coarse grained pyrite c) pyrite infillings between clasts d) coarse grained pyrites intergrown with marcasite

drill hole (Figs. 2.6–2.8). Sedimentary pyrite occurs in the form of individual microcrystals, aggregates of microcrystals, or framboids (Fig. 2.6a–e). Nodular concretions are also common (Fig. 2.6f). Small microcrystals (<10 μ) of pyrite are disseminated throughout the matrix in all samples. Coarser grains of pyrite are present in some samples (Fig. 2.7a, b, d). Pyrite also occupies inter-granular spaces in rare cases (Fig. 2.7c). Lens shaped clasts (carbonate) are abundant in most

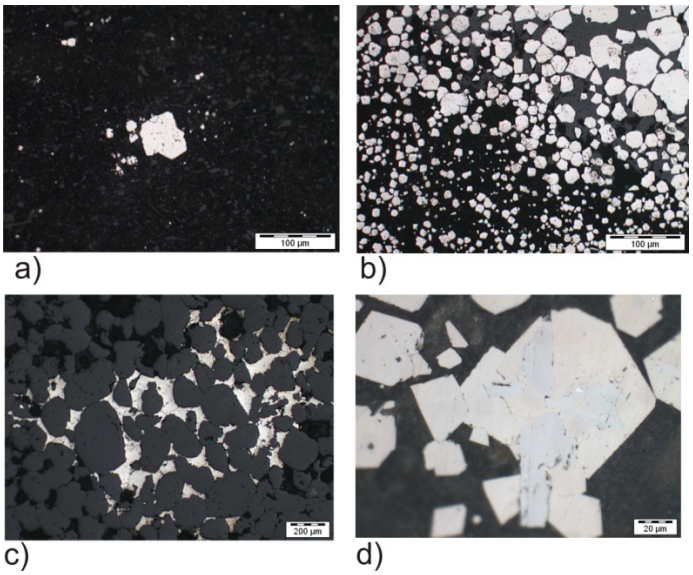

Fig 2.8. a) & b) Micronodules/lens shaped pyritic clasts and c) & d) pyritic textures possibly of microbial origin observed in Urapunga-4

samples (Fig. 2.8a) where pyrite appears to replace the clasts (Fig. 2.8b). Textures that possibly indicate a microbial origin are represented as Fig. 2.8c, d. They may be clusters of individual microcrystals of pyrite. However, considering the abundance of microfossils in the Velkerri Formation reported by others (Peat et al., 1978; Javaux et al., 2004), pyritic textures of microbial origin remain a possibility. Fine to coarse grained euhedral pyrites such as those in Fig. 2.7, were not analysed as their trace element budget is affected because of recrystallization (Large et al., 2014) possibly due to contact metamorphism (doleritic sill intrusions observed in some intervals).

2.4.2 Whole rock analyses

Both major and trace elements were analysed for the Velkerri Formation and Corcoran Formation and the data is presented in Table 2.1. According to the data presented in Table 2.1 and Fig. 2.9, the Upper Velkerri Formation (100–230 m) is more enriched in certain trace elements such as P, Cd, Mo, Ni, Se, U and V in comparison to the Lower Velkerri (200–375 m) and underlying Corcoran Formation (400–500 m). The increase in U and V is however subtle and even though they show a similar trend like pyrite related trace elements, they are less pronounced. This could possibly be due to bottom water oxygenation and/or bioturbation that tend to weaken the U signature (Tribovillard et al., 2006). Cobalt, on the other hand does not show any distinct difference. The Upper Velkerri Formation also has high TOC and TS contents (Fig. 2.9).

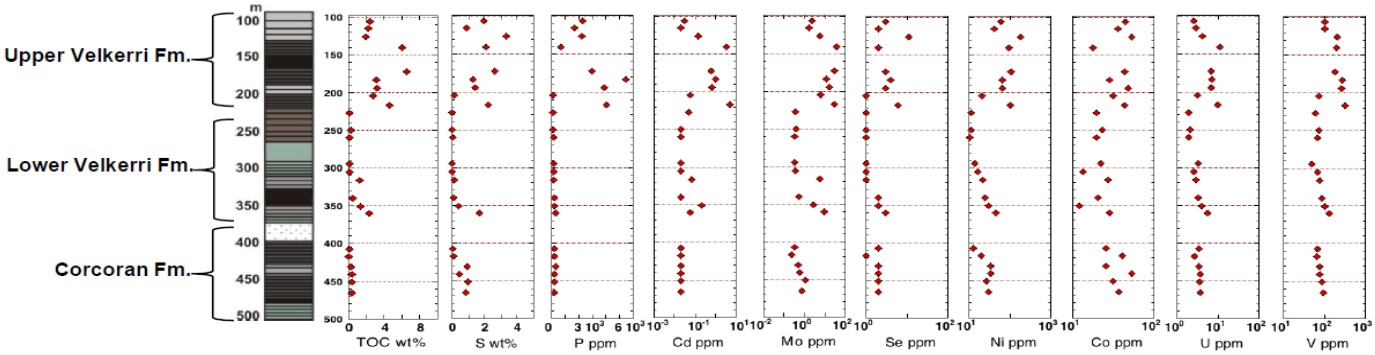

Fig 2.9. Down hole bulk rock analyses of the Velkerri Formation and underlying Corcoran Formation (Note: Each division in the P (ppm) scale bar is 1000 ppm; 3 *10^3 = 3000 ppm)

2.4.3 LA-ICP-MS analyses of sedimentary pyrite

Sedimentary pyrites were analysed using LA-ICP-MS to obtain down hole trends for redox sensitive trace elements (Fig. 2.10). Molybdenum in pyrite shows a marked up-sequence increase from Corcoran Formation (400–500 m) to Lower Velkerri Formation (375–200 m) to Upper Velkerri Formation (100–230 m) (Fig. 2.10). Selenium and Ni in pyrite do not show any distinctive trend unlike their whole rock counterparts although average Se and Ni for Upper Velkerri Formation is ~33 ppm and ~615 ppm respectively and average Se and Ni for Lower Velkerri and Corcoran Formations are ~19 ppm and ~547 ppm respectively. Analyses of a sample from 417.3 meter interval in the Corcoran Formation, yielded exceptionally high Se, Ni and Co values, which need to be considered with caution due to a very low Ni:Co ratio (0.15) which is abnormal for marine pyrite (Ni/Co for sedimentary pyrite is generally above 1; Large et al., 2014; Gregory et al., 2015). Elements such as V and U analysed in the black shale matrix also show a gradual increase stratigraphically upwards (Fig. 2.11). They also seem to show moderate correlation with TOC as these elements concentrate in the organic matter rich black shale matrix rather than in pyrite. Cobalt in pyrite, unlike other trace elements shows a decrease stratigraphically upwards, from ~328 ppm in the Corcoran Formation & Lower Velkerri Formation to ~100 ppm in the Upper Velkerri Formation (Fig. 2.10).

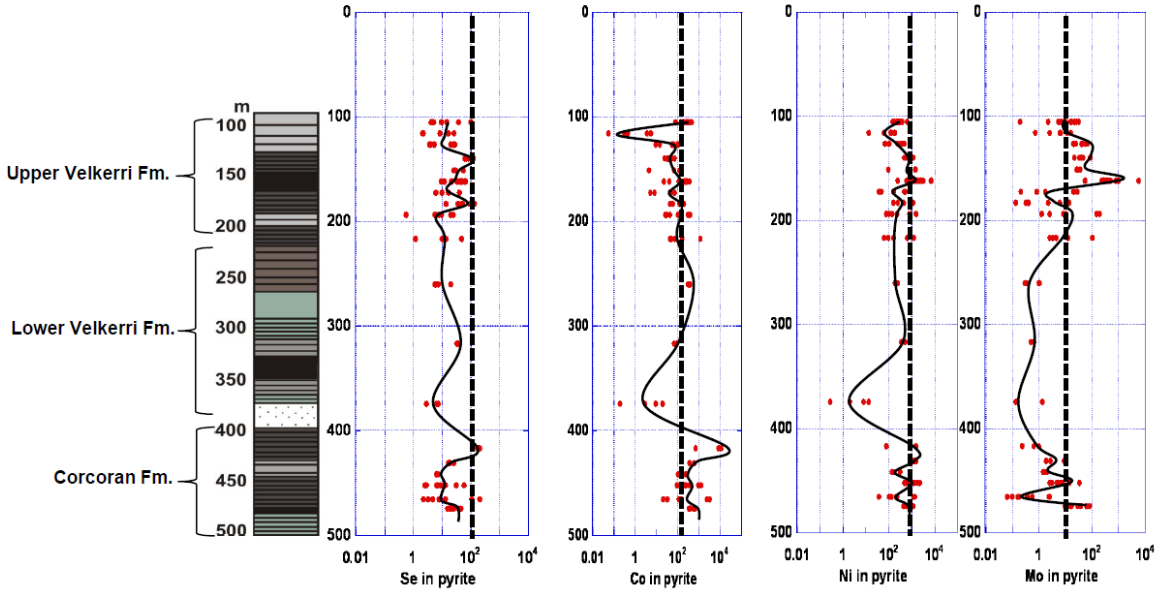

Fig 2.10. Down hole trace element analyses of sedimentary pyrites of the Velkerri Formation and underlying Corcoran Formation Black solid line obtained after joining mean of analyses of individual samples (~10 spot analyses per sample); Black dashed line denotes global mean value of ~ 4000 pyrite analyses undertaken by Large et al, 2015.

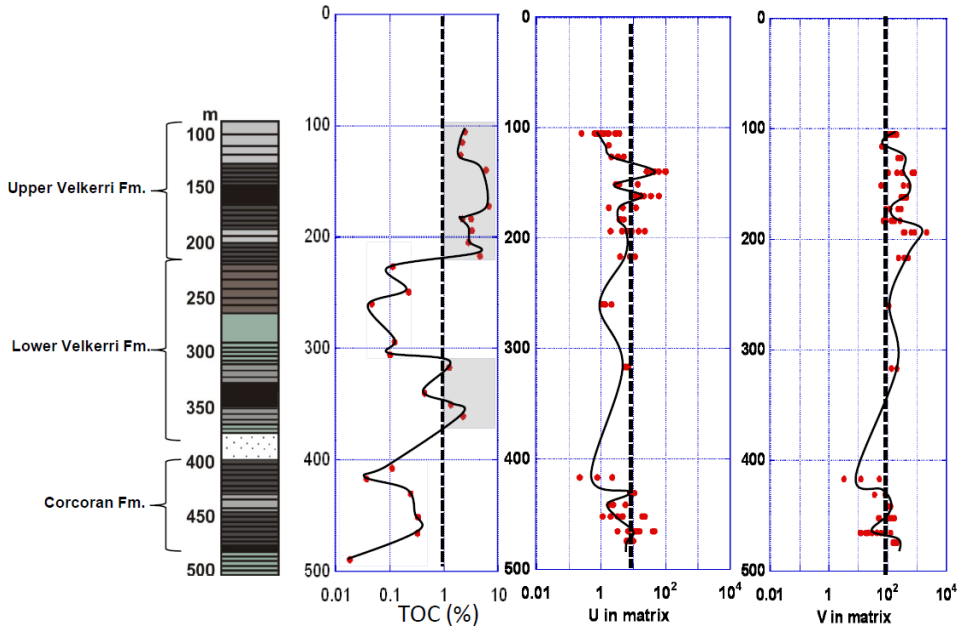

Fig 2.11. Down hole trace element analyses of black shale matrix of the Velkerri Formation and the underlying Corcoran Formation Black solid line obtained after joining mean of analyses of individual samples Black dashed line in U and V denotes global mean value of ~ 4000 black shale matrix analyses undertaken by Large et al, 2015.

2.5 Discussion

2.5.1. Whole rock analyses

Whole rock analyses indicate an increase in trace elements (P, Cd, Mo, Ni, Se, U and V), TOC and TS stratigraphically upwards from Corcoran Formation to Upper Velkerri Formation. Total organic carbon and TS data show an excellent correlation with one another. This is possibly because organic matter in sediments provides a favourable environment for biogenic pyrite formation, which is reflected in the TOC-TS relationship (Berner, 1970; Raiswell and Berner, 1985; Krauskopf and Bird, 1995). Their trend is also similar to the trace element trends down hole as in Fig. 2.9 for P, Cd, Mo, Se, Ni, U and V because these trace elements are adsorbed into organic matter and are drawn down into pyrite and/or the organic matter fraction of the shale, as organic matter settles in the sea floor muds. However, Co does not show any specific trend, as it does not appear to be controlled by productivity and organic matter settling. Certain trace elements that generally are adsorbed into organic matter fractions of the rock (U, V, P, Cd) can be used as paleoproductivity indicators (Henderson, 2002; Algeo and Lyons, 2006; Algeo and Tribovillard, 2009). A combination of TOC and P, U, V concentrations (Fig. 2.9) therefore, indicate increased paleoproductivity stratigraphically upward. This is also supported by a marked increase in redox sensitive trace elements such as Ni, Se and Mo which are a measure of nutrient supply that promote productivity (Anbar and Knoll, 2002; Large et al., 2015a, b).

2.5.2 Pyrite LA-ICP-MS analyses

Sedimentary pyrite LA-ICP-MS data also indicates that certain redox sensitive elements such as Se, Ni, Mo increase stratigraphically upwards unlike Co that decreases. The unique response of Co to changes in redox compared to other trace elements has been previously observed in the rock record (Large et al., 2014, 2015a, b; Swanner et al., 2014). Recently, Co/Ti ratio of iron formations was used as a proxy for seawater Co concentration through time (Swanner et al., 2014). Also, LA-ICP-MS analyses of pyrites (Archean to recent) were undertaken by Large et al. (2014). Both studies indicate that Co concentration, in comparison to other trace elements that are used as oxygenation proxies (Mo, Se, Ni, U), has decreased through time. Also, thermodynamic modelling by Zerkle et al. (2005), demonstrated that Co is more abundant in the ocean under lower pO_2 conditions, and less abundant when pO_2 rises unlike Mo. Higher sea water Co concentration (higher Ni/Fe and Co/Ti values) could also be because of anoxia and higher riverine flux of Co related to erosion of komatiites (Konhauser et al., 2011, 2009). Hydrothermal flux related to mantle plume activity was also suggested as another source of Co in the marine reservoir (Barley et al., 2005). Alternatively, Large et al. (2015a, b) demonstrated that first order trends of mean Mo and Co in marine pyrites are related to their supply in the ocean which is a function of pO_2 in the atmosphere and

that their concentration in marine pyrite is consistent with thermodynamic calculations by Co (Zerkle et al., 2005) and Mo (Saito and Goepfert, 2008). Cyclic trace element variations in the Phanerozoic also clearly underpin the inverse relationship of Co with Mo and Se with a negative correlation of –0.38 Co-Mo and –0.35 Co-Se (Large et al., 2015a, b). An explanation as to why Co should behave differently to Mo and Se due to changes in redox can be understood in terms of the ionic form of the soluble species i.e., cationic or anionic. Cobalt predominantly occurs in its cationic form (Co^{2+}, $CoCl^{+}$ or CoO) whereas Mo and Se in their anionic form (MoO_4^{2-} and SeO^{3-}) (Violante et al., 2008). It is known that sorption (including competitive sorption)–desorption and biotic–abiotic processes control solubility of these elements. Mobility of trace elements due to sorption and complexation processes also depends on their ionic forms, for instance trace elements, in their cationic form show a much greater affinity for the OH^- ion. Also, humic substances and Fe–Mn hydroxides appear to scavenge cationic species much more effectively (Jackson, 1998; Huang and Germida, 2002; Sparks, 2003). Complexation reactions of trace elements in cationic form with organic and inorganic ligands also play a major role in their sorption–desorption processes, toxicity and phytoavailability (Violante et al., 2008). On the other hand, even though metal oxides and allophones adsorb elements of anionic origin, their mobility mainly depends on available sites and/or reduction of

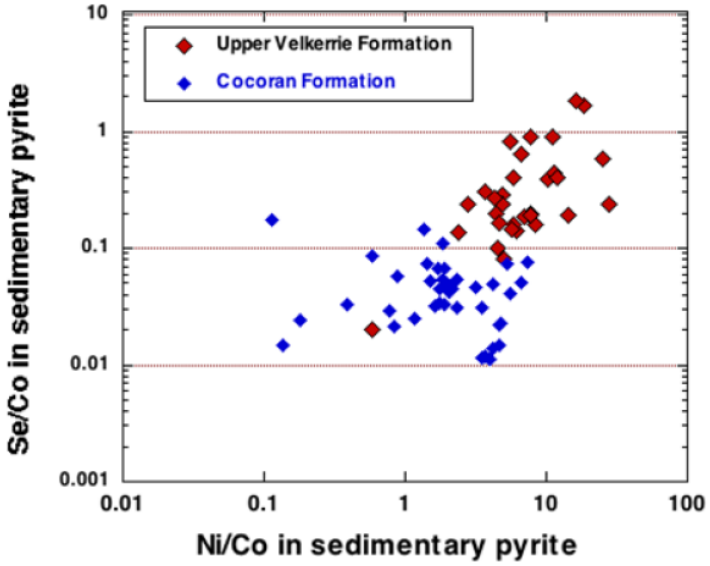

Figure 2.12. Comparison of marine pyrite mean chemical ratios Ni/Co vs Se/Co (pO_2 proxies) between Upper Velkerri and Corcoran Formation

the surface charge of the sorbents between foreign ligands and trace elements. Experimental evidence suggests that Co shows an exceptional affinity towards Mn hydroxides in comparison to other trace elements (Murray, 1968, 1975). It should also be noted that Mn-oxides and hydroxides are much more efficient scavengers of trace elements than Fe–Al hydroxides (Violante et al., 2008; Pickering, 1979).

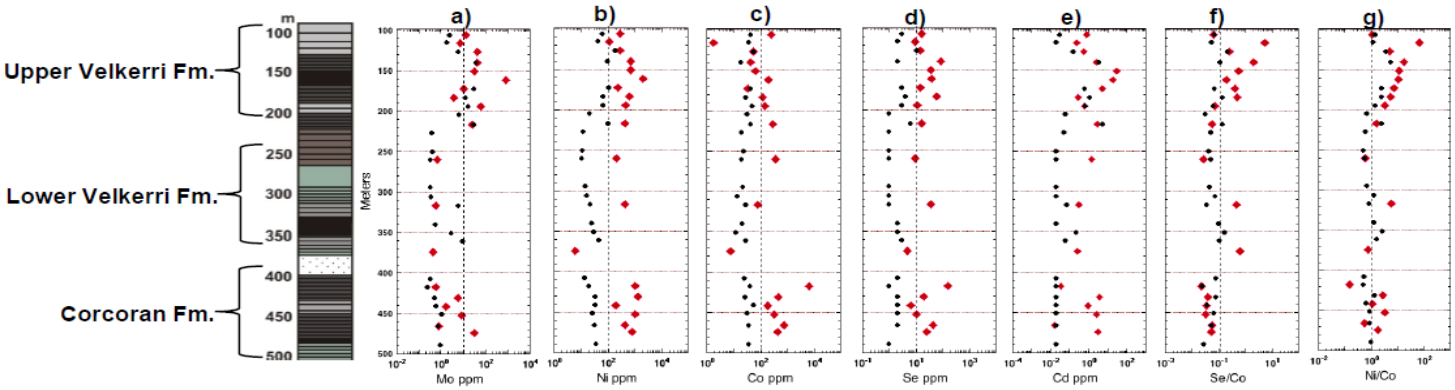

Fig 2.13. Whole rock (black dots) vs mean pyrite LA-ICP-MS analyses (red dots) for each sample

It is widely considered that the dominant source for the trace elements in the marine reservoir is riverine flux where trace elements are transported in their soluble/particulate form (SCOR Working Group, 2007; Scott et al., 2008; Sahoo et al., 2012; Algeo and Rowe, 2012; Large et al., 2014). Based on the above discussion, Co can be expected to behave in an opposite manner to Mo and Se when transferred from continents to the ocean in the riverine flux. Oxidative erosion would release Co from continental pyrite as cationic species, Co^{2+}, $CoCl^{+}$, which is immobilised by absorption on Fe and Mn oxides and hydroxides. In comparison, Mo and Se are carried by the riverine flux to the ocean as the soluble MoO_4^{2-} and SeO^{3-} species. Molybdenum increases up to ~100 ppm in Upper Velkerri compared to 6–8 ppm in Lower Velkerri and Corcoran Formation whereas the rise in Se is far less from 19 to 33 ppm. The reason could be partly due to competitive sorption processes operative on mineral surfaces during continental weathering. For instance, Wu et al. (2001) show how molybdate sorption is unaffected by the presence of equimolar selenate. However, selenate sorption is reduced (up to ~30%) in the presence of molybdate at pH < 7.0. Also, Mo substitutes for iron whereas Se substitutes sulfur, where the latter is more strongly bonded to the structure of the iron sulphide than the former (Large et al., 2014). Intense weathering may be required to release Se out of the pyrites during continental weathering of sulphides on land. Mild oxygenation events, in other words, less intense oxidative weathering on land, may release Mo more easily from the structure of pyrite in comparison to Se. This may be manifested in the form of only a subtle increase in Se concentration in comparison to Mo in the sedimentary pyrites we analyse.

Considering that we suggest certain elements (Ni, Mo and Se) exhibit an increase in the ocean with rise in pO_2 in the atmosphere, whereas Co in the ocean decreases with rise in pO_2, their ratios such as Mo/Co, Ni/Co and Se/Co can also prove to be useful to indicate changes in redox in the atmosphere–ocean system. The Se/Co and Ni/Co ratios in pyrite are much higher for the Upper Velkerri Formation than the underlying Lower Velkerri and Corcoran Formations (Fig. 2.12) offering a clear upward trend particularly through the Velkerri Formation, which supports our contention of a possible rise in pO_2, associated with

the deposition of the Upper Velkerri Formation (Fig. 2.13f, g). Overall, trace element trends through the Roper Group depict a gradual increase in trace element concentration in sedimentary pyrites and whole rock from Corcoran Formation to Velkerri Formation in URAP-4. The change could be attributed to changes in trace element supply in the water column and/or as a result of host phase availability/unavailability (particularly organic matter). Weathering, erosion, sorption–desorption processes on land and solubility coefficients of the elements mainly control trace element supply in the marine reservoir. Tectonic processes and fluctuations in oxygen in the atmosphere mainly drive these processes. It is possible that an increase in atmospheric carbon dioxide concentrations may increase rates of chemical weathering via dissolution. However, it is oxidative weathering and not dissolution, which is dominantly responsible for the release of redox-sensitive elements from sulphides, such as, pyrite (Bertine and Turekian, 1973; Taylor and Mclennan, 1995; Scott et al., 2008; Sahoo et al., 2012; Crowe et al., 2013; Large et al., 2014). Hydrothermal sources also contribute to the trace element budget. Kendall et al. (2009) suggest a hydrothermal influence on the basis of low seawater $^{187}Os/^{188}Os$ ratios (Upper Velkerri $^{187}Os/^{188}Os$ ratios is 10.6–14.0). However, that would also require the Lower Velkerri Formation to have different values to that of Upper Velkerri Formation, which is not the case within analytical error (Lower Velkerri $^{187}Os/^{188}Os$ ratios is 9.3–12.4; Kendall et al., 2009). Hydrothermal imprint in the Roper Group stratigraphy can be discounted here as the rocks lack any evidence of hydrothermal alteration. Also, the pyrite textures and chemistry exhibit no evidence of a hydrothermal overprint. Magmatic/volcanic input can also be discounted because of lack of "hot" organic rich intervals (radiogenic) and lack of tuffaceous intervals in the Velkerri Formation.

Total organic carbon and total sulfur data indicate there has been a distinct change in organic matter production in the mudstones of the Roper Group as described earlier. Trace elements (and their ratios) in whole rock and pyrite depict the same. It is possible that rates of sedimentation could have affected organic matter preservation and hence organic matter content in the shales. Slower rates would allow more organic matter preservation and formation of black organic matter rich shales (pyritic) and higher rates would in turn form grey shales. The grey shale intercalations within the black shales of the Velkerri Formation possibly reflect this change in rates of sedimentation. Rates have been higher (indicated by grey shale laminations) and lower (indicated by black mudstones; glauconitic intervals) in the Velkerri Formation. Fig. 2.5 elucidates the fact that both upper and lower Velkerri formations have grey shale intercalations within black shales/- mudstones, have glauconitic intervals (Jackson and Raiswell, 1991; Abbott and Sweet, 2000) and organic rich intervals (Kendall et al., 2009; this study) indicating slower sedimentation rates, in other words similar sedimentological conditions yet different trace element concentrations. Therefore, higher trace element concentrations in the Upper Velkerri Formation due to slower rates of sedimentation can be discounted.

It can therefore be inferred from the data of this study that there was a significant change in trace element availability in the water column, which affected primary productivity and subsequently affected organic matter production. Although, TOC does not represent the entire fraction of organic matter production, it certainly is proportional to it (Algeo and Rowe, 2012). It could be argued that lack of trace elements in the lower section is due to lack of host phase availability, which is organic matter that assists vertical drawdown of most trace elements. However most redox sensitive trace elements ultimately reside in marine pyrite. As long as anoxic conditions favour the formation of sulphides (either syngenetic or diagenetic), trace elements will be concentrated in pyrite. The above can be explained using an example from this study; Ni in pyrite shows very little variation down hole (Fig. 2.13) indicating Ni concentration in pyrite is unaffected by changes in TOC. The reason as to why trace elements are incorporated in sedimentary-diagenetic pyrites can be understood in terms of their degree of trace metal pyritization (DTMP). It is controlled by various factors outlined by Morse and Luther (1999) such as elemental electronic configuration, ligand field stabilisation and kinetics for water exchange, but how much of the trace element is concentrated, will depend mainly on their availability. Therefore, the up-stratigraphy change we observe is probably indicative of change in trace element supply in the water column. Therefore, an increased flux of nutrient trace elements, phosphorus (as indicated by the results of this study) and sulphate in the ocean (Kah et al., 2004; Luo et al., 2015) point towards enhanced weathering and erosion on land, likely due to an oxygenation event and active tectonics during the Velkerri Formation time. As discussed earlier, the Roper Group sediments deposited in a ramp style basin possibly close to a tectonically active orogen.

Available data in the literature so far suggest that the Isan orogeny occurred between 1580 and 1480 Ma along with the Anmatjira Uplift between 1500 and 1400 Ma. This along with a rise in pO_2 may have played a major role in enhancing erosional processes that gradually increased the trace element nutrient flux in the ocean which we observe at the ~1361 Ma Upper Velkerri depositional time. Increased nutrient trace element supply subsequently promoted an increase in primary productivity as indicated by TOC and phosphorus content in the rocks and possibly triggered the eukaryotic diversity observed by Javaux et al. (2004), considering the vital role of certain bio-essential trace elements particularly Mo in sustenance and growth of microorganisms (Anbar and Knoll, 2002). It has also been noted that stromatolite diversity and abundance show a prominent increase during the Roper Group deposition time (Sheldon, 2013) also supporting the above contention of rise in pO_2.

A systematic study of the trace elements using the technique introduced by Large et al. (2014) in URAP-4, allowed us to not only document nutrient trace element trends but appreciate the differences in the two black shale Formations (Velkerri and Corcoran). This variation can be linked with other biogeochemical

parameters to understand geo-biological processes operative during their sedimentation. A rise in pO_2 has been suggested to be the cause for the increase in certain redox sensitive trace elements (e.g. Mo, Se, Ni) and decrease in Co in the Upper Velkerri. It is however, beyond the scope of this study to quantify the magnitude of the rise other than to report it may have been significant enough to play a role in biological development during the "Boring Billion". This has important implications on how we perceive the oxygen trend during the Mesoproterozoic, as the study suggests oxygen levels did not remain stable and low, as proposed by Planavsky et al. (2014).

2.5.3 Comparison between laser pyrite and whole rock geochemical data

Conventionally, bulk rock analyses are undertaken to study the variation in redox sensitive elements in black shales (Algeo and Lyons, 2006; Algeo and Tribovillard, 2009; Scott et al., 2008). In this study one aim was to compare the whole rock technique with the pyrite LA-ICP-MS approach in order to understand sources and sinks of trace elements in black shales and how a combination of techniques can aid in trace element studies in general. This following discussion is based on comparison of the two techniques (refer Fig. 2.13). Large et al. (2014) described the advantages of the laser based approach w.r.t. whole rock, the most important one being the sensitivity of the technique for the obvious reason that elements present in trace amounts need instrumentation that allows better detection limits. The laser-based technique also effectively normalises the data for sulfur, which is a major variable in these rocks. Despite the fact that LA-ICP-MS data may have a wide analytical spread it provides important information on the minimum, maximum and mean values. The laser technique also enables superior detection limits particularly for samples with low overall Se contents. Whole rock data interpretation place emphasis on the maximum values (Scott et al., 2008). However, it is equally important for us to take into account the range of values and finally assign an average concentration in pyrite from all spot based analyses. Fig. 2.13 clearly illustrates the fact that the trace elements concentrate in pyrite 1–2 orders of magnitude more than whole rock, as pyrite is the common sink for most of these elements. The redox sensitive trace element (Mo, Ni, Co, Se and Cd) in Fig. 2.13, commonly shows greater enrichment in pyrite than whole rock for any given sample through the stratigraphy. For instance, enrichment factors (TE_{Py}/TE_{WR}) for Se and Mo are different for each element and between Formations (Table 2.3), where both elements concentrate in pyrite ~10 times more than whole rock. Nevertheless, Mo is 14–25 times enriched and has twice as much Se in Upper Velkerri than Corcoran Formation as indicated by $TE_{Upper\ Velkerri}/TE_{Corcoran}$ in Table 2.3.

It can therefore be concluded that bulk rock analyses are a better representation of major elements and trace elements that concentrate in the organic or detrital fractions of the rock (U, V, Ba, Cr) even though

U, V in black shale matrix measured by LA-ICP-MS act as good proxies for (U and V) whole rock. Redox sensitive chalcophile trace elements should preferably be analysed using the LA-ICP-MS as it allows us to observe variations in trace element trends that would otherwise go unnoticed (e.g. Se/Co trend in Fig. 2.13).

Table 2.3 LA-ICP-MS vs whole rock analyses of pyrites of Upper Velkerri, Lower Velkerri and Corcoran Formation py=pyrite; WR=whole rock

Formation	Mo_{WR}	Mo_{Py}	Mo_{Py}/Mo_{WR}	Se_{WR}	Se_{Py}	Se_{Py}/Se_{WR}
Upper Velkerri	15	111	7.4	4	33	8.3
Corcoran	0.6	8	13.3	2	21	10.5
$TE_{Upper\ Velkerri}/TE_{Corcoran}$	25	14	-	2	1.57	-

*Average values in ppm

2.5.4 Comparison with previous studies

Shen et al. (2003) calculated iron speciation and degree of pyritisation for samples of this particular drill hole (URAP-4), the results of which show an excellent correlation with TOC and TC of this study in Fig. 2.14. Although Raiswell et al. (1994) suggested that organic matter preservation does not always control degree of pyritization (DOP), Fig. 2.14 clearly illustrates that it does in fact correlate well with DOP in the Velkerri Formation mudstones. Luo et al. (2015), through sulfur isotope studies, constrained paleo-seawater [SO_4^{2-}] based on measured values of $^{34}S_{CAS\text{-}PY}$ and $\partial^{34}S_{CAS}/\partial t_{(max)}$ through the Proterozoic. It was noted that the Velkerri Formation time saw a pulse of higher seawater sulphate levels in the ocean and, a possible transient oxygenation event was suggested as a causative factor (Kah et al., 2004; Luo et al., 2015). Javaux et al. (2004) described pronounced diversity of eukaryotic assemblages that imparted morphological complexity in the Roper Group (complex acritarchs e.g., T. Plana and other microfossils). This is also supported by the marked increase in phosphorus in the Upper Velkerri Formation. This too, could be attributed to physico-chemical changes in the water column as an effect of pO_2.

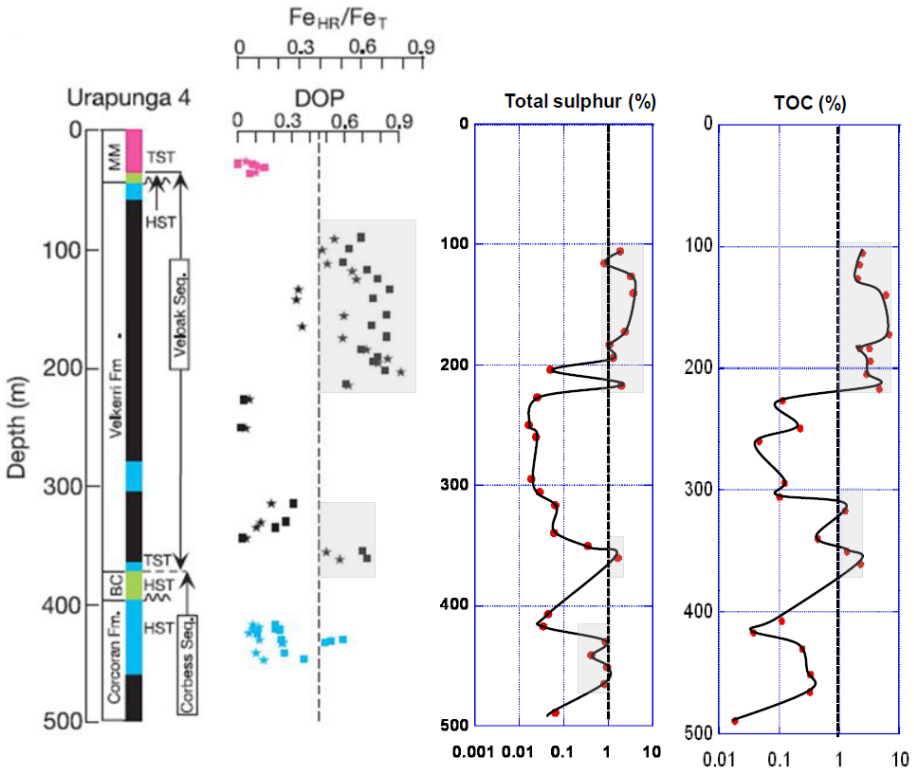

Fig 2.14. Comparison of degree of pyritization (DOP) and $Fe_{HighlyReactive\ (HR)}/Fe_{Total\ (T)}$ from Shen et al, 2003 with total sulfur and total organic carbon analyses from this study

2.6 Conclusions

The present study indicates that application of the pyrite LAICP-MS technique on the carbonaceous mudstones of Velkerri Formation & Corcoran Formation, combined with whole rock analyses and available published data enables a more complete understanding of nutrient trace element supply, productivity and atmospheric oxygenation between 1450 and 1350 Ma. Deposition of the Upper Velkerri Formation records a mild oxygenation event, manifested in the form of enriched trace element concentrations in its contained pyrite (Se, Mo, Se/Co, Ni/Co, P, Cd, Mo, Se, Zn, Ni, U, V, Cd), increased sulphate in the ocean observed by Luo et al. (2015) and high organic matter concentration. This rise in trace element and related pO_2, could explain the prominent diversification of the acritarchs and complexity observed in Roper Group microfossils.

Recent research has proposed the Mesoproterozoic was a period of low and stable oxygen levels resulting in a biological stasis (Planavsky et al., 2014). However, our research suggests a change (increase) in oxygen levels at ~1400 Ma that has major implications for the perception of oxygen levels and biological evolution during this critical period of Earth history.

2.7 Acknowledgements

This research was funded by Australian Research Council (ARC) project DP 150102578 awarded to RRL. We appreciate the help and support offered to us by the NTGS core facility staff. We also acknowledge help, advise and instruction from Leonid Danyushevsky, Sarah Gilbert, Elena Lounjeva and Paul Olin in the LA-ICP- MS laboratory and from Sean Johnson for carbon and sulfur analyses at CODES.

2.8 References

Abbott, S.T., Sweet, I.P., 2000. Tectonic control on third-order sequences in a siliciclastic ramp-style basin: an example from the Roper Superbasin (Mesoproterozoic), northern Australia. Aust. J. Earth Sci. 47, 637–657.

Ahmad, M., Dunster, J.N., Munson, T.J., 2013. Chapter 15: McArthur Basin: in Ahmad M and Munson TJ (compilers). 'Geology and mineral resources of the Northern Territory'. Northern Territory Geological Survey. Special Publication 5.

Algeo, T.J., Lyons, T.W., 2006. Mo–total organic carbon covariation in modern anoxic marine environments: Implications for analysis of paleoredox and paleohydrographic conditions. Paleoceanography 21

(PA1016), 23.

Algeo, T.J., Rowe, H., 2012. Paleoceanographic applications of trace-metal concentration data. Chem. Geol. 324, 6–18.

Algeo, T.J., Tribovillard, N., 2009. Environmental analysis of paleoceanographic systems based on molybdenum-uranium covariation. Chem. Geol. 268, 211–225.

Anbar, A.D., Knoll, A.H., 2002. Proterozoic ocean chemistry and evolution: a bioinorganic bridge? Science 297, 1137–1142.

Barley, M.E., Bekker, A., Krapezˇ, B., 2005. Late Archean to Early Paleoproterozoic global tectonics, environmental change and the rise of atmospheric oxygen Earth Planet. Sci. Lett. 238, 156–171.

Berner, R.A., 1970. Sedimentary pyrite Formation. Am. J. Sci. 268, 1–23.

Bertine, K.K., Turekian, K.K., 1973. Molybdenum in marine deposits. Geochim. Cosmochim. Acta 37, 1415–1434.

Canfield, D.E., 1998. A new model for Proterozoic ocean chemistry. Nature 396, 450–453.

Canfield, D.E., 2005. The early history of atmospheric oxygen: Homage to Robert M. Garrels. Annu. Rev. Earth Planet. Sci. 33, 1–36.

Crick, I.H., 1992. Petrological and maturation characteristics of organic matter from the Middle Proterozoic McArthur Basin, Australia. Aust. J. Earth Sci. 39, 501–519.

Crick, I.H., Boreham, C.J., Cook, A.C., Powell, T.G., 1988. Petroleum geology and geochemistry of Middle Proterozoic McArthur Basin, northern Australia II: assessment of source rock potential. Am. Assoc. Petrol. Geol. Bull. 72, 1495–1514.

Crowe, S.A., Døssing, L.N., Beukes, N.J., Bau, M., Kruger, S.J., Frei, R., Canfield, D.E., 2013. Atmospheric oxygenation three billion years ago. Nature 501, 535–538.

Danyushevsky, L., Robinson, P., Gilbert, S., Norman, M., Large, R., McGoldrick, P., Shelley, M., 2011. Routine quantitative multi-element analysis of sulphide minerals by laser ablation ICP-MS: standard development

and consideration of matrix effects. Geochem. Explor. Environ. Anal. 11, 51–60.

Dunn, P.R., 1963. Urapunga, Northern Territory, Sheet SD/53-10, Bureau of Mineral Resources 1:250000 geological series explanatory notes.

Embry, A.F., Podruski, J.A., 1989. Third-order depositional sequences of the Mesozoic succession of Sverdrup Basin. In: James, D.P., Leckie, D.A. (Eds.), Sequences, Stratigraphy, Sedimentology: Surface and Subsurface, 15. Canadian Society of Petroleum Geologists Memoir, pp. 73–84.

Ettensohn, F.R., 1994. Tectonic control on Formation and cyclicity of major Appalachian unconformities and associated stratigraphic sequences. In: Dennison, J.M., Ettensohn, F.R. (Eds.), Tectonic and Eustatic Controls on Sedimentary Cycles, 4. SEPM (Society for Sedimentary Geology) Concepts in Sedimentology and Paleontology, pp. 217–242.

George, S.C., Ahmed, M., 2002. Use of aromatic compound distributions to evaluate organic maturity of the Proterozoic Middle Velkerri Formation, McArthur Basin, Australia. In: Keep, M., Moss, S.J. (Eds.), The Sedimentary Basins of Western Australia, 3. Proceedings of the Petroleum Exploration Society of Australia Symposium, pp. 253–270.

Gorter, G., Grey, K., 2012. Velkerri Formation: Depositional Model – Beetaloo Subbasin, Northern Territory, Australia: Biostratigraphy and Organic Enrichment. CABS symposium.

Gregory, D.D., Large, R.R., Halpin, J.A., Lounejeva Baturina, E., Lyons, T.W., Wu, S., Sack, P.J., Chappaz, A., Maslennikov, V.V., Bull, S.W., Danyushevsky, L., 2015. Trace element content of sedimentary pyrite in black shales. Econ. Geol. 110, 1389–1410.

Grotzinger, J.P., Mccormick, D.S., 1988. Flexure of the Early Proterozoic lithosphere and the evolution of Kilohigok Basin (1.0 Ga), northwest Canadian Shield. In: Kleinspehn, K., Paola, C. (Eds.), New Perspectives in Basin Analysis. Springer- Verlag, New York, pp. 405–430.

Harris, C.W., Eriksson, K.A., 1990. Allogenic controls on the evolution of storm to tidal shelf sequences in the Early Proterozoic Uncompahgre Group, southwest Colorado, USA. Sedimentology 37, 189–213.
Henderson, G.M., 2002. New oceanic proxies for paleoclimate. Earth Planet. Sci. Lett. 203, 1–13.

Huang, P.M., Germida, J.J., 2002. Chemical and biochemical processes in the rhizosphere: metal pollutants. In: Huang, P.M., Bollag, J.M., Senesi, N. (Eds.), Interactions between Soil Particles and Microorganisms:

Impact on the Terrestrial Ecosystem. Wiley, New York, pp. 381–438.

Jackson, T.A., 1998. The biogeochemical and ecological significance of interactions between colloidal minerals and trace elements. In: Parker, A., Rae, J.E. (Eds.), Environmental Interactions of Clays. Springer-Verlag, Berlin, pp. 93–205.

Jackson, M.J., Raiswell, R., 1991. Sedimentology and carbon-sulfur geochemistry of the Velkerri Formation, a Mid- Proterozoic potential oil source in northern Australia. Precamb. Res. 54, 81–108.

Jackson, M.J., Powell, T.G., Summons, R.E., Sweet, I.P., 1986. Hydrocarbon shows and petroleum source rocks in sediments as old as 1.7 * 109 years. Nature 322, 727– 729.

Jackson, M.J., Simpson, E.L., Eriksson, K.A., 1990. Facies and sequence stratigraphic analysis in an intracratonic thermal-relaxation basin: the early Proterozoic, lower Quilalar Formation and Ballara Quartzite, Mount Isa Inlier, Australia. Sedimentology 37, 1053–1078.

Javaux, E., Knoll, A.H., Walter, M.R., 2003. Recognizing and interpreting the fossils of early eukaryotes. Orig. Life Evol. Biosph. 33, 75–94.

Javaux, E., Knoll, A.H., Walter, M.R., 2004. TEM evidence for eukaryotic diversity in mid-Proterozoic oceans. Geobiology 2, 121–132.

Jochum, K.P., Pfänder, J., Woodhead, J.D., Willbold, M., Stoll, B., Herwig, K., Amini, M.,
Abouchami, W., Hofmann, A.W., 2005. MPI-DING glasses: new geological reference materials for in situ Pb isotope analysis. Geochem. Geophys. Geosyst. 6, 1525–2027.

Johnston, D.T., Farquhar, J., Summons, R.E., Shen, Y., Kaufman, A.J., Masterson, A.L., Canfield, D.E., 2008. Sulfur isotope biogeochemistry of the Proterozoic McArthur Basin. Geochim. Cosmochim. Acta 72, 4278–4290.

Kah, L.C., Lyons, T.W., Frank, T.D., 2004. Low marine sulphate and protracted oxygenation of the Proterozoic bio-sphere. Nature 431, 834–838.
Kendall, B., Creaser, R.A., Gordon, G.W., Anbar, A.D., 2009. Re-Os and Mo isotope systematics of black shales from the Middle Proterozoic Velkerri and Wollogorang Formations, McArthur Basin, northern Australia. Geochim. Cosmochim. Acta 73, 2534–2558.

Konhauser, K.O., Pecoits, E., Lalonde, S.V., Papineau, D., Nisbet, E.G., Barley, M.E., Arndt, N.T., Zahnle, K., Kamber, B.S., 2009. Oceanic nickel depletion and a methanogen famine before the Great Oxidation Event. Nature 458, 750–753.

Konhauser, K.O., Lalonde, S.V., Planavsky, N.J., Pecoits, E., Lyons, T.W., Mojzsis, S.J., Rouxel, O.J., Barley, M.E., Rosiere, C., Fralick, P., Kump, L.R., Bekker, A., 2011. Aerobic bacterial pyrite oxidation and acid rock drainage during the Great Oxidation Event. Nature 478, 369–373.

Krauskopf, K.B., Bird, D.K., 1995. Introduction to Geochemistry, third ed. McGraw Hill Inc, New York, p. 647.

Large, R.R., Halpin, J.A., Danyushevsky, L.V., Maslennikov, V.V., Bull, S.W., Long, J.A., Gregory, D.D., Lounejeva, E., Lyons, T.W., Sack, P.J., McGoldrick, P., Calver, C.R., 2014. Trace element content of sedimentary pyrite as a new proxy for deep time ocean-atmosphere evolution. Earth Planet. Sci. Lett. 389, 209–220.

Large, R.R., Gregory, D.G., Steadman, J.A., Tomkins, A.G., Lounejeva, E., Danyushevsky, L.V., Halpin, J.A., Maslennikov, V.V., Sack, P.J., Mukherjee, I., Hickman, A., 2015a. Gold in the oceans through time. Earth Planet. Sci. Lett. 428, 139–150.

Large, R.R., Halpin, J.A., Lounejeva, E., Danyushevsky, L.V., Maslennikov, V.V., Gregory, D., Sack, P.J., Haines, P.W., Long, J.A., Makoundi, C., Stepanov, A.S., 2015b. Cycles of nutrient trace elements in the Phanerozoic ocean. Gondwana Res. 28 (4), 1282–1293.

Luo, G., Ono, S., Huang, J., Algeo, T.J., Li, C., Zhou, L., Robinson, A., Lyons, T.W., Xie, S., 2015. Decline in oceanic sulfate levels during the early Mesoproterozoic. Precambr. Res. 258, 36–47.

Lyons, T.W., Reinhard, C.T., Planavsky, N.J., 2014. The rise of oxygen in Earth's early ocean and atmosphere. Nature 506, 307–315.

Morse, J.W., Luther III, G.W., 1999. Chemical influences on trace metal-sulfide interactions in anoxic sediments. Geochim. Cosmochim. Acta 63, 3373–3378.
Murray, J.W., 1968. The adsorption of aqueous metal on colloidal hydrous manganese oxide. Adv. Chem. Ser. 79, 74–81.

Murray, J.W., 1975. The interaction of cobalt with hydrous manganese dioxide. Geochim. Cosmochim. Acta 39, 635–647.

Peat, C.J., Muir, M.D., Plumb, K.A., Mckirdy, D.M., Norvick, M.S., 1978. Proterozoic microfossils from the Roper Group, Northern Territory, Australia, Bureau of Mineral Resources, Australia. J. Aust. Geol. Geophys. 3, 1–17.

Pickering, W., 1979. Copper retention by sediment/soil components. In: Nriagu, J.O. (Ed.), Copper in the Environment, Ecological Cycling, vol. I. Wiley, New York, pp. 217–253.

Planavsky, N.J., McGoldrick, P., Scott, C.T., Li, C., Reinhard, C.T., Kelly, A.E., Chu, X., Bekker, A., Love, G.D., Lyons, T.W., 2011. Widespread iron-rich conditions in the mid-Proterozoic ocean. Nature 447, 448–451.

Planavsky, N.J., Reinhard, C.T., Wang, X., Thomson, D., McGoldrick, P., Rainbird, R.H., Johnson, T., Fischer, W.W., Lyons, T.W., 2014. Low Mid-Proterozoic atmospheric oxygen levels and the delayed rise of animals. Science 346, 635–638.

Raiswell, R., Berner, R.A., 1985. Pyrite Formation in euxinic and semi-euxinic environments. Am. J. Sci. 285, 710–724.

Raiswell, R., Canfield, D.E., Berner, R.A., 1994. A comparison of iron extraction methods for the determination of degree of pyritisation and the recognition of iron-limited pyrite Formation. Chem. Geol. 111, 101–110.

Sahoo, S.K., Planavsky, N.J., Kendall, B., Wang, X., Shi, X., Scott, C., Anbar, A.D., Lyons, T.W., Jiang, G., 2012. Ocean oxygenation in the wake of the Marinoan glaciation. Nature 489, 546–549.

Saito, M.A., Goepfert, T.J., 2008. Zinc–cobalt colimitation of Phaeocystis antarctica. Limnol. Oceanogr. 53, 266–275.

SCOR Working Group, 2007. GEOTRACES – an international study of the global marine biogeochemical cycles of trace elements and their isotopes. Chem. Erde 67, 85–131.

Scott, C., Lyons, T.W., Bekker, A., Shen, Y., Poulton, S.W., Chu, X., Anbar, A.D., 2008. Tracing the stepwise oxygenation of the Proterozoic ocean. Nature 452, 456–459.

Sheldon, N.D., 2013. Causes and consequences of low atmospheric pCO2 in the Late Mesoproterozoic. Chem. Geol. 362, 224–231.

Shen, Y., Knoll, A.H., Walter, M.R., 2003. Evidence for low sulphate and anoxia in a mid-Proterozoic marine

basin. Nature 423, 632–635.

Silverman, M.R., Landon, S.M., Leaver, J.S., Mather, T.J., Berg, E., 2007. No fuel like an old fuel: Proterozoic oil and gas potential in the Beetaloo Basin, Northern Territory, Australia. In: Munson, T.J., Ambrose, G.J., (Eds.). Proceedings of the Central Australian Basins Symposium (CABS), Alice Springs, Northern Territory, 16–18 August, 2005. Northern Territory Geological Survey, Special Publication 2.

Sparks, D.L., 2003. Environmental Soil Chemistry, second ed. Academic Press, San Diego, CA.

Stüeken, E.E., Buick, R., Bekker, A., Catling, D., Foriel, J., Guy, B.M., Kah, L.C., Machel, H.G., Montañez, I.P., Poulton, S.W., 2015. The evolution of the global selenium cycle: secular trends in Se isotopes and abundances. Geochim. Cosmochim. Acta 162, 109–125.

Summons, R.E., Taylor, D., Boreham, C.J., 1994. Geochemical tools for evaluating petroleum generation in Middle Proterozoic sediments of the McArthur Basin, Northern Territory, Australia. Aust. Petrol. Explor. Assoc. J. 34, 692–706.

Swanner, E.D., Planavsky, N.J., Lalonde, S.V., Robbins, L.J., Bekker, A., Rouxel, O.J., et al., 2014. Cobalt and marine redox evolution. Earth Planet. Sci. Lett. 390, 253–263.

Sweet, I.P., Jackson, M.J., 1986. BMR stratigraphic drilling in the Roper Group, Northern Territory. Bureau of Mineral Resources Record 1986/19.

Sweet, I.P., Brakel, A.T., Rawlings, D.J., Haines, P.W., Plumb, K.A. Wygralak, A.S., 1999. Mount Marumba, Northern Territory, sheet SD/53-6 (2nd edition). Australian Geological Survey Organisation and Northern Territory Geological Survey (National Geoscience Mapping Accord) 1:250000 geological map series explanatory notes.

Taylor, S.R., Mclennan, S.M., 1995. The geochemical evolution of the continental crust. Rev. Geophys. 33, 241–265.

Tribovillard, N., Algeo, T.J., Lyons, T., Riboulleau, A., 2006. Trace metals as paleoredox and paleoproductivity proxies: an update. Chem. Geol. 232, 12–32.

Violante, A., Krishnamurti, G.S.R., Pigna, M., 2008. Mobility of trace elements in soil environments. In: Violante, A., Huang, P.M., Gadd, G.M. (Eds.), Biophysico-Chemical Processes of Metals and Metalloids in Soil Environments. John Wiley & Sons, Hoboken, NJ, pp. 169–213.

Warren, J.K., George, S.C., Hamilton, P.J., Tingate, P., 1998. Proterozoic source rocks: sedimentology and

organic characteristics of the Velkerri Formation, Northern Territory, Australia. Am. Assoc. Petrol. Geol. Bull. 82, 442–463.

Wu, C.H., Shang, L.L., Cheng, F.L., Chao, Y.K., 2001. Modeling competitive adsorption of molybdate, sulfate and selenate on c-Al2O3 by the triple-layer model. J. Colloid Interface Sci. 233, 259–264.

Zerkle, A.L., House, C.H., Brantley, S.L., 2005. Biogeochemical signatures through time as inferred from whole microbial genomes. Am. J. Sci. 305, 467–502

Chapter 3

Application of Pyrite Trace Element Chemistry to Exploration for SEDEX style Zn-Pb Deposits: McArthur Basin, Northern Territory, Australia

(Mukherjee, I., and Large, R.R., 2017. Ore Geology Reviews 81, 1249–1270)

Indrani Mukherjee and Ross Large
Centre of Excellence in Ore Deposits (CODES), University of Tasmania

3.0 Abstract

Sedimentary pyrites in black shales contain abundant trace elements that provide information on the chemistry of the seawater at the time of sedimentation. This study focuses on the Barney Creek Formation (~1640 Ma) in the McArthur Basin in the Northern Territory of Australia, which is host to one of the world's largest SEDEX Zn-Pb-Ag deposits, and several smaller deposits. Fine-grained sedimentary pyrite was sampled from three drill holes through the Barney Creek Formation at various distances from SEDEX mineralisation. Samples were selected through the stratigraphy of each hole and analysed by LA-ICPMS for a suite of 14 trace elements. The data show that sedimentary pyrite at the base of the Barney Creek Formation, closest (within 1 km) to SEDEX mineralisation, is strongly enriched in Zn and Tl by one to two orders of magnitude compared to the global average for sedimentary pyrite. In contrast, sedimentary pyrite from the hole furthest from SEDEX mineralisation (~ 60 km) contains mean Zn and Tl values equal to, or less than, the global average. Based on the three drill hole pyrite data sets it is concluded that trace elements that are contributed to the basin during hydrothermal exhalations, and adsorbed into contemporaneous sedimentary pyrite, are principally Zn, Tl, Cu, Pb, Ag and As. In contrast, trace elements that are adsorbed into sedimentary pyrite from background seawater are principally Mo, Ni, Co, Se and As. These differences have enabled the development of a SEDEX fertility diagram for sedimentary basins, based on the composition of sedimentary pyrite, that distinguish high Zn, but barren shales, from high zinc SEDEX-related shales. In parallel with the increase in Zn and Tl in sedimentary pyrite approaching mineralisation there is a decrease in Ni, Co and Mo. This means that the ratios Zn/Ni and Tl/Co are particularly good pyrite vectors to SEDEX mineralisation in the McArthur Basin, varying over 4 to 6 orders of magnitude from barren shales to mineralised shales. It is speculated that the reverse relationship between Ni, Co and Zn, Tl may be caused by hydrothermal exhalations into the water column that affect the ion-exchange pyrite surface complexation processes, altering the uptake of these elements into sedimentary pyrite.

Another important conclusion of this study is that hydrothermal exhalations into a sedimentary basin may affect the redox sensitive trace element chemistry of sedimentary pyrite and therefore the trace element chemistry of pyritic black shales. Nickel, Co and Mo all decrease in proximity to hydrothermal vents that form SEDEX deposits, whereas Zn, Tl and Pb increase. Selenium and bismuth are the only redox sensitive trace elements that appear to be unaffected by hydrothermal activity in the McArthur Basin. This has implications on how trace element concentrations of black shales and pyrite are used to reflect past global ocean chemistry.

3.1 Introduction

The McArthur Basin in Northern Australia is known to be a significant repository of base metals. The Barney Creek Formation (BCF), particularly the HYC Pyritic shale member hosts several stratiform SEDEX style Zn-Pb ore deposits, including the McArthur River deposit (formerly known as HYC deposit) which is one of the world's largest of its type. Because it is undeformed and unmetamorphosed, the McArthur River deposit has been used as the basis to develop the classic model for sediment hosted stratiform Zn-Pb deposits (Croxford 1968; Lambert and Scott, 1973; Murray 1975; Cook et al., 2000; Large et al., 2002; Chen et al., 2003; Large et al., 2005) and to determine the primary geochemical halo to mineralization (Lambert and Scott, 1973; Corbett et al., 1975; Large et al., 1998; Large et al., 2000; Maier, 2011). Previous research has identified lithogeochemical (element & alteration halos), isotopic (C, O, Sr, S & Pb) and geophysical signatures in rocks hosting and surrounding the ore body, which have helped to refine exploration techniques (Large et al., 2005; Duffet, 1997). The McArthur River deposit is also considered to record palaeobiological processes operative within the hydrothermal system, which provides information on the role of microbiology in ore formation (Chen et al., 2003). Several prospects with varying proximity to the McArthur River deposit have been identified that impact on our understanding of the McArthur River style of mineralisation and its stratigraphic position in the Barney Creek Formation.

Research on pyrite trace element (TE) content using Laser Ablation Inductively Coupled Plasma Mass Spectrometry (LA-ICP-MS) has aided construction of ore deposit models and helped to solve conjectures related to ore-genesis (Large et al., 2007; Large et al., 2009; Thomas et al, 2011; Steadman et al., 2015; Gregory et al., 2015). Recently, the trace element content of sedimentary pyrite has been used to help understand past ocean chemistry and its relation to major ore deposit cycles, particularly orogenic gold deposits (Large et al., 2015). Maier (2011) explored the potential of sedimentary pyrite trace element content in order to compare two Northern Australian SEDEX deposits (McArthur River, N.T. and Bluebush

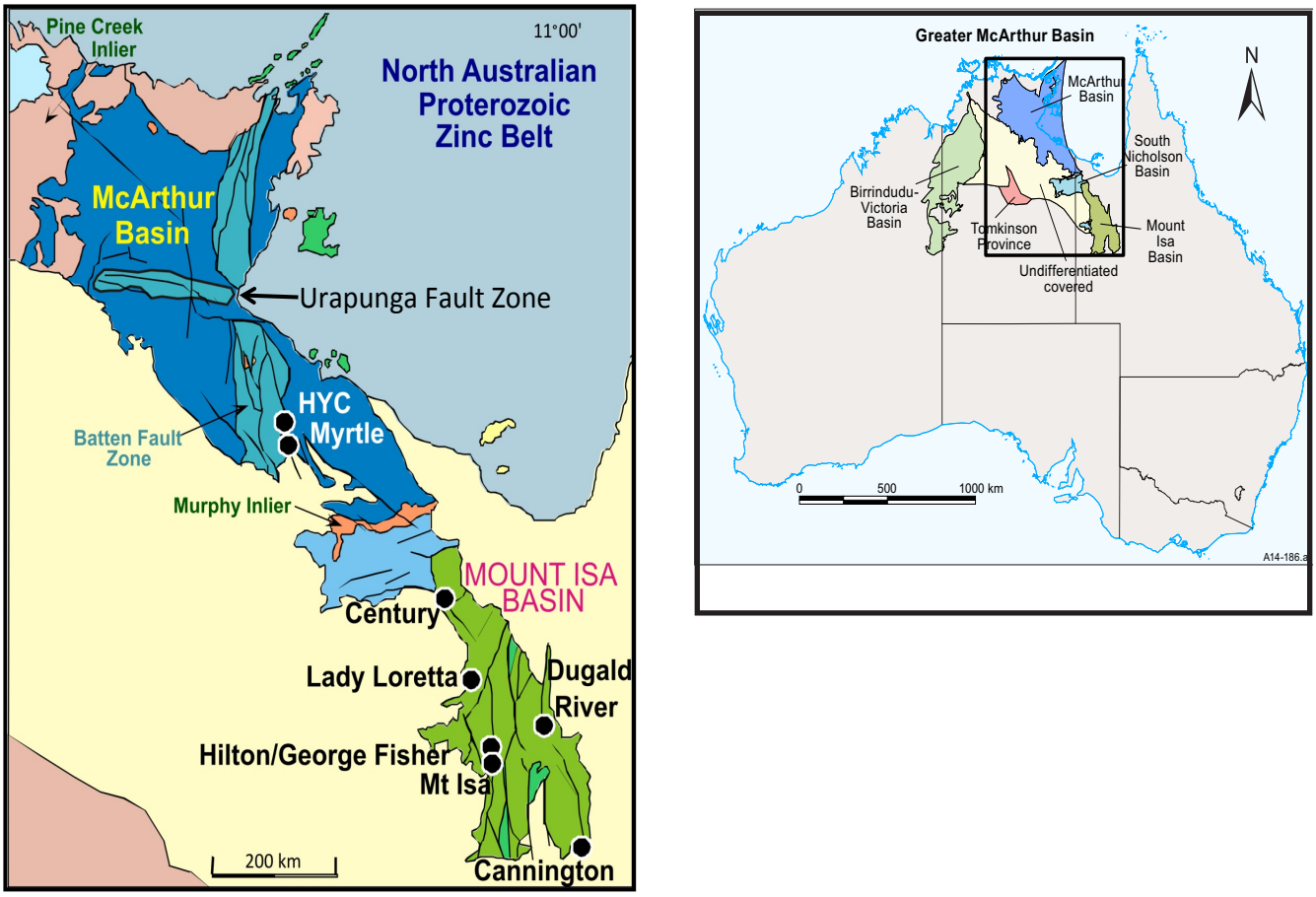

Fig 3.1 Geology of the McArthur Basin with location of major stratiform Zn-Pb-Ag deposits (After Large et al., 2005)

prospect, Queensland) and construct potential geochemical guides (TE haloes) to mineralisation for Northern Australian SEDEX deposits. An important outcome was that certain pyrite trace element ratios in pyrite such as Tl:As, Tl:Ag, Tl:Mo, Bi:As and Co:Ni, were shown to be useful vectors to mineralisation as they exhibited an increase towards the ore body. The study also described various factors that would alter or affect pyrite trace element chemistry such as basin redox condition, basin- wide mass flow sedimentation, pyrite recrystallization, timing and composition of hydrothermal fluids. Recently, Gadd et al., (2015) studied trace element variation (Co, Ni, Cu, Se, Mo, Bi, Zn, Pb, Mn, Tl, As, Ag, Sb) in different generations of pyrites in the Howards's Pass SEDEX Zn-Pb district, Selwyn Basin in Yukon using a combination of electron probe microanalysis (EPMA) and Laser Ablation Inductively Coupled Plasma Mass Spectrometry (LA-ICP-MS). This was primarily done to understand sources of the various trace elements. Two groups (A and B) of trace elements were identified on the basis of their concentration in pyrite and whole rock and have been attributed to different sources. Elements such as Zn, Pb, Mn, Tl, As, Ag, Sb were categorised as Group A and are believed to have a SEDEX-forming hydrothermal fluid origin. On the other hand, Group B comprised Co, Ni, Cu, Se, Mo and Bi that are sourced from ambient seawater at the sediment water

interface. The study concluded that Group A elements were added to pyrite through the syn-diagenetic mineralising fluids and Group B from ambient pore water.

Pyritic carbonaceous shales of the BCF therefore, present an excellent opportunity to study sedimentary pyrite TE chemistry in black shales using LA-ICP-MS to further develop the work initially carried out by Maier (2011). This study is a first attempt to observe differences (if any) in sedimentary pyrite TE chemistry in barren and base metal bearing black shales in the same stratigraphic horizon that could possibly be attributed to effects of mineralization & hydrothermal activity. Pyritic shales from varying proximity to the ore body (farthest, intermediate and closest) i.e., from drill holes Matchbox diamond drill hole 001 (MBXDD001) and Leila Yard (LY1) through the unmineralized Barney Creek Formation and mineralised BCF Myrtle-4 (MY4) were sampled for TE analyses of pyrite. This paper discusses: a) TE chemistry of barren black shales of the BCF and implications of the data in understanding Palaeoproterozoic ocean chemistry, b) effect of hydrothermal exhalations on the TE content of sedimentary pyrite chemistry, and c) how pyrite chemostratigraphy can be used in the explorer's toolkit for sediment hosted Zn-Pb deposits.

3.2 Geological background

3.2.1 Stratigraphy

The Palaeo-Mesoproterozoic McArthur Basin in Northern Australia is composed of an unmetamorphosed and mildly deformed ~10 km thick package of sedimentary rocks including minor volcanics (Plumb and Wellman, 1987). The basin is divided into the northern and southern McArthur Basin with the Urapunga Fault zone being the dividing line (Fig 3.1). Both northern and southern basins comprise of Walker and Batten fault zones respectively that further divide the northern basin into northeastern and northwestern basins and southern into southeastern and southwestern basins. The northern McArthur comprises the Groote Eylandt, Katherine River, Donydji, Parsons Range, Habgood, Balma, Mount Rigg, Nathan and Roper groups. The Tawallah (oldest), McArthur, Nathan and Roper (youngest) Groups define the stratigraphy of the southern McArthur Basin (Rawlings et al., 1997; Rawlings 1999; Ahmad et al., 2013) (Fig 3.2).

The Murphy Province and Scrutton Inlier represent the cratonised basement units formed during the Barramundi orogeny accompanied by widespread felsic magmatism and continent-wide deformation at ~1870 Ma (Duffet et al., 1997). It is overlain by sedimentary packages of four main groups (Tawallah, McArthur, Nathan and Roper Groups). Arenaceous rocks of the Tawallah Group (lowest in the stratigraphy) are exposed in the southeastern McArthur Basin and the Batten Fault zone unconformably overlain by rocks of the Nathan Group and McArthur Group respectively.

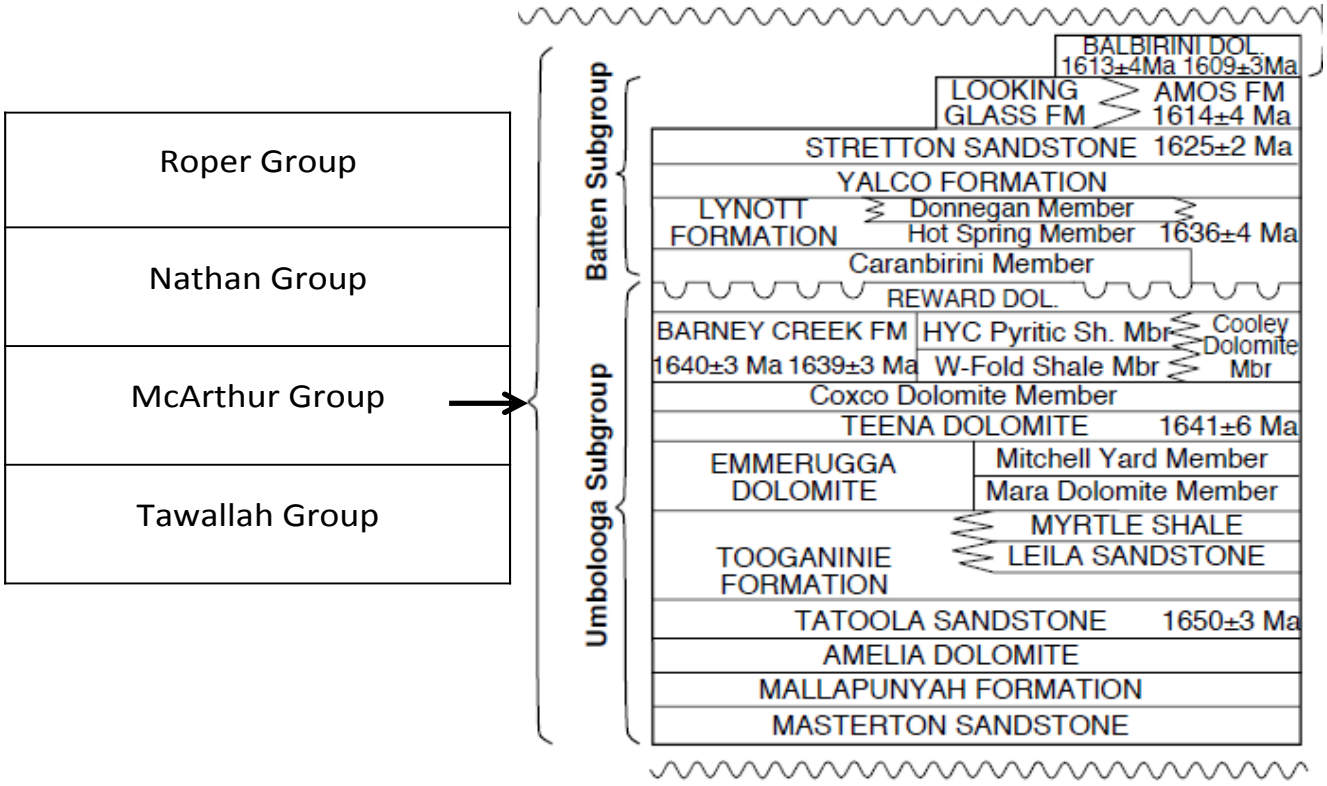

Fig 3.2 General stratigraphy of the McArthur Basin (left) and detailed stratigraphy of McArthur Group (right) adapted from Ahmad et al., 2003

A ~5 km thick package of platformal stromatolitic dolostone and clastic sedimentary rocks with local pyritic carbonaceous siltstone units form the McArthur Group. It is further divided into two subgroups, which are Batten and Umbolooga subgroups. The BCF (1640 ± 3 Ma; Page and Sweet, 1998) is part of the Umbolooga Subgroup with Reward dolostone above it and Teena Dolostone below. The BCF is further divided into Cooley Dolostone member, W-Fold Shale Member and HYC Pyritic Shale Member. The Cooley Dolostone Member comprises fault-related breccias and is thought have been derived locally. Green and red dolomitic siltstone and shale with vitric tuff categorise the W-Fold Shale Member. The HYC Pyritic Shale member is made up of laminated pyritic, dolomitic siltstone/mudstone with minor tuffaceous mudstone.

The facies architecture of the Barney Creek Depositional Sequence (BCDS) of the Middle McArthur Group, which comprises three units, Coxco Dolomite Member, Barney Creek Formation and Reward Dolomite encompass the development of numerous sub-basins (Winefield, 1999). The sub-basins are a result of a combination of ~N-S trending fault systems adjacent to which the thickest accumulations of the BCDS occur and ~E-W trending structures which are in association with rapid lateral facies variation. The positioning of the HYC deposit has been attributed to the

structural framework of the sub-basin i.e., orientation of the fault systems and other structures associated with it. For example, the McArthur River deposit is adjacent to the ~N-S trending Emu Fault, toward the base of a thick succession of pyritic, carbonaceous dolomitic siltstone. A number of structural models have been suggested that explain the deposition of this thick sequence; for instance, activation of ~N-S strike slip faults and generation of pull-apart sub-basins have been suggested as a possible mechanism (Jackson et al., 1987; Davidson and Dashlooty, 1993). Etheridge and Wall (1994) suggested that ~N-S faults acted as passive transfers to E-W orientated growth faults that favoured deposition of the BCDS during the sag phase deposition of the McArthur Group. Later, Winefield (1997a) suggested that the deposition of BCDS was either because of accommodation along ~N-S faults developed due to ~NW-SE compression or ~E-W depressions due to flexural subsidence. This was later modified by Winefield (1999) on the basis of sedimentological (facies architecture), structural and geophysical studies, that the BCDS could not have been deposited under an entirely compressive regime as suggested earlier, but only locally along ~N-S fault systems and that ~E-W structures (in some cases for e.g., Myrtle sub-basin) played an important role in initial subsidence and sub-basin formation (Bull and Scott, 1998). Overall, it was concluded that the fault and associated structures responded differently to the ~ N-S strike slip regime (transtension and transpression), such that the deposition of thick accumulations of BCDS occurred in transtensional areas and condensed accumulations in tranpressional areas (Fig 3.3) (McGoldrick et al., 2010).

3.2.2 Depositional environment

Overall, the BCF was deposited in a quiet, anoxic, below sub-wave base environment in an actively subsiding third order basins where fluctuations in the water depth resulted in the different facies present as W-Fold Shale Member and HYC Pyritic Shale Member (Bull, 1998). Microfossil assemblages indicate deposition below photic zone (Oehler and Logan, 1977). Although previous sedimentological studies have concluded the BCF to be shallow-water or lacustrine (Jackson et al., 1987), it is now considered to be of marine origin (Jackson et al., 2000; Shen et al., 2002; Bull, 2001). Additional evidence from saturated hydrocarbon biomarker studies by Chen et al., (2003) confirm the deep water, marine depositional environment.

3.2.3 Mineralization

Stratiform, sedimentary base metal occurrences in the McArthur Basin are mainly hosted by pyritic carbonaceous shale and dolomitic siltstone. Sediment hosted Zn-Pb-Ag mineralisation in the BCF is hosted by the lower part of the HYC Pyritic Shale Member, with nature of mineralisation being either

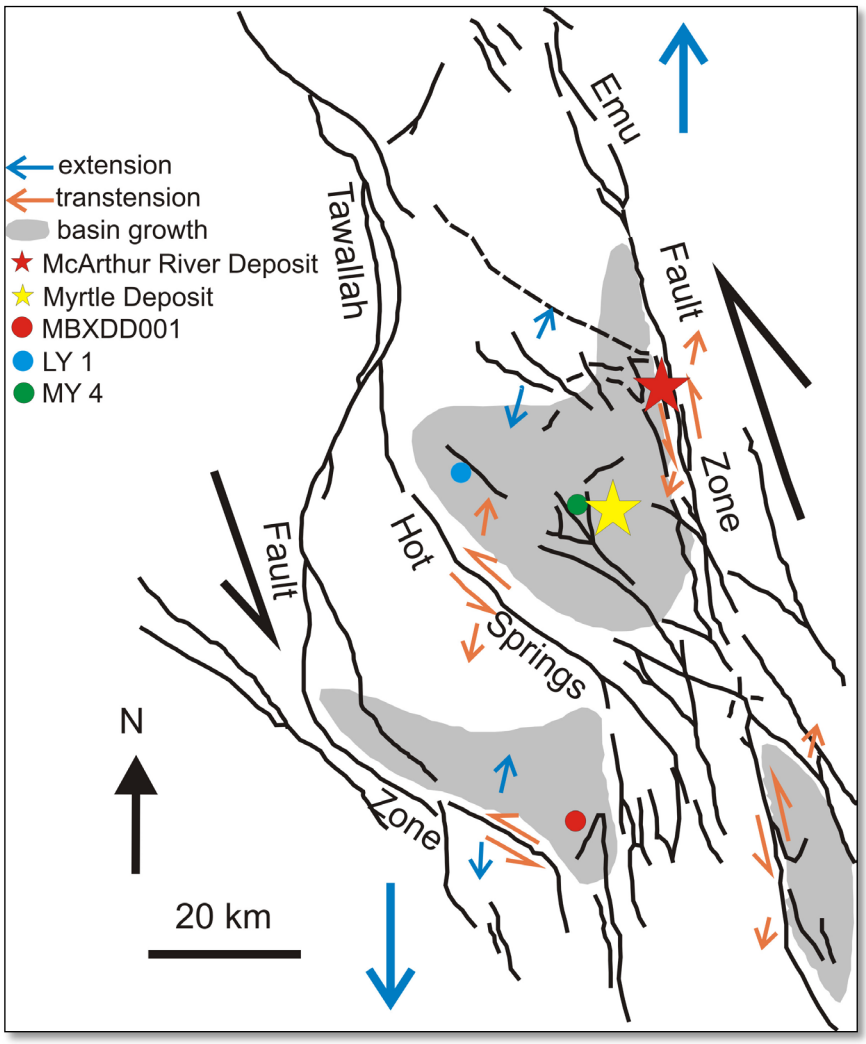

Fig 3.3 Sub basins and structures within the McArthur Basin (After McGoldrick et al., 2010)

stratabound or stratiform (Logan et al., 1990; Hinman, 1995; Large et al., 1998; Large et al., 2000b). A combination of tectonic setting, hydrothermal exhalation and sea floor depositional environment has played a very important role in the formation of this style of deposit (Large et al., 2005; Goodfellow, 2004), a summary of which is presented in Table 3.1. Tectonic settings govern the shape of the basin, structures within the basin (extensional or compressional), and geometry of active faults that act as conduits for focussed mineralised fluid flow (Garven et al., 2001; Leach et al., 2010). An epicontinental rift basin has been suggested as a possible tectonic setting that favoured McArthur River mineralisation (Large et al., 2005). Mineralisation is interlayered with mass flow breccias indicating local synsedimentary faults systems were active, acting as effective conduits for hydrothermal fluids (Walker et al., 1977; Williams 1978a; Rohrlach et al., 1998). Mineralisation is considered to have taken place during sedimentation at

Table 3.1 Geological information on McArthur River style Zn-Pb deposits (Ahmad et al., 2003)

Tectonic Setting	Magamatism/volcanism	Hydrothermal system
Epicontinental marine platform/ intracontinental rift	Minor tuffaceous horizons; No magmatic source identified	Moderate to low temperature (< 200°C), oxidised and high salinity (>15 wt % NaCl), Pb-Zn undersaturated fluids

the sediment-water interface or within the sediment during early diagenesis where low-temperature, oxidised and saline hydrothermal fluids were introduced in these third order basins to precipitate the metal sulphides (Large et al, 2002; Large et al., 2005). After the ore-enriched sediment formed, its burial and diagenesis took place during the most substantial sub-basin development (Bull, 2001). Although, magmatism results in high heat flows that produce productive hydrothermal systems and act as source of some metals (Goodfellow et al., 2004), it has not been linked to the McArthur River deposit and related prospects. Very fine grained, laminated and/or massive sphalerite, galena, Ag-sulphosalts and pyrite (most predominant) occur in the carbonaceous (bituminous) parts of the shale and are present in the form of single or multiple lenses (Large et al., 2005). At least two generations of pyrite (Py 1 and Py 2) have been identified (Williams 1978a, b). Very small (10-15 μ), euhedral to spherical aggregates of Py 1 represent an earlier generation whereas Py 2 occurs as overgrowth or infilllings within Py 1 (Ahmad et al., 2013). Sphalerite and galena are present in the form of monomineralic layers and with fine-grained disseminations. Sphalerite and chalcopyrite is also seen to occur as elongate bodies while galena as streaks within sphalerite (Ahmad et al., 2013).

The BCF and its mineralised counterparts are unmetamorphosed, however variably deformed with both synsedimentary and late brittle deformation structures being observed. However, most primary depositional textures are preserved in the rock along with recrystallised textures (Large et al., 2005).

3.2.4 Alteration haloes

Dispersion of elements particularly, Zn, Pb, Ag, Mn and Tl in SEDEX deposits are generally related to how the ore fluids have moved from sites of exhalations, i.e., along the sea floor and within sediment layers, since mineralization is largely syngenetic. Patterns are more likely to extend along strike (up to hundreds of metres or several kilometres) and have a limited vertical extent. Hence, the McArthur River deposit has a well-developed geochemical halo that has been studied

extensively (Lambert and Scott, 1973; Corbett et al., 1975; Large et al., 1998; Large et al., 2000).

Whole rock analyses of carbonaceous shales and dolostones undertaken by Lambert and Scott (1973) and Corbett et al., (1975), led to the conclusion that elements such Zn, Pb, Ag, Hg increase in concentrations in shales in near vicinity to a SEDEX style ore deposit. Also, the shales are more pyritic and rich in potassium in proximity to ore. The dolostones show an increase in their Fe and Mn content with the latter being enriched in sediments in the footwall of the deposit. Later, Large et al., (2000) used geochemical vectors previously applied for Lady Loretta deposit in Mt. Isa Basin, Australia to characterize lithogeochemical haloes around the McArthur River deposit. They concluded that Zn-Pb-Tl haloes in pyritic black shales in hanging wall and footwall extended along strike of the deposit with the Tl halo extending the farthest (Fig 3.4). A Fe-Mn dolomite halo, which roughly coincided with the Zn-Pb-Tl halo was found to extend along the base of the HYC Pyritic Shale with most iron-rich dolomites being present in the ore zone and Mn halo in carbonates being more extensive than the Fe halo in carbonates. Using an unconventional approach, Maier (2011) used trace metal concentrations in sedimentary pyrites of the McArthur River deposit and the Bluebush Prospect to note the differences and similarities between them in terms of their sedimentary pyrite trace element content. The study showed that certain trace element ratios (Tl/As, Tl/Ag, Tl/Mo, Bi/As and Co/Ni) could be used as vectors to mineralization to the McArthur River deposit as they progressively increased towards the ore body. Also, it was noted that elements such Ni and Co concentrations decreased in sedimentary pyrites in mineralised black shales in proximity to ore.

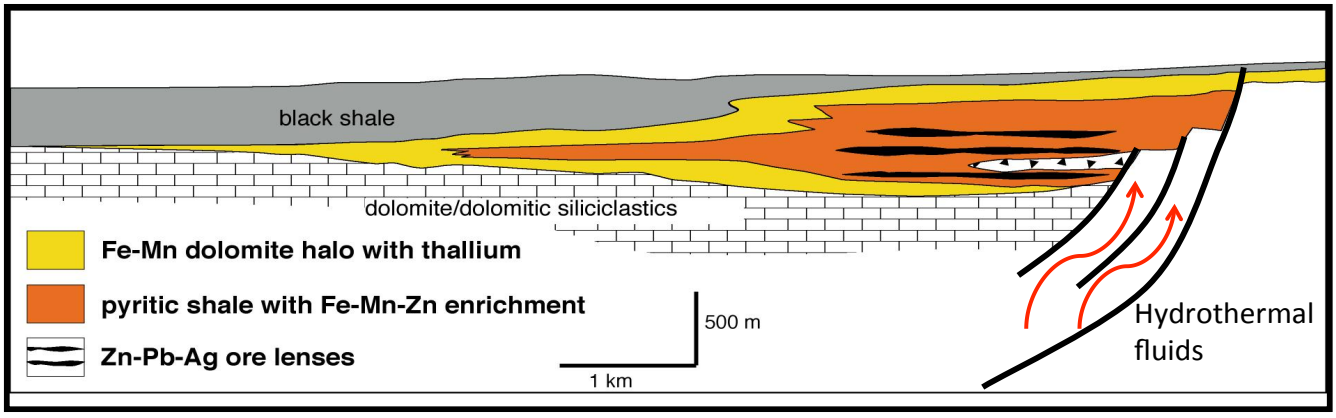

Fig 3.4 Litho-geochemical haloes identified for McArthur River deposit (Large et al., 2000)

3.3 Methods

3.3.1 Geological context of the drill holes and sampling

Three drill holes through the BCF (MBXDD001, LY1 and MY4) with similar facies architecture, in different sub-basins, at varying proximity to the ore body were selected for this study (Fig 3.3). Diamond drill hole 001 (MBXDD001) was drilled about 60 km south of the McArthur River Zinc Mine (8121952.0 mN; 606036.0 mE) in the Gorge sub Basin adjacent to the NW trending Abner Fault. Leila yard 1 (LY1) was drilled ~50 km WSW of McArthur River deposit (8163118.0 mN; 592608.0 mE) in the Leila Creek sub-basin, adjacent to Hot Springs Fault. Myrtle 4 (MY4) was drilled in the mineralized northern Myrtle sub-basin, 20 km away from the HYC deposit (8164181.0 mN; 612912.0 mE) Table 3.2. The Northern Territory Geological Survey (NTGS) in Darwin housed the drill core for the study and samples were collected at the NTGS core shed facility. Carbonaceous dolomitic-siltstones were collected every ~10 m down-hole and polished laser mounts were prepared, for petrography using reflected light microscopy, and LA-ICP-MS analyses at CODES, University of Tasmania.

3.3.2 Rationale behind sampling

Past research on the McArthur River deposit has been focused on constructing litho-geochemical and geophysical haloes in and around the deposit using whole rock and pyrite major and trace element analyses. On the basis of these analyses, it has been well established that certain elements show distinctive trends towards and further away from the ore body. The aim of this study was to firstly, characterize TE concentrations in pyrite vertically through the stratigraphy of the BCF rather than observe lateral variation along the same mineralized stratigraphic horizon, mainly because this has already been studied in detail (Maier, 2001). The first drill hole, MBXDD001, was chosen, as it is farthest away from any ore body known in the basin and was considered to represent barren black shales. Leila Yard 1 (LY1) on the other hand is not known to be mineralized, however is relatively close to the McArthur River deposit. It was chosen in order to determine

Table 3.2 Geological information on McArthur River and Myrtle deposit

Deposit	Location	Stratigraphy	Host rocks	Grade
McArthur River	16°26'N; 136°06'E (725 km SE of Darwin)	HYC Pyritic Shale Member of the BCF	Interbedded carbonaceous shales with dolomitic siltstone	227 Mt @ 9.2% Zn, 4.1% Pb, 41 g/t Ag, 0.2% Cu.
Myrtle	20 km S of McArthur River (730 km SE Darwin)	HYC Pyritic Shale Member of the BCF	Well bedded calcareous, pyritic shale interpreted as HYC Pyritic Shale equivalent	43.6 Mt @ 4.05% Zn, 0.95% Pb

effects of hydrothermal exhalations related to the McArthur River event, if any. Drill hole Myrtle Yard 4 (MY4), is known to occur closest to a mineralized body and this drill hole was chosen to note effects of mineralization on sedimentary pyrite TE content. Furthermore, analyses from the deposit (McArthur River) itself were also undertaken for further characterization of pyrite very proximal to ore. Although the shales belong to different sub-basins, it should be noted that in all three cases the sub-basins share similar structural history and sedimentary pyrite formation mechanisms also remains the same in each case. The second aim of the study was to highlight the advantage of using sedimentary pyrite trace element concentrations via LA-ICP-MS technique and utilize it as an independent tool for exploration of this type of mineralization in the McArthur Basin.

3.3.3 Laser Ablation Inductively Coupled Plasma Mass Spectrometry (LA-ICP-MS)

Laser based analyses were carried out using a New Wave Research UP-213 Nd:YAG laser microprobe coupled to an Agilent 7500a quadrupole ICP-MS. The laser instrument operated with ~3.5 J/cm^2 laser fluence and 5 Hz laser repetition rate. Samples were ablated in an atmosphere of pure He flowing at a rate of 0.8 l/min, immediately after which He carrier gas was mixed with Ar (0.85 l/min) for improved efficiency of aerosol transport within the cell. The ICP-MS instrument was optimized to maximize sensitivity on mid- to high-mass isotopes (in the range 80– 240 amu) and production of molecular oxide species (i.e., 232Th16O+/232Th+) & doubly charged ion species (i.e., 140Ce++/140Ce+) were maintained at levels below 0.2% (cf. Large et al, 2014). Dwell times on each mass varied between 5 and 30 msec, depending on the count rates and total sweep time (time required to measure all isotopes once) was 0.76 sec. Samples for analyzed for the following elements and isotopes, 13C, 23Na, 24Mg, 27Al, 29Si, 34S, 39K, 43Ca, 49Ti, 51V, 53Cr, 55Mn, 57Fe, 59Co, 60Ni, 65Cu, 66Zn, 75As, 77Se, 85Rb, 88Sr, 90Zr, 95Mo, 107Ag, 111Cd, 118Sn, 121Sb, 125Te, 137Ba, 157Gd, 178Hf, 181Ta, 182W, 195Pt, 197Au, 202Hg, 205Tl, 206Pb, 207Pb, 208Pb, 209Bi, 232Th, 238U. A 30 second background analysis was carried out (for better detection limits) before signal acquisition for 40-60 seconds. Three primary calibration standards, STDGL2b2, an in-house standard for primary calibration for quantifying siderophile and chalcophile elements (Danyushevsky et al., 2011), GSD-1G (USGS reference material; Jochum et al., 2005) for lithophile elements and pure pyrite for quantifying sulfur, were used as reference materials. They were run prior to analyses of the unknown samples as well as after every 1.5 hours (~ after analyses of two samples) to record instrumental drift during the course of analyses. The mode of analyses was spot, i.e., approximately 10 pyrite spot analyses and 5 black shale matrix spot analyses were conducted on each laser mount. Laser spot sizes varied from 35-105 m for standards to 10-35 m for pyrite analyses. Due to fine-grained nature of the sedimentary pyrites, matrix material of the black shales was analysed for TE too, in order to negate effects of matrix contamination during laser ablation of fine-grained pyrite. The data generated (in counts per seconds) is converted to parts per million

using CODES in house software designed according to standard methods (Longerich et al., 1996), using Fe as the internal standard element.

3.4 Results

3.4.1 Facies description of Barney Creek Formation

Samples were collected down hole for each drill hole taking the sedimentological Facies variations into consideration. All three drill holes broadly represent the same stratigraphy within the Barney Creek Formation overlain by the Reward Dolomite and underlain by the Teena Dolomite and similar facies types within different formations. Below we summarize a brief facies description of the BCF in the three drill holes that were noted during the process of sample collection.

3.4.1.1 MBXDD001 (farthest from ore body)

Five different facies were observed in the BCF in drill hole MBXDD001 (Fig 3.5a). An ~ 10 m planar bedded dolomitic siltstone to coarse sandstone termed Facies 1 was interpreted as Reward dolomite. Facies 2 comprises laminated carbonaceous pyritic black shale, interbedded with dolomitic siltstone interpreted as the Barney Creek Formation. This Facies makes up most of the drill core (Upper and Lower BCF; ~15-75 m and ~135-164 m respectively). Very minor galena and pyrite was observed in brecciated veins within BCF at ~146m. Another facies (Facies 3) of the BCF was carbonaceous pyritic mudstone/shales/siltsone with layers of fine-grained pyrite (~75-135 m) that represented the Middle BCF. Facies 2 and 3 compose the HYC Pyritic Shale Member of the BCF. Planar thin interbedded tan/grey dolomitic siltstone to fine sandstone with lesser dolomitic carbonaceous shale between ~164-177 m was classified as Facies 4 and was interpreted as the W-fold Shale Member of the BCF. Below the W-Fold Shale Member, i.e., between ~180-200 m, we observed Facies 5, grey/cream with patchy pale pink fine impregnated hematite, thin bedded and dissolution brecciated dolostone with occasional occurrence of Coxco needles interpreted as Teena Dolomite.

3.4.1.2 Leila Yard 1 (intermediate distance from ore body)

Four different facies types were observed in the LY1 drill hole (Fig 3.5b). Thinly bedded dolomitic siltstone and silty dololutite with interbeds of fine-grained sandstone between ~200-345 m was classified as Facies 1 and was identified as Hot Spring Member of the Lynott Formation. Thinly bedded to laminated, dolomitic, carbonaceous and pyritic shale and siltstone was classified as Facies 2 which represented the

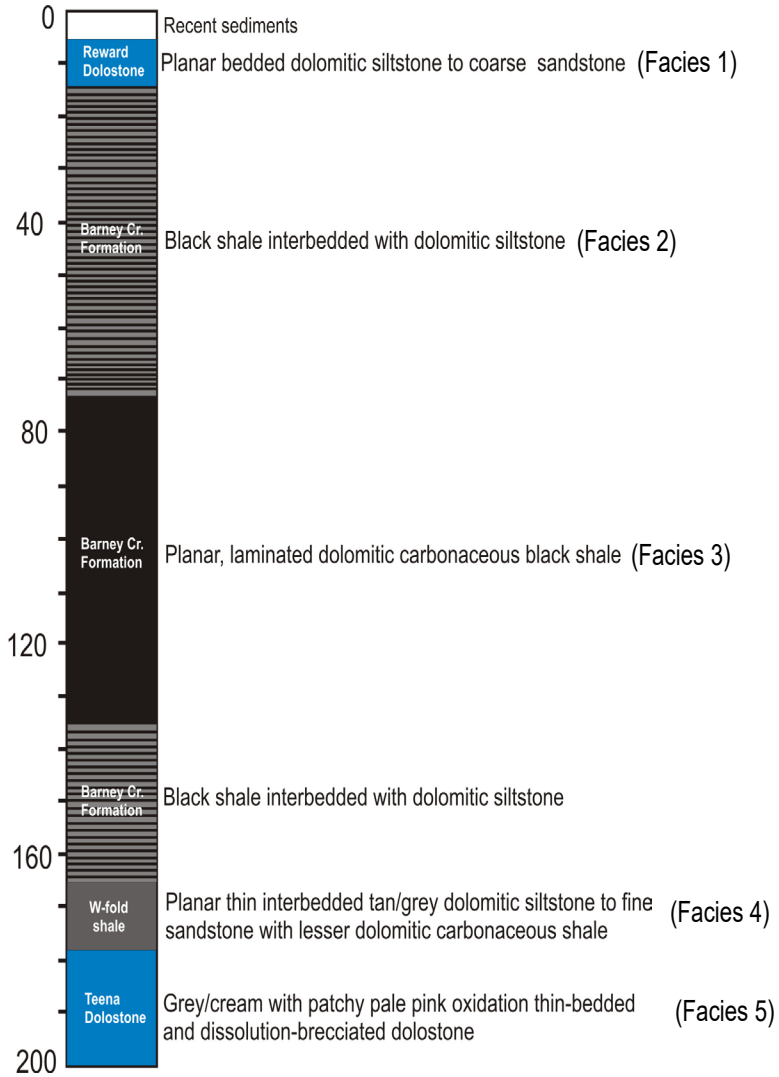

Fig 3.5a Simplified log of drill hole MBXDD1

Caranbirini Member of the Lynott Formation (345-355 m) and the HYC Pyritic Shale Member of the Barney Creek Formation (365-510 m). The W-Fold Shale Member of the BCF is represented by Facies 3 (510-520 m), which is green and red dolomitic siltstone and shale and green vitric tuff. The Reward Dolomite (360-365 m) and the Teena Dolomite (525-550 m) are represented by Facies 4, which are dololutite, silty dololutite, minor dolarenite, shale and local dolostone breccia.

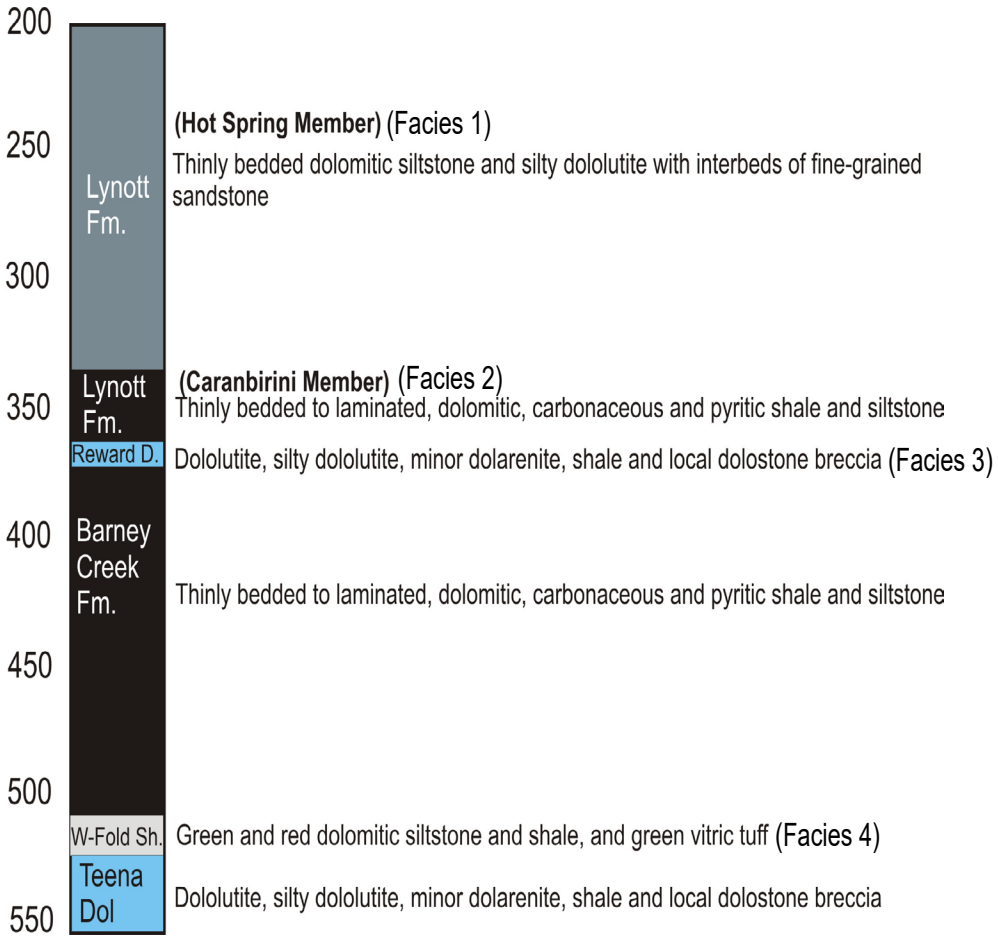

Fig 3.5b Simplified log of drill hole Leila Yard 1

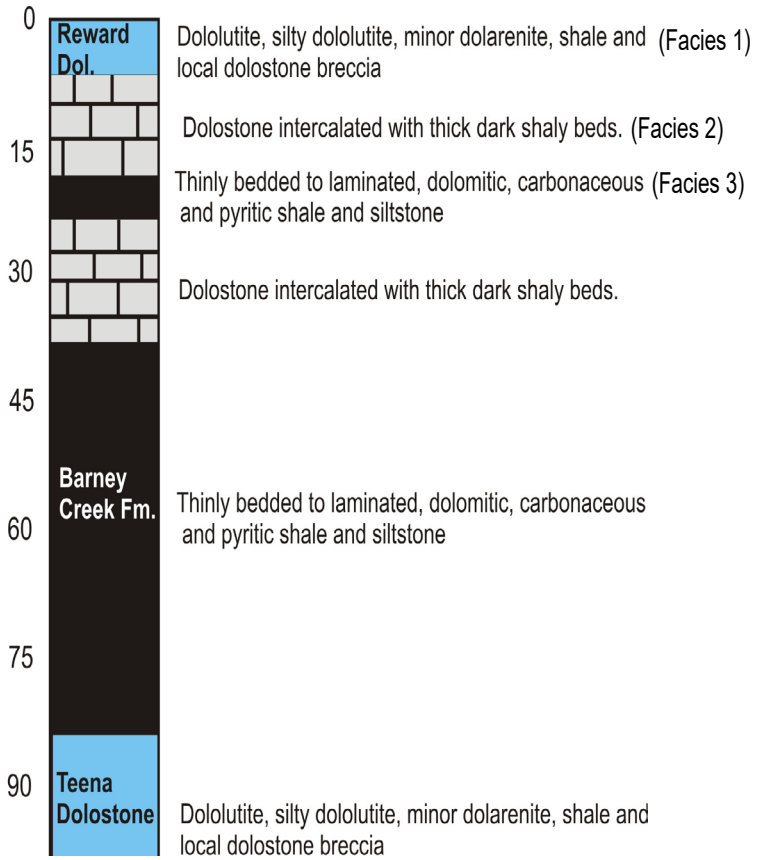

Fig 3.5c Simplified log of drill hole Myrtle-4

3.4.1.3. Myrtle Yard 4 (close to mineralised zone)

Similar facies were observed in the MY4 drill hole (Fig 3.5c) as described for MBXDD001 and LY1. Dololutite, silty dololutite, minor dolarenite, shale and local dolostone breccia, Facies 1 represents Reward Dolostone (0-19 m) and Teena Dolostone (87.5-105 m). The dolostone in Reward Dolostone also seems to be composed of Facies 2, which is intercalated with thick dark shaly beds (5-19 m). The Barney Creek Formation in MY4 is represented by two Facies, 2 and 3, dolostone intercalated with thick dark shaly beds and thinly bedded to laminated, dolomitic, carbonaceous and pyritic shale and siltstone respectively.

3.4.2 Textures of pyrite

Petrographic study of the variety of pyrite textures displayed in the samples, enabled the early stage sedimentary pyrite suitable for this study to be identified, compared with late diagenetic and metamorphic pyrite types. The same type of fine-grained sedimentary pyrite in each sample was preferred for analysis as our objective was to determine if an ore-related exhalative signal could be detected in the early sedimentary pyrite. Pyritic textures are described for each drill hole in the following paragraphs.

3.4.2.1 MBXDD001 (farthest from ore body)

A variety of textures were observed in the pyritic shales collected from the drill hole MBXDD001. The pyrites in the black shales exhibited both sedimentary-diagenetic and late stage hydrothermal textures. In some instances, recrystallised (metamorphic) pyrites were present. Microcrystals of pyrite occured either as layers parallel to the bedding plane (Fig 3.6a), in layer-parallel aggregates (Fig 3.6b and 3.6c) or as fine disseminations within the shale matrix (3.6d). Most pyrites in the hole were classified as sedimentary-diagenetic primarily because of the size of the pyrite grains and its relationship with the host rock. These textures were therefore believed to have retained their sedimentary form. Pyrite in some samples appeared to be much more massive rather than fine-grained. Pyrite micro-folds were observed (Fig 3.6e and 3.6f) possibly due to layer-parallel compressive forces. However, these forces possibly operated on a local scale as these textures were observed in just one sample. At certain intervals down hole, pyrite occurred in veins (Fig 3.6g) and generally coarser grained than elsewhere (Fig 3.6h). Etching of some of the coarser grained pyrites revealed overgrowths around sooty cores (Fig 3.6h). In other cases, they appeared to be brecciated (possibly due to hydrothermal veination?) and were associated with sphalerite and galena (Fig 3.6i). Bedding parallel layers of very coarse-grained pyrite (~ >200 micron) were also observed (Fig 3.6j). Pyrite was classified as hydrothermal and in some cases metamorphic (Figs 3.6g to 3.6j) mainly because of the size of the pyrite grains in comparison to their sedimentary counterparts, their relationship with the host rock (both cross-cutting and layer-parallel) and presence of features like overgrowths and euhedral shapes.

3.4.2.2 Leila Hill 1 (intermediate distance from ore body)

Similar to MBXDD001, two main types of textures (sedimentary & diagenetic) were observed. Microcrystals of pyrite in layers (Fig 3.7a), in bedding-parallel aggregates (Fig 3.7b) and in small nodular to lenticular shapes were observed (Fig 3.7c, 3.7d). In Figs 3.7a-3.7d, fine crystals of pyrite were disseminated throughout the shale. These textures were again indicative of their sedimentary origin. Other textures were classified as late diagenetic or hydrothermal; Figs 3.7e and 3.7f show pyrite in veins; coarse-grained pyrites with overgrowths were also observed (Figs, 3.7g and 3.7h); some pyrite grains appeared to have a furry overgrowth over coarser grains (Fig 3.7g).

3.4.2.3 Myrtle Yard 4 (within mineralised zone)

Both extremely fine-grained and coarse-grained pyrites were observed. Microcrystals of pyrite were disseminated all through the shale (Fig 3.8a) in clusters (Fig 3.8b), in layer parallel aggregates (Fig 3.8c), partially replacing a carbonate micro-nodule (Fig 3.8d) and in thin layers parallel to the bedding (Fig 3.8f). Figs 3.8a to 3.8f were classified as early sedimentary mainly due to their size and occurrence parallel to primary stratification.

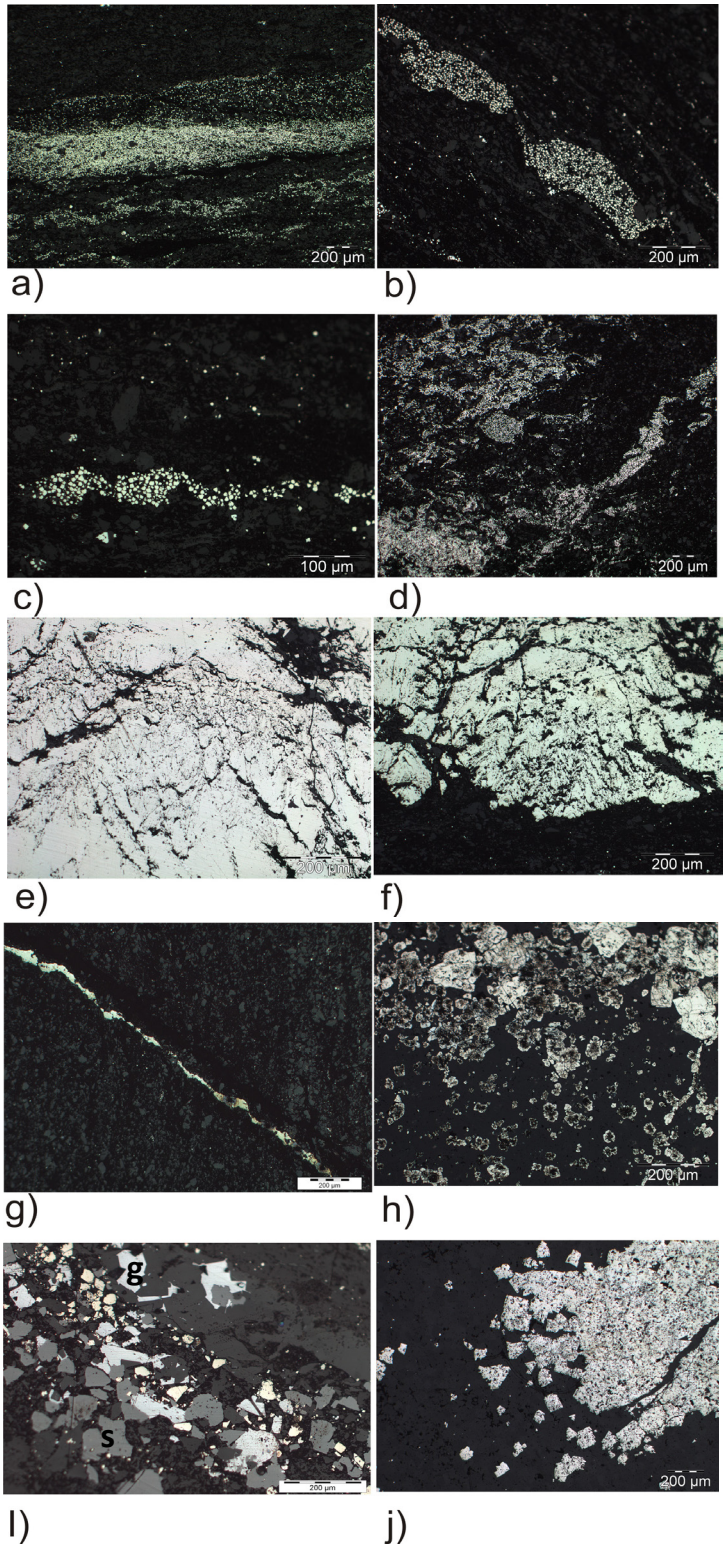

Fig 3.6 Textural description of pyrites from drill hole MBXDD001 a) fine grained sedimentary pyrite in layers b) & c) fine grained pyrite in layer parallel aggregates d) fine disseminations of pyrite within black shale matrix e) and f) pyrite microfoldsMBXDD001 g) pyritic veins cutting across black shale matrix h) coarse grained pyrite; etched to reveal zoning i) coarse grained pyrite co-occurring with sphalerite (s) and galena (g) j) layer parallel very coarse grained pyrite (>200 micron)

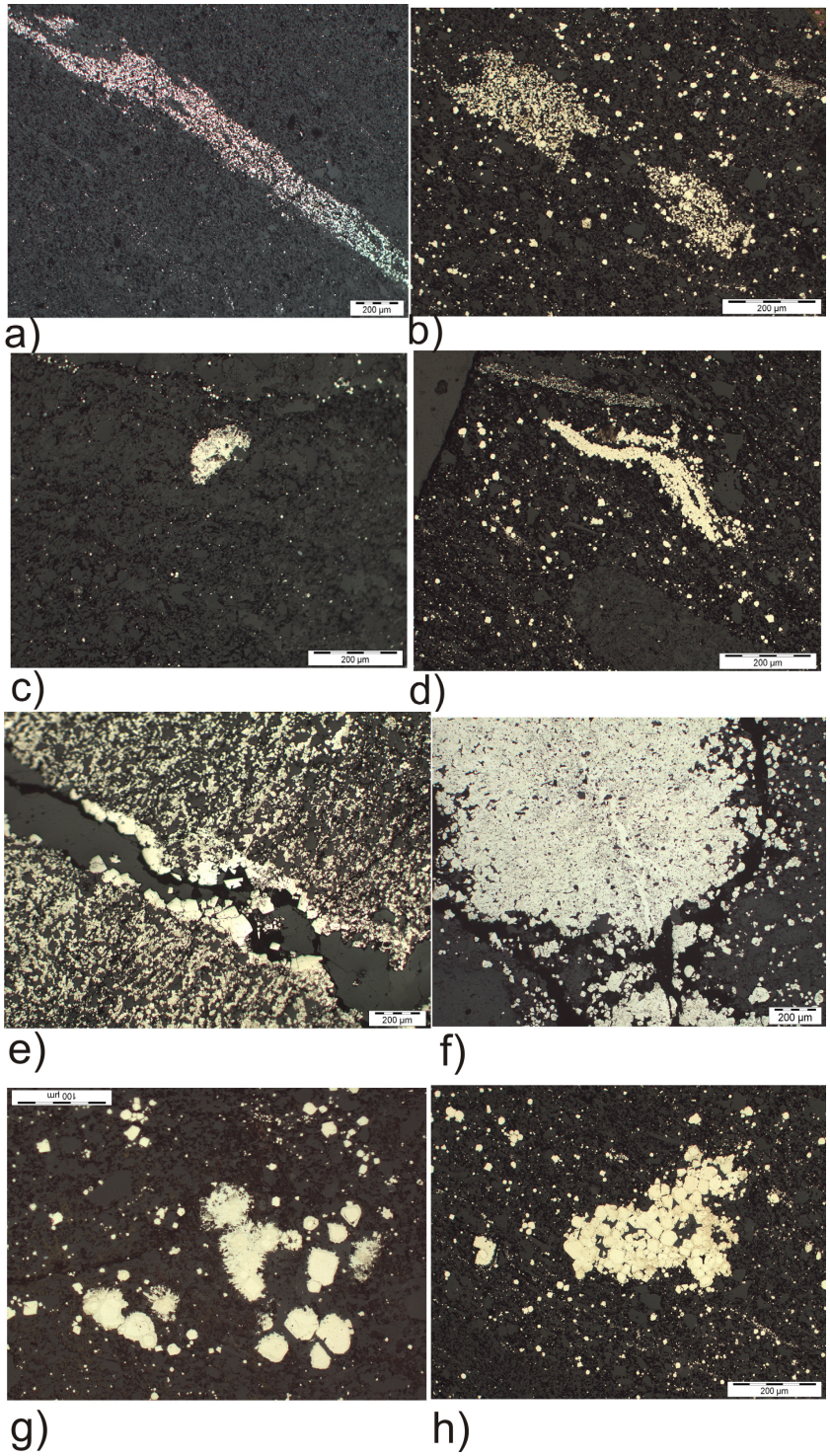

Fig 3.7 Textural description of pyrites from drill hole LY1 a) fine grained sedimentary pyrite in layers b), c) and d) fine grained pyrite in layer parallel aggregates e) and f) pyrite in veins g) and h) coarse grained pyrite

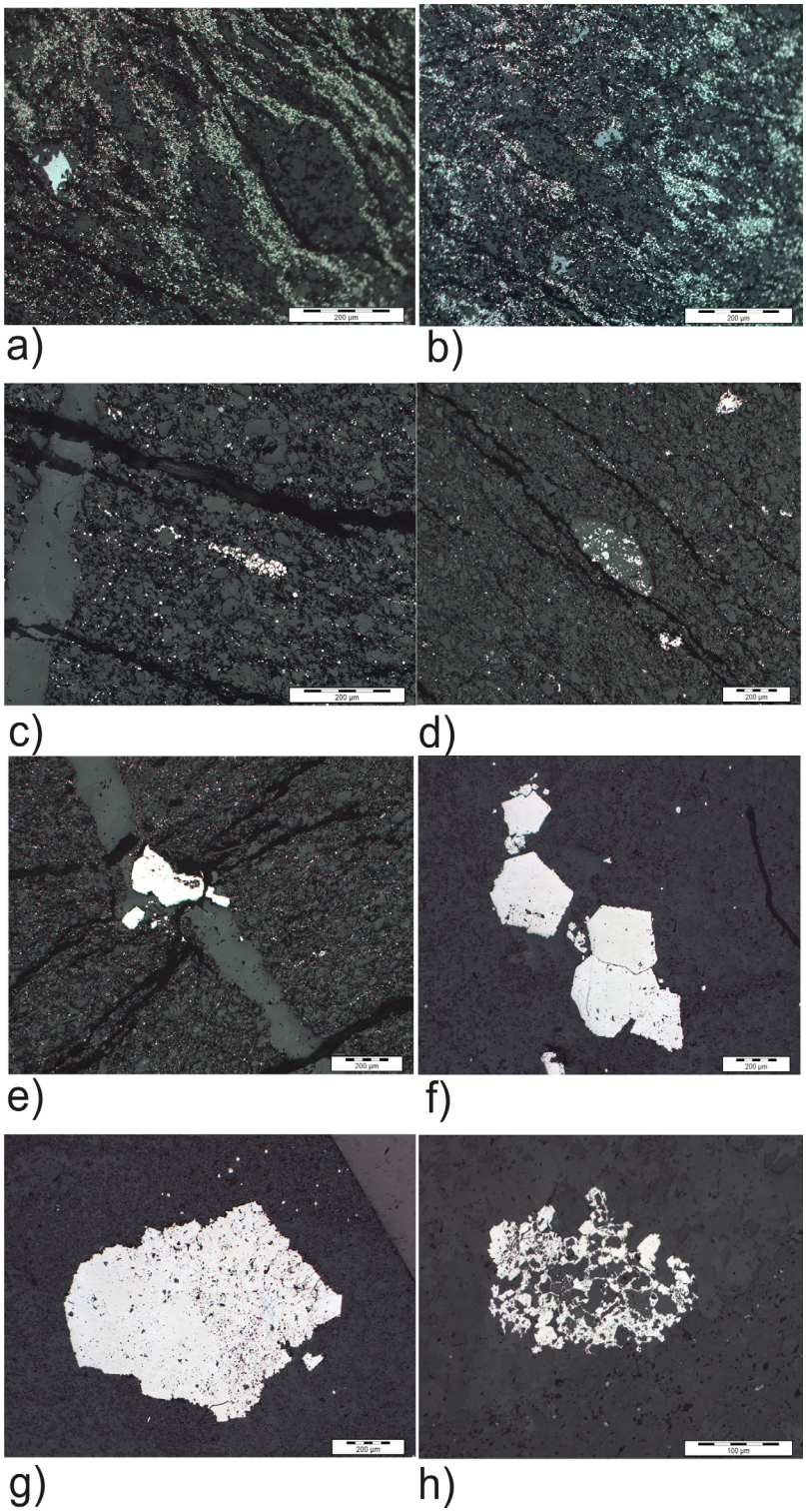

Fig 3.8 Textural description of pyrites from drill hole My4 a) and b) fine grained sedimentary pyrite disseminations c) pyrite clusters d) fine grained pyrite replacing carbonate clast e) pyrite in veins f) coarse grained pyrite g) coarse grained pyrite zoned with arsenopyrite inclusions h) pyrite replacing matrix

Coarse pyrites in veins (Fig 3.8 e), euhedral and zoned pyrites (Fig 3.8f, 3.8g), coarse pyrite with inclusions with arsenopyrite (Fig 3.8g) and pyrite in inter-granular spaces of carbonate clasts were also observed (Fig 3.8h), and considered to be late diagenetic, metamorphic or hydrothermal.

3.4.3 LA-ICP-MS Pyrite trace element chemistry

Trace element incorporation in sedimentary pyrite can be due to several processes such as adsorption, trace metal inclusion, metal exchange reactions, coprecipitation and surface redox reaction (Rickard et al., 2012). It is beyond the scope of this paper to address how each trace element undertaken in this study has been finally sequestered in to sulphides. However, based on Morse and Luther III (1999) it depends on a number of different factors (electronic configuration, rates of water exchange, amount of hydrogen sulphide in the water column and metal sulphide solubility) as to which incorporation mechanism will be dominant. For example, Ni and Co exhibit slow rates of water exchange which results in their adsorption on to pyrite or coprecipitation with iron sulphide phases and ultimately in solid solution in the structure of pyrite. In contrast, Zn and Pb have much higher rates of water exchange which causes precipitation of their own sulphides (ZnS and PbS) rather being in solid solution with pyrite (Morse and Luther III, 1999).

A total of 329 spot analyses were undertaken in samples from all three drill holes using LA-ICP-MS which included analyses of both fine sedimentary and coarser pyrite types (Tables A3.1, A3.2, A3.3, A3.4). Careful screening using textures, Fe/S and Ni/Co ratios allowed separation of sedimentary pyrite analyses from coarse-grained types affected by recrystallization. Different pyrite textures observed in each drill hole were especially analysed to note differences in their TE content if any. For instance, in drill hole LY 1, pyrites from an interval of 360 meters, recorded marked differences in their TE content (Fig 3.9). The fine-grained variety of pyrite is more enriched in TEs in comparison to its coarse counterpart. This can be attributed to the different origin of pyrites i.e., the fine-grained pyrites of sedimentary origin contain more TEs than coarse/recrystallised hydrothermal pyrites. Trace elements are commonly released from the structure of pyrite during recrystallization to euhedral shapes (Gregory et al., 2015). Alternatively, it is possible that hydrothermal pyrites are low in TE content owing to lack of TE in the hydrothermal fluid. Nevertheless, textural study allowed us to select the appropriate pyrite of sedimentary origin that preserves the original-slightly modified TE content, which suits the purpose of this study.

Only analyses of fine-grained early sedimentary pyrite are plotted in the down-hole plots in Figs 3.10 to 3.15. Although pyritic shales above and below the BCF were analysed, only the BCF pyrite analyses have been plotted. Although there is considerable scatter in some of the pyrite data, down hole trends were determined using the means of spot analyses in each sample for Zn, Pb, Ag, Mo, Se, Ni, Co and Tl for each drill hole (Figs. 3.10 to 3.15). This was done in order to evaluate the variation down through the stratigraphy in the BCF in all three drill holes. Also,

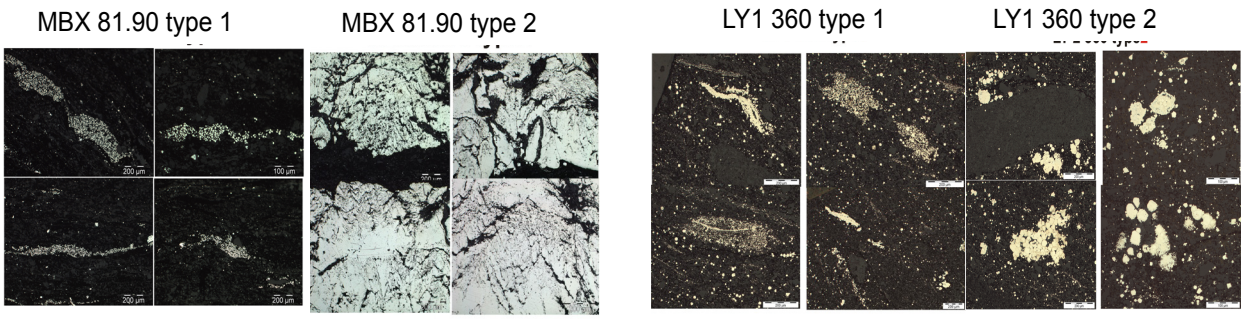

	MBX 81.90 type 1	MBX 81.90 type 2
Co	137	6
Ni	330	11
Cu	99	30
Zn	71	9
As	373	38
Se	6	5.07
Mo	214	4
Ag	2	0.08
Tl	7	39
Pb	409	37

	LY1 360 type 1	LY1 360 type 2
Co	59	20
Ni	69	30
Cu	218	237
Zn	1965	1007
As	1889	2226
Se	4	2
Mo	31	14
Ag	3	3
Tl	670	894
Pb	1626	849

* All values are in ppm

Fig 3.9 Trace element concentrations in fine grained pyrite and coarser grained of pyrite

summary sedimentary pyrite analyses from all three drill holes for certain elements (Co, Ni, Cu,Zn, As, Se, Mo, Ag, Sb, Tl, Pb, Bi, Zn/Ni, Tl/Co) were combined in plots (Figs 3.16 to 3.18) so that a comparison could be made between the bulk pyrite chemistry in each hole at a glance.

3.4.4 Down hole pyrite TE trends (MBXDD001, LY1, MY4)

In drill hole MBXDD001, redox sensitive trace elements such as Se, Ni, Co and Mo in pyrite show minor variation down hole and remain mostly less than or close-to the global mean value which represents the average of ~ 2000 sedimentary pyrite analyses (in case of Mo and Co) (Fig 3.10; Large et al., 2014). Nickel and Co in pyrite show the same break in cycle i.e., both show a sharp decrease at ~ 70 m interval like Mo, possibly due to change in facies. Selenium is fairly uniform throughout with no obvious cycles like Mo, and the mean is about an order of magnitude below the global mean for pyrite, which suggests the possibility of relatively low levels of atmosphere oxygenation throughout the BCF period (Large et al., 2014; 2015). Elements significant from exploration, such as Zn, Pb, Ag and Tl also show minimum variation down hole except at intervals between 30-40 m where a sharp increase in Zn is noticed, but no increase in Tl. (Fig 3.11). This strong Zn in pyrite anomaly at 25 m below the top of BCF, is interpreted as an indicator of a possibly local syn-diagenetic (?) Zn mineralization in the sub-basin. However, the lack of Tl suggests a very

local effect. However, Tl seems to be 10 times more enriched in the pyrite from sample interval 125-150 m, which is also the stratigraphic position of the HYC ore lenses, 60 km to the NE of MBXDD001. Lead and Ag do not show a particular trend with minor variations down hole and values remaining below a 1000 ppm and 10 ppm for Pb and Ag respectively. In summary, most redox sensitive trace elements in syngenetic and diagenetic pyrite in the BCF in MBXDD001 are fairly uniform and below the global mean (Mo, Se, Co, Ni) suggesting little change in seawater conditions during the BCF sedimentation time. Two local metal anomalies were detected in the syn/diagenetic pyrite; the first a Zn-only anomaly occurs about 25 m below the top contact of the BCF and the second anomaly is in the basal 40 m of shales in the BCF and is defined by a broad enrichment of Tl in pyrite about 10 times background which is at the stratigraphic position of the 60-km distant HYC ore lenses, and may represent a very distal effect from the HYC exhalative event.

In drill hole Leila Yard 1, Se, Ni, Co down-hole trends show very little variation and are mostly below the global mean value (Fig 3.12). Nickel and Co show a decrease in the Caranbirini Formation but overall, they are uniform. Selenium shows no particular trend and remains fairly constant down hole. On the other hand, Mo shows a distinct change i.e., increases in concentration between 400-500 m interval (Barney Creek Formation) with values up to 1000 ppm. This may indicate more strongly anoxic (euxinic) conditions in the Leila Yard sub-basin compared with the other two sub-basins (Fig 3.12). Zinc and Tl show moderate enrichments in the Caranbirini Member of the Lynott Formation but the trend down hole remains uniform (Fig 3.13). Lead and Ag values in LY1 do not fluctuate and show similarities with MBXDD001 in term of their mean values. It is noted that the two hydrothermal TE, Zn and Tl, in LY1 particularly in the BCF, are higher than the Zn and Tl concentrations in BCF of MBXDD001. Also, pyrite trace element chemistry indicates there is a Zn-Tl anomaly in the Caranbirini Member of the Lynott Formation

In drill hole Myrtle Yard 4, down hole Se, Ni, Co and Mo trends show a uniform pattern without varying significantly (Fig 3.14) and are lower than the global mean value similar to MBXDD001 and LY1. They are also much lower than Ni, Co and Mo values in MBXDD001 and LY1. The down hole Se trend is fairly uniform but, with a steady decrease. However, average selenium for MY4 is similar to average Se in MBXDD001 and LY1 drill holes. Zinc and Tl also show a certain trend down hole i.e., they increase in the basal part of the hole. This is also the stratigraphic interval for the McArthur River mineralisation (Fig 3.15). Even though MY4 drill hole is not from the mineralised zone, it is the closest to mineralisation in comparison to other holes. Zinc concentrations in MY4 are not only highest ($>10^4$ ppm) below the 80 m interval but are also higher than Zn values in LY1 and MBXDD001 samples. Lead and Ag concentrations do not fluctuate down hole in MY4 and are similar to LY1 and MBXDD001 (Fig 3.15).

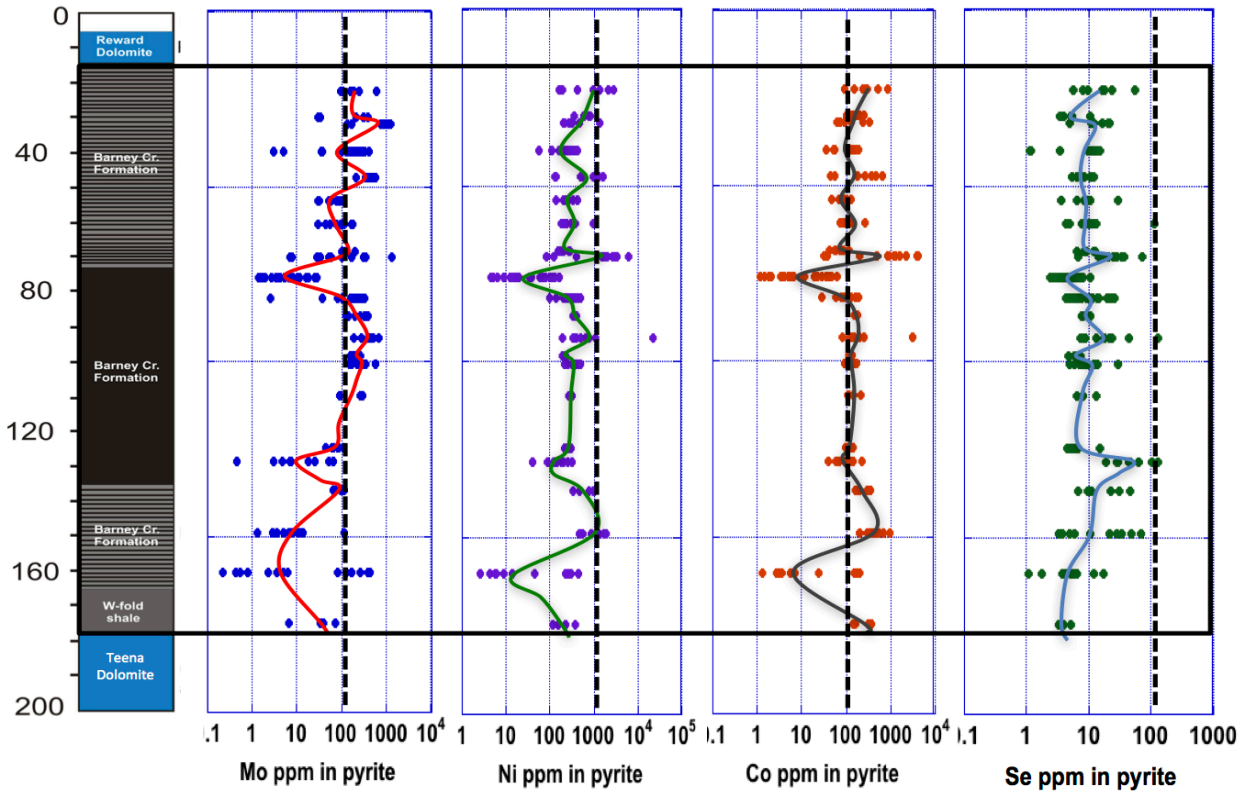

Fig 3.10 Down hole trends for Mo, Ni, Co and Se in pyrite for drill hole MBXDD001; Solid line represents average of spot analyses and dashed line global mean value of ~4000 pyrite analyses (Large et al., 2014); rectangle represents the Barney Creek Formation

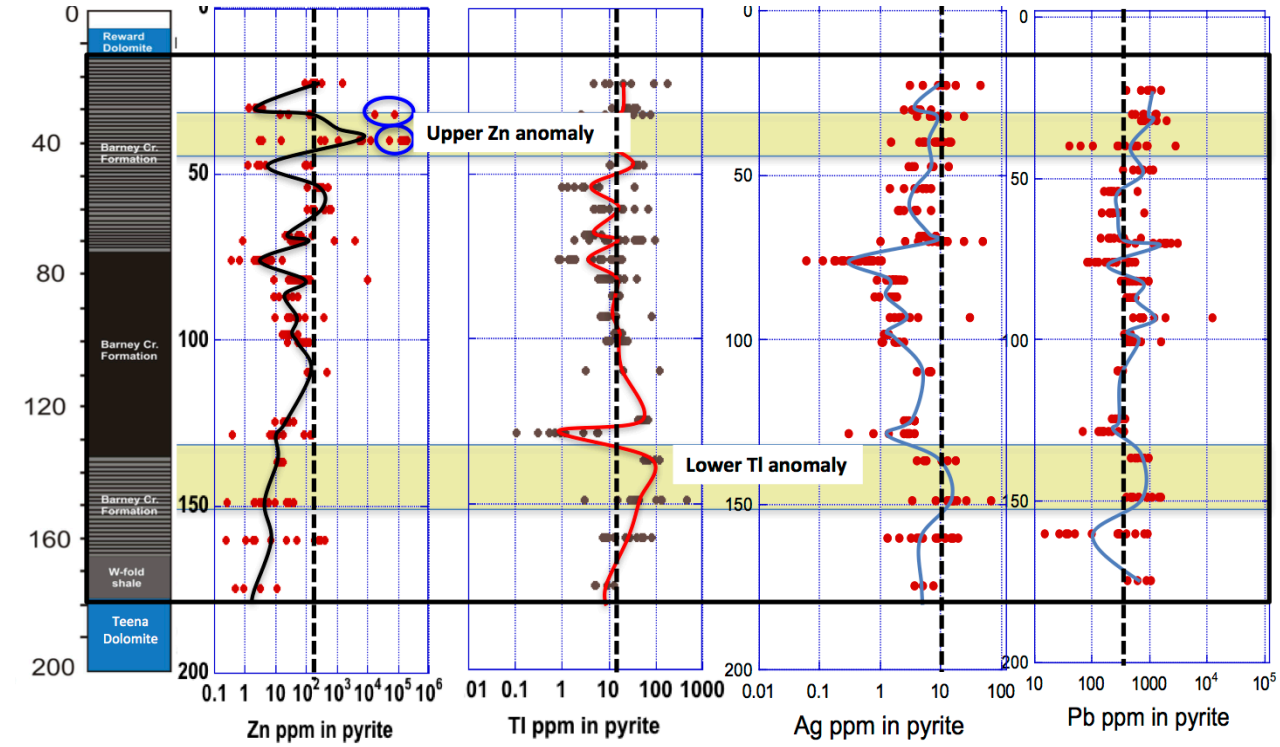

Fig 3.11 Down hole trends for Zn, Tl, Ag and Pb in pyrite for drill hole MBXDD001; Solid line represents average of spot analyses; rectangle represents the Barney Creek Formation and dashed line global mean value of ~4000 pyrite analyses (Large et al., 2014)

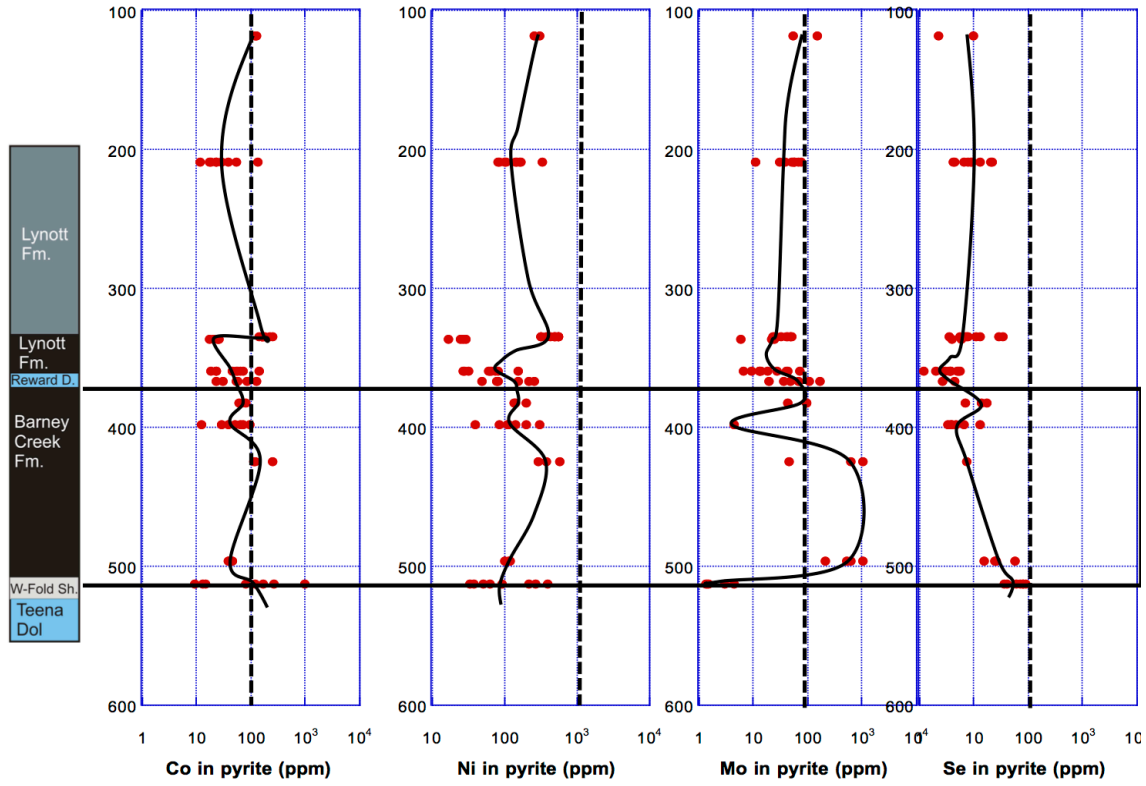

Fig 3.12 Down hole trends for Mo, Ni, Co and Se in pyrite for drill hole LY1; Solid line represents average of spot analyses and dashed line global mean value of ~4000 pyrite analyses (Large et al., 2014); rectangle represents the Barney Creek Formation

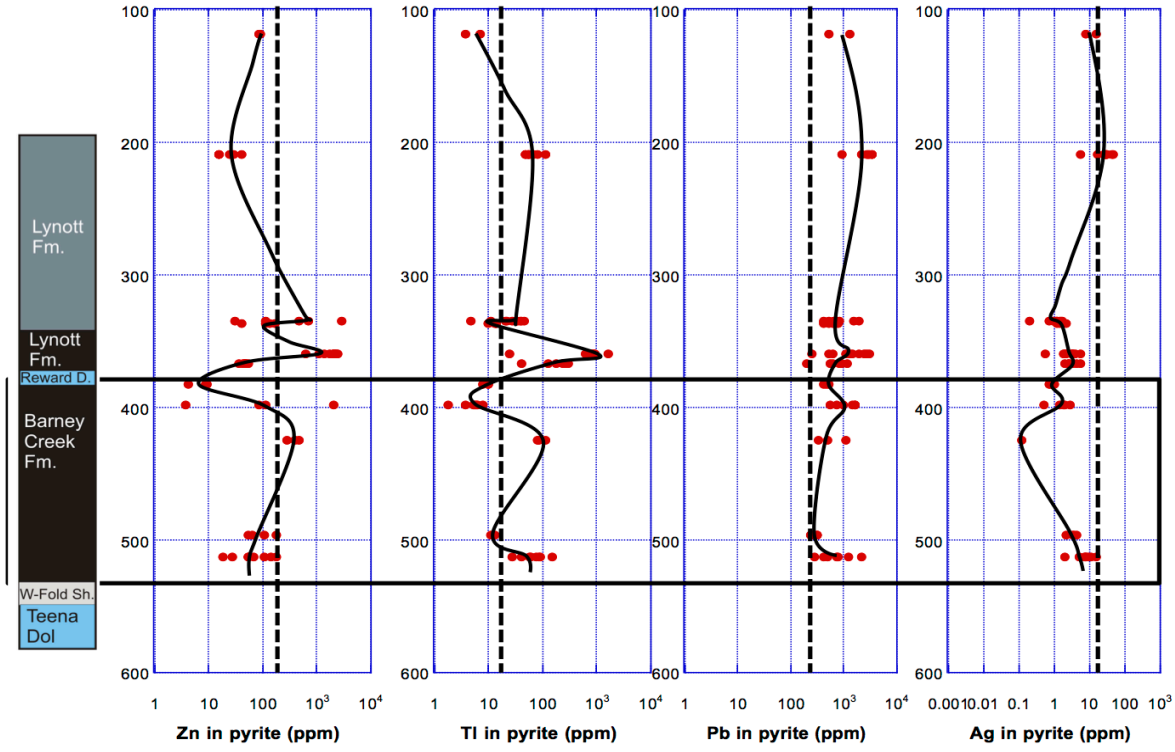

Fig 3.13 Down hole trends for Zn, Tl, Ag and Pb in pyrite for drill hole LY 1; Solid line represents average of spot analyses; rectangle represents the Barney Creek Formation; dashed line global mean value of ~4000 pyrite analyses (Large et al., 2014)

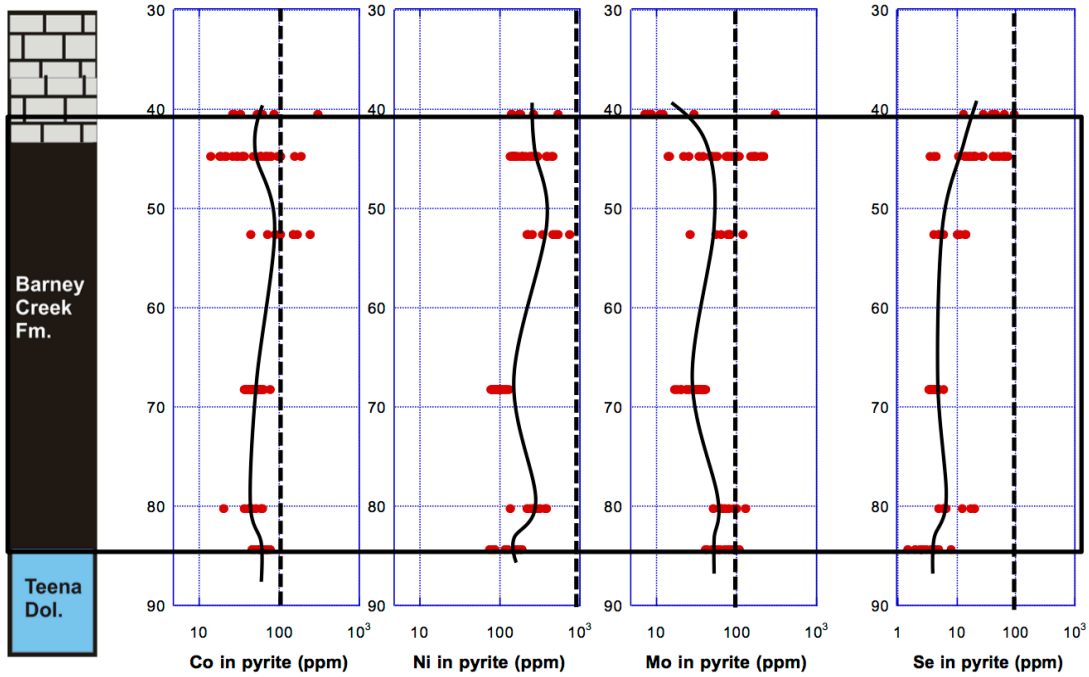

Fig 3.14 Down hole trends for Mo, Ni, Co and Se in pyrite for drill hole MY4; Solid line represents average of spot analyses and dashed line global mean value of ~4000 pyrite analyses (Large et al., 2014); rectangle represents the Barney Creek Formation

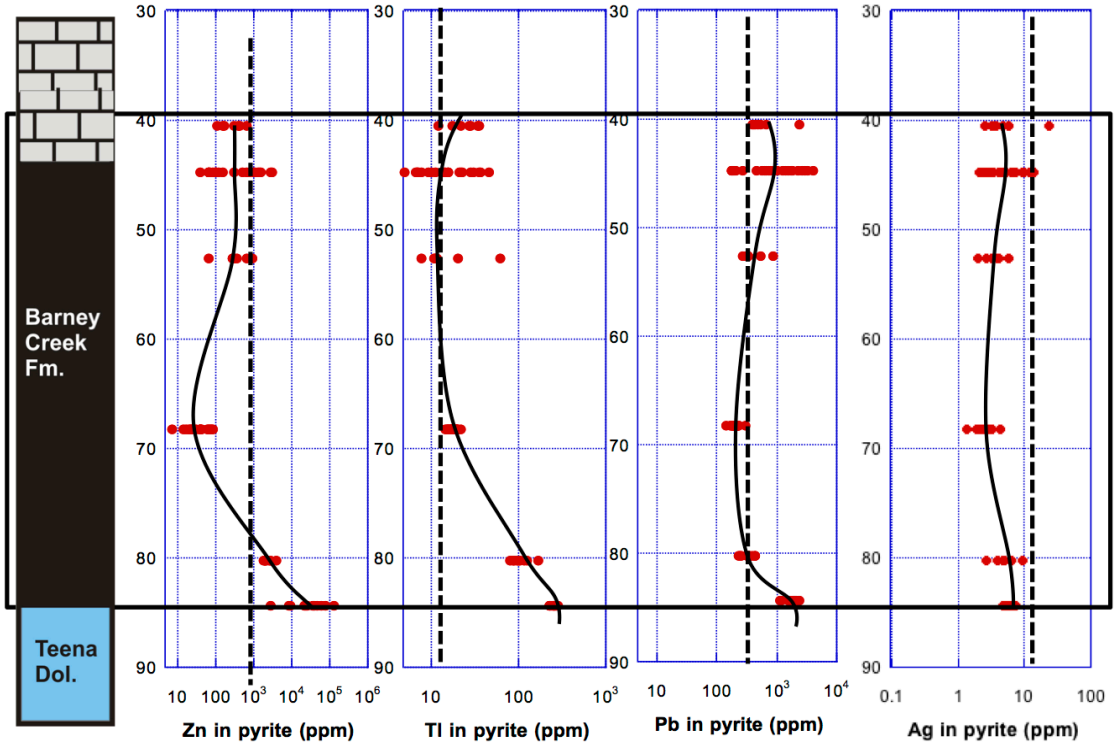

Fig 3.15 Down hole trends for Zn, Tl, Ag and Pb in pyrite for drill hole MY4; Solid line represents average of spot analyses; rectangle represents the Barney Creek Formation; dashed line global mean value of ~4000 pyrite analyses (Large et al., 2014)

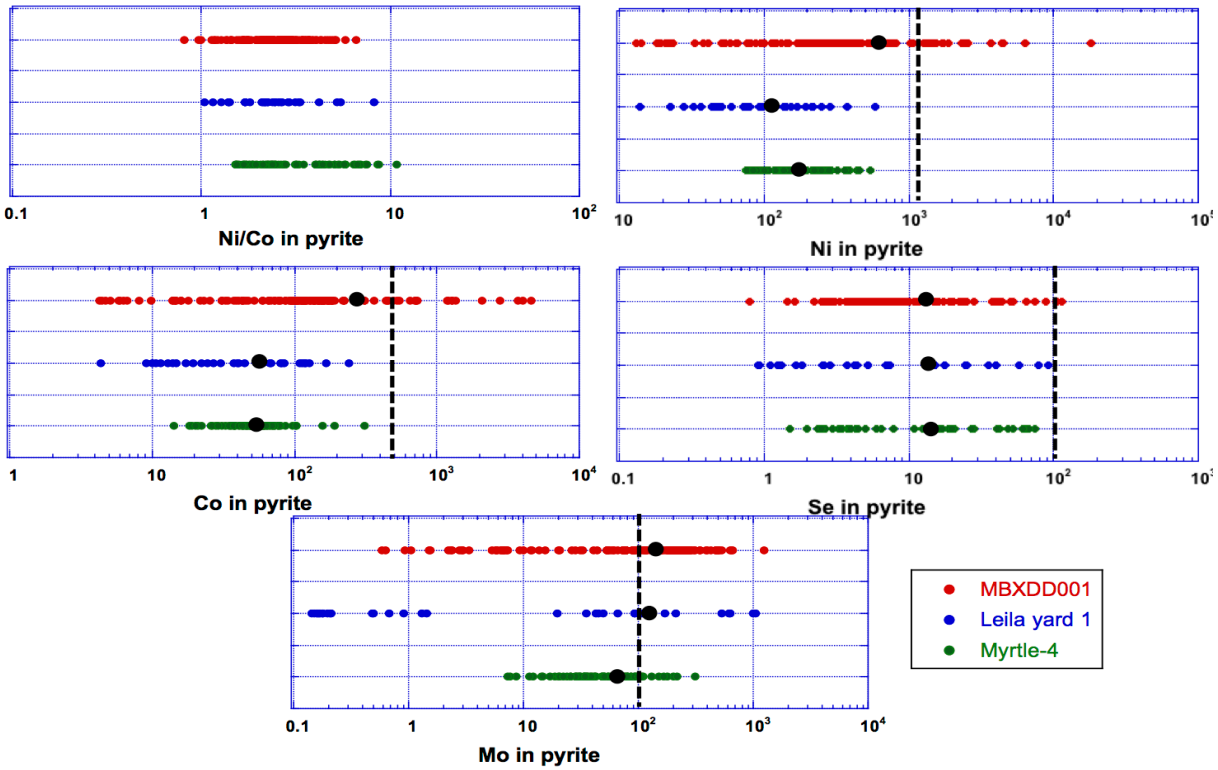

Fig 3.16 Comparison of datasets for Ni/Co, Ni, Co, Se and Mo in pyrite from individual drill holes; black dot represents average of the spot analyses; black dashed line represents global mean value from Large et al., 2014

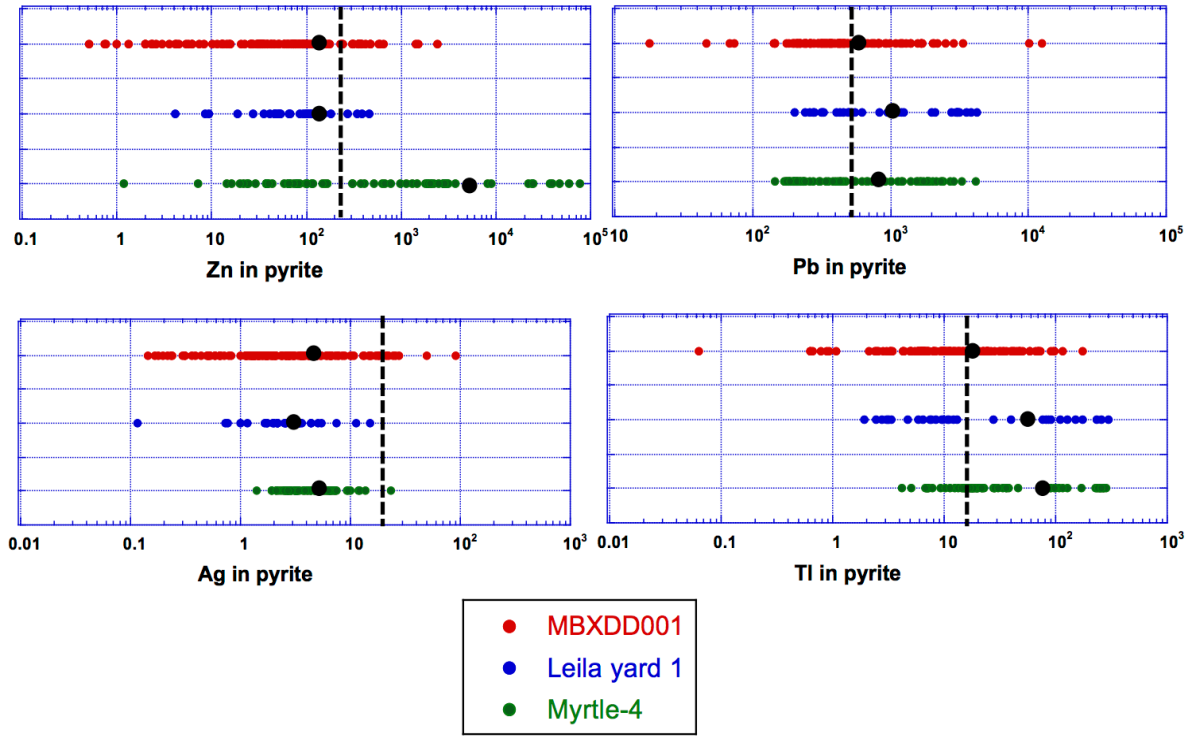

Fig 3.17 Comparison of datasets for Zn, Pb, Ag and Tl from individual drill holes; black dot represents average of the spot analyses; black dashed line represents global mean value from Large et al., 2014

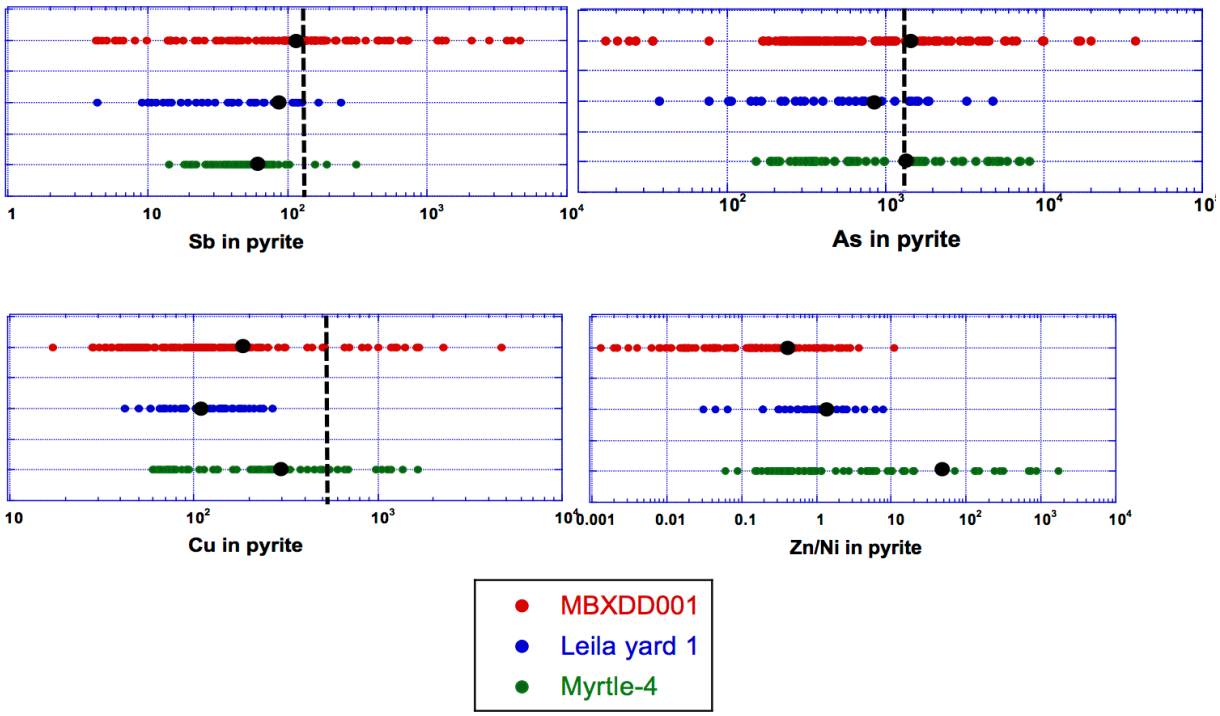

Fig 3.18 Comparison of datasets for Sb, As, Cu and Zn/Ni from individual drill holes; black dot represents average of the spot analyses; black dashed line represents global mean value from Large et al., 2014

3.5 Discussion

3.5.1 Comparison of pyrite TE between drill holes

Down hole trends are important to appreciate variations through the stratigraphy but we need to be able to compare similar geological datasets of each drill hole. Therefore, as mentioned earlier, combined element plots were used in order to compare analyses from the three drill holes. Only analyses of the BCF were used in these plots (Figs 3.16, 3.17, 3.18). The Ni/Co ratio of the spot analyses in Fig 3.16 lies within the sedimentary-diagenetic pyrite range (0.5 < Ni/Co < 100; Gregory et al., 2015). Considering Ni, Co and Mo, it appears as though pyrites in MBXDD001 display a wide range of values (over 3 orders of magnitude), LY1 displays an intermediate range and values in MY4 are relatively tightly clustered (within one order of magnitude). Also, the average Ni and Co concentrations are significantly lower in LY1 and MY4 in comparison to MBXDD001 (Fig. 3.16). Molybdenum also shows a bimodal distribution in LY1 Fig 3.16. Selenium on the other hand shows a similar range in all three drill holes with the average values being roughly the same (Fig 3.16). Zinc in pyrite shows a significant increase in its concentration from MBXDD001 to LY1 to MY4 (Fig 3.17). It is important to note that certain analyses have negative Zn values whereas others have very high contents. The former indicates Zn is below detection limits in other words less than the value presented in the tables. The latter is representative of micro-inclusions of sphalerite

within pyrite and matrix. We believe that this does not affect the overall trend of the trace elements in pyrite. Most trace elements reside in pyrite than sphalerite except Cd which can be partitioned in ZnS (Gregory et al., 2015). Also, ZnS is not a major phase and is only present as inclusions, in other words, not a significant enough phase to cause TE partitioning to an extent that it affects pyrite TE trends. Also, these microinclusions are likely to have been exsolved from the original sedimentary pyrite itself during diagenesis and metamorphism (Deditius et al., 2011). Overall Zn concentrations increase from MBXDD001 to LY1 and MY4. A similar trend is noted for Tl content in pyrite (Fig 3.17). Although the average values of both Tl and Ag are not very different, in both cases, the lowest value of ranges in individual drill holes denotes a pattern ($Ag_{Lowest\ value\ MBXDD001} < Ag_{Lowest\ value\ LY1} < Ag_{Lowest\ value\ MY4}$; $Tl_{Lowest\ value\ MBXDD001} < Tl_{Lowest\ value\ LY1} < Tl_{Lowest\ value\ MY4}$). Lead concentrations in the three drill holes display a similar range (Fig 3.17). Antimony, As and Cu concentrations in MBXDD001 like Mo, Ni and Co show wide variations in their values (3-4 orders of magnitude) unlike LY1 and MY4 which are more clustered (Fig 3.18). Since Zn and Ni behave in an opposite manner, we plotted Zn/Ni ratios of the sedimentary pyrite analyses. We can observe a systematic increase in the Zn/Ni ratio in the three drill holes. This feature is also clear in the average of the analyses (Fig. 3.18; Table 3.3/3.4).

In summary, the concentrations of redox sensitive TE, Ni, Co, Mo, Cu and Sb, are relatively high in sedimentary pyrites from MBXDD001 followed by pyrites from LY1 and are lowest in sedimentary pyrites from MY4. It was noted that Ni, Mo and Co in pyrite drop significantly in the more mineralised black shales.Low concentrations of Ni, Co, Mo, Cu in mineralised shales in comparison to mineralised shales are possibly because of ambient pore water conditions or lower availability of these elements during the mineralisation event (Maier, 2011; Gadd et al., 2015). However, the reason for this is not well understood. As outlined by Kornicker and Morse (1991) there are a number of factors that affect trace element adsorption on pyrite, such as pyrite concentration, pH, salinity, site competition with major cations, ionic strength, and tendency of a metal to hydrolyze. Particularly for Zn^{2+}, Ni^{2+} and Co^{2+}, an ion-exchange complexation model over a wide range of ionic strength is suggested (Kornicker and Morse, 1991). It is possible that hydrothermal exhalations in the water column may have an affect on ion-exchange surface complexation processes and pH that alter the uptake of these elements into pyrite. Zn and Tl may be favoured compared with Ni and Co in the ion-exchange adsorption process. This may explain why hydrothermal elements like Zn & Tl concentrations; Zn/Ni and Tl/Co ratios are lowest in pyrites from MBXDD001, followed by LY1, with the highest values being represented by pyrites from MY4, which is closest to hydrothermal venting. On the other hand, Bi and Se do not show any change and remain the same in all three drill holes, irrespective of proximity to mineralisation. This fact suggests these elements are not hydrothermal, and not affected by competition by other hydrothermal elements during ion-exchange adsorption processes. Although the average values of As, Ag, and Pb in the three drill holes do

not appear to show a trend similar to other hydrothermal elements, the lowest values of the dataset in each drill hole denote a trend i.e., lowest As, Ag, and Pb concentrations are in MBXDD001 followed by LY1 and then MY4. Even though generally the major emphasis is on the maximum or the average values, the minimum values also display a trend that can be observed using the LA-ICP-MS technique, and may be significant in an exploration vectoring sense.

Table 3.3 Trace element concentration (average values in ppm) of both sedimentary and coarse pyrites in the three drill holes

	n=175	n=72	n=84
Elements	**MBX (all data)**	**LY1 (all data)**	**MY4 (all data)**
Co	268	77	65
Ni	607	153	203
Cu	1786	284	308
Zn	7206	377	7327
As	1689	1694	1622
Se	12	12	13
Mo	185	72	65
Ag	5.5	5.6	4.8
Sb	117	73	59
Tl	19	177	65
Pb	683	1335	821
Bi	9	7.7	10.9
Zn/Ni	31	7.7	70
Tl/Co	0.1	2.3	1.0

3.5.2 Whole rock vs LA-ICP-MS

Conventionally, exploration companies for reconnaissance studies undertake whole rock analyses. An attempt was made to compare whole rock analyses conducted for MBXDD001 by the company at the time of exploration, with pyrite LA-ICP-MS analyses of the same drill hole presented here (Fig 3.19). In general, the whole rock analyses of selected samples of MBXDD001, did not identify element enrichments in the drill hole and gave relatively flat multi-element results except for a Zn-Pb anomaly at 150 m depth, related to a thin sphalerite-galena vein in black shale. In contrast the LA-ICPMS pyrite analyses revealed two anomalies, one in the upper BCF shales with a Zn-Cd response (up to 1000X background for Zn), and a second toward the base of the BCF with a broad Tl response (up to 10X background), which coincides,

Table 3.4 Trace element concentration (average values in ppm) of sedimentary pyrites in the three drill holes

	n=128	n=34	n=76
Elements	**MBX (BCF)**	**LY1 (BCF)**	**MY4 (BCF)**
Co	299	59	58
Ni	670	128	181
Cu	241	131	324
Zn	119	111.3	7991
As	1894	869	1605
Se	13	13	14
Mo	163	145	65
Ag	5.3	2.7	4.9
Sb	119	88.6	61
Tl	20	59.8	70
Pb	682	1400	866
Bi	9	9.0	11
Zn/Ni	0.4	1.5	77
Tl/Co	0.1	1.0	1.2

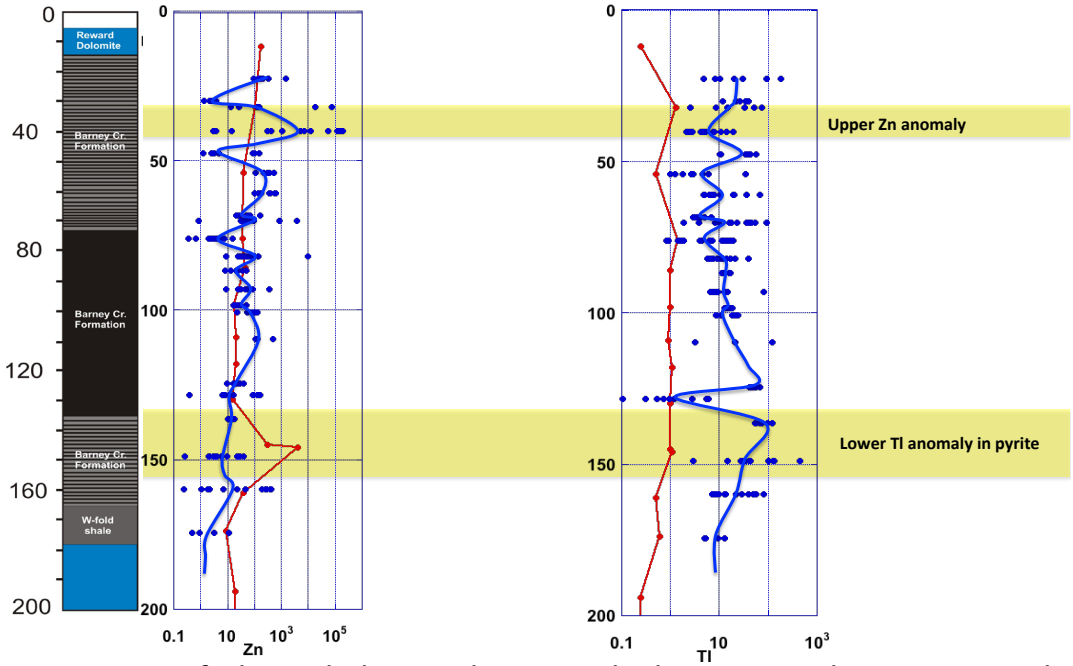

Fig 3.19 Comparison of down hole trends Zn and Tl pyrite analyses compared with whole rock analyses in drill hole MBXDD001; Red line denotes whole rock analyses and blue line denotes LA-ICP-MS pyrite analyses

with the position of the galena-sphalerite vein logged during exploration drilling. Note that the whole rock shale analyses method did not identify the upper or lower thallium anomaly. A possible explanation is that the whole rock geochemical method employed did not dissolve all the pyrite (which hosts the Tl) in the samples. The pyrite LA-ICP-MS pyrite method is shown here to be more sensitive for identifying geochemical anomalies in drill holes, than the standard whole rock multi-element method.

3.5.3 Pyrite discrimination diagrams for SEDEX Zn-Pb

A fertility diagram based on Ni, Mo, Zn, As and Tl in pyrite was constructed using pyrite analyses from the three drill holes in this study, plus sedimentary pyrite from the immediate host rocks to the McArthur River deposit (Table 3.6). Background sedimentary pyrite from black shales unrelated to SEDEX mineralisation are also plotted from Large et al., (2014), to provide a field for marine pyrite from barren black shales (Fig 3.20a). The x-axis in this figure, Ni + 2Mo, is an expression of two elements that are absorbed into pyrite from seawater and are unrelated to hydrothermal activity. The y-axis 2Zn + 5As + 20Tl is an expression of three elements that are dominantly contributed by SEDEX hydrothermal activity. The multipliers in the two expressions are designed to give each TE the same weighting. It is noted that most of the analyses

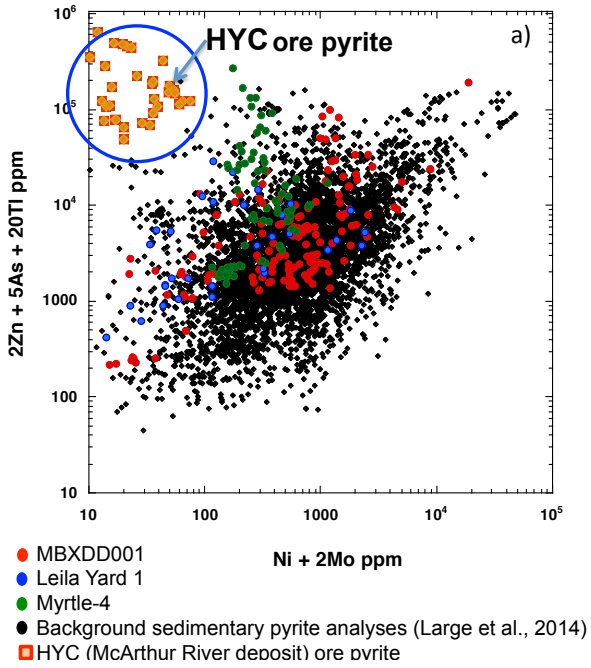

Fig 3.20a. Fertility diagram with analyses from three drill holes, McArthur deposit and background sedimentary pyrite analyses by Large et al., 2014

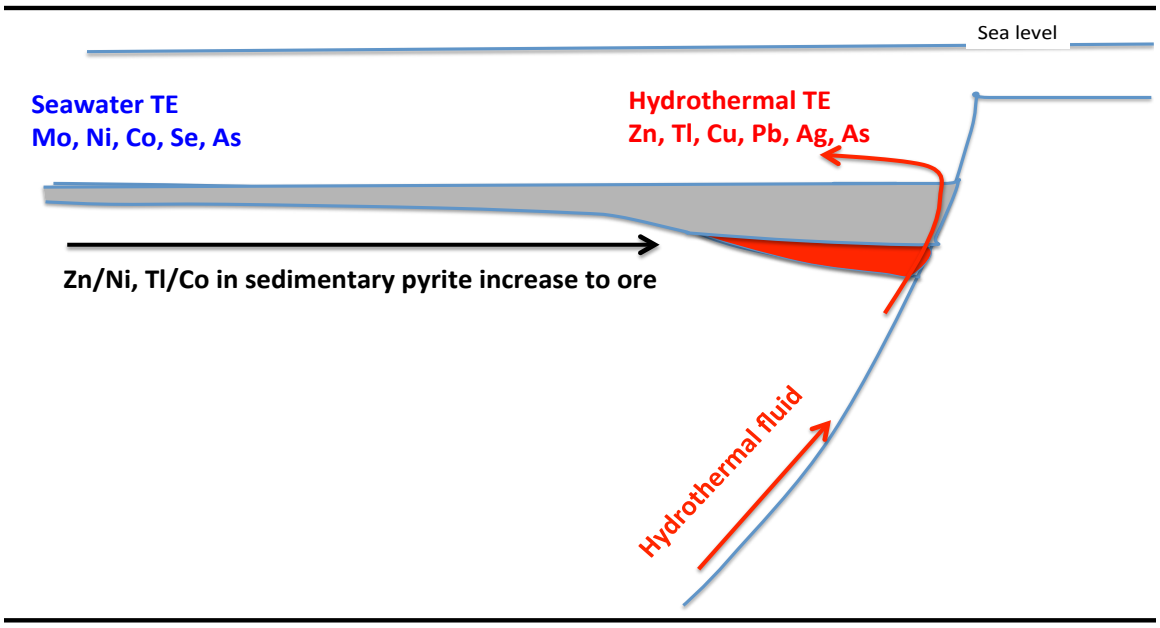

Fig 3.20b. Schematic of elements contributed to sedimentary pyrite from SEDEX hydrothermal activity compared with sea water

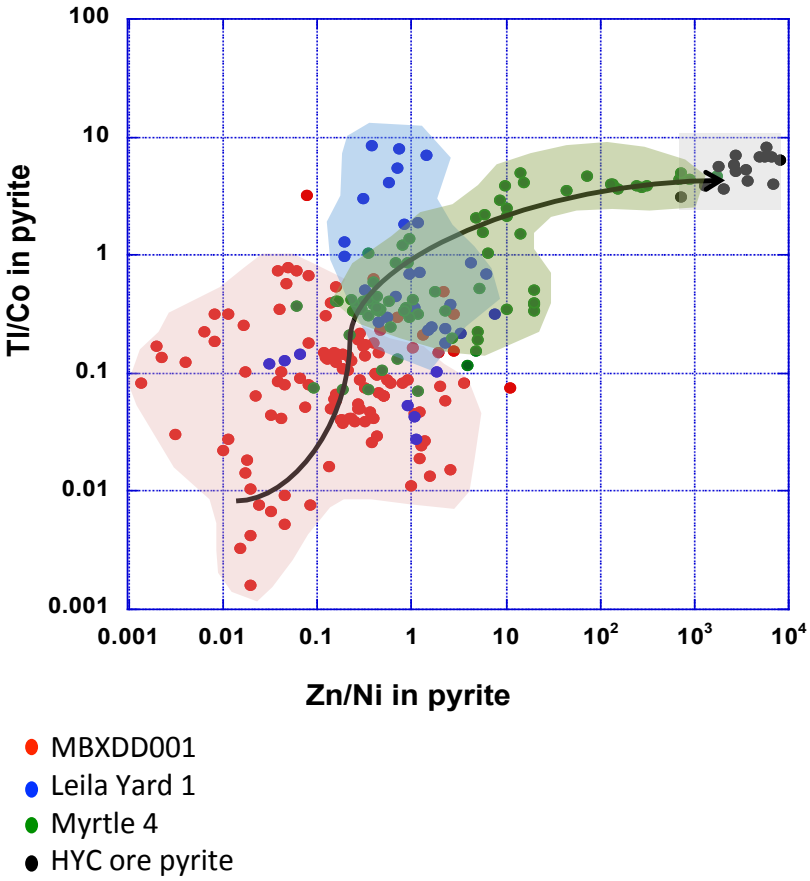

Fig 3.21 Pyrite vector diagram using Zn/Ni and Tl/Co ratios in pyrite

from MBXDD001 and LY1 fall within the confines of the background sedimentary pyrite cloud (denoted by black dots) in Fig 3.20a. However, analyses from MY4 (green dots) shows a trend towards the ore body field (yellow square dots) in the figure. It can be surmised that elements such as Mo, Ni, Co Se and As are adsorbed on to pyrite from the water column and represent contemporaneous sea water trace element concentrations (Fig 20b). The primary and dominant source of these elements in the ocean is riverine flux. It is believed, oxidative weathering on land causes these elements to be carried to the ocean in their soluble states (e.g., MoO_4^{2-} , Ni^{2+}, $Se0_3^{2-}$, $Se0_4^{2-}$) via riverine flux to become incorporated into pyrite on encountering the redox boundary at or below sediment water interface (Large et al., 2014). Elements like Zn, Tl, Cu, Pb, Ag and As, that may be present in the seawater, are mainly added in the water column via hydrothermal exhalations related to SEDEX mineralisation (Fig 3.20b).

A vector diagram for sedimentary pyrite in black shales is suggested in Fig. 3.21. This diagram is based on our observations in this study, that while Zn and Tl increase toward mineralisation Ni and Co in pyrite decrease, possibly being out-competed by ion-exchange processes. This diagram shows that MBXDD001 sedimentary pyrite is the most unlike HYC sedimentary pyrite (from the ore zone), whereas the Myrtle 4 sedimentary pyrite trends toward the same composition as the HYC sedimentary pyrite.

3.6 Conclusions

3.6.1 Implications for Paleoproterozoic seawater chemistry

Redox sensitive trace element contents of black shales and TE concentrations in pyrite have been used to throw light on seawater chemistry. This study shows that certain trace elements (Ni, Co, Mo, Zn, Pb) in the BCF seem to be affected by mineral exhalation into the McArthur Basin at the time of sedimentation. Nickel, Co and Mo decrease in concentration, whereas Zn, Tl and Pb increase in concentration proximal to hydrothermal vents. Selenium on the other hand, is not affected by hydrothermal activity making it a robust proxy for ocean chemistry. This study demonstrates that caution must be taken when using trace element concentrations of black shales affected by mineralisation/hydrothermal activity to interpret Proterozoic seawater chemistry. Black shales preferably farthest from an ore body (> ~50 km) are likely to represent the original, unaltered seawater signature.

3.6.2 Implications for exploration

The present study concludes that elements like Zn, Tl show high concentrations in the sedimentary pyrites in black shales from the MY4 due its close proximity to the Myrtle deposit (McArthur River style mineralisation hosted by the HYC-Pyritic Shale Member of the BCF). Sedimentary pyrites from

MBXDD001 on the other hand would possibly represent background values of the shale, least affected by any hydrothermal activity. The weak Tl in pyrite anomaly at the base of the BCF in MBX may represent a very distal (~60 km) signal of the McArthur River SEDEX ores. Drill hole LY1, according to the results of the study; reflect an intermediate circumstance where distal exhalative hydrothermal Zn-Tl-Pb fluids have significantly altered the trace element chemistry of sedimentary pyrite. Fertility and vector diagrams for SEDEX ores have been developed to quantify the pyrite TE data and provide a robust method of applying TE in sedimentary pyrite as a valuable addition to the exploration toolkit for SEDEX Zn-Pb.

This study concludes that the sedimentary pyrite trace element content of Barney Creek Formation black shales provides information on two aspects 1) exploration of Zn-Pb SEDEX deposits and 2) understanding past ocean trace element chemistry. The LA-ICP-MS approach adopted here allows superior detection limits, making the technique more sensitive, but also enables analysis of the suitable pyrite (sedimentary-diagenetic) rather than whole rock method where trace element signals become diluted by other host rock minerals. Also, our work demonstrates that prior to analyses by sophisticated instrumentation, textural studies should be undertaken in order to distinguish sedimentary pyrite from other generations/kind of pyrites present to ensure the suitability of the pyrite grains for analysis.

3.7 Acknowledgments

The Northern Territory Geological Survey (NTGS), Darwin, provided samples for the study. Research was funded by the Australian Research Council (DP150102578). The authors are most grateful to Dr. Rodney Maier, whose PhD thesis contributed to a better understanding of pyrite chemistry in the McArthur Basin. We also acknowledge Prof. Mihir Deb for his valuable comments.

3.8 References

Ahmad M., Dunster J.N. and Munson T.J., 2013. Chapter 15: McArthur Basin: in Ahmad M and Munson TJ (compilers). 'Geology and mineral resources of the Northern Territory'. Northern Territory Geological Survey, Special Publication 5

Bull S. W., 1998. Sedimentology of the Palaeoproterozoic Barney Creek Formation in DDH BMR McArthur 2, Southern McArthur Basin, Northern Territory. Australian Journal of Earth Sciences 45, 21–23

Bull, S and Scott, R., 1998. Geology of the BCDC in the Myrtle Basin area, Southern McArthur Basin, Northern Territory. AMIRA/ARC project P384A Final report, 9

Bull, S.W., 2001, Implications of tectono-sedimentary setting for genetic and exploration models for northern Australian Proterozoic sediment-hosted Zn- Pb-Ag deposits [ext. abs.]: Townsville, Queensland, Australia, James Cook University of North Queensland, Economic Geology Research Unit Contribution 59, 363

Chen, J., Walter, M.R., Logan, G.A., Hinman, M.C. and Summons, R.E., 2003. The Paleoproterozoic McArthur River (HYC) Pb/Zn/Ag deposit of northern Australia: organic geochemistry and ore genesis. Earth and Planetary Science Letters 210, 467-479

Cooke, D.R., Bull, S.W., Large, R.R and McGoldrick, P.J., 2000. The importance of oxidised brines for the formation of Australian Proterozoic stratiform, sediment hosted Pb-Zn (SEDEX) deposits. Economic Geology 95, 1–18

Corbett, J.A., Lambert, I.B., Scott, K.M., 1975. Results of analyses of rocks from McArthur Area, Northern Territory, Australia. CSIRO Tech. Comm. 57, Minerals Research Laboratories, August, 35

Croxford, N.J.W., 1968. A mineralogical examination of the McArthur lead-zinc-silver deposit. Proceedings of the Australasian Institute of Mining and Metallurgy 226, 97–108

Danyushevsky, L., Robinson, P., Gilbert, S., Norman, M., Large, R., McGoldrick, P., Shelley, M., 2011. Routine quantitative multi-element analysis of sulphide minerals by laser ablation ICP-MS: Standard development and consideration of matrix effects. Geochem., Explor. Environ. Anal. 11, 51–60

Davidson, G.J. and Dashlooty, S.A., 1993. The Glyde Sub-basin: A volcaniclastic-bearing pull-apart Basin coeval with the McArthur River base-metal deposit, Northern Territory. Australian Journal of Earth Sciences 40, 527–543

Deditius, A.P., Utsunomiya, S., Reich, M., Kesler, S.E., Ewing, R.C., Hough, R., Walshe,J., 2011. Trace metal nanoparticles in pyrite. Ore Geol. Rev. 42, 32–46.

Duffett, M.L. and Leaman, D.E., 1997. McArthur Basin architecture – a new perspective from geophysics and GIS. Exploration Geophysics 28, 39–42

Gadd., .G., Matthews, D.L., Peter, J.M. and Paradis, S.J., 2015. The World-class Howard's Pass SEDEX Zn-Pb district, Selwyn Basin, Yukon. Part I: trace element compositions of pyrite record input of hydrothermal, diagenetic and metamorphic fluids to mineralization. Mineralium Deposita 3, 319-342

Garven, G., Bull, S. W. and Large, R. R., 2001. Hydrothermal fluid flow models of stratiform ore

genesis in the McArthur Basin, Northern Territory, Australia. Geofluids, 1: 289–311

Goodfellow, W.D., 2004. Sediment Hosted Lead-Zinc Sulphide Deposits Geology, Genesis and Exploration of SEDEX Deposits, with emphasis on the Selwyn Basin, Canada, in: Deb, M., and Goodfeloow, W.D. (Eds.), Sediment-hosted Lead-Zinc deposits. Narosa Publishing house, New Delhi, 24-99

Gregory, D.D., Large, R.R., Halpin, J.A., Lounejeva Baturina, E., Lyons, T.W., Wu, S., Sack, P.J., Chappaz, A., Maslennikov, V.V., Bull, S.W., Danyushevsky, L., 2015b. Trace element content of sedimentary pyrite in black shales. Econ. Geol. 110, 1389–1410.

Hinman, M.C., 1995, Base metal mineralization at McArthur River: Structure and kinematics of the HYC-Cooleyzone at McArthur River: Australian Geological Survey Organisation Record 1995/5, 29

Jackson, M.J., and Southgate, P.N., 2000. Evolution of three unconformity-bounded sandy carbonate successions in the McArthur River region of northern Australia: the Lawn, Wide and Doom Supersequences in the proximal part of the Isa SuperBasin. Australian Journal of Earth Sciences 47, 600–625

Jackson, M.J., Muir, M.D. and Plumb, K.A., 1987. Geology of the southern McArthur Basin, Northern Territory. Bureau of Mineral Resources, Canberra, Bulletin, 220

Jochum, K.P., Pfänder, J., Woodhead, J.D., Willbold, M., Stoll, B., Herwig, K., Amini, M., Abouchami, W. and Hofmann, A.W., 2005. MPI-DING glasses: New geological reference materials for in situ Pb isotope analysis. Geochemistry Geophysics Geosystems 6. 1525-2027

Kornicker, W.A., and Morse, J.W., 1991. Interactions of divalent cations with the surface of pyrite. Geochimica et Cosmochimica Acta 55, 2159-2171

Lambert, I.B. and Scott, K.M., 1973. Implications of geochemical investigations of sedimentary rocks within and around the McArthur zinc-lead-silver deposit, Northern Territory. Journal of Geochemical Exploration 2, 307–330

Large R.R., Gregory, D.G., Steadman, J.A., Tomkins, A.G., Lounejeva, E., Danyushevsky, L.V., Halpin, J.A., Maslennikov, V.V., Sack, P.J., Mukherjee, I. and Hickman, A., 2015. Gold in the oceans through time. Earth and Planetary Science Letters, 428. 139-150

Large, R.R. and McGoldrick, P.J., 1998. Carbonate alteration halos associated with Australian

Proterozoic stratiform Zn-Pb-Ag deposits: in Holm O, Pongratz J and McGoldrick PJ (editors) ores: a special symposium convened by the Centre for Ore Deposit Research and the SEG Student Chapter, University of Tasmania' University of Tasmania, Centre for Ore Deposit Research (CODES), Special Publication 2, 29–36

Large, R.R., Bull, S.W. and Winefield, P.R., 2001. Carbon and oxygen isotope halo in carbonates related to the McArthur River (HYC) Zn-Pb-Ag deposit, north Australia: Implications for sedimentation, ore genesis, and mineral exploration. Economic Geology 96(7), 1567–1593

Large, R.R., Bull, S.W., Cooke, D.R., McGoldrick, P.J., 1998. A genetic model for the HYC deposit, Australia: Based on regional sedimentology, geochemistry, and sulfide-sediment relationships. Economic Geology 93, 1345–1368

Large, R.R., Bull, S.W., Selly, D., Yang, J., Cooke, D.R., Garven, G., McGoldrick, P., 2002. Controls on the formation of giant stratiform sediment-hosted Zn- Pb-Ag deposits: with particular reference to the north Australian Proterozoic: in Cooke DR and Pongratz J (editors) 'Giant ore deposits: Characteristics, genesis, and exploration.' Centre for Ore Deposit Research (CODES), Special Publication 4, University of Tasmania, Australia, 107–149

Large, R.R, Halpin, J.A., Lounejeva, E., Danyushevsky, L.V., Maslennikov, V.V., Gregory, D., Sack, P.J., Haines, P.W., Long, J.A., Makoundi, C., Stepanov, A.S., 2015. Cycles of nutrient trace elements in the Phanerozoic ocean, Gondwana Research 28 (4). 1282-1293

Large, R.R., Bull, S.\V., and McGoldrick, P.J., 2000, Lithogeochemical halos and geochemical vectors to stratiform sediment hosted Zn-Pb-Ag deposits. P a t 2: HYC deposit, Northern Territory: Journal of Geochemical Explo- ration, v. 64, 105-126

Large, R.R., Danyushevsky, L., Hollit, C., Maslennikov, V., Meffre, S., Gilbert, S., Bull, S., Scott, R., Emsbo, P., Thomas, H., Singh, B., Foster, J., 2009. Gold and trace element zonation in pyrite using a laser imaging technique: Implications for the timing of gold in orogenic and Carlin-style sediment-hosted deposits. Econ. Geol. 104, 635–668

Large, R.R., Halpin, J.A., Danyushevsky, L.V., Maslennikov, V.V., Bull, S.W., Long, J.A., Gregory, D.D., Lounejeva, E., Lyons, T.W., Sack, P.J., McGoldrick, P. and Calver, C.R., 2014. Trace element content of sedimentary pyrite as a new proxy for deep-time ocean- atmosphere evolution. Earth and Planetary Science Letters, 389. 209-220.

Large, R.R., Maslennikov, V.V., Robert, F., Danyushevsky, L.V., Chang, Z., 2007. Multistage sedimentary and metamorphic origin of pyrite and gold in the Giant Sukhoi log deposit, Lena Gold

Province, Russia. Econ. Geol. 102, 1233–1267.

Large, R.R., and Bull, S.W. and McGoldrick, P.J., and Walters, S.G. 2005. Stratiform and Strata-Bound Zn-Pb-Ag Deposits in Proterozoic Sedimentary Basins, Northern Australia. Economic Geology, 100th. 931-963.

Leach, D.L., Bradley, D.C., Huston, D., Sergei A. Pisarevsky, S.A., and Gardoll, S., 2010. Sediment-hosted lead-zinc deposits in Earth history: Economic Geology, 105

Logan, R.G., Murray, W.J., and Williams, N., 1990, HYC silver-lead-zinc deposit, McArthur River, in Hughes, F.E., ed., Geology of the mineral de- posits of Australia and Papua-New Guinea: Melbourne, Australasian Institute of Mining and Metallurgy, 907-911

Longerich, H.P., Jackson, S.E. & Günther, D., 1996. Laser ablation inductively coupled plasma mass spectrometric transient signal data acquisition and analyte concentration calculation. J. Anal. At. Spectrom. 11, 899-904

Maier, R. C., 2011. Pyrite Trace Element Haloes to Northern Australian SEDEX Deposits, PhD thesis, University of Tasmania.

Morse J, Luther G (1999) Chemical influences on trace metal-sulfide interactions in anoxic sediments. Geochim Cosmochim Acta 63, 3373–3378

McGoldrick, P., Winefield, P., Bull, S., Selley, D., and Scott, R., 2010. Sequences, Synsedimentary Structures, and Sub-basins: the Where and When of SEDEX Zinc Systems in the Southern McArthur Basin, Australia. Society of Economic Geologists, Inc. Special Publication 15, 367–389

Murray, W.J., 1975. McArthur River HYC lead-zinc and related deposits, Northern Territory: in Knight CL (editor) 'Economic Geology of Australia and Papua New Guinea. 1. Metals.' Australasian Institute of Mining and Metallurgy, Monograph 5, 329–339

Oehler, J.H. and Logan, R.G., 1977. Microfossils, cherts and associated mineralization in the McArthur deposit, NT, Australia. Economic Geology 72, 393–409

Page, R.W. and Sweet, I.P., 1998. Geochronology of Basin phases in the western Mt Isa Inlier and correlation with the McArthur Basin. Australian Journal of Earth Sciences 45(2), 201–232

Plumb, K.A. and Wellman, P., 1987. McArthur Basin, Northern Territory: mapping of deep troughs using gravity and magnetic anomalies. BMR Journal of Australian Geology and Geophysics 10, 243–252

Rawlings, D.J., 1997. High-level intrusions in the McArthur Basin, NT: deformation styles in the host stratigraphy and metallogenic implications: in 'New developments in research for ore deposit exploration; Third national conference of the Specialist Group in Economic Geology'. Geological Society of Australia, Abstracts 44, 59

Rawlings, D.J., 1999. Stratigraphic resolution of a multiphase intracratonic Basin system: the McArthur Basin, northern Australia. Australian Journal of Earth Sciences 46, 703–723

Rickard, D., 2012. Sulfidic sediments and sedimentary rocks. In: Van Loon, A.J. (Ed.),
Developments in Sedimentology. Elsevier, p. 801.

Rohrlach, B.D., Fu, M., and Clarke, J.D.A., 1998, Geological setting, paragenesis and fluid history of the Walford Creek Zn-Pb-Cu-Ag prospect, Mt Isa Basin, Australia: Australian Journal of Earth Sciences, v. 45, 63–81

Shen, Y., Canfield, D. E. and Knoll, A. H., 2002. Middle Proterozoic ocean chemistry: evidence from the McArthur Basin, northern Australia. Am. J. Sci. 302 (2), 81–109

Steadman, J.A., Large, R.R., Meffre, S., Olin, P.H., Danyushevsky, L.V., Gregory, D.G., Belousov, I., Lounejeva, E., Ireland, T.R., and Holden, P. 2015. 'Synsedimentary to early diagenetic gold in black shale-hosted pyrite nodules at the Golden Mile Deposit, Kalgoorlie, Western Australia', Economic Geology, 110 (5), 1157-1191

Thomas, H.V., Large R.R., Bull, S.W., Maslennekov, V.V., Berry, R.F., Fraser, R., Froud, S., and Moye, R., 2011, Pyrite and pyrrhotite textures and com- position in sedimentary rocks, laminated quartz veins, and gold reefs at the Bendigo mine, Australia: Insights for ore genesis: Economic Geology, 106, 1–31

Walker, R.N., Logan, R.G., and Binnekamp, J.G., 1977, Recent geological advances concerning the HYC and associated deposits, McArthur River, Northern Territory: Journal of the Geological Society of Australia, 24, 365-380

Williams, N., 1978a. Studies of the base metal sulphide deposits at McArthur River, Northern Territory, Australia. I: The Cooley and Ridge deposits. Economic Geology 73, 1005–1035.

Winefield, P., Selley, D., and Bull, S.W., 1997, Day 6 and Day 7—McArthur Basin: AMIRA/ARC project P384, A Proterozoic sediment-hosted base metal deposits Report 4 Sponsors Field Meeting, 1997, 53–77.

Winefield, P.R., 1999. Sedimentology and diagenesis of Late Palaeoproterozoic carbonates, southern McArthur Basin, northern Australia. PhD thesis, Key Centre for Ore Deposits and Exploration Studies (CODES), University of Tasmania, Hobart.

Chapter 4

Pyrite trace element and sulphur isotope geochemistry of Paleo-Mesoproterozoic McArthur Basin: Proxy for Oxidative weathering

Mukherjee, I., Large, R.R., Bull, S., Gregory, D., Stepanov, A., Ávila, J., Ireland, T. and Corkrey, R., 2017. Geochimica et Cosmochimica Acta (revision submitted)

Indrani Mukherjee[1*], Ross R Large[1], Stuart Bull[1], Daniel G Gregory[2], Aleksandr S. Stepanov[1], Janaína Ávila[3], Trevor. R. Ireland[3] and Ross Corkrey[4]

1. Centre for Ore Deposit and Earth Sciences (CODES), University of Tasmania, Private Bag 126, Hobart, Tasmania 7001, Australia

2. Department of Earth Sciences, University of California, Riverside, CA 92521, USA

3. Research School of Earth Sciences, The Australian National University, Canberra, ACT 2601, Australia

4. Tasmanian Institute of Agricultural Research (TIAR), University of Tasmania, Hobart, Tasmania 7001, Australia

*Corresponding author: Indrani Mukherjee, email: Indrani.Mukherjee@utas.edu.au

4.0 Abstract

Redox sensitive trace elements and sulphur isotope compositions of sedimentary pyrites from marine black shales are used to track atmosphere-ocean redox conditions between ~1730 and ~1360 Ma in the McArthur Basin, northern Australia. Three black shale formations within the basin, (Wollogorang Formation 1730 $\pm$ 3 Ma, Barney Creek Formation 1640 $\pm$ 3 Ma and Upper Velkerri Formation 1361 $\pm$ 21 Ma) display systematic stratigraphic variations in pyrite trace element compositions. The concentrations of several trace elements and their ratios, such as Se, Zn, Se/Co, Ni/Co, Zn/Co, Mo/Co, Se/Bi, Zn/Bi, Ni/Bi, increase from the stratigraphically lower Wollogorang Formation to the Upper Velkerri Formation. Cobalt, Bi, Mo, Cu and Tl, show a consistent decrease in abundance while Ni, As and Pb show no obvious trends.

We interpret these trace element trends as a response to the gradual increase of oxygen in the atmosphere-ocean system from ~1730 to 1360 Ma. Elements more mobile during erosion under rising atmospheric

oxygen show an increase up stratigraphy (e.g. Zn, Se) whereas elements that are less mobile show a decrease (e.g. Co, Bi). We also propose the increase of elemental ratios (Se/Co, Ni/Co, Zn/Co, Mo/Co, Ni/Bi and Zn/Bi) up stratigraphy are strong indicators of atmospheric oxygenation.

Sulphur isotopic compositions ($\delta^{34}S$) of marine pyrite from these formations are highly variable, with the Wollogorang Formation exhibiting less variation ($\delta^{34}S$ = –29.4 to +9.5‰; mean: –5.03‰) in comparison to the Barney Creek ($\delta^{34}S$ = –13.8 to +41.8‰; mean: +19.88‰) and Velkerri Formations ($\delta^{34}S$ = –14.2 to +52.8 ‰; mean: +26.9‰). We propose that the shift in mean $\delta^{34}S$ to heavier values upsection corresponds to increasing deep water oxygenation from ~1730 to 1360 Ma. Incursion of oxygenated waters possibly caused a decrease in the areal extent of anoxic areas, at the same time, creating a possibly efficient reducing system. A stronger reducing system caused the $\delta^{34}S$ of the sedimentary pyrites to become progressively heavier. Interestingly, heavy $\delta^{34}S$ in pyrites overlaps with the increase in the concentration of certain trace elements (and their ratios) in sedimentary pyrites (Se, Zn, Se/Co, Ni/Co, Zn/Co, Mo/Co, Ni/Bi and Zn/Bi). This study concludes that there was a gradual increase of atmospheric oxygen accompanied by ocean oxygenation through the first ~400 million years of the Boring Billion (1800-1400 Ma) in the McArthur Basin.

4.1 Introduction

Sedimentary rocks of the McArthur Basin in northern Australia have been the focus of various studies on the application of bio-geochemical techniques to understand ocean and atmospheric redox conditions during the Paleo-Mesoproterozoic. These sedimentary packages are unmetamorphosed, relatively undeformed and believed to preserve imprints of the biological and geochemical processes operative during their deposition (Brasier et al., 1998; Anbar and Knoll, 2002; Shen et al., 2002; Arnold et al., 2004; Brocks et al., 2005; Javaux et al., 2001, 2004; Scott et al., 2008; Johnston et al., 2008; Kendall et al., 2009; Planavsky et al., 2011; Planavsky et al.., 2014; Lyons et al., 2014; Large et al., 2014). Particular interest in the McArthur Basin arises because it provides an insight into the "Boring Billion" period (1800-800 Ma), which has been of great interest since being referred to as "one of the dullest period in Earth's history" (Buick, 1995) and as "a billion year of environmental stasis" (Brasier and Lindsay, 1998). Several techniques have been used to decipher the depositional conditions in order to interpret basin redox structure and its impact on biological processes. Isotopic (C, Sr, S, Mo, Cr) and biomarker studies have been undertaken to provide an overall perspective on the McArthur Basin redox conditions (Brasier and Lindsay; 1998; Lindsay and Brasier, 2000; Shen et al., 2002; Chen et al., 2003; Kah et al., 2004; Brocks et al., 2005; Johnston et al., 2008; Scott et al., 2008; Planavsky et al., 2014; Luo et al., 2015). Bulk rock trace element concentrations in sedimentary rocks, particularly black shales and ironstones, have also enhanced our understanding of Proterozoic ocean biogeochemistry (Lyons et al., 2003; Tribovillard et al., 2006; Konhauser et al., 2009; Sahoo et al., 2012; Reinhard et al., 2013; Partin et al., 2013; Planavsky et al., 2014). Recently, studies by

Large et al. (2014), Large et al. (2015 a, b), Gregory et al. (2014, 2015a, 2017), and Mukherjee and Large (2016, 2017) have shown that trace element concentrations in marine sedimentary pyrite from black shales can also be used to infer ocean-atmosphere redox relationships. Using the technique introduced by Large et al., (2014), potential oxygenation during the Velkerri Formation depositional period (~1360 Ma) has been proposed (Mukherjee and Large, 2016) on the basis of enrichment of certain redox sensitive trace elements (Se, Mo, Ni, Zn) in pyrite in the black shales.

The aim of the present contribution is to further our understanding of marine conditions (redox state of the atmosphere and ocean, nutrient trace element availability) in the McArthur Basin by measuring trace element concentrations and S isotopic compositions of marine pyrite in three black shale formations from the McArthur basin stratigraphy. These are the Velkerri Formation (~1400 Ma), Barney Creek Formation (~1650 Ma) and Wollogorang Formation (~1730 Ma) located in in the Roper, McArthur and Tawallah Groups respectively.

The McArthur Basin was chosen for this study for several reasons. First, the basin is a multiphase tectonic system with five coherent packages (Wilton, Favenc, Glyde, Goyder and Redbank), each with a characteristic age, lithostratigraphy, volcanism (style and composition), basin architecture and micropaleontology (Rawlings, 1999). Of the five packages, three comprise marine black shale formations, which makes the McArthur Basin an ideal location to apply the technique introduced by Large et al. (2014; 2017), of using trace element concentrations of sedimentary pyrite in marine black shales to infer redox conditions of the ocean and atmosphere. The McArthur also provides an opportunity to investigate possible factors such as atmosphere-ocean redox and basin tectonics that controlled the pyrite trace element concentrations. Second, previous studies (Bull, 1998; Jackson et al., 2000; Shen et al., 2002; Brocks et al., 2008; Johnston et al., 2008; Kendall et al., 2009) have shown that the intracratonic McArthur Basin was connected to the global ocean, possibly allowing us to infer global redox conditions between 1730 Ma and 1360 Ma.

4.1.1 Importance of combining sedimentary pyrite trace element and sulphur isotope compositions

Certain redox-sensitive trace elements (Mo, U, Cr, V, Zn) in black shales have been used previously as paleoredox indicators of the water column (Algeo et al., 2006; Tribovillard et al., 2006; Algeo et al., 2009; Algeo et al., 2012; Meyer et al., 2008; Gordon et al., 2009; Sahoo et al., 2012; Sahoo et al., 2016). Also, they have been used to track atmospheric oxygenation through time (Scott et al., 2008; Partin et al., 2013; Lyons et al., 2014). Recently, Large et al. (2014) proposed that trace element concentrations in sedimentary pyrite formed in marine black shales could also be used as proxies for ocean trace element chemistry and atmospheric oxygenation. The pyrite technique relies on the fact that most redox-sensitive trace elements, in bottom waters and pore waters, are readily and efficiently incorporated into sedimentary pyrites (Huerta-Diaz and Morse, 1992; Morse and Arakaki, 1993, Rickard et al., 2012; Gregory et al., 2014;

Large et al., 2014; Gregory et al., 2015a; Mukherjee and Large, 2016, 2017). The premise on which the technique is based is that enhanced oxidative weathering on land causes an increase in the supply of redox-sensitive trace elements in the riverine flux (dominant source) in the ocean (Bertine and Turekian, 1973; Taylor and McLennan, 1995; Scott et al., 2008; Sahoo et al., 2012; Crowe et al., 2013). This is coupled with a decrease in areal extent of sulfidic bottom waters, a main sink for several trace elements (Sahoo et al., 2016). On encountering a redox-boundary, these trace elements become readily adsorbed by sedimentary pyrites forming in anoxic black shales, either in the water column or in the upper most part of the sediments. Hence, an increase in concentrations of redox sensitive trace elements in sedimentary pyrites can act as an indirect proxy for an increase in atmospheric oxygenation (Gregory et al., 2014; Large et al., 2014; Gregory et al., 2015a; Mukherjee and Large, 2016; 2017).

Bulk-rock sulphur isotope compositions of the McArthur Basin sediments have been studied previously (Donnelly and Crick, 1988; Canfield, 1998; Shen et al., 2002; Shen et al., 2003; Kah et al., 2004; Lyons et al., 2006; Johnston et al., 2008). Those studies produced $^{34}S/^{32}S$ compositions but additional information on depositional environment, microbial activity and connectivity to the global ocean can be obtained using isotopes such as ^{33}S and ^{36}S abundances (Johnston et al., 2008). Sulphur isotopic compositions of the McArthur Basin sediments have also been reported previously to understand changes in sea water sulphate concentration and the sulphate reservoir, biogeochemical sulphur isotope fractionation patterns, global oxidative sulphur cycling and redox stratification of the Proterozoic oceans (Shen et al., 2002; Kah et al., 2004; Johnston et al., 2008; Luo et al., 2015). In this study, we carried out sulphur isotope analyses of sedimentary pyrites with SHRIMP-SI (Ireland, 2008) and combined them with trace element concentrations to provide additional insight into changes in putative biogeochemical processes operative during the deposition of the three black shales formations.

There are several advantages of using a combined marine pyrite trace element and S-isotope approach for understanding ocean chemistry. Second, both techniques offer high spatial resolution so measurements can be performed within a single grain domain, avoiding the problem of differing amounts of the detrital component that may adversely affect whole rock analyses. Many TE, such as Mo, are partitioned between minerals in the shale (Tribovillard et al., 2006), and thus variations in mineral composition can affect the bulk rock analyses (Chappaz et al., 2014). Third and most important, the effects of diagenesis, metamorphism and hydrothermal activity, all of which affect trace element concentrations and sulphur isotopic compositions, can be identified by textural studies of the pyrite (Gregory et al., 2017). For example, Large et al. (2007; 2009) demonstrated that recrystallization of pyrite during metamorphism releases most trace elements and results in subhedral to euhedral forms of pyrite with low trace element abundances. Hydrothermal pyrites, on the other hand, may be enriched or depleted in trace elements depending on the conditions of formation (temperature, salinity, proximity to vents). These hydrothermal pyrite concentrations therefore do not reflect primary trace element concentrations of the sea water (Large et al., 2014; Mukherjee and Large, 2017).

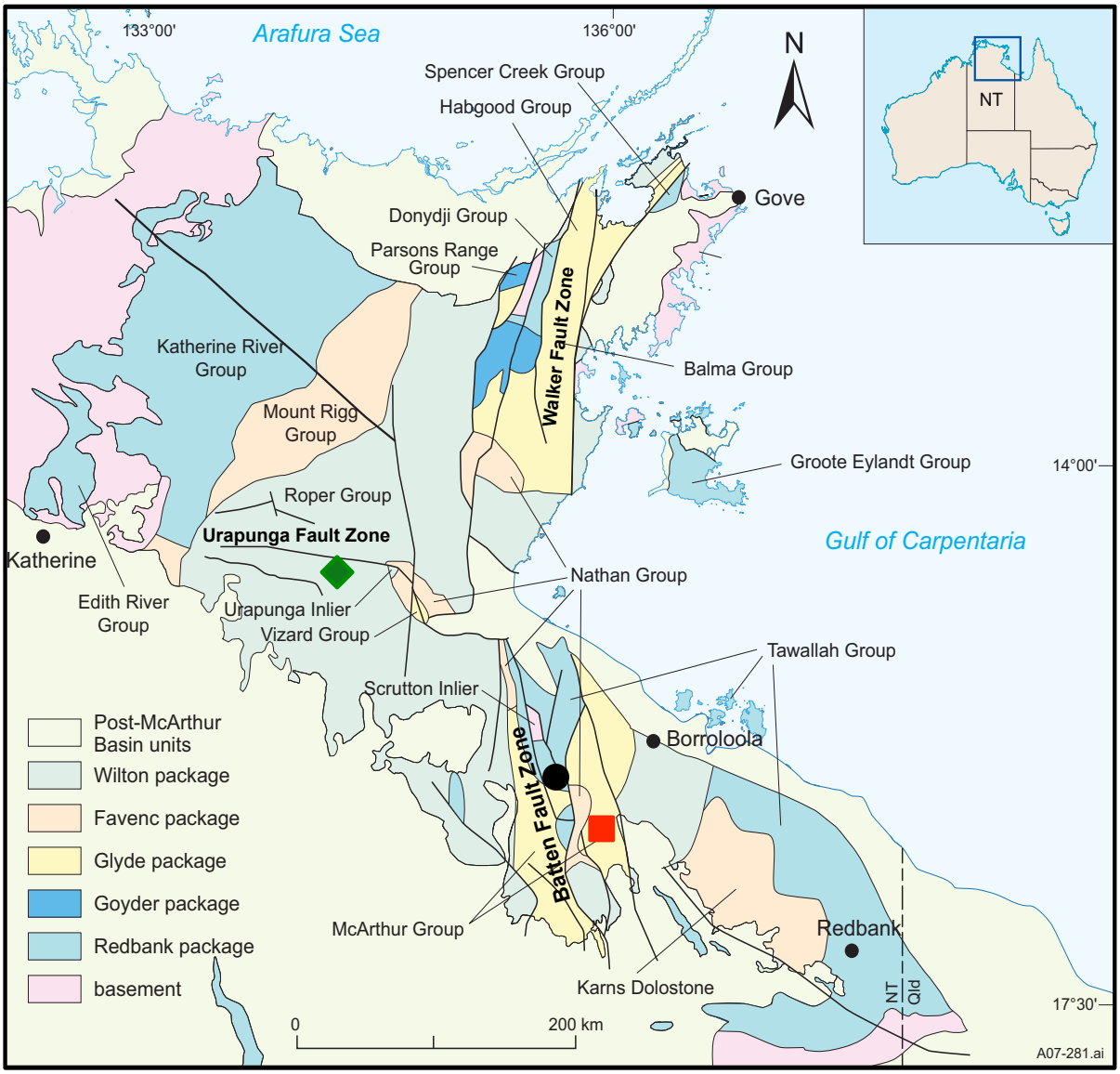

Group	Formation	Age (Ga)	Drill hole	Symbol
Roper	Velkerri	~1.4	Urap-4	◆
McArthur	Barney Creek	~1.64	MBXDD001	■
Tawallah	Wollogorang	~1.73	Mt Young	●

Fig 4.1 Drill hole locations for the three black shale formations (Figure adapted from Ahmad et al., 2013)

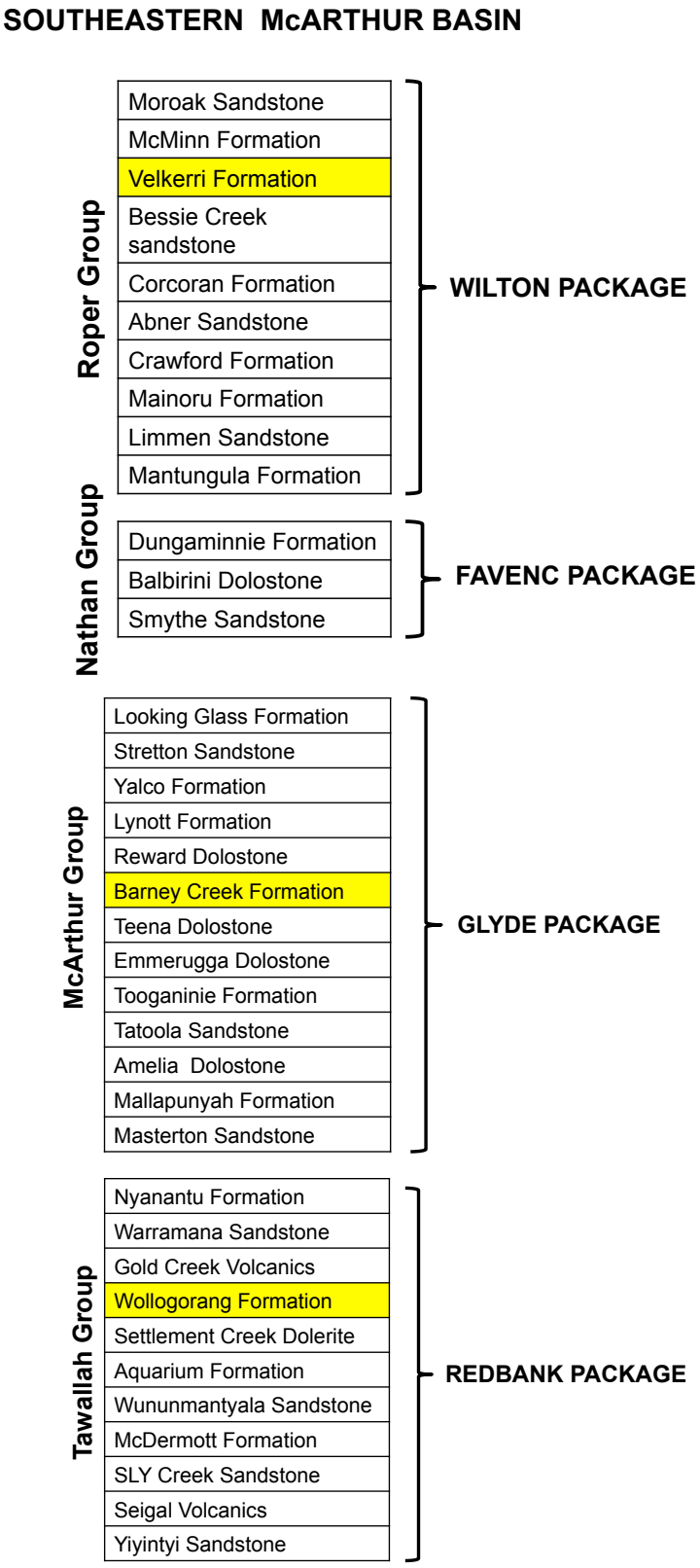

Fig 4.2 Generalized stratigraphy of the southern McArthur Basin, Australia adapted from Rawlings (1999); highlighted in yellow are the three black shale formations examined in this study.

4.2 Geological Setting

The McArthur Basin, northern Australia, preserves a Paleo-Mesoproterozoic volcano-sedimentary history (Plumb, 1979a, b; Rawlings et al., 1999) (Fig. 4.1). The basin is divided into northern and southern elements by the roughly east-west trending Urapunga Fault zone. Both basin elements comprise a central N-S trending element (Walker and Batten Fault Zone respectively) with flanking "shelves". For this paper, we will refer to the stratigraphy of southeastern part of the Batten Fault Zone, in which the basin fill is divided into four major groups (Tawallah, McArthur, Nathan and Roper, Figure 4.1). With the exception of the Nathan Group, each includes black shale formations i.e., Wollogorang Formation, Barney Creek Formation, and Velkerri Formation in the Tawallah, McArthur, and Roper Groups respectively (Fig. 4.2).

4.2.1 Stratigraphy and depositional environments of the three black shale formations

4.2.1.1 Wollogorang Formation

The Wollogorang Formation was deposited 1730 Ma $\pm$ 4 Ma based on U-Pb zircon ages from interbedded tuffs (Page et al., 2000). It is 100-150 m thick and is divided into upper and lower units on the basis of lithology. The upper Wollogorang Formation comprises mudstone and dolomitic sandstone whereas the lower part of the formation consists of black shales and dolomitic siltstone (Jackson et al., 1985; Donnelly and Jackson, 1988). The Wollogorang Formation black shales is interpreted to be deposited in a low sulphate, marine intracratonic basin with oxic surface waters and euxinic deep water conditions prevalent during deposition (Jackson et al., 2000; Page et al., 2000; Southgate et al., 2000; Shen et al., 2002).

4.2.1.2 Barney Creek Formation

The Barney Creek Formation has a depositional age of 1640 $\pm$ 3 Ma (Page and Sweet, 1998). It is divided into the Cooley Dolostone member, W-Fold Shale member and HYC Pyritic Shale member (~100 m). The HYC Pyritic Shale member consists of laminated pyritic, dolomitic carbonaceous siltstone/mudstone and minor tuffaceous mudstone. The black shales of the Barney Creek Formation were deposited in an anoxic environment, in a subsiding basin in which morphological traps were forming due to local contemporaneous vertical tectonism (Bull, 1998).

4.2.1.3 Velkerri Formation

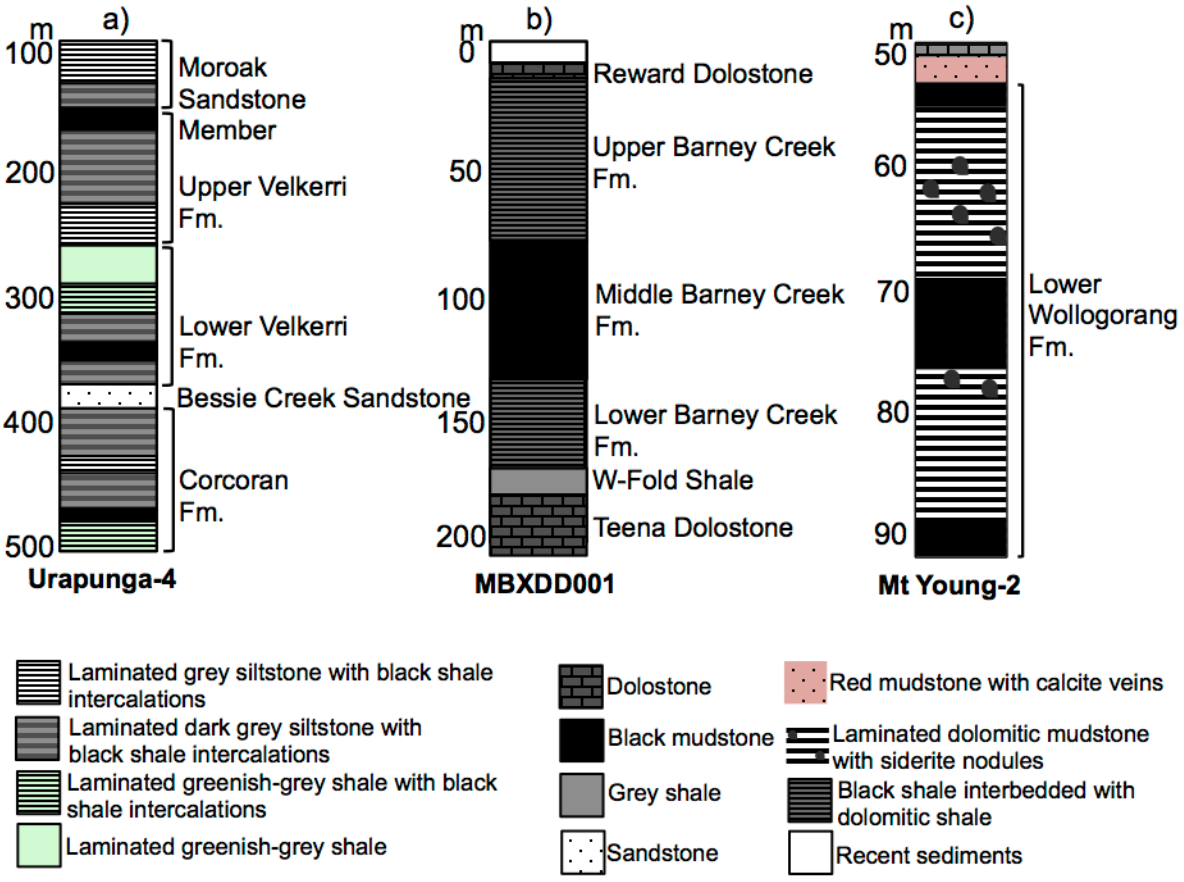

Fig 4.3 a, b, c Simplified logs of the three drill holes used for the study.

The Velkerri Formation is 330 m thick and is composed dominantly of black carbonaceous mudstones with minor grey siltstones and very fine-grained sandstones along with minor calcite nodules, pyritic stringers and glauconitic siltstones (Abbott et al., 2000). The Velkerri is essentially unmetamorphosed and is relatively undeformed. The depositional age of the Velkerri Formation is 1361 $\pm$ 21 Ma for the Upper Velkerri Formation and 1417 $\pm$ 29 Ma for the Lower Velkerri Formation based on according to Re-Os dating (Kendall et al., 2009). The Velkerri Formation black shales were deposited in a low energy offshore environment (Abbott et al., 2000) as a result of hemipelagic sedimentation under anoxic conditions with cyanobacterial and algal biotic communities as the source of organic matter (Crick et al., 1988; Javaux et al., 2001; Gorter and Grey, 2012).

4.3 Materials and Method

4.3.1 Sampling Rationale

The black shale units of these three formations were chosen for the present study after considering their similarity in lithology (organic-matter rich shales; TOC% & their depositional environments) and importantly, their stratigraphic position (black shales of three different ages). The varying stratigraphic positions will allow the tracking of changes in ocean chemistry. (See Appendix 4.1 (A1.1); Table A1). Mineralogically, they are similar except that both the Wollogorang and Barney Creek Formations are associated with carbonates while the Velkerri Formation is not (Ahmad et al., 2013).

4.3.2 Sample details

Only drill core samples were used for the present study (Fig. 4.1, 4.3). Samples were obtained from Mt Young 2, MBXDD001 and URAPUNGA-4 drill holes for Wollogorang, Barney Creek and Velkerri Formations, respectively (Fig. 4.2). The Mount Young 2 (located in the Batten fault zone) and Urapunga 4 (in the Roper Bar area – Urapanga fault zone according to the map) drill cores were provided by Geoscience Australia. The MBXDD001 drill core was provided by the Northern Territory Geological Survey (NTGS) drill core facility. Considering that the Barney Creek Formation hosts the McArthur River SEDEX deposit, the drillhole (MBXDD001) farthest away (~60 km south of the deposit) from the ore body was selected in order to minimize possible effects of hydrothermal fluids (Mukherjee and Large, 2017). Black were selected from all three drill cores. Samples were collected every ~10 m down-hole and rock chips from each interval were set in 2.5 cm diameter epoxy mounts and polished with 1-micron diamond paste. Polished laser mounts were examined using reflected light microscope.

4.3.3 LA-ICP-MS pyrite trace element analyses

The LA-ICP-MS analyses of trace elements in pyrite and the black shale matrix were conducted at CODES, University of Tasmania. Analyses were carried out using a New Wave Research UP-193ss laser microprobe coupled to an Agilent 7700s quadrupole ICP-MS for the following elements and their respective isotopes, ^{13}C, ^{23}Na, ^{24}Mg, ^{27}Al, ^{29}Si, ^{34}S, ^{39}K, ^{43}Ca, ^{49}Ti, ^{51}V, ^{53}Cr, ^{55}Mn, ^{57}Fe, ^{59}Co, ^{60}Ni, ^{65}Cu, ^{66}Zn, ^{75}As, ^{77}Se, ^{85}Rb, ^{88}Sr, ^{90}Zr, ^{95}Mo, ^{107}Ag, ^{111}Cd, ^{118}Sn, ^{121}Sb, ^{125}Te, ^{137}Ba, ^{157}Gd, ^{178}Hf, ^{181}Ta, ^{182}W, ^{195}Pt, ^{197}Au, ^{202}Hg, ^{205}Tl, ^{206}Pb, ^{207}Pb, ^{208}Pb, ^{209}Bi, ^{232}Th and ^{238}U. STGL2b2 (in-house reference material for calibration of relative element sensitivities; Danyushevsky et al., 2011), GSD-1G (USGS reference glass; Jochum et al., 2005) and a stoichiometric pyrite PPP-1 crystal (Gilbert et al., 2014) were the three primary reference materials used to quantify the abundances of chalcophile elements, lithophile elements, and sulphur abundances, respectively. All three reference materials were analysed twice, before and thereafter, 15 to 20 analyses (~every 1.5 hours) as well as at the beginning and end of a run. Backgrounds were analysed for 30-seconds before the signal from the ablated sample was acquired for 40-60 seconds. The laser was operated with ~3.5 J/cm^2 laser fluence and 5 Hz laser repetition rate. Samples were ablated in a He atmosphere flowing at a rate of 0.8 l/min, followed by mixing of the ablation stream with the Ar carrier gas (0.85 l/min) for introduction to the ICPMS.

The ICP-MS instrument was optimized to maximize sensitivity on mid- to high-mass isotopes (>80 amu). Production of molecular oxide species (monitored as $^{232}Th^{16}O^+/^{232}Th^+$) and doubly charged ion species (monitored as $^{140}Ce^{++}/^{140}Ce^+$) were maintained at levels below 0.2%. Dwell times on each mass varied between 5 and 30 msec, depending on the count rates. Total sweep time (time required to measure all isotopes once) was 0.76 sec. A total of ~10 spot analyses, with spot size ranging from 15-35 mm, of sedimentary pyrites were performed on each sample The pyrite (PPP-1) standard was analysed with same spot as unknowns in order to account for Fe-S fractionation during ablation (Gilbert et al., 2014). The glass standards were analysed with 51 mm spot size in order to alleviate heterogeneity of the standards for key elements such as Au and Tl. Also, 5 spot analyses of the black shale matrix (material surrounding the pyrites) were carried out on each sample to measure concentrations of chalcophile and lithophile elements in siliciclastic matrix of the black shales. Approximately, 10-12 analyses were performed on fine grained sedimentary pyrite grains, containing abundant matrix inclusions, hence producing mixed analyses. Therefore, it was necessary to deconvolute the analyses and extract the composition of clean pyrite. Both matrix and pyrite analyses were used in the data reduction process in order to account for mixing of pyrite and matrix components during LA-ICP-MS analyses of small pyrite grains. The analyses of samples from the Velkerri and Wollogorang formations were processed by an algorithm based on subtraction of the matrix component estimated from mass balance (Large et al. 2014). The disadvantages of this method were subjectivity in selection of the pyrite and matrix compositions and difficulty in determining uncertainties. The samples from the Barney Creek Formation were reduced by the method

of linear regression followed by normalization of the total, which is described below. Uncertainties on analyses processed using the regression method are presented in Appendix 4.2. The analysis of a number of samples from the Barney Creek were processed by both methods and produced consistent results within 10% (Appendix 4.3).

The LA-ICP-MS analyses of pyrite from the Barney Creek formation were processed by an Excel based data reduction software developed in-house, which uses a linear regression based algorithm for determining chalcophile and siderophile abundances relative to sulphur, for calculation of sulfide composition The conversion of raw data (counts per second) into concentrations in ppm involved splitting the integration curve obtained from counts per second vs analysis time, into five segments of equal duration. Concentrations represented by each of these segments were reduced using time-equivalent portions of the signal obtained for each of the calibration materials. The data in counts per second were then converted to preliminary ppm values according to established methods (Longerich et al., 1996; Norman et al. 1996), using Fe as the internal standard element. The method assumes a stoichiometric Fe content of pyrite for calculating preliminary compositions, which are then normalized to a 100% total of all measured elements with the exception of C and Hg. To calculate the final concentrations, a linear regression equation using S content was employed such that the sum of the chalcophile elements is 100%. Regression fits for individual analyses were visually inspected for all samples. The resulting compositions were close (Appendix 4.2) to major element composition of stoichiometric pyrite. The analytical precision was estimated using regression analysis for estimation of uncertainty on prediction, however ignoring uncertainties on the measurements. For Se, As, Sb, Ni, Zn, Cu, Pb and Co at high concentrations, the 90% relative uncertainty is <20% for the majority of the analyses. However, uncertainty increases at lower concentrations. The relative analytical precision of the replicate analyses of the standards was less than 5% Considering that concentrations of many elements vary by 2-3 orders of magnitude in different samples, we conclude the observed trends are outside of analytical uncertainty.

Sedimentary pyrites from the three black shale units were analysed for Co, Ni, Cu, Zn, As, Se, Mo, Tl, Pb, Bi concentrations using the LA-ICP-MS (Table A2 a, b, c in Appendix 4.2). A total of 29 black shale samples were selected for the study (Wollogorang Formation: 5; Barney Creek Formation: 15; Velkerri Formation: 9) and ~ten pyrite spot analyses were performed on each sample.

The pyrite data from the two formations i.e., Velkerri and Barney Creek have been published in Mukherjee and Large (2016) and Mukherjee and Large (2017) respectively. Pyrite data form the Wollogorang formation have been recently published in Mukherjee et al (2018) along with other global Proterozoic formations in a large database provided as background information in the Supplementary Information section of that paper. Here we provide the data for the three formations again as it is the subject of detailed statistical treatment, discussion and interpretation in the context of the McArthur Basin specifically.

4.3.4 SHRIMP sulphur isotopes

Sulphur isotope compositions ($\delta^{34}S$ and $\Delta^{33}S$) of the pyrites were measured in-situ with the SHRIMP-SI ion microprobe at the Research School of Earth Sciences, The Australian National University (ANU). The same mounts used for laser ablation analysis were used for SHRIMP analysis, in some cases the same grains Mounts were cleaned using ethanol, a dilute alkaline cleaning solution, de-ionised water and dried in a vaccum oven at 60 °C for 24h. Mounts were then coated with a film of ca. 40 nm of Au before pumping down in the sample lock overnight. SHRIMP-SI measurements were performed with a Cs^+ primary beam of ~ 2 nA focused to sputter an area of ~ 25 µm in diameter. The sample mount was held at –10 kV resulting in a final impact energy at the target of 15keV. Analytical conditions of the analyses are similar to those described in Ireland et al. (2014). Faraday cups were used for simultaneous detection of $^{32}S^-$, $^{33}S^-$, and $^{34}S^-$. $^{32}S^-$ was collected on a 10^{11} Ω resistor (50V range), $^{33}S^-$ and $^{34}S^-$ on 10^{11} Ω resistors (5V range).

Under the operating conditions used for these analyses, typical count rates on $^{32}S^-$ were ~ $0.2 – 1.2 \times 10^9$ cps, on $^{33}S^-$ about $1.2 – 9.2 \times 10^6$ cps, and on $^{34}S^-$ about $0.7 – 5.2 \times 10^7$ cps. Data collection consisted of 1 or 2 sets of 6-10 subsets, 20 s each, with each subset comprising ten 2 s integrations.

Analyses of unknown pyrites were bracketed by measurements of pyrite reference material Balmat ($\delta^{34}S$ = +15.1 ± 0.2‰, Crowe and Vaughan, 1996). The $^{33}S/^{32}S$ and $^{34}S/^{32}S$ ratios, corrected for instrumental mass fractionation, are expressed here in standard delta notation in permil (‰) relative to V-CDT (VCDT: Vienna-Canyon Diablo Troilite) scale, with

$$\delta^{33}S_{V-CDT} = 1000 \times \left[\frac{\left(^{33}S/^{32}S\right)_{corrected}}{\left(^{33}S/^{32}S\right)_{reference}} - 1 \right] (‰)$$

$$\delta^{34}S_{V-CDT} = 1000 \times \left[\frac{\left(^{34}S/^{32}S\right)_{corrected}}{\left(^{34}S/^{32}S\right)_{reference}} - 1 \right] (‰)$$

Capital delta values ($\Delta^{33}S$) have been calculated following Farquhar et al. (2003), where

$$\Delta^{33}S = \delta^{33}S - 1000 \times \left(\left(1 + \frac{\delta^{34}S}{1000} \right)^{0.515} - 1 \right)$$

Internal precision of single spot analyses of $\delta^{34}S$ and $\Delta^{33}S$ are usually better than 0.08‰ and 0.3‰ (2SE; SE

= standard error), respectively. External reproducibility of $\delta^{34}S$ and $\Delta^{33}S$ values, calculated as the 1sigma standard deviation (SD) of all analyses on the Balmat reference material over the course of an analytical session, were between 0.2 and 0.3‰.

4.4 Results

4.4.1 Pyrite Textures

Only pyrite with framboidal textures, aggregates of fine-grained pyrite, or layers of fine-grained pyrite, identified using reflected light microscopy, were selected for LA-ICP-MS and SHRIMP-SI analyses as these are interpreted as primary diagenetic pyrite (Fig A1 in Appendix 4.1). Pyrites from all three formations exhibited similar textures i.e., fine-grained pyrite aggregates (10-100 µm) with the size of individual crystals varying between 5-10 µm. However, at two intervals in the Wollogorang Formation intersection (65.8 m and 82.8 m), the pyrites were coarser grained and possibly of hydrothermal origin. These grains were excluded from this study because recrystallized and hydrothermal pyrites are known to have different trace element concentrations and therefore would not reflect contemporaneous seawater trace element chemistry (Large et al., 2009; Large et al., 2014; Gregory et al., 2015a; Mukherjee et al., 2017). For instance, both coarse grained and fine grained pyrites analyses in the same laser mount in the Barney Creek Formation yielded different trace element concentrations (Fig A2 in Appendix 4.1)

4.4.2 LA-ICP-MS pyrite trace element and matrix analyses

Geometric means of individual sample intervals from all three formations are presented in Table 4.1. Geometric means were calculated because trace element analyses in pyrite tend to approximate log-normal distributions. Multiplicative standard deviations (MSD) of trace elements are presented in Table 4.2. For all the elements presented, MSD ranges between 1 and 3. Mean (geometric) pyrite trace element concentrations of the entire set of analyses in the three black shale units are also compared in Table 4.3.

Copper, Co, Tl and Bi show marked decreases in concentrations upsection from the Wollogorang Formation to the Upper Velkerri Formation (Fig 4.4). Mean Co concentrations decrease from 457 ppm in the Wollogorang Formation to 48 ppm in the Upper Velkerri Formation (~9-fold decrease), while Cu decreases from 377 ppm in the Wollogorang Formation to ~81 ppm in the Upper Velkerri Formation (~5-fold decrease). Molybdenum shows a gradual decrease in concentration with higher concentrations in the Wollogorang (77 ppm) and Barney Creek Formations (79 ppm) compared to the Upper Velkerri Formation (20 ppm). Thallium shows a gradual decrease up stratigraphy with mean values decreasing

from 20 to 5 ppm. On the other hand, concentrations of Zn and Se increase up stratigraphy (Fig 4.4). The Zn mean increases from 28 ppm to 96 ppm, almost 3 times, whereas the Se mean increases from 9 ppm to 19 ppm, only 2 times. Nickel, As, Ag and Pb show no obvious trends with stratigraphy (Fig 4.4).

Trace element ratios Se/Co, Se/Bi, Ni/Co, Ni/Bi, Zn/Co, Zn/Bi and Mo/Co for the three formations all increase upsection from the Wollogorang Formation to the Velkerri Formation, with Mo/Bi remaining roughly constant (varying little between 6-13) in all three formations (Fig 4.4). Downhole plots of Se, Mo, Co, Se/Co and Mo/Co for all three formations (Fig 4.5) also indicate that [Se], Se/Co and Mo/Co increase, and Co and Mo decrease, upsection. The down hole trends are compared with global mean values obtained from analyses of ~5000 pyrites by Large et al. (2014, 2015a, b), as denoted by the black dashed line in Fig 4.5.

Statistical T tests were performed on the dataset to confirm that the differences in the geometric mean concentration of TEs of the three formations are significant (Table 4.4). Mean Mo, Se, Zn, Co, Bi concentrations of the Velkerri Formation are statistically significantly different from those of the Wollogorang and Barney Creek Formations. Mean concentrations of Co and Bi differ significantly between the Barney Creek Formation and Wollogorang Formation, with no significant differences in the means of Mo, Se and Zn concentrations. The mean Ni concentrations of all three black shales do not differ significantly. Other statistical tests such as Spearman Correlations and Analyses of Variance (AOVs) confirm the T-test results (See A1.3 in Appendix 4.1 and AOVs in Appendix 4.5).

Black shale matrix analyses for Ti, Zr, Th and Cr for evaluation of provenance, are presented in Table 4.5. The mean Ti/Zr of the Velkerri, Barney Creek, and Wollogorang Formations are 22, 37 and 25 respectively. The Th/Cr ratios of Velkerri and Barney Creek Formations are ~1 and are slightly lower in the Wollogorang Formation (~0.40). Statistical treatment of the data on matrix elements confirm no significant differences between the means of Ti/Zr and Th/Cr ratios in the three black shale formations (Refer Appendix 4.6).

a)

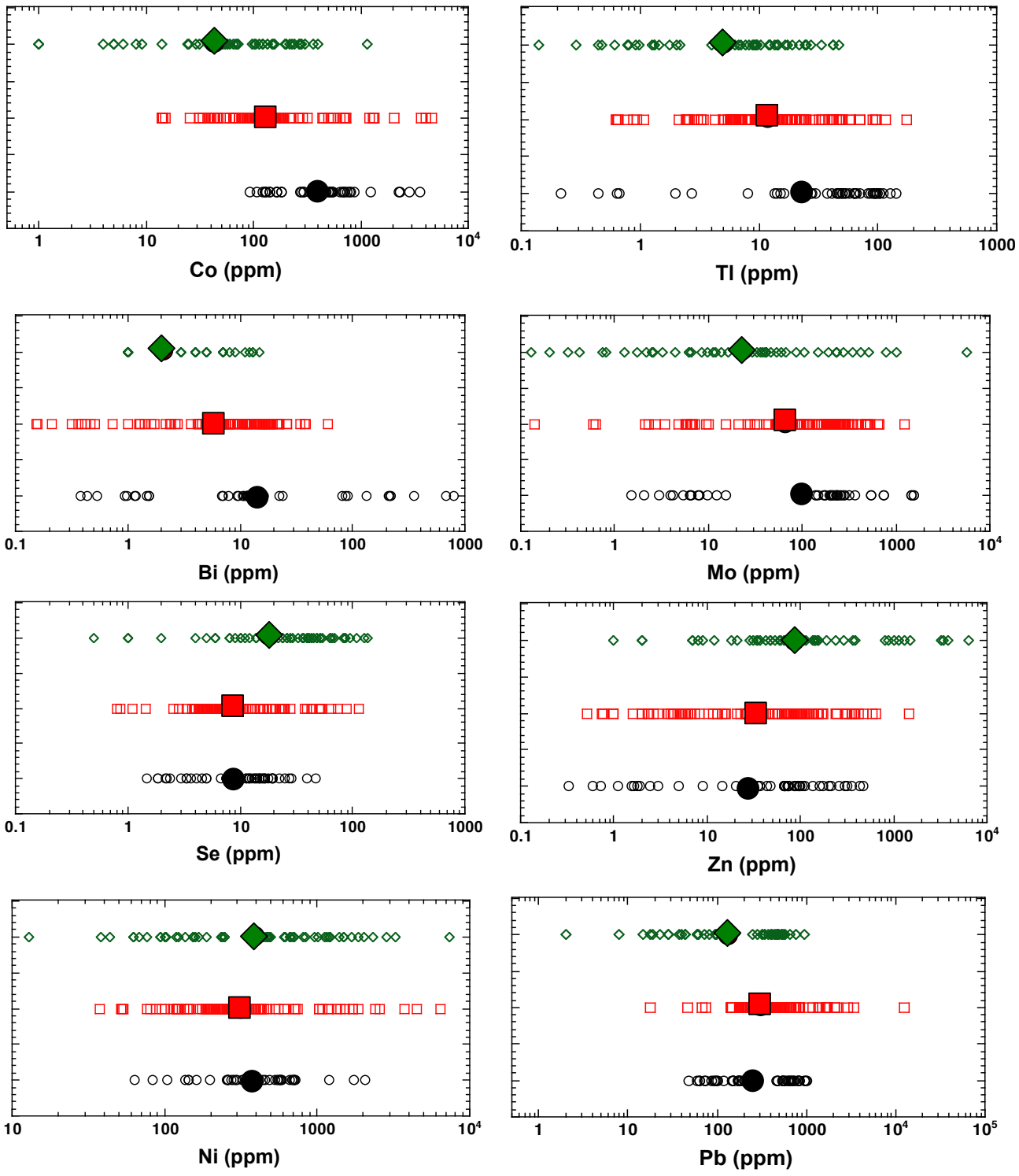
Co (ppm)
Tl (ppm)
Bi (ppm)
Mo (ppm)
Se (ppm)
Zn (ppm)
Ni (ppm)
Pb (ppm)
Velkerri Formation (Mukherjee and Large, 2016)
Barney Creek Formation (Mukherjee and Large, 2017
Wollogorang Formation

b)

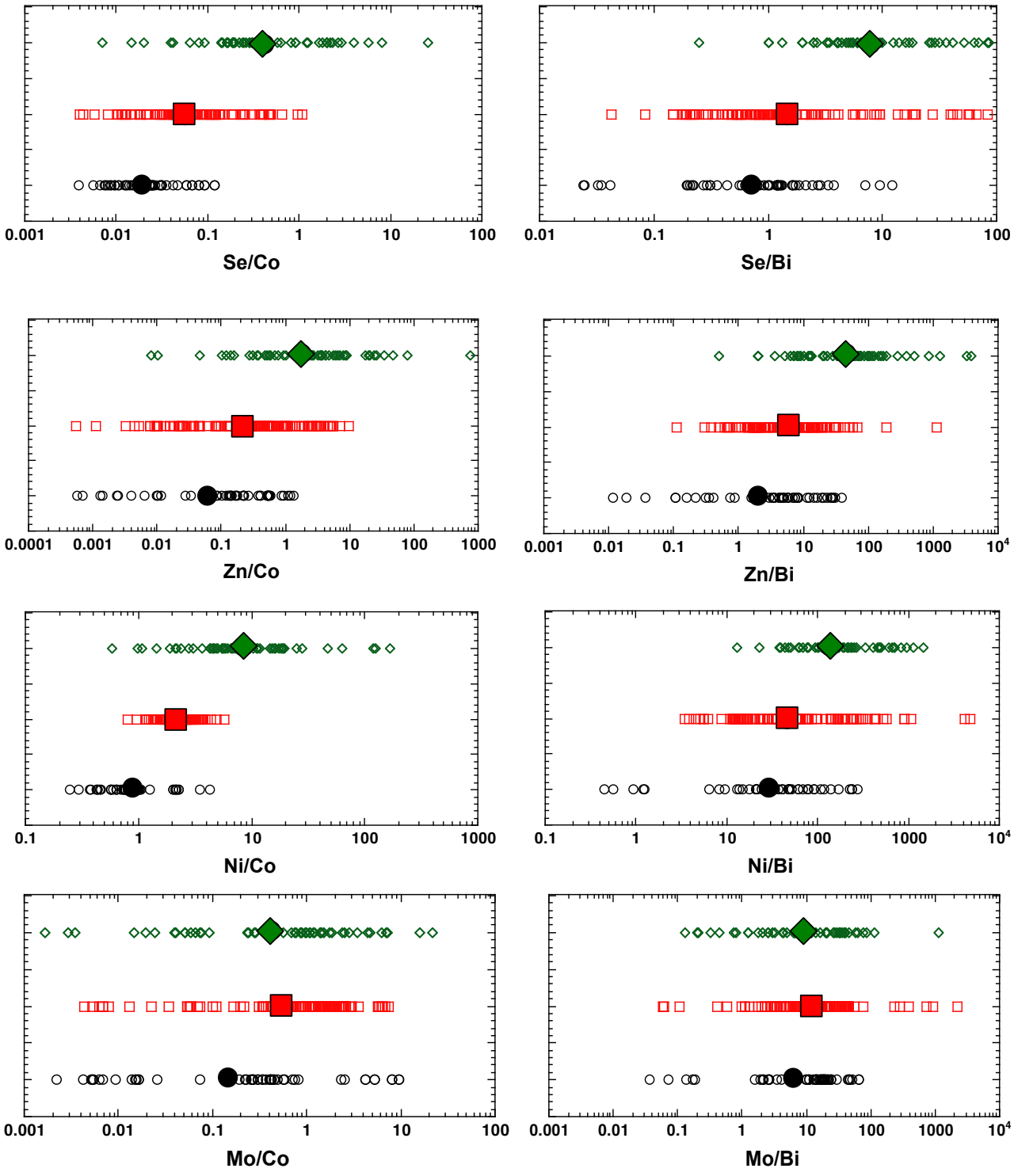

Fig 4.4 a, b Comparison of trace elements in pyrite and their ratios in the three black shale formations

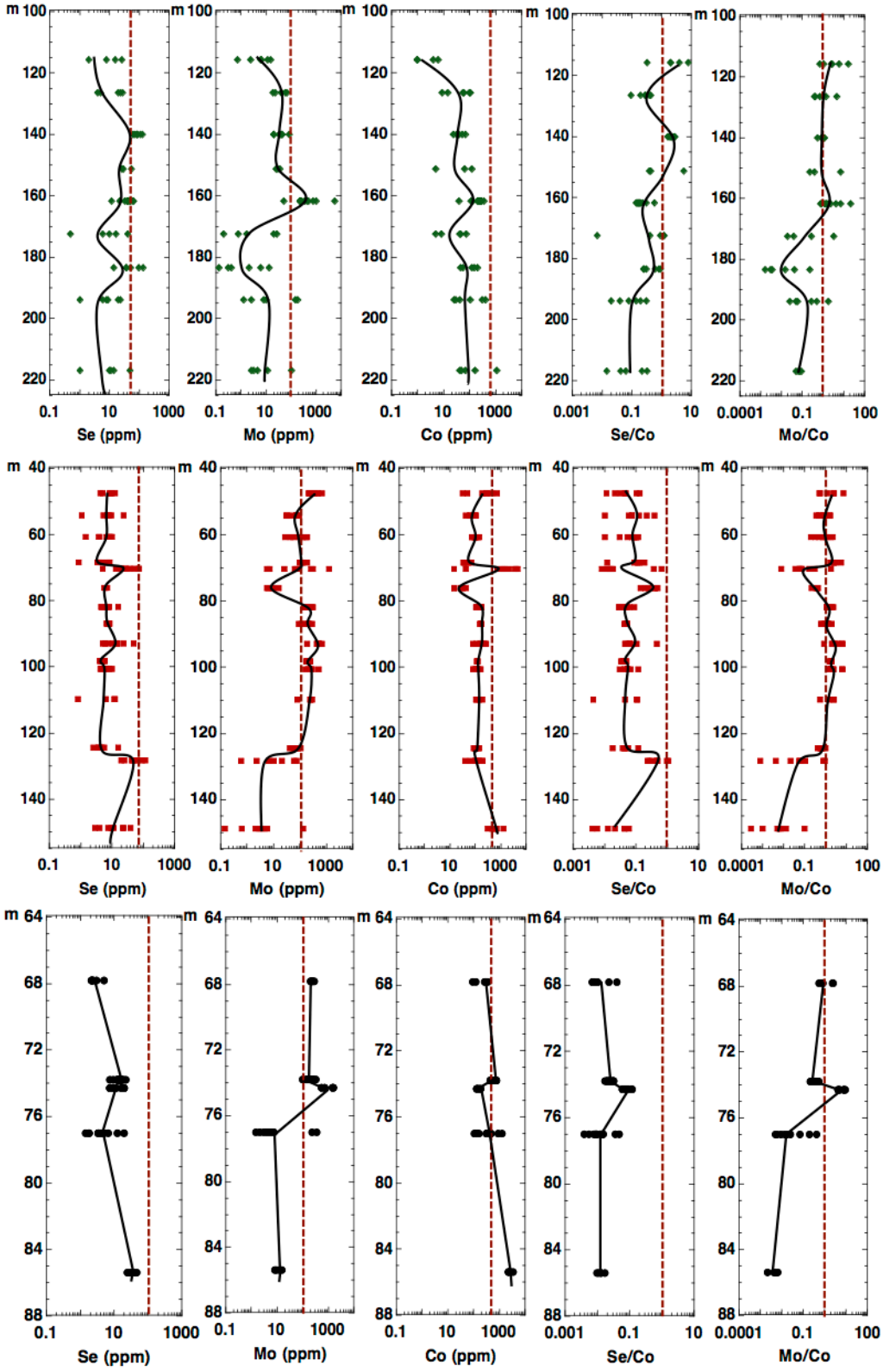

Fig 4.5 Downhole variation of TEs (Se, Mo, Co (in ppm) & Se/Co, Mo/Co) for the Velkerri, (top), Barney Creek (middle) and Wollogorang (bottom) formations; Red dashed line represents global mean value of ~5000 pyrites for Se, Mo, Co (from Large et al., 2014); and unity for Se/Co & Mo/Co (Data source for Velkerri Formation: Mukherjee and Large, 2016 and Barney Creek Formation: Mukherjee and Large, 2017)

Table 4.1 LA-ICP-MS pyrite analyses (geometric mean) for the Wollogorang Formation(n=46), Barney Creek Formation (n=115) and Velkerri Formation (n=55) in ppm; m=meters from top of the drill hole.

Formation	Depth in meters (m)	Co	Ni	Cu	Zn	As	Se	Mo	Tl	Pb	Bi	Data source
Wollogorang Formation	**67.8**	212	320	64	138	936	3	226	78	113	11	This study
Wollogorang Formation	**73.8**	590	511	468	103	2958	14	201	32	666	13	This study
Wollogorang Formation	**74.3**	148	314	110	75	2027	12	871	8	217	80	This study
Wollogorang Formation	**77**	354	179	744	4	8472	4	9	62	169	1.29	This study
Wollogorang Formation	**85.4**	2596	1102	964	1	6938	32	12	1	148	113	This study
Barney Creek Formation	**47.5**	183	475	109	11	965	8	357	21	970	3	Mukherjee and Large, 2017
Barney Creek Formation	**54.2**	76	218	59	323	262	7	59	3	236	14	Mukherjee and Large, 2017
Barney Creek Formation	**60.8**	94	242	102	229	393	6	79	10	222	15	Mukherjee and Large, 2017
Barney Creek Formation	**68.5**	53	141	92	88	375	4	106	5	114	11	Mukherjee and Large, 2017
Barney Creek Formation	**70.2**	775	1258	770	17	1587	24	71	23	1474	4	Mukherjee and Large, 2017
Barney Creek Formation	**76.1**	22	73	44	2	269	6	8	10	323	0.425	Mukherjee and Large, 2017
Barney Creek Formation	**81.9**	148	354	102	96	346	6	215	7	380	6	Mukherjee and Large, 2017
Barney Creek Formation	**86.8**	158	335	92	11	1192	8	169	15	462	9	Mukherjee and Large, 2017
Barney Creek Formation	**93**	160	479	293	45	1769	13	446	9	838	11	Mukherjee and Large, 2017
Barney Creek Formation	**98.3**	118	202	136	29	972	5	202	16	428	5	Mukherjee and Large, 2017
Barney Creek Formation	**100.7**	112	275	108	74	380	6	274	18	493	8	Mukherjee and Large, 2017
Barney Creek Formation	**109.8**	133	271	44	159	307	5	194	12	288	19	Mukherjee and Large, 2017
Barney Creek Formation	**124.5**	108	231	43	21	1473	5	67	51	274	18	Mukherjee and Large, 2017
Barney Creek Formation	**128.4**	106	170	121	9	1321	49	5	1	190	2	Mukherjee and Large, 2017
Barney Creek Formation	**148.8**	572	1246	240	5	7442	11	3	53	933	4	Mukherjee and Large, 2017
Velkerri Formation	**115.7**	2	85	48	22	20	5	5	0.412	5	1	Mukherjee and Large, 2016
Velkerri Formation	**126.3**	40	223	41	47	36	10	38	1	80	3	Mukherjee and Large, 2016
Velkerri Formation	**140.1**	40	685	100	107	7512	87	37	7	404	1	Mukherjee and Large, 2016
Velkerri Formation	**151.2**	34	444	64	1560	821	34	30	10	121	3	Mukherjee and Large, 2016
Velkerri Formation	**161.8**	187	1671	176	397	605	38	415	18	371	8	Mukherjee and Large, 2016
Velkerri Formation	**172.4**	22	144	39	118	1921	7	3	10	111	1	Mukherjee and Large, 2016
Velkerri Formation	**183.4**	105	504	104	8	4787	48	1	13	384	2	Mukherjee and Large, 2016
Velkerri Formation	**193.9**	85	260	112	165	173	8	14	4	97	2	Mukherjee and Large, 2016
Velkerri Formation	**216.9**	122	236	54	81	380	9	9	3	56	2	Mukherjee and Large, 2016

Table 4.2 Multiplicative standard deviation for the Wollogorang Formation (n=46), Barney Creek Formation (n=115) and Velkerri Formation (n=55) in ppm

Formation	Depth in meters (m)	Co	Ni	Cu	Zn	As	Se	Mo	Tl	Pb	Bi
Wollogorang Formation	**67.8**	1.27	1.09	1.11	1.84	1.07	1.15	1.06	1.19	1.28	1.04
Wollogorang Formation	**73.8**	1.09	1.12	1.32	1.33	1.06	1.11	1.14	1.31	1.10	1.08
Wollogorang Formation	**74.3**	1.07	1.08	1.21	1.04	1.28	1.18	1.24	3.11	1.52	2.12
Wollogorang Formation	**77**	1.37	1.34	1.49	2.46	1.37	1.39	2.12	1.19	1.37	1.51
Wollogorang Formation	**85.4**	1.09	1.28	1.30	3.08	1.19	1.12	1.13	1.88	1.19	1.20
Barney Creek Formation	**47.5**	1.65	1.57	1.26	2.68	1.49	1.18	1.18	1.38	1.68	2.74
Barney Creek Formation	**54.2**	1.16	1.14	1.31	1.14	1.13	1.49	1.22	1.80	1.20	1.11
Barney Creek Formation	**60.8**	1.11	1.11	1.31	1.29	1.14	1.33	1.32	1.48	1.10	1.15
Barney Creek Formation	**68.5**	1.22	1.11	1.12	1.56	1.21	1.38	1.21	1.36	1.65	2.32
Barney Creek Formation	**70.2**	2.46	2.04	1.55	3.07	1.33	1.41	2.15	1.60	1.39	2.42
Barney Creek Formation	**76.1**	1.23	1.17	1.03	1.25	1.15	1.03	1.17	1.07	1.02	1.14
Barney Creek Formation	**81.9**	1.08	1.10	1.06	1.42	1.14	1.15	1.10	1.10	1.06	1.05
Barney Creek Formation	**86.8**	1.02	1.02	1.12	1.52	1.07	1.04	1.19	1.06	1.04	1.15
Barney Creek Formation	**93**	1.19	1.28	1.49	1.59	1.53	1.39	1.17	1.13	1.17	1.07
Barney Creek Formation	**98.3**	1.01	1.02	1.05	1.11	1.04	1.07	1.05	1.04	1.03	1.05
Barney Creek Formation	**100.7**	1.11	1.14	1.15	1.18	1.17	1.13	1.18	1.19	1.07	1.20
Barney Creek Formation	**109.8**	1.11	1.05	1.08	1.37	1.08	1.76	1.31	2.14	1.08	1.09
Barney Creek Formation	**124.5**	1.09	1.08	1.23	1.25	1.16	1.31	1.16	1.09	1.11	1.03
Barney Creek Formation	**128.4**	1.26	1.35	1.52	2.35	1.56	1.29	3.09	1.97	1.25	1.51
Barney Creek Formation	**148.8**	1.19	1.19	1.25	1.08	1.46	1.48	2.34	1.38	1.24	1.31
Velkerri Formation	**115.7**	1.43	1.54	2.36	1.51	1.93	1.66	1.63	2.10	1.55	1.00
Velkerri Formation	**126.3**	1.56	1.42	1.36	1.14	1.33	1.51	1.24	1.27	1.23	1.25
Velkerri Formation	**140.1**	1.16	1.16	1.24	1.39	1.10	1.11	1.24	1.10	1.10	1.00
Velkerri Formation	**151.2**	2.09	1.83	1.15	1.41	1.26	1.19	1.08	1.94	1.83	1.55
Velkerri Formation	**161.8**	1.31	1.47	1.52	1.93	1.30	1.24	1.66	1.27	1.32	1.31
Velkerri Formation	**172.4**	1.67	1.72	1.41	2.60	2.86	2.06	2.50	1.25	1.67	1.14
Velkerri Formation	**183.4**	1.30	1.43	1.67	2.31	2.12	1.42	2.21	1.27	1.54	1.31
Velkerri Formation	**193.9**	1.68	1.68	2.40	1.53	2.19	1.64	2.46	2.13	1.63	1.41
Velkerri Formation	**216.9**	1.79	1.75	2.21	2.45	2.20	1.84	1.94	2.36	1.81	1.51

Table 4.3 LA-ICP-MS pyrite analyses (geometric mean) for all three black shale formations

Formation	Age	Co	Ni	Cu	Zn	As	Se	Mo	Tl	Pb	Bi	Se/Co	Ni/Co	Zn/Co	Mo/Co	Se/Bi	Ni/Bi	Zn/Bi	Mo/Bi
Upper Velkerri (n=55)	~1360 Ma	48	387	81	96	502	19	20	5	137	2	0.40	8.00	1.98	0.42	8.29	166	41	9
Barney Creek (n=115)	~1640 Ma	138	318	120	33	772	8	79	11	419	6	0.06	2.30	0.24	0.58	1.36	51	5	13
Wollogorang (n=46)	~1730 Ma	457	377	377	28	3527	9	77	20	254	13	0.02	0.83	0.06	0.17	0.71	30.03	2.24	6.14

Table 4.4 Staistical t-test for equality of means in the three black shale formations; VF: Velkerri Formation, BCF: Barney Creek Formation, WF: Wollogorang Formation (See supplementary information for details)

-critical	p-value	Hypotheses of equal means (μ1=μ2)	Reason*	Difference in means
1.98	0.00	Reject	-(t-critical) > t-value	significant
1.98	0.00	Reject	-(t-critical) > t-value	significant
1.98	0.74	Cannot reject	t-value < (t-critical)	insignificant
1.98	0.00	Reject	t-value > (t-critical)	significant
1.98	0.00	Reject	t-value > (t-critical)	significant
1.98	0.58	Cannot reject	-(t-critical) < t-value	insignificant
1.98	0.32	Cannot reject	t-value < (t-critical)	insignificant
1.98	0.90	Cannot reject	t-value < (t-critical)	insignificant
1.98	0.20	Cannot reject	-(t-critical) < t-value	insignificant
1.98	0.00	Reject	t-value > (t-critical)	significant
1.98	0.00	Reject	t-value > (t-critical)	significant
1.98	0.65	Cannot reject	t-value < (t-critical)	insignificant
1.98	0.00	Reject	-(t-critical) > t-value	significant
1.98	0.00	Reject	-(t-critical) > t-value	significant
1.98	0.00	Reject	-(t-critical) > t-value	significant
1.98	0.00	Reject	-(t-critical) > t-value	significant
1.98	0.00	Reject	-(t-critical) > t-value	significant
1.98	0.02	Reject	-(t-critical) > t-value	significant

means if -(t-critical) > t-value > t-critical and p < 0.10 (α)

Table 4.5 Black shale matrix analyses of Ti, Zr, Cr, Th in ppm and their ratios (Data source: this study)

Formation	Depth in meters	Ti	Cr	Zr	Th	Ti/Zr	Th/Cr	Data source
Velkerri Formation	115.7	254.43	1.00	67.87	5.66	3.75	5.66	This study
Velkerri Formation	126.3	1156.76	55.71	74.27	7.72	15.57	0.14	This study
Velkerri Formation	140.1	8746.43	95.92	186.07	36.59	47.01	0.38	This study
Velkerri Formation	151.2	1609.06	88.71	109.70	3.01	14.67	0.03	This study
Velkerri Formation	151.2	1407.51	92.83	44.21	1.52	31.83	0.02	This study
Velkerri Formation	151.2	111.99	17.36	7.18	5.20	15.60	0.30	This study
Velkerri Formation	151.2	1042.86	66.30	53.70	3.25	19.42	0.05	This study
Velkerri Formation	161.8	2705.62	45.95	202.31	12.76	13.37	0.28	This study
Velkerri Formation	172.4	713.61	1879.43	72.14	15.72	9.89	0.01	This study
Velkerri Formation	183.4	890.25	1.00	43.49	3.59	20.47	3.59	This study
Velkerri Formation	193.9	4580.01	419.61	194.32	8.65	23.57	0.02	This study
Velkerri Formation	216.9	3947.04	91.32	73.88	7.96	53.43	0.09	This study
					Mean	**22.38**	**0.88**	
Barney Creek Formation	47.50	4587.66	5.60	206.66	61.56	22.20	10.99	This study
Barney Creek Formation	54.20	2149.17	57.77	229.04	16.80	9.38	0.29	This study
Barney Creek Formation	60.80	4409.26	42.65	93.34	10.84	47.24	0.25	This study
Barney Creek Formation	68.50	1038.77	20.66	38.61	6.96	26.90	0.34	This study
Barney Creek Formation	70.20	77793.00	81.04	424.32	24.97	183.33	0.31	This study
Barney Creek Formation	76.10	19067.05	129.94	649.72	72.99	29.35	0.56	This study
Barney Creek Formation	81.90	3001.76	64.46	139.79	14.89	21.47	0.23	This study
Barney Creek Formation	86.80	4728.15	62.08	107.23	26.64	44.09	0.43	This study
Barney Creek Formation	93.00	3864.95	87.86	150.62	18.39	25.66	0.21	This study
Barney Creek Formation	98.30	4351.58	58.97	269.40	29.19	16.15	0.50	This study
Barney Creek Formation	100.70	3430.80	70.19	133.39	19.57	25.72	0.28	This study
Barney Creek Formation	109.80	2294.94	44.83	100.62	20.59	22.81	0.46	This study
Barney Creek Formation	124.50	1106.57	24.27	30.34	4.97	36.47	0.20	This study
Barney Creek Formation	128.40	1751.79	80.22	160.18	26.67	10.94	0.33	This study
Barney Creek Formation	136.50	20401.09	90.28	293.52	32.43	69.50	0.36	This study
Barney Creek Formation	148.80	4484.17	213.02	698.77	196.19	6.42	0.92	This study
					Mean	**37.35**	**1.04**	
Wollogorang Formation	67.8	7108.46	71.76	340.36	28.81	20.88	0.40	This study
Wollogorang Formation	73.8	818.41	42.32	49.26	7.32	16.61	0.17	This study
Wollogorang Formation	74.3	527.13	30.96	61.57	3.01	8.56	0.10	This study
Wollogorang Formation	77	468.06	1.00	7.85	1.15	59.64	1.15	This study
Wollogorang Formation	85.4	660.50	27.28	38.30	6.41	17.25	0.23	This study
					Mean	**24.59**	**0.41**	

4.4.3 SHRIMP-SI pyrite sulphur isotopes analyses

A total of 124 sedimentary pyrite spot analyses were obtained for the three black shale formations (Wollogorang Formation: 31; Barney Creek Formation: 31; Velkerri Formation: 62) (Table 4.6). The $\delta^{34}S_{VCDT}$ values of the pyrites from the Wollogorang Formation range between -29.4 to +9.5‰ with an average of -5.03 ± 13.62‰ (n = 31; 1SD) (Table 4.6). Pyrites from the Barney Creek Formation have a wider range of $d^{34}S_{VCDT}$ (-13.8 to +41.8 ‰) with an average of +19.88 ± 17.7‰ (n = 31; 1SD) (Table 4.6). The $\delta^{34}S_{VCDT}$ values of pyrites from the Velkerri Formation range from -14.2 to +65.6‰ with an average of +26.9 ± 16.5‰ (n = 62; 1SD), slightly higher than pyrites from the Barney Creek Fm. (Table 4.6). The $D^{33}S$ values of pyrites from all three formations are low, with values close to zero and an average of 0.36 ± 0.51‰ (n = 31; 1SD), 0.08 ± 0.28‰ (n = 31; 1SD) , and 0.01 ± 0.18‰ (n = 62; 1SD) for the Wollogorang, Barney Creek, and Velkerri Formations, respectively (Table 4.6).

Table 4.6 SHRIMPI-SI pyrite analyses for all three black shale formations in ‰ (Data source: this study)

SPOT #	$\delta^{33}S_{VCDT}$	± Internal error (2σ)	$\delta^{34}S_{VCDT}$	± Internal error (2σ)	$\Delta^{33}S$	± Internal error (2σ)	^{32}S cps (median)	^{33}S cps (median)	^{34}S cps (median)	Sets, scans
Velkerri Formation										
172.4-08-2.1	16.03	0.09	31.74	0.03	-0.20	0.10	9.5E+08	7.5E+06	4.3E+07	2, 10
172.4-08-1.1	8.60	0.07	17.45	0.04	-0.35	0.08	5.5E+08	4.4E+06	2.5E+07	2, 10
172.4-08-3.1	18.01	0.08	35.55	0.03	-0.14	0.08	1.1E+09	8.8E+06	5.0E+07	2, 10
161.8-03-1	7.92	0.15	15.74	0.04	-0.15	0.15	8.7E+08	6.8E+06	3.8E+07	2, 10
161.8-03-2	9.10	0.09	17.77	0.03	-0.01	0.09	1.0E+09	8.0E+06	4.5E+07	2, 10
161.8-03-5	7.95	0.13	16.21	0.03	-0.36	0.13	9.0E+08	7.1E+06	4.0E+07	2, 10
161.8-03-6	8.35	0.10	16.31	0.03	-0.01	0.11	9.1E+08	7.2E+06	4.0E+07	2, 10
144.3-01	12.49	0.10	24.43	0.03	-0.02	0.11	9.5E+08	7.5E+06	4.2E+07	2, 10
144.3-02	15.07	0.08	29.46	0.03	0.01	0.09	9.5E+08	7.6E+06	4.3E+07	2, 10
115.2_1	23.41	0.24	45.58	0.04	0.19	0.26	5.4E+08	4.3E+06	2.5E+07	1, 10
115.2_2	24.07	0.30	45.77	0.04	0.76	0.33	5.5E+08	4.4E+06	2.5E+07	1, 10
115.2_3	23.46	0.25	45.78	0.04	0.14	0.29	5.5E+08	4.4E+06	2.5E+07	1, 10
115.2_4	15.40	0.32	30.34	0.05	-0.11	0.33	5.6E+08	4.5E+06	2.5E+07	1, 10
115.2_5	22.25	0.16	43.95	0.04	-0.15	0.17	5.6E+08	4.5E+06	2.6E+07	1, 10
115.2_6	23.29	0.33	46.05	0.03	-0.16	0.34	5.4E+08	4.4E+06	2.5E+07	1, 10
140.1_1	11.70	0.21	22.40	0.04	0.22	0.22	5.9E+08	4.7E+06	2.6E+07	1, 10
140.1_2	11.35	0.20	22.07	0.04	0.04	0.21	5.8E+08	4.6E+06	2.6E+07	1, 10
140.1_3	11.07	0.41	22.16	0.04	-0.28	0.41	5.9E+08	4.7E+06	2.6E+07	1, 10
140.1_4	11.04	0.15	21.98	0.04	-0.22	0.16	5.9E+08	4.7E+06	2.6E+07	1, 10
140.1_5	11.46	0.22	22.50	0.04	-0.07	0.23	5.5E+08	4.4E+06	2.5E+07	1, 10
140.1_6	11.78	0.29	23.00	0.04	0.00	0.32	5.9E+08	4.7E+06	2.6E+07	1, 10
193.9-01	12.95	0.14	24.90	0.03	0.21	0.14	9.1E+08	7.3E+06	4.1E+07	2, 10
193.9-02	10.01	0.11	19.15	0.03	0.19	0.11	9.7E+08	7.7E+06	4.3E+07	2, 10
183.4-01	21.73	0.06	42.30	0.03	0.17	0.06	1.1E+09	8.7E+06	5.0E+07	2, 10
183.4-02	19.49	0.13	37.72	0.03	0.24	0.14	1.1E+09	8.8E+06	5.0E+07	2, 10
183.4-03	19.78	0.08	38.50	0.03	0.14	0.08	1.0E+09	8.0E+06	4.5E+07	2, 10
183.4-04	20.03	0.10	39.18	0.03	0.05	0.10	1.1E+09	8.7E+06	5.0E+07	2, 10
183.4-05	23.00	0.16	44.94	0.03	0.11	0.17	9.9E+08	7.9E+06	4.5E+07	2, 10
183.4-06	19.55	0.09	37.93	0.03	0.19	0.10	1.0E+09	8.2E+06	4.7E+07	2, 10
183.4-07	18.19	0.19	35.37	0.03	0.13	0.20	7.0E+08	5.6E+06	3.2E+07	2, 10
126.3-01	-3.06	0.14	-5.92	0.03	0.00	0.14	1.0E+09	8.1E+06	4.5E+07	2, 10
126.3-02	12.08	0.07	23.46	0.03	0.07	0.07	1.2E+09	9.2E+06	5.2E+07	2, 10
126.3-03	12.79	0.11	25.08	0.02	-0.05	0.12	1.2E+09	9.2E+06	5.2E+07	2, 10
126.3-04	2.62	0.10	4.95	0.02	0.07	0.10	9.7E+08	7.7E+06	4.3E+07	2, 10
126.3-05	-4.33	0.12	-8.23	0.03	-0.08	0.13	9.7E+08	7.6E+06	4.2E+07	2, 10
126.3-06	12.50	0.11	24.35	0.03	0.03	0.11	9.2E+08	7.3E+06	4.1E+07	2, 10
126.3-07	-3.26	0.14	-6.64	0.03	0.17	0.16	9.8E+08	7.7E+06	4.3E+07	2, 10
126.3-07	7.87	0.08	15.26	0.03	0.04	0.09	9.7E+08	7.6E+06	4.3E+07	2, 10
374.4-01	22.50	0.08	43.92	0.02	0.11	0.09	9.3E+08	7.4E+06	4.2E+07	2, 10
374.4-2	24.35	0.11	47.75	0.03	0.04	0.12	9.7E+08	7.8E+06	4.4E+07	2, 10
374.4-3	33.29	0.12	65.59	0.02	0.03	0.13	9.9E+08	8.1E+06	4.6E+07	2, 10
374.4-4	24.91	0.10	48.56	0.03	0.19	0.11	1.1E+09	8.6E+06	4.9E+07	2, 10
374.4-5	22.75	0.13	44.26	0.03	0.19	0.15	9.9E+08	8.0E+06	4.5E+07	2, 10
374.4-6	22.72	0.12	44.10	0.03	0.24	0.13	1.0E+09	8.2E+06	4.7E+07	2, 10
374.4-7	24.48	0.12	48.02	0.03	0.03	0.13	9.8E+08	7.9E+06	4.5E+07	2, 10
374.4-8	24.79	0.06	48.37	0.03	0.16	0.06	1.0E+09	8.3E+06	4.7E+07	2, 10
374.4-9	-7.36	0.07	-14.19	0.03	-0.02	0.07	1.1E+09	8.5E+06	4.7E+07	2, 10
374.4-10	26.93	0.09	52.79	0.03	0.08	0.10	1.0E+09	8.1E+06	4.6E+07	2, 10
183.4-01	12.28	0.09	24.14	0.03	-0.08	0.09	1.1E+09	8.4E+06	4.8E+07	2, 10
183.4-02	11.35	0.10	22.32	0.02	-0.08	0.11	1.4E+09	1.1E+07	6.4E+07	2, 10
151.2-01	11.83	0.24	22.89	0.03	0.11	0.25	5.7E+08	4.5E+06	2.5E+07	2, 10
151.2-02	13.54	0.08	26.68	0.03	-0.12	0.07	1.0E+09	8.0E+06	4.5E+07	2, 10
151.2-03	11.11	0.11	21.72	0.03	-0.01	0.12	7.2E+08	5.7E+06	3.2E+07	2, 10
151.2-04	12.15	0.10	23.80	0.03	-0.04	0.10	7.7E+08	6.1E+06	3.5E+07	2, 10
151.2-05	13.55	0.19	26.35	0.03	0.06	0.19	7.1E+08	5.7E+06	3.2E+07	2, 10
328.1-01	2.05	0.09	4.03	0.03	-0.03	0.09	9.3E+08	7.3E+06	4.1E+07	2, 10
328.1-02	3.57	0.13	7.29	0.02	-0.18	0.13	1.1E+09	8.7E+06	4.9E+07	2, 10
328.1-03	3.18	0.07	6.54	0.04	-0.19	0.07	8.1E+08	6.4E+06	3.6E+07	2, 10
328.1-04	2.02	0.11	4.03	0.04	-0.05	0.11	7.7E+08	6.0E+06	3.4E+07	2, 10
316.8_3	7.23	0.16	14.81	0.03	-0.37	0.16	6.3E+08	4.9E+06	2.8E+07	1, 10
316.8_1	7.58	0.15	14.98	0.04	-0.10	0.17	6.4E+08	5.1E+06	2.8E+07	1, 10
316.8_2	14.52	0.15	28.65	0.04	-0.14	0.15	5.0E+08	4.0E+06	2.3E+07	1, 10
		Mean	**26.87**		**0.01**					
		Std. Dev	**16.48**		**0.18**					

Table 4.6 SHRIMPI-SI pyrite analyses for all three black shale formations in ‰ (Data source: this study)

SPOT #	$\delta^{33}S_{VCDT}$	± Internal error (2σ)	$\delta^{34}S_{VCDT}$	± Internal error (2σ)	$\Delta^{33}S$	± Internal error (2σ)	^{32}S cps (median)	^{33}S cps (median)	^{34}S cps (median)	Sets, scans
Barney Creek Formation										
MBX_47.50_B1	-2.13	0.15	-4.76	0.05	0.33	0.15	6.2E+08	4.8E+06	2.7E+07	1, 10
MBX_47.50_B2	-3.30	0.17	-6.83	0.04	0.23	0.18	7.0E+08	5.5E+06	3.0E+07	1, 10
MBX_47.50_B3	-2.82	0.31	-5.28	0.04	-0.09	0.33	6.1E+08	4.8E+06	2.7E+07	1, 10
MBX_47.50_B4	4.39	0.32	8.83	0.04	-0.15	0.34	5.8E+08	4.5E+06	2.5E+07	1, 10
MBX_47.50_B5	7.41	0.11	14.71	0.04	-0.14	0.11	5.7E+08	4.5E+06	2.5E+07	1, 10
MBX_47.50_B6	-7.17	0.32	-13.79	0.05	-0.05	0.34	5.7E+08	4.5E+06	2.5E+07	1, 10
MBX124.5_1	17.92	0.25	34.68	0.04	0.21	0.25	4.6E+08	3.6E+06	2.1E+07	1, 10
MBX22.7_2	4.18	0.55	7.79	0.12	0.17	0.55	1.1E+08	8.7E+05	4.9E+06	1, 10
MBX22.7_4	5.93	0.19	12.01	0.04	-0.23	0.20	4.6E+08	3.6E+06	2.0E+07	1, 10
MBX30.10_7B	13.76	0.18	26.50	0.03	0.20	0.20	6.0E+08	4.8E+06	2.7E+07	1, 10
MBX30.10_1B	8.97	0.17	17.11	0.03	0.19	0.19	6.2E+08	4.9E+06	2.7E+07	1, 10
MBX30.10_2B	9.76	0.31	18.30	0.03	0.38	0.34	6.2E+08	4.9E+06	2.8E+07	1, 10
MBX30.10_3B	10.06	0.17	19.84	0.03	-0.11	0.18	6.5E+08	5.2E+06	2.9E+07	1, 10
MBX30.10_4B	-0.10	0.12	0.17	0.04	-0.19	0.14	6.2E+08	4.9E+06	2.7E+07	1, 10
MBX30.10_5B	-6.72	0.45	-12.88	0.04	-0.06	0.49	6.4E+08	5.0E+06	2.8E+07	1, 10
MBX30.10_6B	-4.80	0.29	-9.35	0.03	0.03	0.31	6.3E+08	4.9E+06	2.7E+07	1, 10
MBX-76.10_1	17.73	0.15	33.55	0.06	0.59	0.17	3.8E+08	3.0E+06	1.7E+07	1, 6
MBX-76.10_2	17.87	0.31	34.59	0.08	0.20	0.36	3.5E+08	2.8E+06	1.6E+07	1, 6
MBX-76.10_3	19.17	0.44	36.35	0.07	0.61	0.53	3.6E+08	2.9E+06	1.6E+07	1, 6
MBX-76.10_4	18.47	0.21	35.76	0.07	0.21	0.20	3.7E+08	2.9E+06	1.7E+07	1, 6
MBX-76.10_5	18.08	0.05	35.45	0.07	-0.02	0.06	3.6E+08	2.9E+06	1.6E+07	1, 6
MBX-76.10_6	16.69	0.12	32.33	0.06	0.17	0.12	3.7E+08	2.9E+06	1.7E+07	1, 6
MBX-76.10_7	17.33	0.41	33.69	0.08	0.11	0.47	3.6E+08	2.9E+06	1.6E+07	1, 6
MBX-76.10_8	16.47	0.06	32.12	0.08	0.06	0.06	3.7E+08	2.9E+06	1.7E+07	1, 6
MBX-76.10_9	17.39	0.14	33.06	0.08	0.50	0.14	3.6E+08	2.9E+06	1.6E+07	1, 6
MBX98.30_1	19.43	0.36	37.21	0.08	0.44	0.41	2.5E+08	2.0E+06	1.1E+07	1, 6
MBX98.30_2	11.69	0.37	22.50	0.10	0.17	0.38	2.7E+08	2.1E+06	1.2E+07	1, 6
MBX98.30_2B	10.52	0.21	21.85	0.07	-0.67	0.24	2.7E+08	2.1E+06	1.2E+07	1, 6
MBX98.30_4	20.24	0.29	39.89	0.06	-0.10	0.36	2.9E+08	2.3E+06	1.3E+07	1, 6
MBX98.30_5	19.94	0.35	39.23	0.10	-0.07	0.43	2.0E+08	1.6E+06	9.1E+06	1, 6
MBX98.30_6	20.99	0.98	41.80	0.13	-0.32	1.15	1.6E+08	1.2E+06	7.1E+06	1, 6
		Mean	**19.88**		**0.08**					
		Std. Dev	**17.74**		**0.28**					

Table 4.6 SHRIMPI-SI pyrite analyses for all three black shale formations in ‰ (Data source: this study)

SPOT #	$\delta^{33}S_{VCDT}$	± Internal error (2σ)	$\delta^{34}S_{VCDT}$	± Internal error (2σ)	$\Delta^{33}S$	± Internal error (2σ)	^{32}S cps (median)	^{33}S cps (median)	^{34}S cps (median)	Sets, scans
Wollogorang Formation										
MTY_67.8_1	3.84	0.10	2.47	0.04	2.57	0.09	5.8E+08	4.6E+06	2.6E+07	1, 10
MTY_70.4_1	2.10	0.10	4.19	0.04	-0.05	0.10	5.7E+08	4.5E+06	2.5E+07	1, 10
MTY_70.4_B2	-1.62	0.24	-3.32	0.04	0.09	0.25	5.4E+08	4.2E+06	2.3E+07	1, 10
MTY_70.4_B3	-1.38	0.24	-2.21	0.03	-0.24	0.26	5.7E+08	4.4E+06	2.5E+07	1, 10
MTY_70.4_B4	-0.16	0.27	-1.10	0.04	0.41	0.28	5.4E+08	4.2E+06	2.4E+07	1, 10
MTY_70.4_B5	-0.61	0.14	-1.04	0.04	-0.08	0.15	5.7E+08	4.4E+06	2.5E+07	1, 10
MTY_70.4_B6	-2.47	0.25	-4.63	0.04	-0.08	0.29	5.6E+08	4.4E+06	2.4E+07	1, 10
MTY_77_1	-13.79	0.18	-27.92	0.04	0.69	0.18	5.3E+08	4.1E+06	2.3E+07	1, 10
MTY_77_10	-12.65	0.10	-25.57	0.05	0.60	0.10	4.3E+08	3.3E+06	1.8E+07	1, 10
MTY_77_11	1.45	0.10	1.24	0.04	0.81	0.11	4.7E+08	3.7E+06	2.1E+07	1, 10
MTY_77_12	-13.98	0.26	-28.24	0.04	0.67	0.28	5.8E+08	4.5E+06	2.5E+07	1, 10
MTY_77_2	-12.70	0.15	-25.59	0.04	0.56	0.15	5.8E+08	4.5E+06	2.5E+07	1, 10
MTY_77_3	-8.27	0.22	-16.63	0.04	0.33	0.23	5.5E+08	4.3E+06	2.4E+07	1, 10
MTY_77_4	2.99	0.10	5.26	0.04	0.28	0.10	5.5E+08	4.3E+06	2.4E+07	1, 10
MTY_77_5	2.16	0.15	3.85	0.04	0.18	0.16	5.1E+08	4.0E+06	2.2E+07	1, 10
MTY_77_6	-13.74	0.13	-27.07	0.04	0.29	0.14	5.1E+08	3.9E+06	2.2E+07	1, 10
MTY_77_7	-9.30	0.16	-19.25	0.04	0.67	0.17	5.2E+08	4.0E+06	2.2E+07	1, 10
MTY_77_8	-14.70	0.22	-29.44	0.05	0.57	0.23	4.8E+08	3.7E+06	2.1E+07	1, 10
MTY_77_9	-13.15	0.22	-26.78	0.04	0.74	0.24	4.7E+08	3.6E+06	2.0E+07	1, 10
MTY_89_B1	1.89	0.30	3.50	0.03	0.09	0.31	8.4E+08	6.6E+06	3.7E+07	1, 10
MTY_89_B2	3.44	0.19	5.66	0.03	0.53	0.19	8.9E+08	7.0E+06	3.9E+07	1, 10
MTY_89_B3	2.57	0.34	4.45	0.02	0.27	0.37	1.0E+09	8.1E+06	4.5E+07	1, 10
MTY_89_B4	3.22	0.29	5.25	0.03	0.52	0.33	9.7E+08	7.6E+06	4.2E+07	1, 10
MTY_89_B5	2.89	0.24	5.25	0.02	0.19	0.29	1.0E+09	7.9E+06	4.4E+07	1, 10
MTY_89_B6	1.23	0.12	2.69	0.03	-0.16	0.11	8.3E+08	6.5E+06	3.6E+07	1, 10
MT_YOUNG_4	4.82	0.35	9.49	0.03	-0.02	0.32	8.9E+08	7.0E+06	4.0E+07	1, 10
MT_YOUNG_1	3.73	0.29	6.65	0.02	0.34	0.23	9.3E+08	7.3E+06	4.1E+07	1, 10
MT_YOUNG_5	3.16	0.28	5.63	0.03	0.30	0.24	9.2E+08	7.2E+06	4.1E+07	1, 10
MT_YOUNG_6	3.62	0.16	7.10	0.02	0.01	0.09	9.4E+08	7.4E+06	4.1E+07	1, 10
MT_YOUNG_3	2.37	0.33	5.25	0.03	-0.30	0.27	8.9E+08	7.0E+06	3.9E+07	1, 10
MT_YOUNG_2	2.79	0.21	4.90	0.04	0.30	0.13	9.2E+08	7.2E+06	4.1E+07	1, 10
		Mean	**-5.03**		**0.36**					
		Std. Dev	**13.62**		**0.51**					

4.5 Discussion

4.5.1 Factors controlling trace element concentrations in pyrite

The trace element composition of primary marine pyrite is considered to be a reflection of the coexisting seawater at the time the pyrite formed (Large et al., 2014; 2015). The trace element composition of sea water, in turn, is a function of the coeval sources and sinks, and the residence time of the element in seawater. The latter depends critically on the speciation of the element in the ocean under ambient conditions at any given time. This study takes into account the geological factors: oxidative weathering, tectonic setting and composition of source rocks as determinants of the TE source flux. Whereas factors such as areal extent and types of sinks (oxic, sub-oxic, anoxic) and residence time, likely determine the sink flux. Our main focus in this paper is to evaluate whether trace element concentrations in diagenetic pyrites were a function of changes in source fluxes or changes in areal extent of sinks, or both, i.e., to evaluate possible causes for the trace element compositional variations measured in sedimentary pyrites of the three formations.

4.5.1.1 Oxidative weathering

Oxidative weathering on the continents results in the release of redox sensitive trace elements to solution. Trace elements are then transported by rivers to continental margins where they are either sequestered into estuaries or continental margin sediments, or transported to seawater etc. Once in the open ocean, they can be sequestered into pelagic sediments by reduction upon encountering a redox boundary in the water column or sediment-water interface where they may form complexes with organic acids and become incorporated into authigenic sulphides.

Trace elements such as Mo, Zn, Se, Co, Ni, Cu, As are known to be redox-sensitive, (i.e., will generally undergo a change in mobility at oxidizing or reducing geochemical barriers) and are known to respond to changes in atmosphere-ocean redox conditions (Calvert and Pedersen, 1993; Jones and Manning, 1994; Wignall, 1994; Crusius et al., 1996; Dean et al., 1997, 1999; Yarincik et al., 2000; Morford et al., 2001; Pailler et al., 2002; Algeo and Maynard, 2004; Algeo et al., 2009; 2012; Tribovillard et al., 2006; Nishri and Halicz, 2014; Smith and Huyck, 1999) Table 4.7. While some elements are not redox-sensitive sensu stricto (Bi, Pb), their speciation in the water column is controlled by redox conditions of the atmosphere-ocean system (Refer Table 4.7). Not all redox sensitive elements in pyrite can be used to infer atmospheric redox conditions because of partitioning into different phases (organic, detrital) other than pyrite. For instance, Ni and Cu may be adsorbed onto organic complexes and Fe-Mn oxides/hydroxides in the sedimentary process. Silver and Tl are not redox sensitive, however Tl in pyrite can be used to screen out pyrites affected by hydrothermal events (Large et al., 2009; Mukherjee and Large, 2016). Some redox sensitive

elements (Pb, As) in pyrites may not record any oxygenation trend solely due to their abundant supply in the water column (high source flux). Arsenic is particularly problematic due it being relatively more mobile under reducing conditions than other redox sensitive TE (Smedley and Kinniburgh, 2002).

An increase in concentrations of redox sensitive elements Se and Zn from ~1730 Ma to 1360 Ma suggests an increased supply of these elements into the water column via oxidative weathering on land. Decreases in concentrations of Co and Bi can also be used to support the hypothesis that these elements may have been retained, relatively more than other elements, by Fe-Mn hydroxides and oxides, an important product of oxidative weathering on land. The premise on which the hypothesis is based is described below.

Experiments have shown that Fe, Al and Mn hydroxides and oxides, and particularly manganese oxides (Gadde and Laitinen, 1974) are efficient scavengers of trace elements in their cationic form (Jackson, 1998; Huang and Germida, 2002; Sparks, 2003; Violante et al., 2008). It is also known that manganese oxide has a special preference for Co compared to other elements in their cationic/anionic form (Smith, 1999). Further evidence lies in experiments designed to understand interactions of certain elements with manganese hydrooxides/oxides (Murray et al., 1968, 1975) where the elements showed affinity in the following order Mg < Ca < Sr < Ba < Ni < Zn < Mn <-Co. Furthermore, manganese oxides specifically, α-Mn_2O_3, is known to adsorb cobalt much more than Ni, Zn or Cu, according to experiments by McKenzie (1972). Therefore it is possible that the supply of cobalt to the ocean is inhibited by oxidative processes on land where it is retained by oxides/hydroxides on land. (Pickering, 1979; Jackson, 1998; Huang and Germida, 2002; Sparks, 2003; Violante et al., 2008).

Another evidence supporting this hypothesis comes from three different lines of research on Co concentrations though time. Thermodynamic modelling of the concentration of Co in the oceans (Zerkle et al., 2005), Co concentrations in sedimentary pyrite (Large et al., 2014) and Co/Ti in iron formations (Swanner et al., 2014) collectively confirm that Co concentrations in the oceans have decreased through time coinciding with increases in atmospheric pO_2. Where elements like Se and Mo have shown an increase through time in response to oxygenation, Co shows a reverse trend (Large et al., 2014).

Bismuth behaves similar to Co (despite not being strictly redox sensitive) in response to increases in oxygenation. The element Bi enters the marine realm via two main sources; atmospheric inputs i.e., eolian dust of volcanic origin (Lee et al., 1985; 1986) or river influx, both being comparable source materials of Bi (Bertine et al., 1996). Bismuth, owing to its extensive hydrolytic activity and strong particle reactivity, is also retained in oxyhydroxides, particularly manganese phases (Barnes, 1967; Fowler et al., 2010), resulting in very low concentrations of Bi in modern sea water (Bertine et al., 1996). Currently

there is no thermodynamically modelled trend for Bi in the oceans through time. Nevertheless, Large et al. (2014) pointed out that Bi was one of the least abundant trace elements in the ocean today, with a very short residence time (in the order of 20 years; Bertine et al.), 1996 and, like Co, possibly decreased in concentration in pyrite as it was retained by Mn-oxides forming in response to oxidative weathering on land.

Surprisingly, our data shows that Mo concentrations in pyrite decreased from 1730 Ma to 1360 Ma. This is surprising because Mo concentration in shales has been used to track redox changes in the ocean and atmosphere (Scott et al., 2008; Gordon et al., 2008; Kendall et al., 2009; Sahoo et al., 2012) and, whereas most other trace element data indicates an increase in oxygenation of the atmosphere, the Mo concentrations measured in the pyrites studied here seem to suggest a decrease in atmospheric oxygen over this period. It is possible that Mo is retained in the black shale matrix rather than pyrite, causing the values in pyrite to be suppressed in the (~1360 Ma) Velkerri Formation. However, that is not the case for our data. Whole rock values of Mo in the Velkerri Formation have previously been compared to their concentration in pyrite by Mukherjee et al., (2016). Whole rock Mo concentrations range between 2-37 ppm compared to 4-795 ppm in pyrite. The other reason for this surprising behavior of Mo could be a source flux issue i.e., a possibly Mo-rich source for the Tawallah Group. The possibility that Mo could be weathered and mobilized even under mildly oxic weathering conditions (Anbar et al., 2007) and is very sensitive to sulphide oxidation (William and Rickaby, 2012) could also potentially lead to Mo-rich pyrites of the Wollogorang Formation.

This unusual decrease in Mo in pyrite suggests caution when using a single particular trace element concentration or isotope ratio as a proxy for tracking changes in redox conditions. Another way of tackling this issue is to use ratios of two elements that exhibit antithetic behavior i.e., one element that might be expected to increase in concentration in pyrite with atmosphere oxidation, and the other that might be expected to decrease in concentration in pyrite. Thus, a more robust way to evaluate atmosphere oxygenation would be to couple certain trace elements that show enrichments in pyrite under conditions of increasing oxygenation (e.g., Se, Zn, Mo, Ni) with others that show depletions in pyrite under conditions of increasing oxygenation (e.g., Co, Bi). For instance, even though pyrite from the Wollogorang Formation shows increased Mo concentrations relative to pyrite from the Velkerri shales, the higher Co and Bi contents of pyrite argue against the possibility of oxygenation Similarly, Ni in pyrite does not display a particular trend, but its concentration increases with respect to Co at any given time through the 370-million-year period. All of the Co/Bi ratios (Ni/Co, Se/Co, Mo/Co, Zn/Co and Zn/Bi ratios in Fig 4.6; Table 4.3) increase with sedimentation age and provide robust evidence for increasing atmosphere oxygenation over this interval of time (1730 to 1360 Ma).

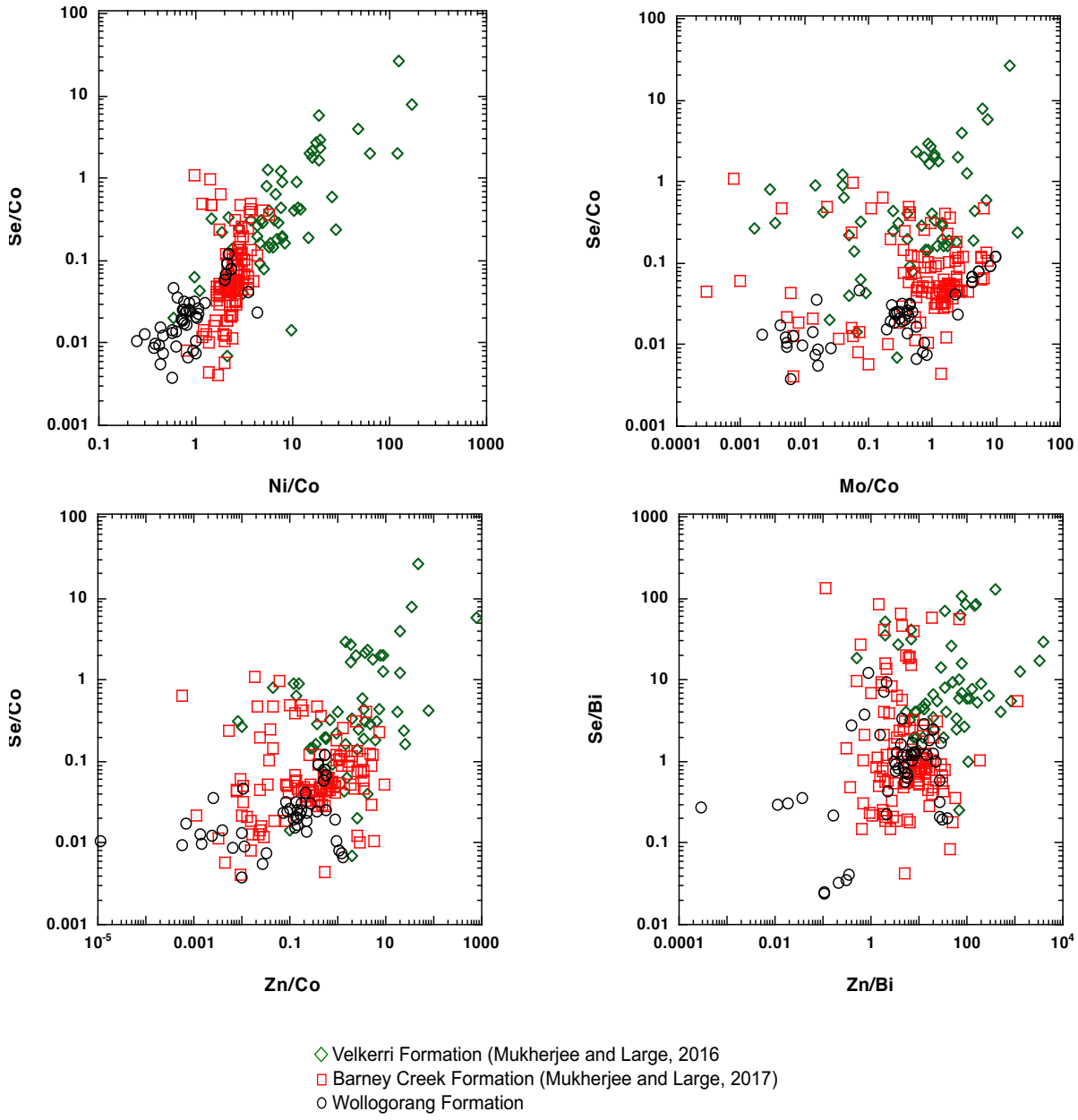

Fig 4.6 Plot of Se/Co: Ni/Co; Se/Co: Mo/Co; Se/Co: Zn/Co; Se/Bi; Zn/Bi for the three black shale formations (black circles: Wollogorang; red squares: Barney Creek; green diamonds:

4.5.1.2 Source rock composition

So far, our discussion of redox-sensitive trace element compositions in pyrite in the Proterozoic marine sediments studied here has been linked to an increase in atmospheric oxygen, which is assumed to be related directly to the intensity of oxidative weathering on the continents. Nevertheless, source rock compositions (dominantly mafic or felsic) and basin tectonics (active or less active) at the time of deposition of these black shales, are important factors that need to be addressed in order to evaluate the nature of the trace element flux. Below we summarise previous work on provenance analyses of the three black shale formations studied here. Past studies of their sedimentology, including paleo current measurements, sequence stratigraphy, and U-Pb zircon geochronology, have indicated that the Wollogorang and Barney Formation sediments were derived from weathering and erosion of the basal Tawallah Group, i.e., local sources. Deposition of these formations was related to stretching and thinning of the basin floor in a rift environment (Rogers, 1996; Giles et al., 2002). On the other hand, the Roper Group was deposited in an intracratonic ramp setting soon after the Isan Orogeny (Abbott and Sweet, 2000). Sediments of the Roper Group are likely to have been derived from the weathering and erosion of the North Australian craton basement rocks (Munsen et al., (2016). The question of whether the characteristic pyrite trace element concentrations in the Velkerri Formation have been affected due to change in provenance, needed to be further investigated.

We used Ti, Zr, Th, and Cr concentrations, augmented by literature data, to investigate potential influences of source rock composition on trace element concentrations in pyrite. Several studies have highlighted the importance of trace element ratios (Cr/Ni, V/Cr, V/Ni, La/Yb, La/Sm, Ti/Zr, Y/Ni, Zr/Cr, etc.) in determining the type of source rocks from which the sediments were derived (Bhatia, 1983; Condie and Wronkiewicz, 1990; McLennan et al., 1990; McLennan and Taylor, 1991; Garver and Scott, 1995; Cingolani et al., 2003; Ali et al., 2014). We have taken a similar approach and used Ti/Zr and Th/Cr ratios of the matrix to infer differences in the types of source rocks (Table 4.5; black shale matrix analyses of Ti, Zr, Cr, Th). This approach is based on the premise that Ti and Cr are more enriched in mafic rocks (means 10,000 and 250 ppm respectively; Riemann and De Caritat, 1998) than felsic rocks (means 3,000 and 10 ppm respectively), while Zr and Th are enriched in felsic rocks (means of 200 and 15 ppm respectively) relative to basic rocks (means 120 and 2.2 ppm). Figure 4.7 illustrates these compositions in a plot between Ti/Zr and Th/Cr with an assigned point for mean basalt and rhyolite. It is evident from Fig 4.7 (Th/Cr and Ti/Zr ratios of analyses) that all three black shale formations cluster together near the rhyolite (felsic) mean rather than showing any consistent variable association. In all three cases, source rocks are interpreted to be similar in terms of composition. The formation that most deviates from a rhyolitic source towards a

mafic source is the Velkerri Formation which is depleted in Co, which would be expected to be enriched if the source of the trace elements was largely detrital. The data suggests that changes in trace element concentrations in the pyrites are most likely related to changes in the redox state of the atmosphere rather than changes in source rock compositions available for erosion.

We have considered only the source flux of the trace elements in the above discussion. However, changes in sink fluxes could be important in controlling trace element concentrations in pyrite, as a result we have used sulphur isotope compositions of pyrite to give us an insight into changes in sinks, described in the next section.

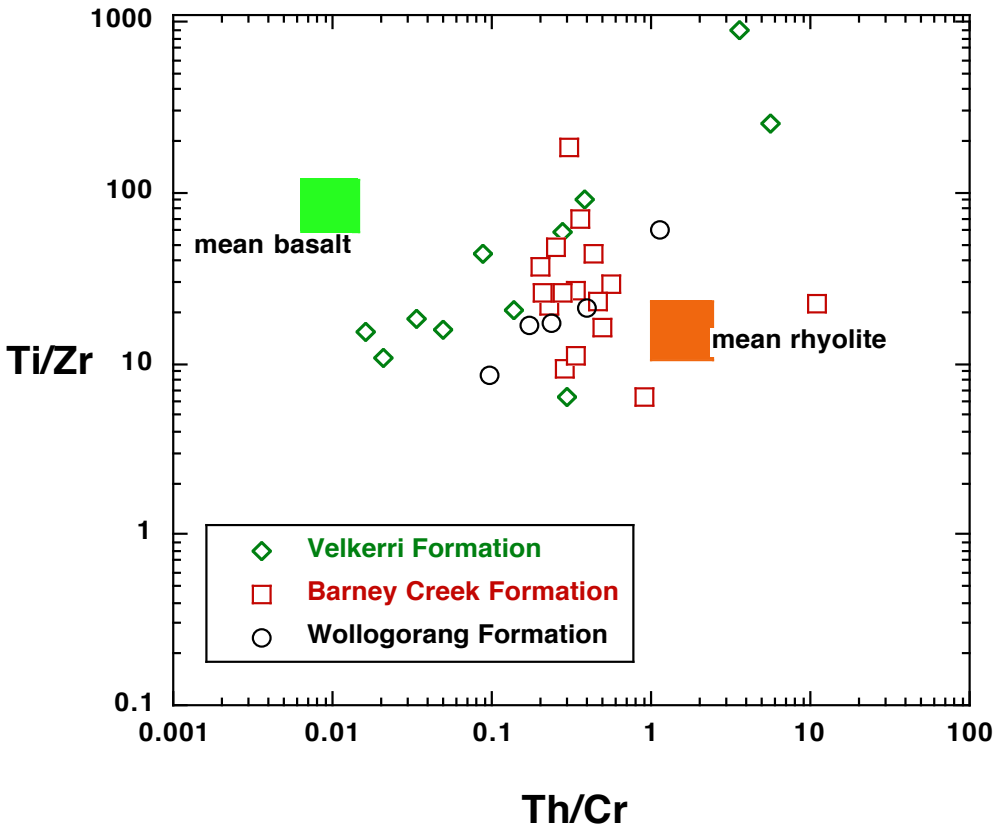

Fig 4.7 Plot of Th/Cr and Ti/Zr ratios for silicate matrix compositions of the black shales to identify source rock composition (felsic or mafic); Ti/Zr and Th/Cr ratios for basalt and rhyolite from Riemann and De Caritat (1998).

4.5.2 Sulphur isotopes in the McArthur Basin

Sulphur isotope compositions of sedimentary sulphides and sulphates of the McArthur Basin sediments have been studied by a number of researchers (Donnelly and Jackson, 1988; Canfield, 1998; Shen et al., 2002; Shen et al., 2003; Kah et al., 2004; Lyons et al., 2006; Johnston et al., 2008). All three black shale units have been sampled for sulphur isotope analysis in order to understand the amount and patterns of fractionation between sea water sulphate and sulphide, including constraining sea water sulphate levels in the Middle Proterozoic (Canfield, 1998). The previous studies (using measured values of $\delta^{34}S_{CAS\text{-}PY}$ and $\partial\delta^{34}S_{CAS}/\partial t_{(max)}$; CAS: Carbonate-associated sulphate and PY: pyrite) indicate that the Middle Proterozoic was a period of very low sea water sulphate values (0.1-1.8mM) compared to 28mM today (Kah et al., 2004; Luo et al., 2015). Based on S-isotope patterns, it has also been suggested that the Wollogorang and Velkerri Formations were deposited in a basin connected to the global ocean (Shen et al., 2002; Shen et al., 2003; Johnston et al., 2008). The Barney Creek Formation, on the other hand, has features that suggest it formed in a semi-restricted basinal environment with progressive interaction with the global sulphate reservoir during its deposition (Johnston et al., 2008).

As part of this study, sedimentary pyrite was analysed for ^{32}S-^{33}S-^{34}S, in order to understand variations of $\delta^{34}S$ in pyrite between the three black shales. $\delta^{34}S_{VCDT}$ in the Velkerri Formation displays the greatest range and the highest mean of all three formations (-14.2 to +52.8 ‰; mean: +26 ‰) (Fig 4.8; Table 4.7). The Barney Creek Formation has a similar range of $\delta^{34}S_{VCDT}$ values but a lower mean (-13.8 to +41.8 ‰; mean: +19.5 ‰), (Fig 4.8). In contrast, the Wollogorang Formation has a more restricted range of $\delta^{34}S_{VCDT}$, extending to the most negative values observed in this study, and the lowest mean (-29.4 to +9.5 ‰; mean: -5.0 ‰) (Fig 4.8).

The in-situ $\delta^{34}S$ values in pyrite obtained using SHRIMP-SI had a similar range and mean when compared to the conventional techniques utilized in previous research (Johnston et al., 2008; Shen et al., 2002). This is indicated in Figure 4.8 where the shaded regions represent the range of data obtained by previous studies. However, in some instances our data show a greater spread compared with other studies. This is to be expected when results of a micro-beam technique are compared with those of a micro-drill technique. We have documented extremely heavy pyrites (^{34}S enriched) in the Barney Creek and Velkerri Formations relative to published data. Based on the $\delta^{34}S$ values presented in Tables 4.6, all three formations also have negative $\delta^{34}S$ values, which could be indicative of microbial activity i.e., bacterial

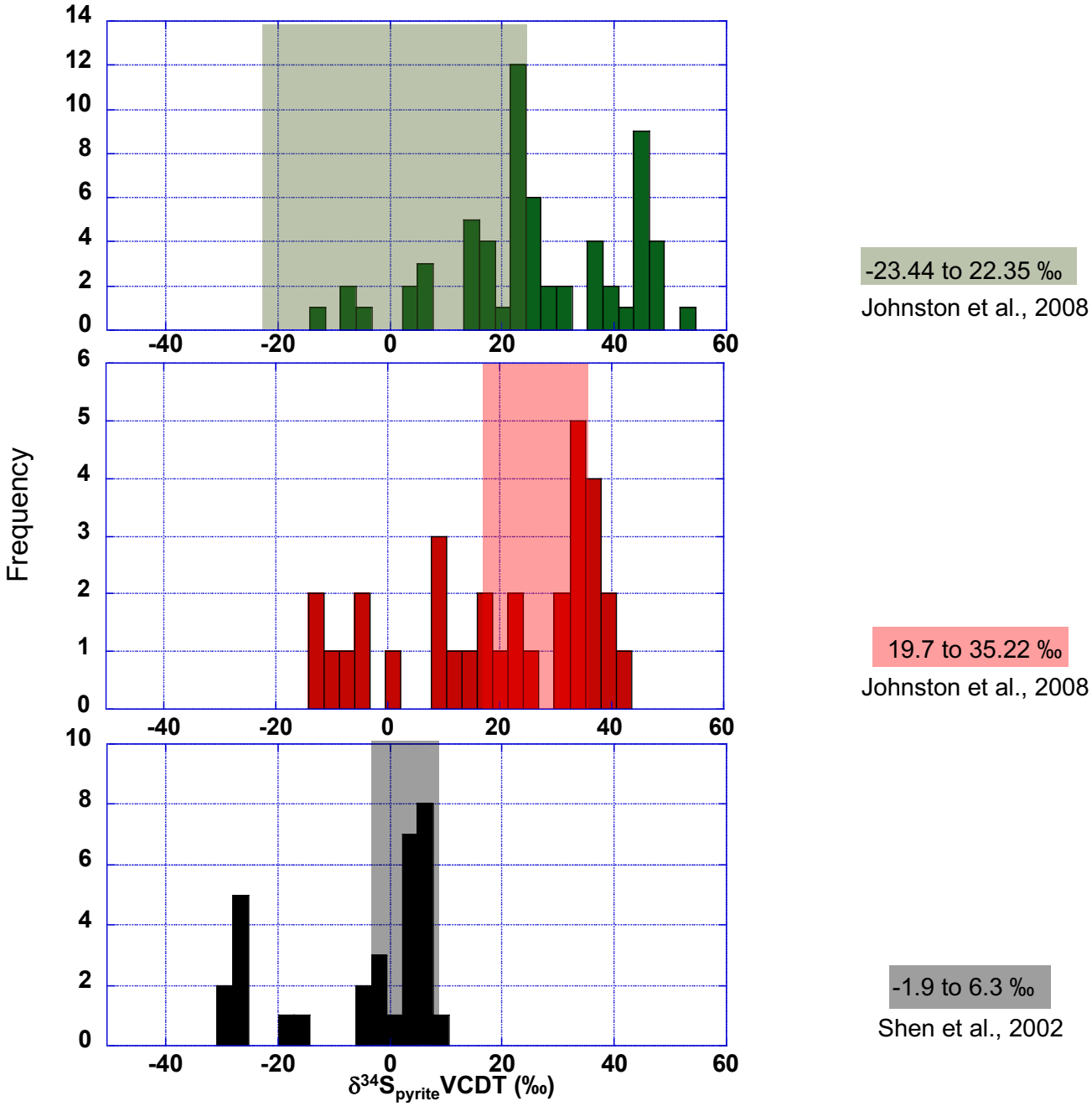

Fig 4.8 Pyrite sulfur isotopic compositions $\delta^{34}S_{VCDT}$ for the three black shale formations (black/bottom: Wollogorang; red/middle: Barney Creek; green/top: Velkerri); shaded regions represent range of sulfur isotopic compositions $\delta^{34}S_{VCDT}$ from Johnston et al. (2008) and Shen et al. (2002) in these formations.

sulphate reduction. Pyrite from the Wollogorang Formation records the most negative $\delta^{34}S$ values (-20 to -30 ‰) relative to the other two formations where the negative $\delta^{34}S$ values range between 0 to -14 ‰ (see above quoted data). Similarly, pyrite in the Wollogorang Formation has the least positive $\delta^{34}S$ values (maximum of +10 ‰), compared to >40 ‰ in the Barney Creek Formation >50 ‰ in the Velkerri Formation. Overall, there is an increase in not only the range of positive $\delta^{34}S$ values but also the $\delta^{34}S$ mean of each formation up stratigraphy (Table 4.6).

This increasing trend of $\delta^{34}S$ values in pyrite upsection could be interpreted in several ways. Negative $\delta^{34}S$ values are generally interpreted as being associated with microbial sulphate reduction because of the preferential uptake of ^{32}S relative to ^{34}S in sulphide, as the process is chemically and kinetically more favourable in metabolic pathways. This causes the $\delta^{34}S$ of the sulphide to be depleted in ^{34}S and this can be reflected in later diagenetic pyrite that forms from the 34-depleted pore fluids. Thus, any increase in $\delta^{34}S$ values of the sulphide is difficult to attribute to microbial activity acting on an effectively infinite reservoir of sulphate. However, diagenetic pyrite could either be more depleted or more enriched in ^{34}S depending on whether it precipitates in an open or close system, which regulates the supply of sulphate in the area of pyrite formation. Generally, heavy pyrites (^{34}S enriched) are attributed to precipitation under a closed system (with limited or no additional supply of sulphate) (Shen et al., 2002; Shen et al., 2003; Johnston et al., 2008; Gregory et al., 2015b). Continuing sulphate reduction leads to progressively ^{34}S-enriched pyrites as they begin to record the isotopic signature of the closed-system sulphate. If that were the case, the data from the present study would indicate that the increasing trend of $\delta^{34}S$ values upsection reflects a transition from an open system in the Wollogorang Formation to a closed system in the Velkerri Formation. However, such a scenario is not compatible with sedimentological, paleontological and geochemical studies that have confirmed an open marine origin for these rocks (Jackson et al., 1991; Abbott and Sweet, 2000; Shen et al., 2003; Javaux et al., 2001; Kendall et al., 2009). Previous studies have attributed the negative $\delta^{34}S$ values in the Velkerri Formation to reduction of sea water sulphate in a basinal setting with non-limiting sulphate supply and vice versa. (Logan et al., 1995; Shen et al., 2003). Johnston et al. (2008) used not only $\delta^{34}S_{pyrite}$ but ^{33}S and ^{36}S (larger variability in $\Delta^{33}S$ inversely correlated to $\Delta^{36}S$) to show that pyrite deposition in the Velkerri Formation black shales occurred in an open marine setting with connectivity to the global ocean. In fact, Kah et al. (2004) and Luo et al. (2015) proposed an increase in sea water sulphate levels based on their measured values of sulphur isotopes in the pyrites from the Velkerri Formation.

The Barney Creek Formation is considered to have formed in a partly restricted basin, and the positive $\delta^{34}S_{pyrite}$ values may be related to the closed system behavior. Indeed, previous studies by Shen et al. (2002) and Johnston et al. (2008) have pointed out that the limited supply of sulphate in a closed system

may have rendered $\delta^{34}S$ values in pyrite close to contemporaneous sea water (+25 ‰). However, we observe much heavier values than reported in the literature so far. Closed system behavior could also be created locally within sediments below the sediment-water interface. That could have led to a tendency toward heavy values in the Barney Creek and Velkerri Formations, but interestingly, very heavy values are absent from the Wollogorang Formation. Therefore, it is not possible to link the increasing trend of $\delta^{34}S$ values we observe in our pyrite to microbial sulphate reduction, lack of connection to global ocean, or quantitative sulphate reduction in the sediments. The increasing trend of $\delta^{34}S$ values upsection demands an alternative explanation, which we explore below.

We suggest a novel explanation for the increasing mean $\delta^{34}S$ trend with the help of a simple schematic diagram (Fig 4.9). Two scenarios are proposed; scenario 1 represents depositional conditions of the Wollogorang Formation, and scenario 2 represents the depositional conditions of the Velkerri Formation. The Barney Creek depositional condition is assumed to be intermediate between these two scenarios. Both scenarios represent open marine conditions. In scenario 1, there is less oxygen in the atmosphere impeding oxidative weathering on land. This leads to a low supply of certain trace elements, sulphate and other nutrients that, in turn, would cause low productivity and growth of the prevalent biologic community at 1730 Ma, and consequent lower organic matter deposition. In this case, it is envisaged that black shales are forming in an anoxic environment mainly due to organic matter deposition and a lack of oxygen in the water column related to low pO_2 in the atmosphere. Scenario 1 reflects anoxic conditions over a large area of the ocean floor, making the system inefficient in causing complete sulphate reduction and consequently forming pyrites that lack heavy $\delta^{34}S_{pyrite}$. It is inefficient for mainly two reasons:

1. There is lower organic matter production (relative to scenario 2 described below), which is one of the prerequisites for the development of anoxic conditions;
2. Deposition of organic matter is over a larger areal extent of ocean-floor anoxia.

Scenario 2 has higher oxygen contents in the atmosphere, causing greater oxidative weathering on land. This leads to a higher input of trace elements, sulphate and nutrients in the ocean, promoting an increase in organic matter production and organic carbon deposition. This causes two important changes. First, increased productivity, leads to increased release of oxygen into the ocean and atmosphere, and second, higher levels of organic carbon production and deposition leads to a strongly reducing environment (anoxic to euxinic). The pockets or sub-basins of anoxia are believed to be more focused, due to basin architecture and also the increase in oxygen of the overall ocean-atmosphere system, causing the region of anoxia/euxinia to shrink (organic matter is regionally oxidized and only locally preserved in sub-basins). However, because organic matter deposition is more efficient and occurs over a smaller area, it causes more efficient sulphate reduction. In turn, this causes a relative increase in $\delta^{34}S$ values

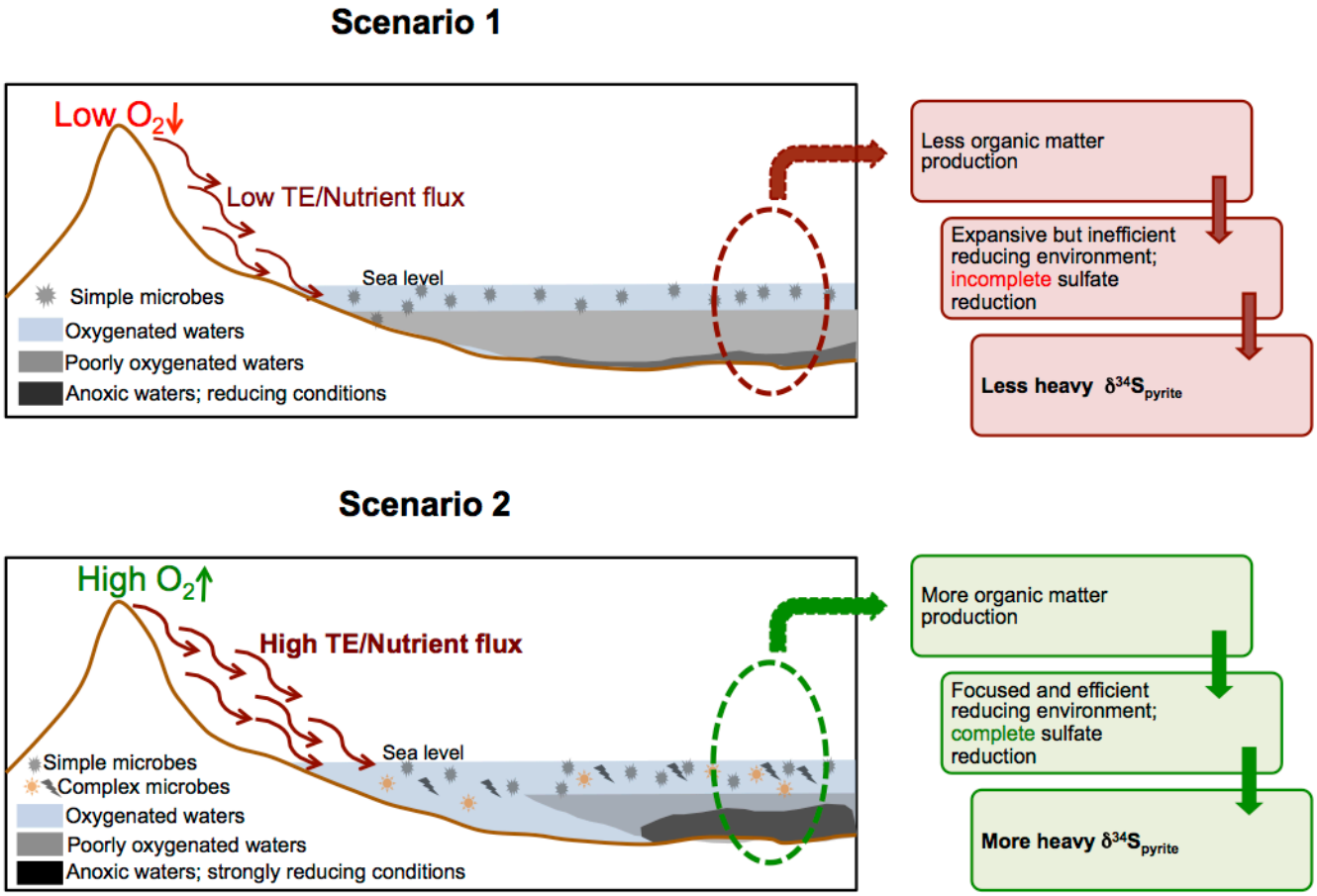

Fig 4.9 Schematic diagram depicting two scenarios (1 with low oxygen conditions and 2 with relatively higher oxygen conditions) that is possibly controlling the sulfur isotope compositions.

in pyrite compared with scenario 1. This conclusion is also consistent with an ocean oxygenation event at ~1400 proposed by Yang et al. (2017) using U isotopes and the previously proposed increase in sea water sulphate concentrations (Kah et al., 2004; Luo et al., 2015) due to oxidative weathering on land. The observed increased complexity of microorganisms in the Velkerri Formation relative to Barney Creek and Wollogorang Formations (Javaux et al., 2001; 2004), may also be attributed to these changes. Although this model is qualitative, speculative and requires further study to evaluate, it is supported by marine S isotope fractionation at another critical time in ocean evolution. The increase of $\delta^{34}S$ values in pyrite during the Neoproterozoic Oxygenation Event (NOE or GOE 2) is apparent at the Precambrian-Cambrian transition (Claypool et al., 1980; Strauss and Schieber, 1990; Strauss et al., 1992; Strauss, 1993) where $\delta^{34}S_{pyrite}$ varies between +7.6 to +53 over the period 600 to 520 Ma, accompanying the Cambrian explosion of life. It is difficult to cite modern day examples for the above scenarios. Such phenomena are, however, found in Ace Lake in Antarctica, where complete sulphate reduction under the current high pO_2, causes the $\delta^{34}S_{sulphate}$ and $\delta^{34}S_{pyrite}$ to be the same i.e., 41.2 ‰ and 41.5 ‰, respectively (Burton and Barker, 1979). In addition, strongly reducing environments, such as those found in the Black Sea and Cariaco Basin, do

not impart heavy values of $\delta^{34}S$ in pyrite compared to Proterozoic black shales. This could be due to the vast reservoir of sea water sulphate (28mM) today compared to the Proterozoic (0.1-1.8mM) [Luo et al., 2015], which could make complete sulphate reduction more difficult in modern euxinic settings.

4.6 Conclusions

There are two main conclusions from this study. First, trace element concentrations and their ratios of sedimentary pyrite in three black shale formations of the McArthur Basin provide evidence for a gradual increase in atmospheric oxygenation from 1730 to 1360 Ma. The increase is manifested in the form of an increase in certain elements and their ratios in pyrite (Se, Zn, Se/Co, Ni/Co, Mo/Co, Zn/Bi) and decrease in other elements (Co, Bi).

Second, we observe a marked change in pyrite sulphur isotopic compositions in the three black shale formations i.e., a marked increase in mean $\delta^{34}S_{pyrite}$ values from the Wollogorang Formation to the Velkerri Formation. This is possibly indicative of expansion of oxygenated waters and decreasing areal extent of anoxia.

4.7 Acknowledgements

This research was funded by Australian Research Council (ARC) project DP 150102578 awarded to RRL. Costs of analyses were also partly covered by an SEG Hugo Dummett Fellowship awarded to IM. We appreciate the help and support offered to us by the NTGS core facility staff. We also acknowledge help, advice and instruction from Leonid Danyushevsky, Ivan Belousov, Sarah Gilbert, Elena Lounjeva and Paul Olin in the LA-ICP-MS laboratory and from Ron Berry and Mihir Deb for their useful comments and suggestions. We thank the reviewers for giving insightful comments and suggestions that helped improve the manuscript significantly. We would also like to thank the Editor and Associate Editor for their time towards improving this manuscript immensely.

4.8 References

Abbott S. T. and Sweet I. P. (2000) Tectonic control on third-order sequences in a siliciclastic ramp-style basin: an example from the Roper Superbasin (Mesoproterozoic), northern Australia. Aust. J. Earth Sci. 47, 637–657.

Ahmad M., Dunster J. N., and Munson T. J. (2013) Chapter 15: McArthur Basin: in Ahmad M and Munson TJ (compilers). 'Geology and mineral resources of the Northern Territory'. Northern Territory Geological Survey. Special Publication 5.

Algeo T. J., Maynard J. B., (2004). Trace element behavior and redox facies in core shales of Upper Pennsylvanian Kansas-type cyclothems. Chemical Geology 206, 289–318.

Algeo T. J., Lyons T. W. (2006) Mo–total organic carbon covariation in modern anoxic marine environments: Implications for analysis of paleoredox and paleohydrographic conditions. Paleoceanography 21, 1- 23.

Algeo T. J., Rowe H. (2012) Paleoceanographic applications of trace-metal concentration data. Chemical Geology 324, 6–18.

Algeo T. J. and Tribovillard N. (2009) Environmental analysis of paleoceanographic systems based on molybdenum-uranium covariation. Chemical Geology 268, 211–225.

Ali S., Stattegger K., Garbe Schöngerg D., Frank M., Kraft S. and Kuhnt W. (2014) The provenance of cretaceous to quaternary sediments in the Tarfaya basin, SW Morocco: evidence from trace element geochemistry and radiogenic Nd-Sr isotopes. J. A fr. EarthSci. 90, 64–76.

Anbar A. D. and Knoll A. H. (2002) Proterozoic ocean chemistry and evolution: a bioinorganic bridge? Science 297, 1137–1142.

Anbar A. D., Duan Y., Lyons T. W., Arnold G. L., Kendall B., Creaser R. A., Kaufman A. J., Gordon G. W., Scott C., Garvin J. and Buick R. (2007) A whiff of oxygen before the great oxidation event? Science 317, 1903–1906.

Arnold G. L., Anbar A. D., Barling J. and Lyons T. W. (2004) Molybdenum isotope evidence for widespread anoxia in Mid-Proterozoic ocean. Science 304, 87-90.

Barnes S. S. (1967) Minor element composition of ferromanganese nodules. Science 157, 63-65.

Bertine K. K., Koide M. and Goldberg E. D. (1996) Comparative marine chemistries of some trivalent metals-

bismuth, rhodium and rare Earth elements. Mar. Chem. 53, 89–100.

Bertine K. K. and Turekian K. K. (1973) Molybdenum in marine deposits. Geochim. Cosmochim. Acta 37, 1415–1434.

Bhatia M. R. (1983) Plate tectonics and geochemical composition of sandstones. Journal of Geology 91 (6), 611–627.

Brasier M. D. and Lindsay J. F. (1998) A billion years of environ- mental stability and the emergence of eukaryotes: new data from northern Australia. Geology 26, 555–558.

Brocks J, Grosjean E and Logan G. (2008) Assessing biomarker syngeneity using branched alkanes with quaternary carbon (BAQCs) and other plastic contaminants, Geochimica et Cosmochimica Acta 72, 871-888.

Brocks J. J., Love, G. D., Summons R. E., Knoll A. H., Logan G. A. and Bowden S. A. (2005) Biomarker evidence for green and purple sulphur bacteria in a stratifi ed Paleoproterozoic sea. Nature 437, 866-870.

Brookins D.G. (1988) Bismuth. In: Eh-pH Diagrams for Geochemistry. Springer, Berlin, Heidelberg

Buick R., Des Marais D. J. and Knoll A. H. (1995) Stable isotopic compositions of carbonates from the Mesoproterozoic Bangemall group, northwestern Australia. Chemical Geology 123 (1–4), 153–171

Bull S. W., (1998) Sedimentology of the Palaeoproterozoic Barney Creek Formation in DDH BMR McArthur 2, Southern McArthur Basin, Northern Territory. Australian Journal of Earth Sciences 45, 21–23.

Burton H. R. and Barker R., J. (1979) Sulfur chemistry and microbiological fractionation of sulfur isotopes in a saline Antarctic lake: Geomicrobiological Journal 1, 329 –340.

Calvert S. E. and Pedersen T. F. (1993) Geochemistry of Recent oxic and anoxic marine sediments: implications for the geological record. Mar. Geol. 113, 67– 88.

Canfield D.E., 1998. A new model for Proterozoic ocean chemistry. Nature 396, 450–453.

Chappaz A., Lyons T. W., Gregory D. D., Reinhard C. T., Gill Bi. C., Li C. and Large R. R., 2014. Does pyrite act as an important host for molybdenum in modern and ancient euxinic sediments? Geochim. Cosmochim. Acta 126, 112–122.

Chen J., Walter M. R., Logan G. A., Hinman M. C. and Summons R. E. (2003) The Paleoproterozoic McArthur River (HYC) Pb/Zn/Ag deposit of northern Australia: organic geochemistry and ore genesis. Earth and Planetary Science Letters 210, 467-479.

Cingolani C. A., Manassero M. and Abre P. (2003) Composition, provenance, and tectonic setting of Ordovician siliciclastic rocks in the San Rafael block: Southern extension of the Precordillera crustal fragment, Argentina. Journal of South American Earth Sciences, 16 (1): 91-106

Claypool G. E., Holser W. T, Kaplan I. R., Sakai H and Zak I. (1980) The age curves of sulfur and oxygen isotopes in marine sulphate and their mutual interpretations. Chem Geol 28, 199-260

Condie K. C. and Wronkiewicz D. S. (1990) The Ce/Th ratio of Precambrian pelites from the Kaapvaal Craton as an index of cratonic evolution. Earth Planetary Sci Lett 97, 256–267

Crick I. H., Boreham C. J., Cook A. C. and Powell T. G. (1988) Petroleum geology and geochemistry of Middle Proterozoic McArthur Basin, northern Australia II: assessment of source rock potential. Am. Assoc. Petrol. Geol. Bull. 72, 1495–1514.

Crowe D. E. and Vaughan R. G. (1996) Characterization and use of isotopically homogeneous standards for in situ laser microprobe analysis of 34S/32S ratios. American Mineralogist 81, 1987-193.

Crowe S. A., Døssing L. N., Beukes N. J., Bau M., Kruger S. J., Frei R. and Canfield D. E. (2013) Atmospheric oxygenation three billion years ago. Nature 501, 535–538.

Crusius J., Calvert S., Pedersen T. and Sage D. (1996) Rhenium and molybdenum enrichments in sediments as indicators of oxic, suboxic and sulfidic conditions of deposition. Earth Planet. Sci. Lett. 145, 65–78.

Danyushevsky L., Robinson P., Gilbert S., Norman M., Large R., McGoldrick P. and Shelley M. (2011) Routine quantitative multi-element analysis of sulphide minerals by laser ablation ICP-MS: Standard development and consideration of matrix effects. Geochem., Explor. Environ. Anal. 11, 51–60.

Dean W. E., Gardner J. V. and Piper D. Z. (1997) Inorganic geochemical indicators of glacial – interglacial changes in productivity and anoxia of the California continental margin. Geochim. Cosmochim. Acta 61, 4507– 4518.

Dean W. E., Piper D. Z. and Peterson L. C. (1999) Molybdenum accumulation in Cariaco basin sediment over the past 24 k.y.: a record of water-column anoxia and climate. Geology 27, 507– 510.

Donnelly T. H. and Jackson M. J. (1988) Sedimentology and geochemistry of a mid-Proterozoic lacustrine

unit from northern Australia. Sedimentary Geology 58, 145–169.

Donnelly T. H. and Crick I. H. (1988) Depositional environment of the middle Proterozoic Velkerri Formation in northern Australia: geochemical evidence. Precambr. Res. 42, 165–172.

Farquhar J. and Wing B. A. (2003) The terrestrial record of stable sulphur isotopes: a review of the implications for evolution of Earth's sulphur cycle: Earth and Planetary Science Letters 213, 1–13.

Fowler S. W., Teyssie J. L. and Church T. M. (2010) Scavenging and retention of bismuth by marine plankton and biogenic particles, Limnology and Oceanography 55, 1093–1104.

Gadde, R.R., and Laitinen, H.A., 1974. Heavy metal adsorption by hydrous iron and manganese oxides. Anal. Chem., 46 (13), 2022–2026

Garver J. I. and Scott T. J. (1995) Trace elements in shale as indicators of crustal provenance and terrane accretion in south Canadian Cordillera. Geol Soc Am Bulletin 107, 440–453

Gilbert S., Danyushevsky L., Goemann K. and Death D. (2014) Fractionation of sulphur relative to iron during laser ablation-ICP-MS analyses of sulphide minerals: implications for quantification. J. Anal. At. Spectrom. 29, 1024–1033.

Giles D., Betts P. G., Lister G. S. (2002) A continental back-arc setting for Early to Middle Proterozoic basins of northeastern Australia. Geology 30, 823–826.

Gordon G. W., Lyons T. W., Arnold G. L., Roe J., Sageman B. B. and Anbar A. D. (2009) When do black shales tell molybdenum isotope tales? Geology 37, 535–538.

Gorter G. and Grey K. (2012) Velkerri Formation: Depositional Model – Beetaloo Subbasin, Northern Territory, Australia: Biostratigraphy and Organic Enrichment. CABS symposium.

Gregory D., Meffre S. and Large R. (2014) Comparison of metal enrichment in pyrite framboids from a metal-enriched and metal-poor estuary: American Mineralogist, v. 99, no. 4, p. 633-644.

Gregory D. D., Large R. R., Halpin J. A., Lounejeva Baturina, E., Lyons T. W., Wu S., Sack P. J., Chappaz A., Maslennikov V. V., Bull S. W. and Danyushevsky L. (2015a) Trace element content of sedimentary pyrite in black shales. Econ. Geol. 110, 1389–1410.

Gregory D. D., Large R. R., Halpin J. A., Steadman J. A., Hickman A. H., Ireland T. R. and Holden P. (2015b) The chemical conditions of the late Archean Hamersley basin inferred from whole rock and pyrite geochemistry with Δ 33 S and δ 34 S isotope analyses: Geochimica et Cosmochimica Acta 149, 223-250.

Gregory D. D., Lyons T. W., Large R. R., Jiang G., Stepanov A. S., Diamond C., Figueroa M. and Olin, P. (2017) Whole rock and discrete pyrite geochemistry as complementary tracers of ancient ocean chemistry: An example from the Neoproterozoic Doushantuo Formation, China: Geochimica et Cosmochimica Acta. http://dx.doi.org/10.1016/j.gca.2017.05.042

Huang P. M. and Germida J. J. (2002) Chemical and biochemical processes in the rhizosphere: metal pollutants. In Interactions Between Soil Particles and Microorganisms: Impact on the Terrestrial Ecosystem, ed. Huang, P. M., Bollag, J.M., and Senesi, N., Wiley, New York, 381–438.

Huerta-Diaz M. A. and Morse J. W. (1992) Pyritization of trace metals in anoxic marine sediments. Geochim. Cosmochim. Acta 56, 2681–2702

Ireland T. R., Schram N., Holden P., Lanc P., Ávila J., Armstrong R., Amelin Y., Latimore A., Corrigan D., Clement S., Foster J. J. and Compston W. (2014) Charge-mode electrometer measurements of S-isotopic compositions on SHRIMP-SI. International Journal of Mass Spectrometry 359, 26-37.

Ireland T., Clement S., Compston W., Foster J., Holden P., Jenkins B., Lanc P., Schram N. and Williams I. (2008) Development of SHRIMP: Australian Journal of Earth Sciences 55, 937–954.

Jackson M. J. (1985) Mid-Proterozoic dolomitic varve sand microcycles from the McArthur Basin, northern Australia. Sedimentary Geology 44, 301–326.

Jackson M. J. and Raiswell R. (1991) Sedimentology and carbon-sulphur geochemistry of the Velkerri Formation, a Mid- Proterozoic potential oil source in northern Australia. Precamb. Res. 54, 81–108.

Jackson M. J. and Southgate P. N. (2000) Evolution of three unconformity-bounded sandy carbonate successions in the McArthur River region of northern Australia: the Lawn, Wide and Doom Supersequences in the proximal part of the Isa SuperBasin. Australian Journal of Earth Sciences 47, 600–625.

Jackson T. A. (1998) The biogeochemical and ecological significance of interactions between colloidal minerals and trace elements. In Environmental Interactions of Clays, ed. Parker, A., and Rae, J. E., Springer-Verlag, Berlin, 93–205.

Javaux E. J., Knoll A. H. and Walter M. R. (2001) Morphological and ecological complexity in early eukaryotic ecosystems. Nature 412, 66–69.

Javaux E., Knoll A. H. and Walter, M. R. (2004) TEM evidence for eukaryotic diversity in mid-Proterozoic

oceans. Geobiology 2, 121–132.

Jochum K. P., Pfänder J., Woodhead J. D., Willbold M., Stoll B., Herwig K., Amini M., Abouchami W. and Hofmann A. W. (2005) MPI-DING glasses: New geological reference materials for in situ Pb isotope analysis. Geochemistry Geophysics Geosystems 6, 1525-2027.

Johnston D. T., Farquhar J., Summons R. E., Shen Y., Kaufman A. J. Masterson A. L. and Canfield D. E. (2008) Sulfur isotope biogeochemistry of the Proterozoic McArthur Basin. Geochim. Cosmochim. Acta 72, 4278–4290.

Jones B. and Manning D. A. C. (1994) Comparison of geochemical indices used for the interpretation of palaeoredox conditions in ancient mudstones. Chem. Geol. 111, 111 – 129.

Kah L. C., Lyons T. W. and Frank T. D. (2004) Low marine sulphate and protracted oxygenation of the Proterozoic bio- sphere. Nature 431, 834–838.

Kendall B., Creaser R. A., Gordon, G. W. and Anbar A. D. (2009) Re-Os and Mo isotope systematics of black shales from the Middle Proterozoic Velkerri and Wollogorang Formations, McArthur Basin, northern Australia. Geochim Cosmochim Acta 73, 2534-2558.

Khan, M.B., Masiol, M., Hofer, A., and Pavoni, B., 2014. Harmful Elements in Estuarine and Coastal Systems (chapter 2) in C. Bini and J. Bech (eds.), PHEs, Environment and Human Health, 37 DOI 10.1007/978-94-017-8965-3_2.

Konhauser K. O., Pecoits E., Lalonde S. V., Papineau D., Nisbet E. G., Barley M. E., Arndt N. T., Zahnle K. and Kamber B. S. (2009) Oceanic nickel depletion and a methanogen famine before the Great Oxidation Event. Nature 458, 750–753.

Large R. R., Gregory D. G., Steadman J. A., Tomkins A. G., Lounejeva E., Danyushevsky L. V., Halpin J. A., Maslennikov V. V., Sack P. J., Mukherjee I. and Hickman A. (2015a) Gold in the oceans through time. Earth and Planetary Science Letters 428, 139-150.

Large R. R, Halpin J. A., Lounejeva E., Danyushevsky L. V., Maslennikov V. V., Gregory D., Sack P. J., Haines P. W., Long J. A., Makoundi C. and Stepanov A. S. (2015b) Cycles of nutrient trace elements in the Phanerozoic ocean, Gondwana Research 28 (4), 1282-1293.

Large R. R., Mukherjee I., Gregory D. G., Steadman J. A., Maslennikov V. V. and Meffre S., (2017) Ocean and Atmosphere Geochemical Proxies Derived from Trace Elements in Marine Pyrite: Implications for Ore Genesis in Sedimentary Basins. Economic Geology 112(2), 423-450

Large R. R., Danyushevsky L., Hollit C., Maslennikov V., Meffre S., Gilbert S., Bull S., Scott R., Emsbo P., Thomas H., Singh B. and Foster J. (2009) Gold and trace element zonation in pyrite using a laser imaging technique: Implications for the timing of gold in orogenic and carlin-style sediment-hosted deposits. Econ. Geol. 104, 635–668

Large R. R., Halpin J. A., Danyushevsky L. V., Maslennikov V. V., Bull S. W., Long J. A., Gregory D. D., Lounejeva E., Lyons T. W., Sack P. J., McGoldrick P. and Calver C. R. (2014) Trace element content of sedimentary pyrite as a new proxy for deep-time ocean- atmosphere evolution. Earth and Planetary Science Letters 389, 209-220.

Large R. R., Maslennikov V. V., Robert F., Danyushevsky L. V. and Chang Z. (2007) Multi stage sedimentary and metamorphic origin of pyrite and gold in the Giant Sukhoi log deposit, Lena Gold Province, Russia. Econ. Geol. 102, 1233–1267.

Lee D. S., Edmond J. M. and Bruland K. W. (1985/1986) Bismuth in the Atlantic and North Pacific Ocean: A natural analogue to plutonium and lead? Earth Planet. Sci. Lett. 76, 254–262.

Lindsay J. F. and Brasier M. D. (2000) A carbon isotope reference curve for ca. 1700-1575 Ma, McArthur and Mount Isa Basins, northern Australia. Precambrian Research 99 (3-4), 271-308.

Logan G. A., Hayes J. M., Hieshima G. B. and Summons R. E. (1995) Terminal Proterozoic reorganization of biogeochemical cycles. Nature 376, 53–56.

Longerich H. P., Jackson S. E. and Günther D. (1996) Laser ablation inductively coupled plasma mass spectrometric transient signal data acquisition and analyte concentration calculation. J. Anal. At. Spectrom. 11, 899-904.

Luo G., Ono S., Huang J., Algeo T. J., Li C., Zhou L., Robinson A., Lyons T. W. and Xie S. (2015) Decline in oceanic sulphate levels during the early Mesoproterozoic. Precambrian Research 258, 36-47.

Lyons T. W., Gellatly A. M., Goldrick P. J. and Kah L. C. (2006) Proterozoic sedimentary exhalative (SEDEX) deposits and links to evolving global ocean chemistry. Geol. Soc. Am. Mem. 198, 169–184.

Lyons T. W., Reinhard C. T. and Planavsky N. J. (2014) The rise of oxygen in Earth's early ocean and atmosphere. Nature 506, 307-315.

Lyons T. W., Werne J. P., Hollander D. J. and Murray R. W. (2003) Contrasting S geochemistry and Fe/Al and Mo/Al ratios across the last oxic to anoxic transition in the Cariaco Basin, Venezuela: Chemical Geology 195, 131–157.

McLennan S. M. and Taylor S. R. (1991) Sedimentary rocks and crustal evolution revisited: Tectonic setting and secular trends. J Geol 99, 1–21

McLennan S. M., Taylor S. R., McCulloch M. T. and Maynard J. B. (1990). Geochemical and Nd – Sr isotopic composition of deep-sea turbidites: Crustal evolution and plate tectonic associations. Geochimica et Cosmochimica Acta 54, 2015–2050.

McKenzie, R.M., 1972. The sorption of some heavy metals by the lower oxides of manganese. Geoderma 8, 29-35.

Meyer K. M. and Kump L. R. (2008) Oceanic euxinia in Earth history: Causes and consequences. Annu. Rev. Earth Planet. Sci. 36, 251–88.

Morford J. L., Russell A. D. and Emerson S. (2001) Trace metal evidence for changes in the redox environment associated with the transition from terrigenous clay to diatomaceous sediment, Saanlich Inlet, BC. Mar. Geol. 174, 355– 369.

Morita, M., Uemoto, H., Watanabe, A., 2007. Reduction of selenium oxyanions in wastewater using two bacterial strains, Eng. Life Sci. 7 (3), 235–240.

Morse J. W. and Arakaki T. (1993) Adsorption and coprecipitation of divalent metals with mackinawite (FeS). Geochim. Cosmochim. Acta 57, 3635–3640

Mukherjee I. and Large R. (2016) Pyrite trace element chemistry of the Velkerri Formation, Roper Group, McArthur Basin: Evidence for atmospheric oxygenation during the Boring Billion: Precambrian Res. 281, 13-26

Mukherjee I. and Large R. (2017) Application of pyrite trace element chemistry to exploration for SEDEX style Zn-Pb deposits: McArthur Basin, Northern Territory, Australia. Ore Geology Reviews 81, 1249-1270.

Mukherjee I., Large R., Corkrey R., Danyushevsky L., (2018). The Boring Billion, a slingshot to complex life on Earth. Scientific Reports 8, Article number 4432.

Munson T. J. (2016) Sedimentary characterisation and correlation of the Wilton package, greater McArthur Basin: in Annual Geoscience Exploration Seminar (AGES) presentations, Alice Springs, Northern Territory 15–16 March 2016. Northern Territory Geological Survey, Record 2016-001.

Murray J. W. (1968) The adsorption of aqueous metal on colloidal hydrous manganese oxide Adv. Chem. Ser., 79, 74–81.

Murray J. W. (1975) The interaction of cobalt with hydrous manganese dioxide. Geochim. Cosmochim. Acta 39, 635–647.

Nishri A., Halicz L. (2014). Dynamics of redox sensitive elements. Chap. 28. In: Zohary, T., Sukenik, A., Berman, T., Nishri, A. (eds.), Lake Kinneret: Ecology and Management. Springer, Heidelberg.

Norman M., Pearson N. J., Sharma a., Griffin W. L. (1996) Quantitative analysis of trace elements in geological materials by laser ablation ICPMS: instrumental operating conditions and calibration values of NIST glasses. Geostandards and Geoanalytical Research 20 (2), 247-261

Page R. W., Jackson M. J. and Krassay A. A. (2000) Constraining the sequence stratigraphy in northern Australian basins: SHRIMP U-Pb zircon geochronology between Mt Isa and McArthur River. Australian Journal of Earth Sciences 47 (3), 431–460.

Page R. W. and Sweet I. P. (1998) Geochronology of Basin phases in the western Mt Isa Inlier and correlation with the McArthur Basin. Australian Journal of Earth Sciences 45(2), 201–232.

Pailler D., Bard E., Rostek F., Zheng Y., Mortlock R. and Van Geen A. (2002) Burial of redox-sensitive metals and organic matter in the equatorial Indian Ocean linked to precession. Geochim. Cosmochim. Acta 66, 849– 865.

Partin C. A., Bekker A., Planavsky N. J., Scott C. T., Gill B. C., Li C., Podkovyrov V., Maslov A., Konhauser K. O., Lalonde S. V., Love G. D., Poulton S. W. and Lyons T. W. (2013) Large-scale fluctuations in Precambrian atmospheric and oceanic oxygen levels from the record of U in shales. Earth Planet. Sci. Lett. 369–370.

Pickering W. (1979) Copper retention by sediment/soil components. In Copper in the Environment Vol. I, Ecological Cycling, ed. Nriagu, J. O., Wiley, New York, 217–253

Planavsky N. J., McGoldrick P., Scott C. T., Li C., Reinhard C. T., Kelly A. E., Chu X., Bekker A., Love G. D. and Lyons T. W. (2011) Widespread iron-rich conditions in the mid-Proterozoic ocean. Nature 447, 448–451.

Planavsky N. J., Reinhard C. T. Wang X., Thomson D., McGoldrick P., Rainbird R. H., Johnson T., Fischer W. W. and Lyons T. W. (2014) Low Mid-Proterozoic atmospheric oxygen levels and the delayed rise of animals. Science 346, 635-638.

Plumb K. A. (1979a) Structure and tectonic style of the Precambrian shields and platforms of northern Australia. Tectonophysics 58, 291-325.

Plumb K. A. (1979b) The tectonic evolution of Australia. Earth Science Reviews 14, 205-249.

Rawlings D. J. (1999) Stratigraphic resolution of a multiphase intracratonic Basin system: the McArthur Basin, northern Australia. Australian Journal of Earth Sciences 46, 703–723.

Reimann C. and De Caritat P. (1998) Chemical Elements in the Environment, Fact Sheets for the Geochemist and Environmental Scientist: Springer-Verlag, Berlin, 397 p.

Reinhard C. T., Planavsky N. J., Robbins L. J., Partin C. A., Gill B. C., Lalonde S. V., Bekker A., Konhauser K. O. and Lyons T. W. (2013) Proterozoic ocean redox and biogeochemical stasis. Proc. Natl. Acad. Sci. USA 110, 5357–5362.

Rickard D. (2012) Sulfidic sediments and sedimentary rocks. In: Van Loon, A.J. (Ed.), Developments in Sedimentology. Elsevier, p. 801.

Rogers J. (1996) Geology and tectonic setting of the Tawallah Group, southern McArthur Basin, Northern Territory. PhD thesis, University of Tasmania.

Sahoo S. K., Planavsky N. J., Jiang G., Kendall B., Owens J. D., Wang X., Shi X., Anbar A. D. and Lyons T. W. (2016) Oceanic oxygenation events in the anoxic Ediacaran ocean. Geobiology 14, 457–468.

Sahoo S. K., Planavsky N. J., Kendall B., Wang X., Shi X., Scott C., Anbar A. D., Lyons T. W., Jiang G. (2012) Ocean oxygenation in the wake of the Marinoan glaciation. Nature 489, 546–549.

Smith, K.S., 1999, Metal sorption on mineral surfaces: An overview with exam- ples relating to mineral deposits, in Plumlee, G.S., and Logsdon, M.J., eds., The environmental geochemistry of mineral deposits, Part A: Processes, techniques, and health issues, Reviews in Economic Geology, vol. 6A, Chap- ter 7: Littleton, Colorado, Society of Economic Geologists, Inc., p. 161–182.

Smith, K.S., and Huyck, H.L.O., 1999, An overview of the abundance, relative mobility, bioavailability, and human toxicity of metals, in Plumlee, G.S., and Logsdon, M.J., eds., The environmental geochemistry of mineral deposits, Part A: Processes, techniques, and health issues, Reviews in Economic Geology, vol. 6A, Chapter 2: Littleton, Colorado, Society of Economic Geologists, Inc., p. 29–70.

Scott, C., Lyons, T.W., Bekker, A., Shen, Y., Poulton, S.W., Chu, X., Anbar, A.D., 2008. Tracing the stepwise oxygenation of the Proterozoic ocean. Nature 452, 456–459.

Shen Y., Canfield D. E. and Knoll A. H. (2002) Middle Proterozoic ocean chemistry: Evidence from the McArthur Basin, northern Australia. Am. J. Sci. 302, 81–109.

Shen Y., Knoll A. H. and Walter M. R. (2003) Evidence for low sulphate and anoxia in a mid-Proterozoic marine basin. Nature 423, 632–635.

Smedley P. L. and Kinniburgh D. G. (2002) A review of the source, behaviour and distribution of arsenic in natural waters. Applied Geochemistry 17, 517–568.

Southgate P. N., Bradshaw B. E., Domagala J., Jackson M. J., Idnurm M., Krassay A. A., Page R. W., Sami T. T., Scott D. L., Lindsay J. F., McConachie B. A. and Tarlowski C. (2000) Chronostratigraphic basin framework for Palaeoproterozoic rocks (1730–1575 Ma) in northern Australia and implications for base-metal mineralisation. Australian Journal of Earth Sciences 47, 461– 483.

Sparks D. L. (2003) Environmental Soil Chemistry, 2nd ed. Academic Press, San Diego, CA. pp.352

Strauss H. and Schieber J. (1990) A sulfur isotope study of pyrite genesis: The Mid-Proterozoic Newland Formation, Belt Supergroup, Montana. Geochim Cosmochim Acta 54, 197–204.

Strauss H. (1993) The sulfur isotopic record of Precambrian sulphates: New data and a critical evaluation of the existing record: Precambrian Research 63, 225–246.

Strauss H. and Moore T. B. (1992) Abundances and isotopic compositions of carbon and sulfur species in whole rock and kerogen samples, in Schopf, J. W., and Kleins, C., editors, The Proterozoic Biosphere: Cambridge, Cambridge University Press, p. 709 –798.

Swanner E. D., Planavsky N. J., Lalonde S. V., Robbins L. J., Bekker A., Rouxel O. J., et al. (2014) Cobalt and marine redox evolution. Earth Planet. Sci. Lett. 390, 253–263.

Taylor S. R. and Mclennan S. M. (1995) The geochemical evolution of the continental crust. Rev. Geophys. 33, 241–265.

Tribovillard N., Algeo T. J., Lyons T. and Riboulleau A. (2006) Trace metals as paleoredox and paleoproductivity proxies: an update. Chem. Geol. 232, 12–32.

Violante A., Krishnamurti G. S. R. and Pigna M. (2008) Mobility of Trace Elements in Soil Environments. In: A. Violante, P.M. Huang, G.M. Gadd (eds). Biophysico-Chemical Processes of Metals and Metalloids in Soil Environments. John Wiley and Sons, Hoboken, NJ, pp.169-213.

Whitehouse M. J. (2013) Multiple S isotope determination by SIMS: Evaluation of reference sulfides for Δ33S with observations and a case study on the determination of Δ36S: Geostandards and Geoanalytical Research 37, 19–33.

Wignall P. B. (1994) Black Shales. Clarendon Press, Oxford. 127 pp.

Williams R. J. P. and Rickaby R. (2012) Evolutions destiny. Co-evolution of the environment and life. London: Royal Society of Chemistry.

Yang S., Kendall B., Lu X., Zhang F. and Zheng W. (2017) Uranium isotope compositions of mid-Proterozoic black shales: Evidence for an episode of increased ocean oxygenation at 1.36 Ga and evaluation of the effect of post-depositional hydrothermal fluid flow. Precambrian Research 298. 187-201.

Yarincik K. M., Murray R. W., Lyons T. W., Peterson L. C., Haug G. H. (2000) Oxygenation history of bottom waters in the Cariaco Basin, Venezuela, over the past 578,000 years: results from redox-sensitive metals (Mo, V, Mn, and Fe). Paleoceanography 15, 593– 604

Zerkle A. L., House C. H. and Brantley S. L. (2005) Biogeochemical signatures through time as inferred from whole microbial genomes. Am. J. Sci. 305, 467–502.

Chapter 5

Sedimentary Pyrites of 1210 Ma Bijaigarh Shales, Vindhyan Basin, India: Textures, Trace Element Chemistry and their Implications

Indrani Mukherjee*[1], Mihir Deb[2], Ross Large[1], Jacqueline Halpin[3], Sebastien Meffre[1] and Ivan Belousov[1]

[1]CODES, University of Tasmania, Hobart, Tasmania, Australia
[2] Professor (Retd.), University of Delhi, Delhi, India
[3]Institute for Marine and Antarctic Sciences, University of Tasmania, Hobart, Tasmania, Australia

5.0 Abstract

The Vindhyan Basin in central India preserves a thick (~5 km) sequence of sedimentary and lesser volcanic rocks that provide a valuable archive of the Proterozoic (~1800-900 Ma) in India. Here we present analysis of key sedimentary pyrite textures and their trace element (TE) concentrations in the Bijaigarh Shale (1210 $\pm$ 52 Ma) in the Vindhyan Supergroup, using reflected light microscopy and LA-ICP-MS respectively. A variety of sedimentary pyrite textures (fine-grained disseminated to aggregates, framboids, lags and microbial pyrite textures) are observed reflecting quiet and strongly reducing water column conditions punctuated by occasional high energy events (storm incursions). Key trace elements (Co, Ni, Zn, Mo, Se) and ratios of (Se/Co, Mo/Co, Zn/Co) measured in sedimentary pyrites from the Bijaigarh Shale are used to infer atmospheric redox conditions during deposition. Most TEs are depleted relative to Proterozoic mean values. Overall, we interpret these low TE signatures to indicate suppressed oxidative weathering on land due to low atmospheric oxygen levels during the Middle Proterozoic.

5.1 Introduction

Several Paleo-Mesoproterozoic and some Neoproterozoic intracratonic basins with thick platformal siliciclastic–carbonate lithologies cover extensive parts of peninsular India. The largest amongst these is the Vindhyan Basin in the Northern Cratonic Block of the peninsular shield (Fig. 5.1 inset). This basin in Central India, comprises a dominantly flat-lying, undeformed and unmetamorphosed sedimentary package (including some volcanics) that wrap around the Archean (>2.5 Ga) Bundelkhand massif in a semicircle to the north and abut against the Paleoproterozoic Aravalli orogenic belt to the northwest, the Cretaceous Deccan Traps to the southwest and the

Paleoproterozoic rocks of the Satpura Mobile belt in the southeast. Structurally, the basin is divided into a number of sub-basins, the biggest amongst which are the Rajasthan sector in the west and Son Valley sector in Uttar Pradesh-Madhya Pradesh-Bihar in the east (Fig. 5.1). In this large space-time framework, spanning from ~1800 to ~ 900 Ma (Crawford and Compston, 1970; Ray et al., 2002, Malone et al., 2008 amongst others) the basin witnessed supercontinental cyles (including apparent polar wandering), volcanic activity, episodic igneous intrusions, formation of mineral deposits and evolution of complex life forms, that has prompted multidisciplinary research in the basin (Gregory et al., 2006; Malone et al., 2008; Azmi et al., 2008; Bengston et al., 2007; Sarkar et al., 2010; Deb and Pal, 2015).

The Vindhyan Basin provides an excellent opportunity to probe the concentration of redox sensitive elements in carbonaceous horizons towards understanding the evolution of oceanic-atmospheric oxygenation patterns in the Middle Proterozoic, forming part of a period known as the "Boring Billion" (cf. Brasier and Lindsey, 1998). Certain organic matter-rich stratigraphic intervals, such as black shales/mudstones can be utilized for this purpose. Previous studies have demonstrated how redox sensitive elements in black shales can be used as paleoenvironmental indicators (Algeo et al., 2004; Algeo and Lyons, 2006; Algeo and Rowe, 2012; Scott et al., 2008; Gordon et al., 2009, Sahoo et al., 2012). Black shales also allow application of certain geochronological techniques, such as Re-Os, to acquire good age constraints. More recently, trace elements in sedimentary pyrite associated with black shales have been used to understand the paleo atmosphere–ocean redox conditions, as these associations are an excellent host for most redox sensitive trace elements (Large et al., 2014; Large et al., 2015a, b; Mukherjee and Large, 2016, 2017). Apart from trace element concentrations, sedimentary pyrite textures also provide insights into depositional conditions and paleo-biological conditions when pyritized microbial textures are present.

The present study focusses on a particular part of the Upper Vindhyan stratigraphy i.e., organic matter-rich pyritic black shales, known as the Bijaigarh Shale (Kaimur Group), as exposed near Amjhore (Fig. 5.1). The Bijaigarh Shale is an excellent repository of a variety of sedimentary pyrite textures, some of which have been described in earlier literature (e.g., Pandalai and Chandra, 1986; Sur et al. 2006) and others being recorded here for the first time. Here we use these pyrite textures and their associated trace element concentrations to reveal ocean and atmosphere redox conditions in the Vindhyan Basin during the deposition of the Bijaigarh Shale. Recent Re-Os geochronology of the Bijaigarh Shale (1210 $\pm$ 52 Ma) by Tripathy and Singh (2015) allows us to further interpret these Mesoproterozoic paleoredox global redoxconditions.

5.2 Geological Background

The Vindhyan basin, like other "Purana" basins in India, is generally considered to have developed as a failed rift basin in Archean to early Paleoproterozoic basements rocks (Chaudhuri et al., 2002). Tholeiitic

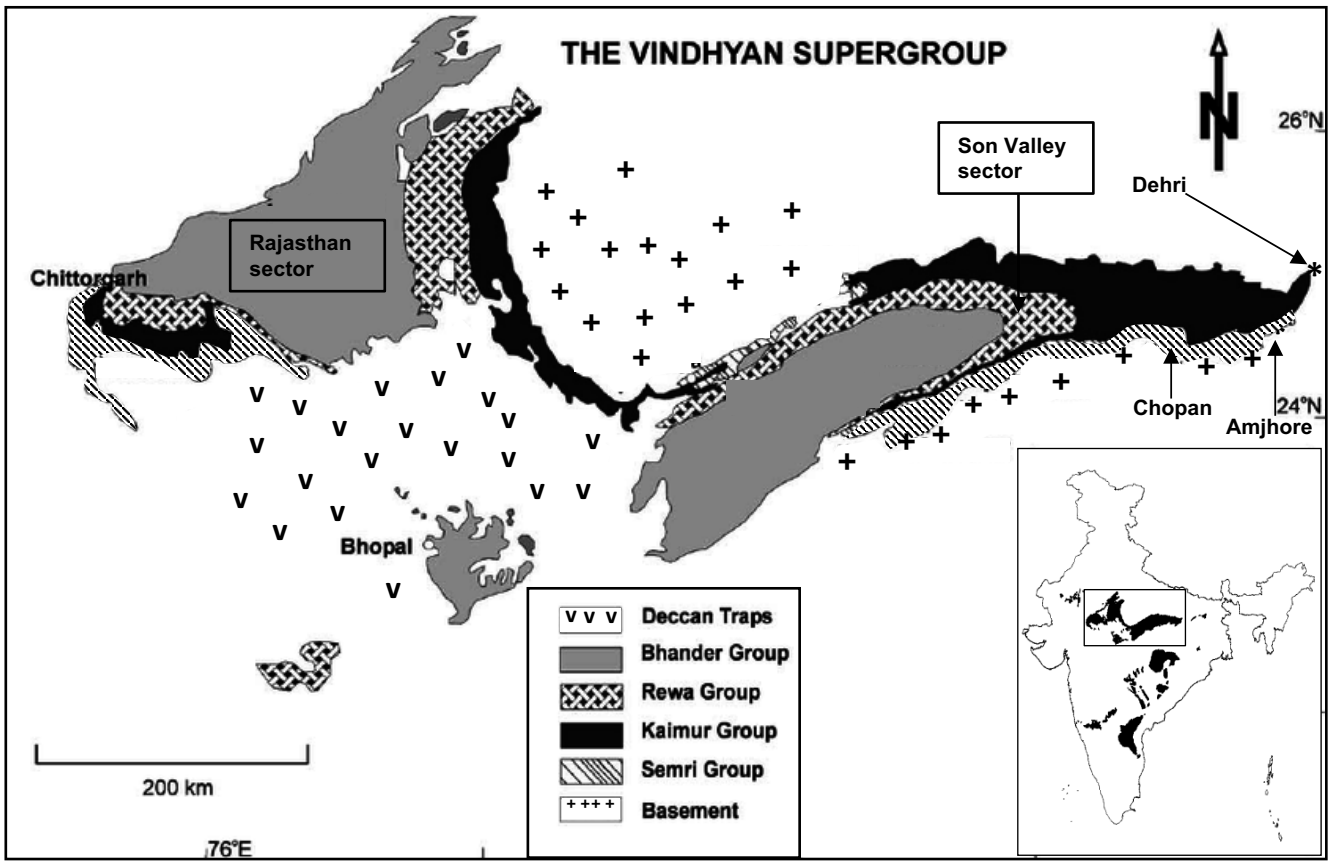

Fig 5.1 Geological map of the Vindhyan basin (after Soni et al., 1987), showing the two main sectors: Rajasthan in the west and Son valley in the east. The inset shows the different Proterozoic basins in India and the location of the Vindhyan basin in the northern cratonic block.

magmatism around 1800 Ma in Bijawar, Sonrai and Gwalior areas, encircling the Vindhyan basin, bear evidence of the extensional growth of the initial rifts. Most workers now agree that the Vindhyan sediments were deposited in a westward-opening epicontinental basin in an intracratonic setting (cf. Chanda & Bhattacharyya 1982; Chakraborty and Karmakar 1998).

5.2.1 Stratigraphy and Age

Stratigraphically, the Vindhyan Basin is divided into the Paleoproterozoic Lower Vindhyan and the mostly Mesoproterozoic Upper Vindhyan (Fig. 5.2), separated from each other by a basinwide unconformity (Soni et al. 1987). The Lower Vindhyan is represented by the Semri Group of rocks which unconformably overlie either the 1854 $\pm$ 7 Ma Hindoli Group of rocks (Deb et al., 2002) of the Aravalli belt or the 2492 $\pm$ 10 Ma Bundelkhand granites (Mondal et al., 2002). The Semri Group comprises an alternating sequence of shales, carbonates and patchy sandstones along with two known periods of volcanic activity, with the Porcellanite Formation being the most conspicuous. The Upper Vindhyan constitutes the Kaimur, Rewa and Bhander Groups with sandstones, shales and marls and volcanic activity recorded at the base of the Rewa Group. Rocks of the Kaimur

Group are also intruded by diamond-bearing kimberlites and lamproites.

The depositional age of the Vindhyan sequence has received a lot of world attention in recent years. The Lower Vindhyan sediments are now well constrained to the Paleoproterozoic between ~1800–1600 Ma through a number of radiometric studies (Fig. 5.2) on the Kajrahat Limestone (Kumar et al., 2001); Porcellanite Fm. (Ray et al., 2002); Rampur Shale (Rasmussen et al., 2002); and Rohtas Limestone (Ray et al., 2003; Sarangi et al., 2004), mostly based on the U–Pb and Pb–Pb dating techniques. In contrast, sediments from the Upper Vindhyan (Kaimur, Rewa and Bhander groups) still lack robust chronological control (Ray, 2006). In the Son valley, a basin wide unconformity exists between the Rohtas limestone of Lower Vindhyan and the overlying Upper Vindhyan Kaimur Group represented by a lower shale unit followed upward by a quartz-rich sandstone including a volcaniclastic deposit (Bose et al., 2001). Amongst the three groups, the Kaimur Group is best constrained mainly due to a recent bulk rock Re-Os isochron depositional age of 1210 $\pm$ 52 Ma for the Bijaigarh Shale (Tripathy and Singh, 2015) in the middle part of the Group. The Majhgawan kimberlite pipe, which cuts across the Semri and Kaimur groups and is exposed near Panna within upper Kaimur (Baghain) sandstones, has an emplacement age of 1073 $\pm$ 13.7 Ma (Gregory et al., 2006). This constrains the age of the uppermost Kaimur Group to the Mesoproterozoic and suggests that the Rewa and Bhander groups may represent Neoproterozoic sequences. Detrital zircon analysis of the Upper Bhander sandstone (Malone et al., 2008) on the other hand identifies a youngest age population at ~1020 Ma. Depositional age for the uppermost Bhander Group has recently been constrained by Pb–Pb dating of three carbonate horizons by Gopalan et al. (2013) at ~900 Ma (Fig. 5.2). This short summary of geochronologic data of Vindhyan Supergroup rocks brackets its age between Late Paleoproterozoic and Early Neoproterozoic, with a substantial part of the Upper Vindhyan sequence deposited in the Mesoproterozoic.

5.2.2 Bijaigarh Shale

The Bijaigarh Shale is a laterally persistent unit of organic matter-rich black shale in the Kaimur Group, up to 70m in thickness, sandwiched between the lower Kaimur sandstone below and the upper Kaimur sandstone above (Fig. 5.2). The thickness of the unit decreases towards the west and the unit pinches out west of Chopan (Auden, 1933). A pyritiferous horizon divides this shale unit into a lower shale (average thickness 32m) and a top shale (average thickness 15m) (Banerjee et al., 2006), best developed at Amjhore, about 20 km south of Dehri-on-Son, in the Vindhyan hills of Rohtas district, Bihar (Fig. 5.1). Here, the pyritic shale occurs as a 0.78 m-thick stratiform horizon within the carbonaceous shales extending over an area of 2.1 km^2. The uniform thickness as well as the conformable nature of the pyrite bed with the overlying and underlying carbonaceous shale

is a conspicuous feature throughout. The bottom shale has fine intercalations of sandstones and siltstones, is less carbonaceous (TOC: 1.53-1.89%, Banerjee et al., 2006) and shows gradational contact with the lower Kaimur sandstone. The upper shale, on the other hand, contains only a few siltstone beds, but is more carbonaceous (TOC: 3.83-4.15%, Banerjee et al., 2006). A transitional zone of siltstone and argillaceous sandstone is reported (Banerjee and Prakash, 1975) to host some galena mineralization near the upper contact of the Bijaigarh Shale with Kaimur sandstone.

Sedimentary pyrite exhibits syn-depositional features within the carbonaceous Bijaigarh Shale (Guha, 1971; Nair and Ray, 1977; Pandalai and Chandra, 1986), and attains substantial local concentration in the form of lenses and beds at Amjhore, where a pyrite mine (N24°43'36.9"; E83°59'40.3") was operated by Pyrites, Phosphate and Chemicals Ltd. (PPCL), a Government of India undertaking, until 2003. The top shale above the pyrite bed also has abundant pyrite disseminations and minute pyrite-rich laminae whereas the bottom shale below the orebody contains fewer disseminated pyrite. All features cumulatively suggest a deeper environment of deposition for the upper shale unit.

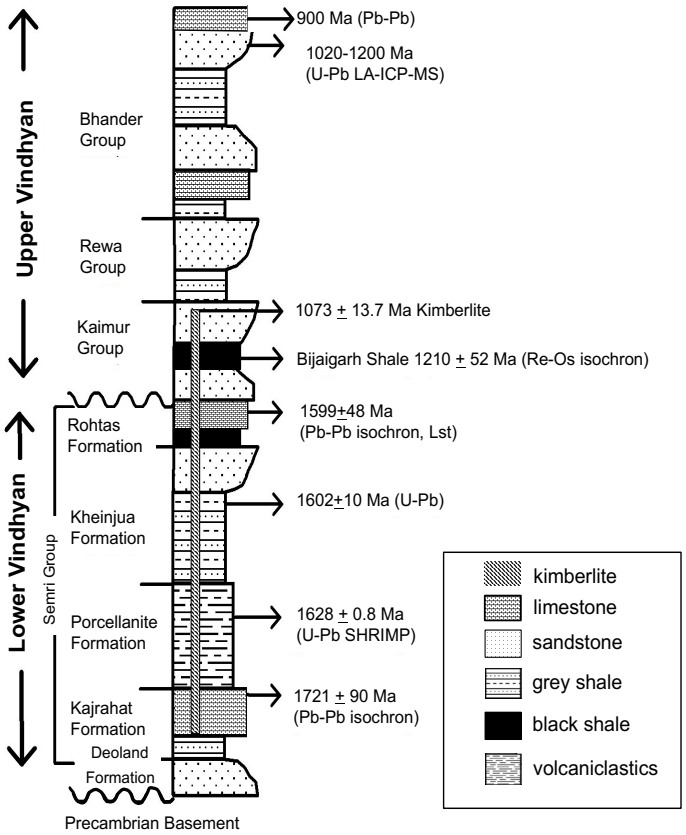

Fig 5.2 A generalised stratigraphic column of the Vindhyan Supergroup showing the major geochronologic data and the position of the Bijaigarh shale in the Upper Vindhyan sequence. (Modified after Sarkar et al., 2010)

The sediments of the Kaimur Group of rocks were deposited in a terrestrial setting, and their environment of deposition changed from alluvial fan, braided plain, fan delta to lacustrine facies (Valdiya, 2010). The Bijaigarh Shale within the Kaimur Group is the only stratigraphic horizon to manifest a strongly anoxic environment with profuse biogenic activity, as evidenced by the prevalence of pyritiferous carbonaceous sediments. It has been considered to represent a lagoonal deposit with an open ocean connection in some studies (Singh, 1980; Tripathy and Singh, 2015) and inner to outer shelf by others (Chakraborty et al., 1995). Based on several sedimentological features, Bose et al. (2001) proposed that the Bijaigarh Shale is a shelf deposit below fair-weather wave base, formed as a result of maximum flooding following a transgressive systems tract (TST), when the Vindhyan basin was an epicratonic sea with an open ocean connection to the northwest. Presence of features like profuse gutter casts suggest intermittent storm incursions during the deposition of the Bijaigarh Shale within the overall transgressive framework (Chakraborty, 2006).

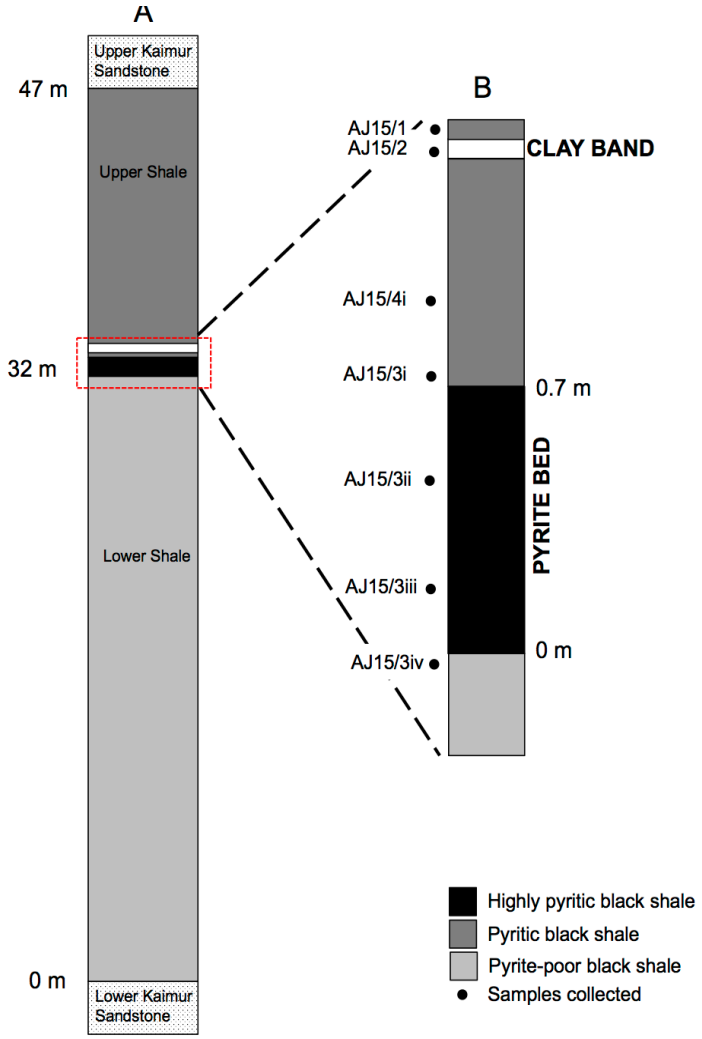

Fig 5.3 (A) Stratigraphic column of the Bijaigarh shale unit at Amjhore (after Banerjee et al., 2006); (B) Location of samples collected for this study.

5.3 Method

The pyrite bed and the immediate bottom and top carbonaceous shales were sampled in two adjacent adits which are accessible in the erstwhile Amjhore mine. A total of nine samples were collected in vertical profiles, out of which seven samples with high to low pyrite content were studied in detail (Fig. 5.3). The two samples rejected did not have any discernible pyrite.

Polished 1-inch laser mounts (pieces of rock mounted in epoxy) were used for reflected light microscopy prior to trace element analyses (66 pyrite analyses) using LA-ICP-MS facility at CODES, University of Tasmania. Analyses were performed in a time-resolved mode using CompexPro 110 ArF Excimer laser microprobe equipped with S155 cell and coupled to an Agilent 7700 ICP-MS. Each analysis consisted of 30 s background and 60 s of ablation signal acquisition in counts per second (cps). Ablation was performed at energy density of 2.7 J/cm^2 and 5 Hz laser repetition rate, dwell times varying between 5 and 50 ms, depending on the count rates and total sweep time (time required to measure all isotopes once) of 0.76 s. Ablation was carried out in pure He atmosphere, introduced at a rate of 0.35 l/min in the ablation cell after which Ar was mixed with a rate of 1.05 l/min for improved efficiency of aerosol transport. Primary reference materials (STGL2b2, GSD-1G and pyrite crystal) were analysed every 1.5 h (after analyses of two samples) in order to quantify and correct for the drift in the sensitivity of the instrument. STDGL2b2 is an in-house standard used for primary calibration for quantifying siderophile and chalcophile elements (Danyushevsky et al., 2011); GSD-1G (USGS reference material; Jochum et al., 2005) was used to quantify lithophile elements; sulfur was quantified using massive pyrite with stoichiometric Fe and S (46.5 wt.% Fe, 53.5 wt.% S). Approximately, 10 pyrite spot analyses and 5 black shale matrix spot analyses were conducted on each laser mount with 29 µ spot size. Due to the fine-grained nature of the sedimentary pyrites, matrix material of the black shales was analysed for trace elements, in order to negate effects of matrix contamination during laser ablation of fine-grained pyrite. Sedimentary pyrites were analysed for ^{13}C, ^{23}Na, ^{24}Mg, ^{27}Al, ^{29}Si, ^{34}S, ^{39}K, ^{43}Ca, ^{49}Ti, ^{51}V, ^{53}Cr, ^{55}Mn, ^{57}Fe, ^{59}Co, ^{60}Ni, ^{65}Cu, ^{66}Zn, ^{75}As, ^{77}Se, ^{85}Rb, ^{88}Sr, ^{90}Zr, ^{95}Mo, ^{107}Ag, ^{111}Cd, ^{118}Sn, ^{121}Sb, ^{125}Te, ^{137}Ba, ^{157}Gd, ^{178}Hf, ^{181}Ta, ^{182}W, ^{195}Pt, ^{197}Au, ^{202}Hg, ^{205}Tl, ^{206}Pb, ^{207}Pb, ^{208}Pb, ^{209}Bi, ^{232}Th and ^{238}U and a range of trace elements such as Co, Ni, Se, Mo, Zn, Pb, Tl and Cu are presented in Table 5.1. Raw LA-ICP-MS generated-data, in counts per seconds were converted into parts per million (ppm) using CODES in-house data reduction software according to standard methods (Longerich et al., 1996). The method uses Fe as the internal standard element and assumes a constant stoichiometric Fe content of pyrite to calculate preliminary compositions which are then normalized to a 100% total of siderophile, chalocophile and oxides of lithophile elements. The conversion involved splitting

the integration curve (curve obtained from counts per second vs analysis time) into five segments of equal duration, calculated using time-equivalent calibration standards. To calculate the final concentrations, a linear regression equation (using S content) was employed such that the sum of the chalcophile and siderophile elements including S was 100%. Also, regression fits for individual analyses were visually inspected. Errors associated with these analyses depends on various factors such as quality of regression fit, concentration of element, abundance of measured isotope etc. For most TEs at higher concentrations, relative error is under 20% for 75% of analyses. However, uncertainty increases at lower concentrations. The analytical errors sourced from the uncertainty on composition of the reference materials is estimated under 5% (Danyushevsky et al., 2011).

5.4 Results

5.4.1 Pyrite textures under reflected light microscope

A textural study of the pyrite grains using reflected light microscopy was undertaken for two reasons. Firstly, sedimentary pyrite textures can provide clues to the depositional conditions including redox levels, water column stratification, energy conditions and microbial activity, as highlighted in several previous studies (Baird and Lash, 1990; Baird and Brett, 1991; Wilkin et al. 1996; Lyons, 1997; Wignall and Newton 1998; Schieber, 1998; Schieber and Baird, 2001; Formolo and Lyons, 2007; Rickard, 2012; Rickard et al., 2017 amongst others). Secondly, pyrite textures were carefully recorded prior to LA-ICP-MS analyses in order to ensure only sedimentary to early-diagenetic pyrites were analysed for the study.

The pyrite bed in Amjhore is characterized by two different varieties of pyrite: a cryptocrystalline massive type and a disseminated type. The bulk of the pyrite belongs to the former type and comprises pyrite spheroids and idiomorphic pyrite crystals within a groundmass of cryptocrystalline pyrite. The disseminated type is made up of dense agglomerations of framboidal pyrite and disseminated subhedral to euhedral grains of pyrite in the carbonaceous shale, with the pyrite spherules ranging in diameter from 100 to 1200 μm (Guha 1971; Pandalai and Chandra, 1986; Pandalai et al. 1991). It also comprises pyritic clasts, either dispersed or concentrated in patches and bands.

This study, focused on the disseminated pyrite types, identified various sedimentary pyrite textures in the Bijaigarh Shale. Most common are fine-grained disseminations of sedimentary pyrite grains in carbonaceous shale, including aggregates of fine-grained pyrite coalesced in sub-rounded to elongated patches parallel to the bedding plane (Fig. 5.4a). Within such bedding foliation, sometimes wavy,

framboids of pyrite are also noted (Fig. 5.4b), which have also been described in previous studies of Amjhore pyrite (Pandalai and Chandra, 1986; Sur et al., 2006; Schieber et al., 2007). In some samples, partial (Figs. 5.4c, 5.4d) to complete (Figs. 5.4e, 5.4f) replacement of preexisting spherical structures in the black shale matrix by pyrite is observed. In some places, pyrite overgrowths around the spheres are also seen (Fig. 5.4f). Some nodular/spheroidal and stromatolitic/microlaminar carbonaceous concentrations (Figs. 5.5a, 5.5b) in the pyritic shale groundmass possibly represent microbial structures. Rounded-sub-rounded clasts of pyrite dispersed in a pyritic black shale matrix are interpreted as pyrite lag deposits (Fig 5.5c, 5.5d), formed by physical reworking of the pyrite bed in a high-energy environment. Both zoned and unzoned pyrite overgrowths are also present in such deposits (Fig 5.5e, 5.5f).

Pyrite infillings in a possibly geopetal structure (Fig 5.6a) or producing a lensoid shape (Fig 5.6b) are observed in some samples. Also, commonly noted are pyrite clasts, possibly representing bioclasts, which have been pyritised later during or after the deposition of the Bijaigarh Shale (Figs. 5.6c, 5.6d, 5.6e, 5.6f). Overall, a variety of sedimentary textures (possibly of both biotic and abiotic origins) characterize the pyrite in the sulfide horizon and also in the lower and upper shales. Interpretation of these textures and several possible formation mechanisms are discussed in a later section (refer textural implications).

The order in which these textures are observed and occur across the pyrite bed i.e., from the top of the bottom carbonaceous shale to the pyrite bed to the upper carbonaceous shale, is interesting to note (Fig. 5.7). As mentioned above, fine-grained pyrite in layers, aggregates (including framboidal) and fine disseminations of microcrystals of pyrite occur all through the section. Black shales underlying the basal pyrite bed are relatively pyrite–poor compared to all other samples and pyrite mainly occurs as microcrystals disseminated in the shale. Further up stratigraphy into the pyrite bed, we observe a very pyritic shale with pyrite spheres and lenses including lag deposits where individual pyrite clasts are fairly well rounded (Fig. 5.7). In these samples, we also observe spherical concretions and stromatolite-like structures (Fig. 5.7). Closer to the contact between the pyrite bed and upper carbonaceous shale, we observe textures like pyrite infillings and lenses that are possible geopetal structures. The upper shale exhibits streaks of fine-grained pyrite in repetitive layers. Close to the clay band, we observe another pyrite lag deposit where pyritised clasts (possibly bioclasts) are plentiful (Fig. 5.7).

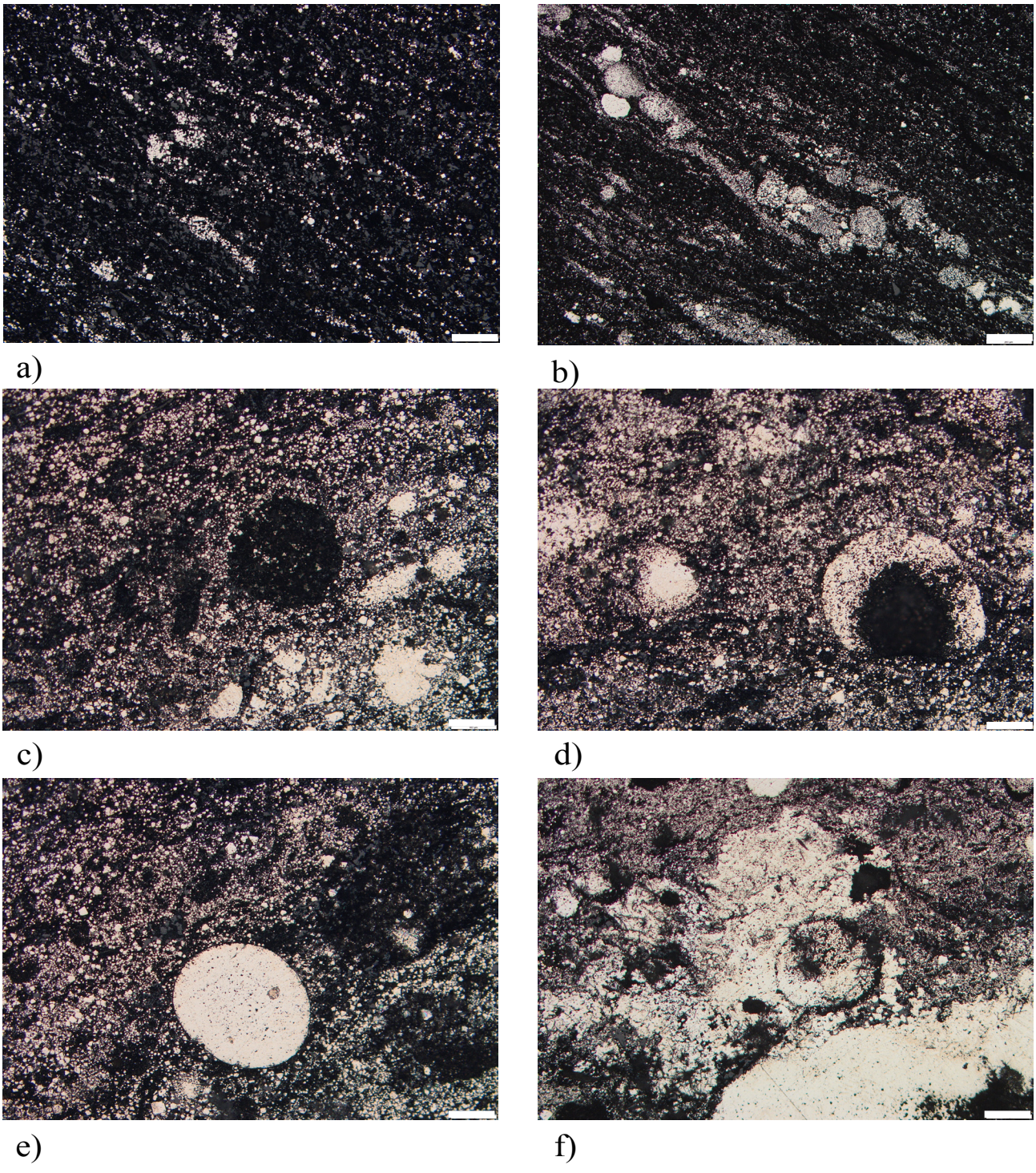

Fig 5.4 Photomicrographs under reflected light; scale bar for a, f=200 μ; for b, c, d, e= 100 μ

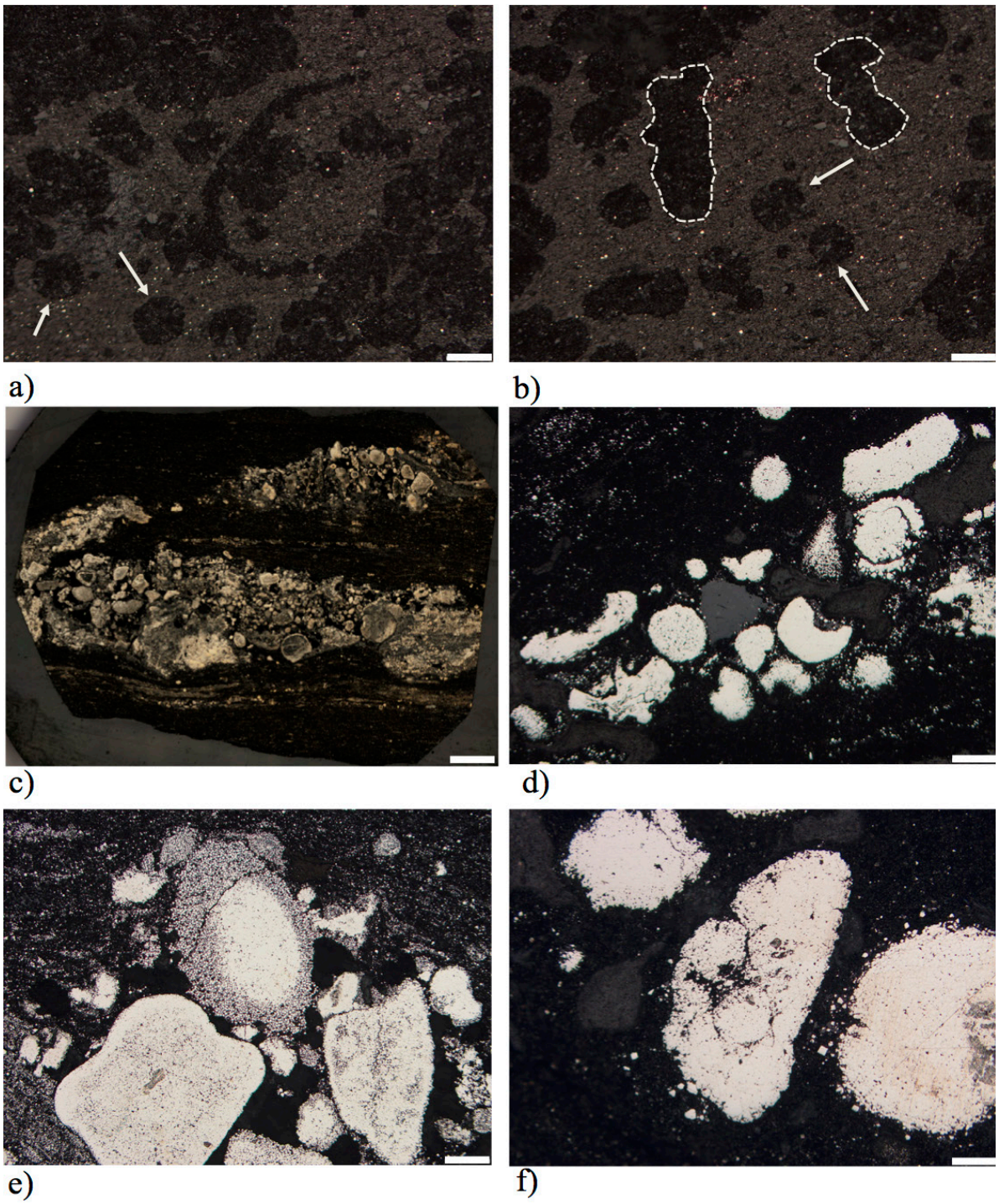

Fig 5.5 Photomicrographs under reflected light; scale bar for a, b, d, e =200 μ; for f = 100 μ; for c=1.6 mm

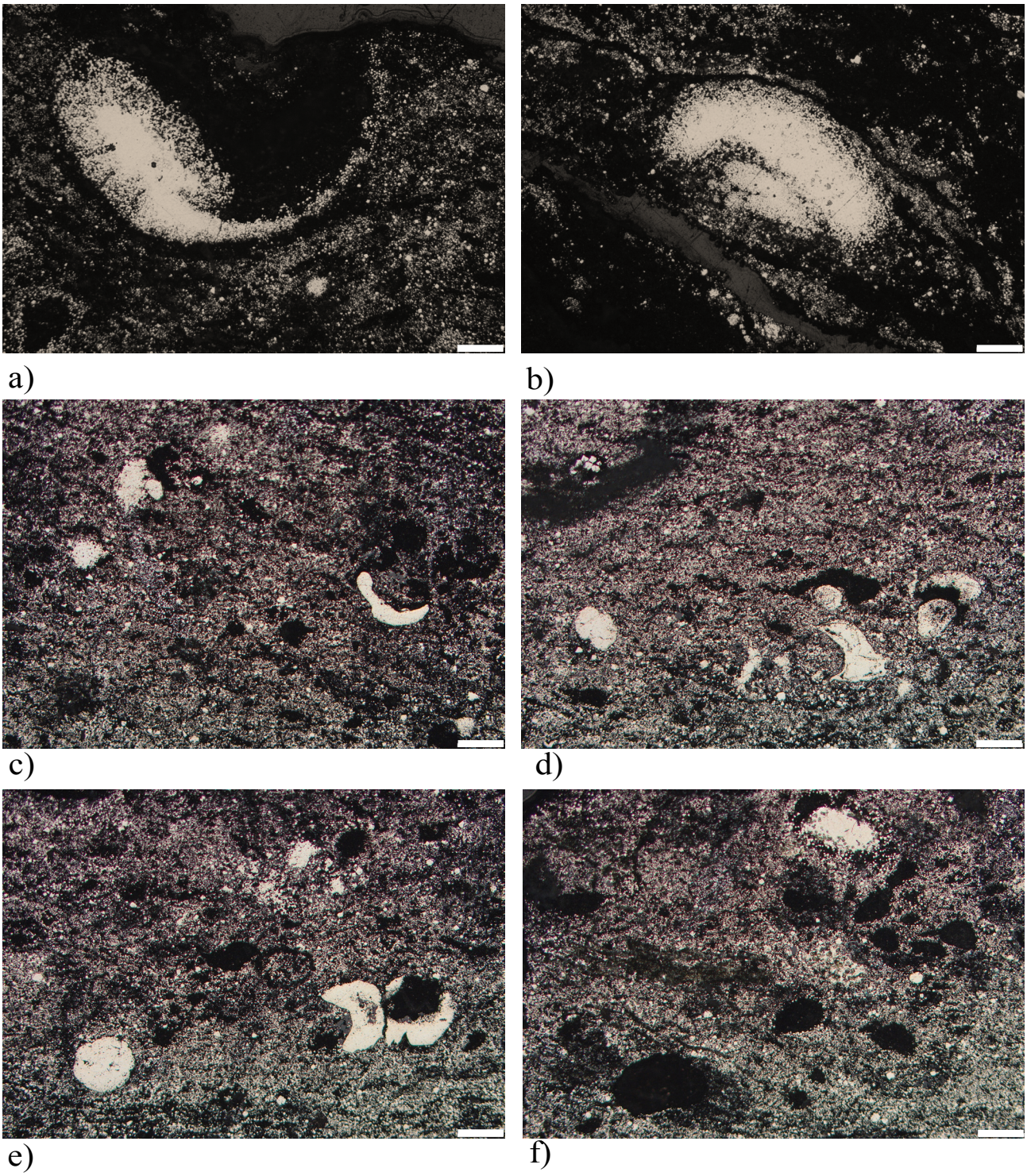

Fig 5.6 Photomicrographs under reflected light; scale bar for a, b, c, d, e, f = 200 μ

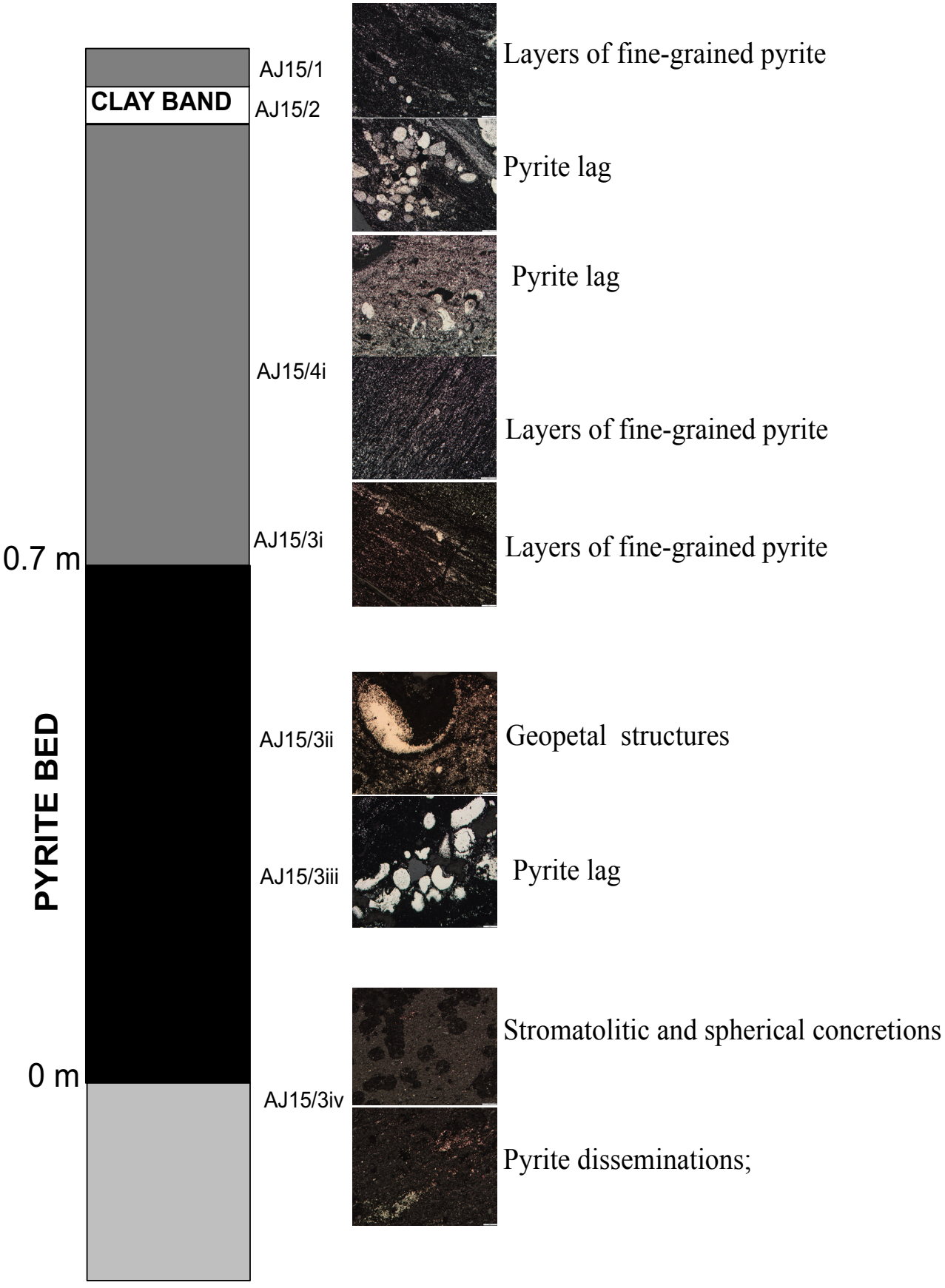

Fig 5.7 Textural variation observed up-stratigraphy

Table 5.1 Mean trace element concentrations of fine-grained pyrite vs pyrite lag

Trace Elements	Bijaigarh Shale (fine grained) n=37	Bijaigarh Shale (pyrite lag) n=29
Co	340	289
Ni	288	134
Cu	155	82
Zn	117	35
Se	15	11
Mo	57	30
Tl	16	10
Pb	202	1301
Se/Co	0.113	0.049
Ni/Co	1.31	0.50
Mo/Co	0.23	0.103
Zn/Co	0.411	0.13

Table 5.2 Mean trace elements in this study compared to mean pyrite analyses by Large et al. (2014, 2015, 2017); concentrations are in ppm

	n	Co_Py	Ni_Py	Cu_Py	Zn_Py	As_Py	Se_Py	Mo_Py	Tl_Py	Pb_Py	Se/Co	Ni/Co	Mo/Co	Zn/Co
Bijaigarh Shale unit (Average)	66	317	220	123	81	614	13	45	14	685	0.085	0.953	0.202	0.287
Phanerozoic	~2900	347	945	356	259	1181	128	137	18	351	31.72	26.61	14.76	21.58
Proterozoic	~1000	439	651	635	157	1276	30	72	17	456	1.311	6.760	1.111	1.534
Archean	~800	1027	1873	494	171	2251	28	13	10	569	0.130	3.304	0.033	1.320

5.4.2 Pyrite LA-ICP-MS Trace Element Chemistry

Redox sensitive trace elements in black shales and more recently, in sedimentary pyrites, have been used to interpret paleoredox conditions in the ocean and atmosphere (Algeo and Lyons, 2006; Trivobillard et al., 2009; Scott et al., 2008; Sahoo et al., 2012; Partin et al., 2013; Large et al., 2014; Mukherjee and Large, 2016). In this study, we measured key trace elements (Ni, Co, Cu, Se, Mo, Zn, Pb, Tl) in sedimentary pyrite using LA-ICP-MS to provide additional insights into the evolving depositional conditions during the formation of the Bijaigarh Shale. Pyrite trace element analyses for fine grained disseminated pyrite and the coarse pyrite lags are presented separately in Tables A5.1 a and b (See appendix).

The fine-grained variety of pyrite in the Bijaigarh Shale unit exhibit slightly higher concentrations of Ni, Cu, Mo and high concentrations of Zn compared with their coarser counterparts (Table 5.1). Mean Ni, Cu and Mo in fine grained pyrite are 288 ppm, 155 ppm and 57 ppm respectively compared to 134 ppm, 82 ppm and 30 ppm respectively in coarser varieties. Mean Zn is ~100 ppm in finer grained pyrites compared to 35 ppm in coarser varieties. Selenium, Co and Tl remain roughly the same in both varieties (Table 5.1); mean Se, Co and Tl in fine grained pyrite are 15 ppm, 340 ppm and 16 respectively, and in coarser grains are 11 ppm, 289 ppm and 10 ppm respectively. Very high Pb concentrations are noted in the coarse pyrite lags (~1300 ppm) compared to the finer grained variety (~200 ppm) (Table 5.2). Ratios of Se/Co, Ni/Co, Mo/Co, Zn/Co are also 2 to 3 times higher in finer grained pyrites compared to coarser varieties (Table 5.1).

Mean of trace element concentrations of both pyrite types and their ratios in this study have been compared with the mean of ~4700 sedimentary pyrite analyses categorized into different time spans i.e., Phanerozoic, Proterozoic and Archean (Large et al., 2014; 2015b; 2017) (Table 5.2). This was mainly done to compare the pyritic Bijaigarh Shale with sedimentary pyrites of varying ages (Table 5.2). Concentrations of trace elements and their ratios in the Bijaigarh Shale unit are significantly lower than the Phanerozoic sedimentary pyrites (Large et al., 2014, 2015b) except Co, Tl which are only slightly lower. Lead however, is higher in the Bijaigarh pyrites relative to the Phanerozoic. When compared to the Proterozoic average, trace element concentrations and their ratios are also lower in the Bijaigarh pyrites. Cobalt, Ni, Cu concentrations, Ni/Co, Zn/Co in the Bijaigarh Shale unit are also significantly lower compared to the Archean, with Zn, Se, Se/Co being only slightly lower. Molybdenum, Tl, Pb and Mo/Co are slightly higher in the Bijaigarh Shale unit compared to the Archean

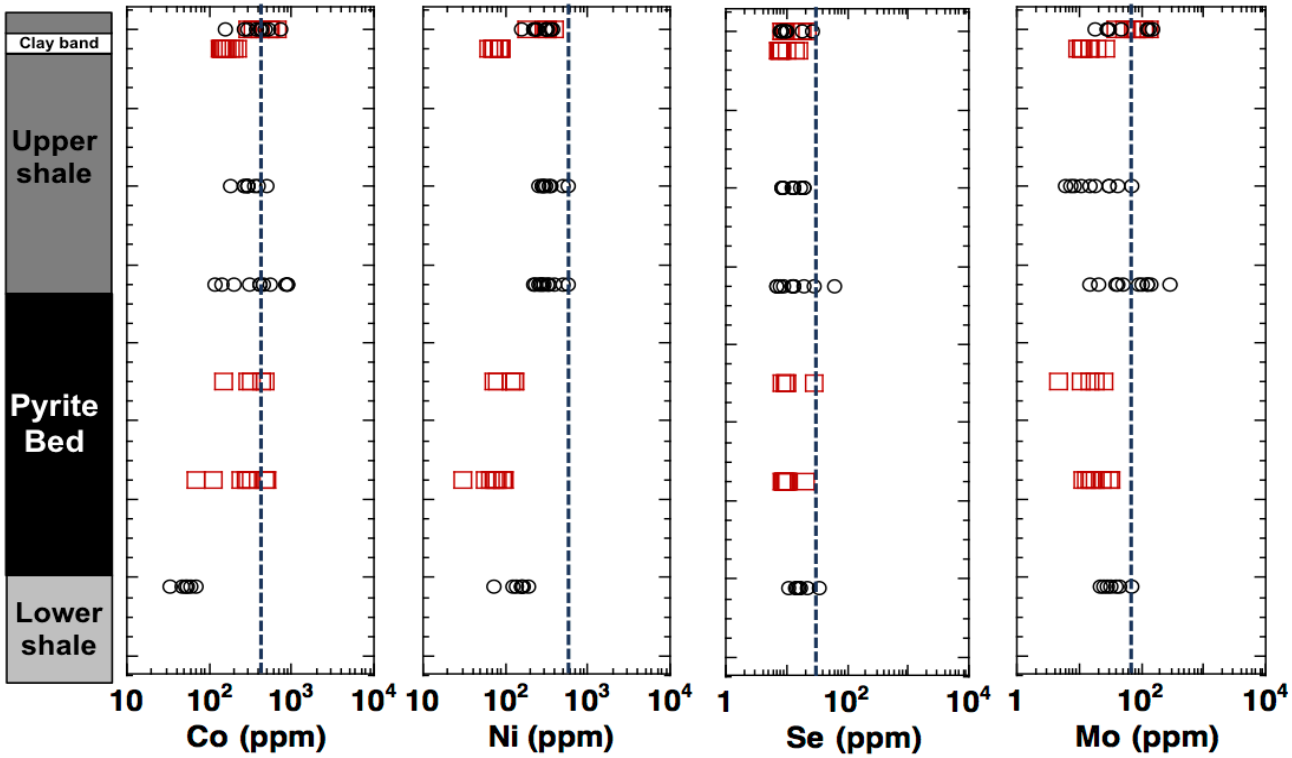

Fig 5.8 Trace element concentrations (Co, Ni, Se, Mo) in the Bijaigarh Black Shale Member; blue dashed line represents Proterozoic mean values (Large et al., 2017); red squares=pyrite lag; black circles=fine-grained pyrite

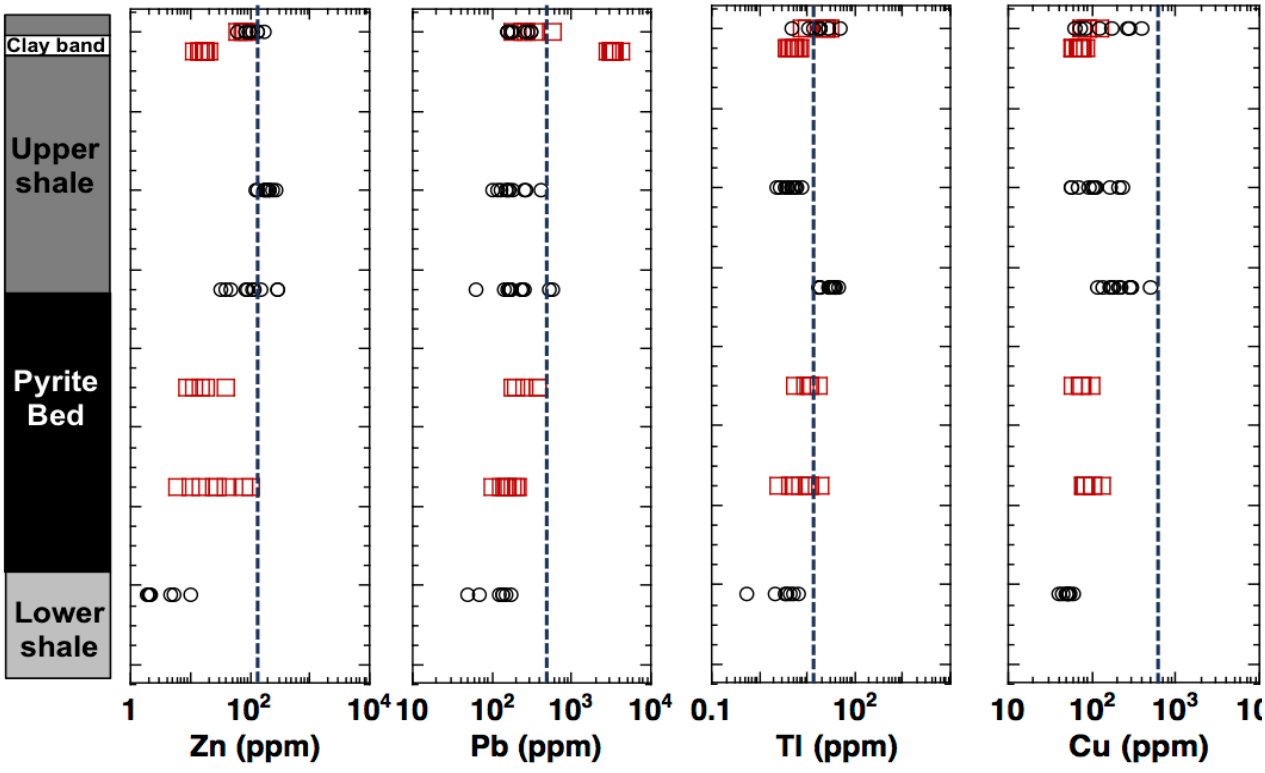

Fig 5.9 Trace element concentrations (Zn, Pb, Tl, Cu) in the Bijaigarh Black Shale Member; blue dashed line represents Proterozoic mean values (Large et al., 2017); red squares=pyrite lag; black circles=fine-grained pyrite

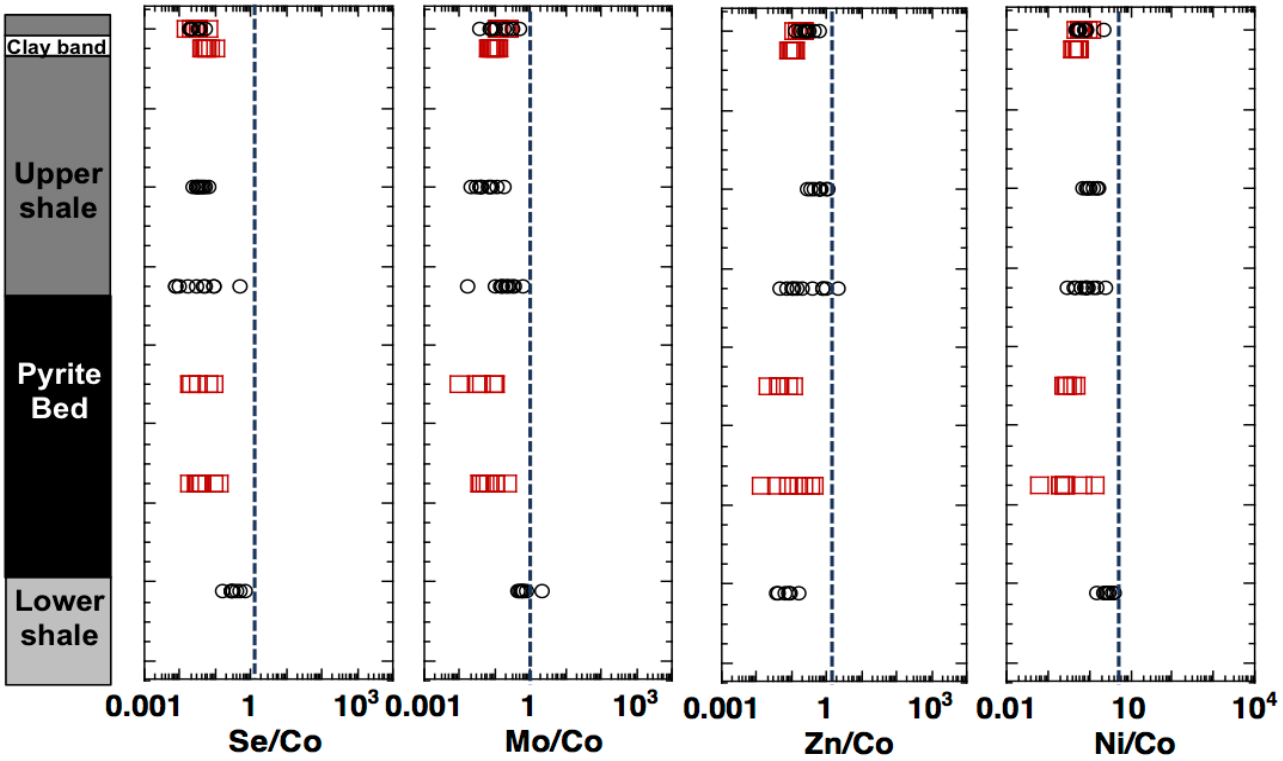

Fig 5.10 Trace element ratios (Se/Co, Mo/Co, Ni/Co, Zn/Co) in the Bijaigarh Shale Member; blue dashed line represents Proterozoic mean values (Large et al., 2017); red squares=pyrite lag; black circles=fine-grained pyrite

5.5 Discussion

5.5.1 Textural implications

The Bijaigarh Shale, particularly the pyrite bed and the upper carbonaceous shale, exhibits a variety of textures possibly recording the various depositional conditions operative during its formation. Sedimentation commenced in an oxygen-poor environment created as a result of decomposition of high levels of organic matter. Assuming an authigenic supply of Fe (from the sediments or water column), bacterial sulphate reduction in the sediment/water column led to the formation of microcrystals of pyrite as evidenced by the pyrite disseminations in the lower carbonaceous shale. With subsequent deposition of abundant organic matter, oxygen was entirely consumed; further bacterial sulphate reduction combined with a steady supply of Fe, the shale became more pyritic. This is indicated by the formation of pyrite in layers and aggregates grading into massive pyrite layers i.e., the pyrite bed.

Occasional reworking of the sediments possibly caused the formation of the pyrite lags. This could

be attributed to high-energy storm incursions during sedimentation. Other sedimentological studies in the formation (tidal bundles, gutter casts etc.) also confirm such disruptive events (Bose and Chaudhari, 1990; Chakraborty, 2006; Sarkar et al., 2010). In the absence of such high-energy events, pyrite formed in layers and aggregates as commonly observed in all the samples. One could argue that the pyrite clasts in the lag deposit were derived from a distant source and not the Bijaigarh Shale. However, if that was the case, then we would expect significant differences in pyrite trace element concentrations in samples (e.g., AJ/15/1) where both fine-grained and pyrite lag were analysed (Table A5.1 a and A5.1 b). The data does not support this situation and we interpret the lags to be derived as a result of reworking of the underlying pyrite laminations.

Textural evidence suggests that some clasts within the pyrite lags may be biogenic (Fig. 5.6). It is possible that pyrite precipitation occurred on surfaces of microbial remnants (hard or soft parts?), manifested in the form of pyritised bioclasts and pyrite infillings. A biogenic origin of these clasts is highly likely, supported by two features: high TOC% (3-4%) observed in the Bijaigarh Shale unit (Banerjee et al., 2006) and the characteristic shapes of these clasts. It is also possible that the spherical clasts are abiogenic and have formed due to extensive reworking. It is interesting to note that these spherical/rounded clasts co-occur with non-spherical clasts. Therefore, extensive reworking could not have caused sphericity/roundness in selective clasts only. Also, phosphatic concretions and microbial mat formation has been described from the Bijaigarh shale in previous studies (Sur et al., 2006; Schieber et al., 2007). Concretions and stromatolite-like structures have been noted in Fig 5.5a, b as well, which points towards a biogenic origin for these clasts.

Differences in trace element concentrations and their ratios have been noted in fine-grained pyrite and pyrite lag textures. Most trace elements except Pb are enriched in the finer grained variety of pyrite relative to the coarser variety. Minor recrystallization of the coarse pyrite during diagenesis and lag formation may be the cause, as noted in other black shale formations (Large et al, 2007; 2014) However, in one sample (AJ15/1) where both types of pyrites were analysed, little differences were observed. This is why we conclude here that the variation is possibly due to changes in depositional conditions up through the stratigraphy.

5.5.2 Atmospheric redox implications

Trace element concentrations, such as Mo, Se, Co, Zn, Ni, Cu, Pb, Tl and certain trace element ratios (Se/Co, Mo/Co, Zn/Co) are used here to interpret paleo-atmospheric redox condition during the deposition of the Bijaigarh Shale. This is based on the fact that oxidative weathering on land

releases these trace elements into the riverine flux, which is a dominant source of these trace elements in the marine system (Bertine et al., 1973; Taylor et al., 1995; Scott et al., 2008; Sahoo et al., 2012; Crowe et al., 2013; Large et al., 2014). However, Co relative to Se, Mo, Ni, Zn is retained by Fe-Mn oxides and hydroxides on land, which decreases its supply in the riverine flux during oxygenation. Whilst Mo, Se, Ni and Zn should increase in concentrations in sedimentary pyrite due to progressive oxygenation on land, Co generally shows an opposite trend (Mukherjee and Large, 2016). Any increase in the former should be accompanied by decrease in Co; therefore, ratios of Se/Co, Mo/Co and Zn/Co are considered as robust paleo-indicators of atmospheric oxygenation. Apart from oxidative weathering, provenance of the sediments also bears a control on the type of trace element flux. Trace element patterns in this study will be discussed in light of these two trace element source parameters.

Most trace element concentrations and their ratios are below or close to the mean values for the Proterozoic, indicated in Figs 5.8, 5.9, 5.10 by the blue dashed line, which is not uncommon for Proterozoic black shales. Several studies have indicated that low atmospheric oxygen during the Proterozoic has resulted in suppressed trace element signatures in black shales (Scott et al., 2008; Sahoo et al., 2012; Partine et al., 2013; Large et al., 2014). Elements like Co, Ni, Se, Mo, Cu, Tl and Zn show a trend where concentrations are mostly below or close to the Proterozoic mean values (blue dashed line in Figs 5.8, 5.9). Lead on the other hand shows a significant enrichment in the clay band present in the upper carbonaceous shale. Reasons as to why the pyrites are enriched in Pb are speculative. There is however a thin band of galena mineralization (0.4% Pb) in the siltstone between the upper carbonaceous shale and the Upper Sandstone. Concentrations of Pb other than in the clay band are generally consistent and low (below the Proterozoic mean values). Ratios of ^{207}Pb and ^{206}Pb of the fine-grained pyrites and Pb-enriched pyrites were calculated and they were similar (= 0.860). That rules out the possibility of a later Pb enrichment in the sediments.
Other oxygenation proxies such as Se/Co, Mo/Co and Zn/Co are all below the Proterozoic mean value (Fig 5.10) indicating an absence of any significant oxygenation. Ratios of Se/Co and Mo/Co of the Bijaigarh Shale unit have also been compared to Archean and Phanerozoic (Fig 5.11). It is evident that although values are significantly lower than the Phanerozoic, they are higher than the Archean. This implies lower atmospheric oxygen levels at ~1.2 Ga relative to the Phanerozoic but higher than the Archean (Fig 5.11). Ratios were also compared with pyrites from Neo-Meso-Paleoproterozoic to demonstrate that the data fits in well with the average Proterozoic analyses (Fig 5.12).

Overall, trace element concentrations and ratios are well below the global mean values (except Pb enrichment in the clay band) suggesting a few possibilities. First, lack of sufficient oxidative weathering

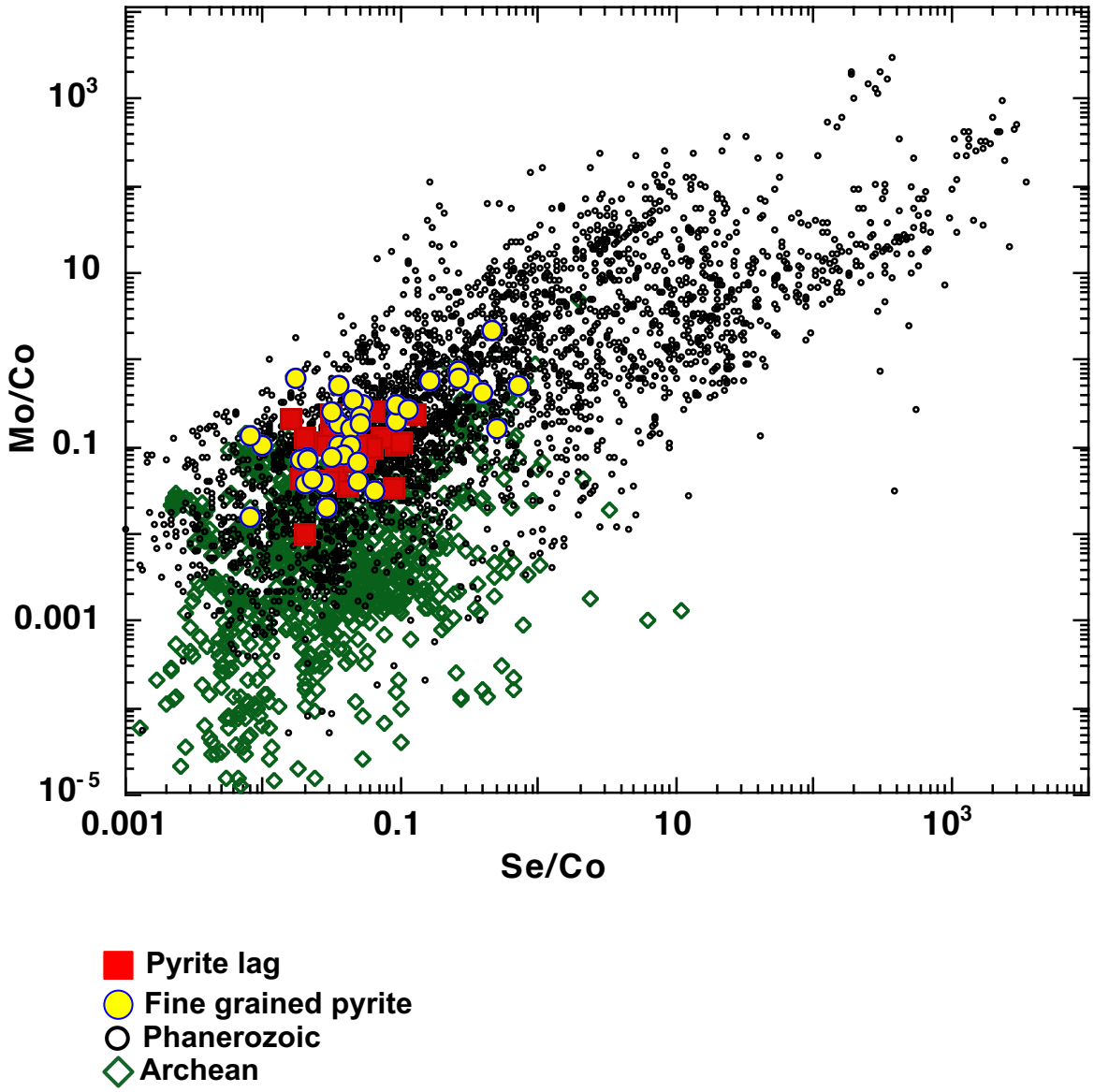

Fig 5.11 Comparison of Se/Co vs Mo/Co in the Bijaigarh Black Shale unit with Archean and Phanerozoic sedimentary pyrites (Large et al., 2014; 2015)

on land led to a decreased supply of trace elements in the marine system via riverine flux rendering the values in pyrite to be lower than or similar to the Proterozoic mean values. It is also possible that provenance played a role in controlling the trace element patterns in the Bijaigarh Shale (Large et al., 2017: Goldschmidt Abstract). Mishra and Sen (2008), proposed a dominantly felsic provenance (post-Archean Proterozoic in age), subjected to severe chemical weathering under high pCO_2 conditions, for the Upper Kaimur Group on the basis of various geochemical discriminants, elemental ratios like K_2O/Na_2O, Al_2O_3/TiO_2, SiO_2/MgO, La/Sc, Th/Sc, Th/Cr, Gd_N/Yb_N and pronounced negative Eu anomalies. The felsic provenance for the Kaimur Group (including the Bijaigarh Shale) combined with low oxidative weathering may have caused the low trace element concentration in pyrites as observed in this study. That is because most redox sensitive and nutrient trace elements (Ni, Co, Mn, Cu, Zn, Se, V) are relatively

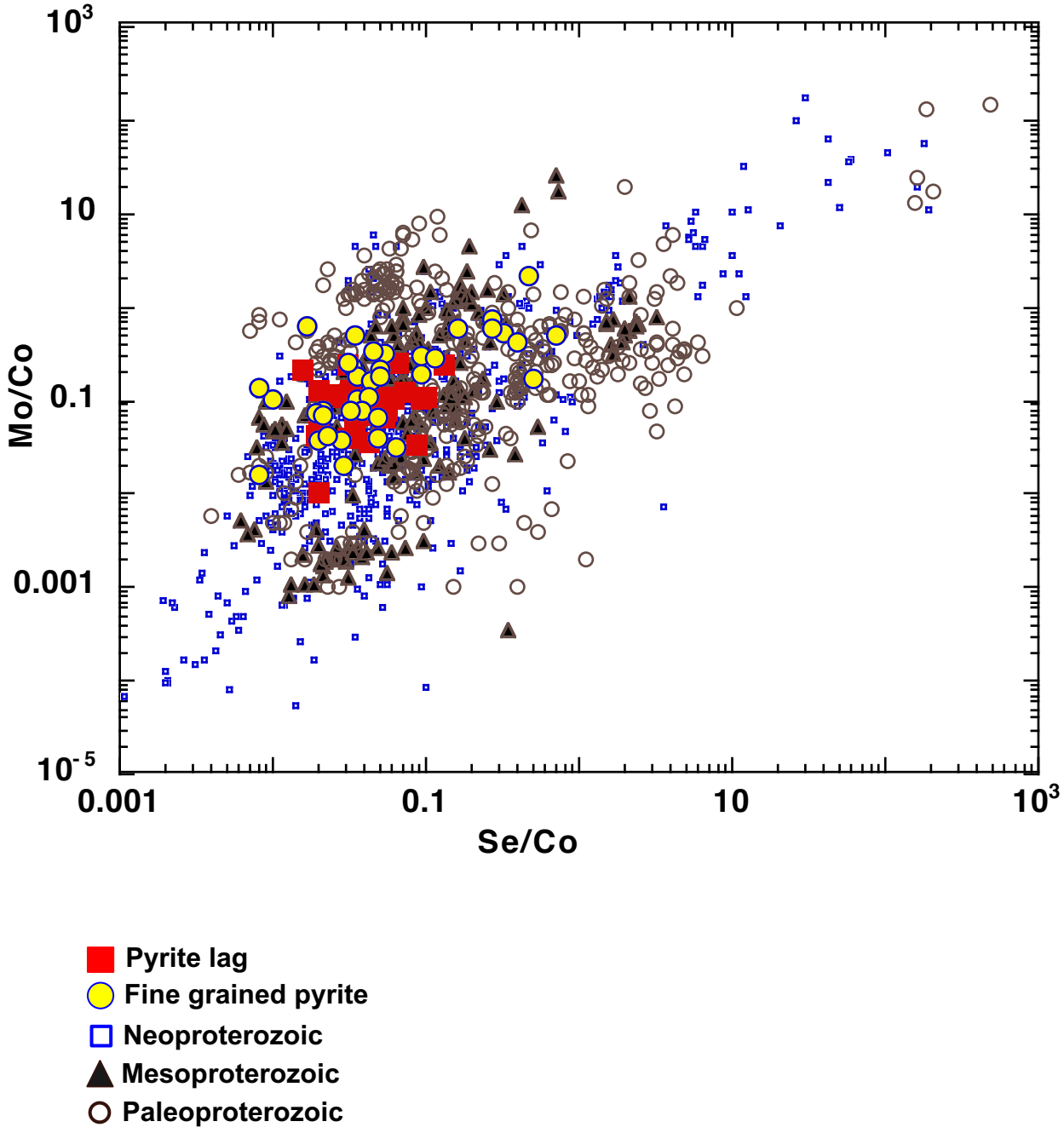

Fig 5.12 Comparison of Se/Co vs Mo/Co in the Bijaigarh Black Shale unit with Proterozoic pyrites (Large et al., 2017)

enriched in mafic rocks compared to felsic rocks (Large et al., 2017; Reimann and Caritat, 1998). Elements like Mo and Tl however, are slightly more enriched in felsic compared to mafics (Reimann and Caritat, 1998).

5.6 Conclusions

In summary, this study involved understanding sedimentary pyrite textures and their trace element

concentrations to reflect on paleo-redox conditions during the deposition of the Bijaigarh Shale unit in the Mesoproterozoic. Sedimentary pyrite textures indicate variable depositional conditions for the Bijaigarh Shale. Deposition began with fine-grained pyrite disseminations in layers and aggregates, suggesting a quiet, low energy environment and mildly reducing water column conditions. With subsequent enhancement of organic matter deposition and its decomposition, the water column gradually became more strongly reducing resulting in the formation of the pyrite bed. Occasional reworking of the pyrite bed during storm incursions caused the pyrite lags to form. Overall, low concentrations of the trace elements particularly Se and Mo and their ratios (i.e., below the global mean values for the Proterozoic) suggest low atmospheric conditions during the deposition of the Bijaigarh Shale. Owing to open ocean connectivity of the Vindhyan Basin during the deposition of the Bijaigarh Shale (1210$\pm$52 Ma), we can infer these paleoredox conditions in a global context. Our data for the Bijaigarh Shale is consistent with previous studies (Large et al., 2014; Lyons et al., 2014; Planavsky et al., 2014) that have proposed low atmospheric oxygen conditions in the Mesoproterozoic.

5.7 Acknowledgements

The project was funded by the Australian Research Council (DP150102578). Thanks to Cassady Harraden for her help with pyrite texture photograph.

5.8 References

Algeo, T.J., Maynard, J.B., 2004. Trace element behavior and redox facies in core shales of Upper Pennsylvanian Kansas-type cyclothems. Chemical Geology 206, 289–318.

Algeo, T.J., Lyons, T.W., 2006. Mo–total organic carbon covariation in modern anoxic marine environments: Implications for analysis of paleoredox and paleohydrographic conditions. Paleoceanography 21: PA1016-23.

Algeo, T.J., and Rowe, H., 2012. Paleoceanographic applications of trace-metal concentration data. Chemical Geology 324, 6–18.

Auden, J. B., 1933. Vindhyan sedimentation in Son valley. Geol. Surv. India, Memoir 62: 141–150.

Azmi, R.J., Joshi, D., Tewari, B.N., Joshi, M.N., Srivastava, S.S., 2008. A synoptic view on the current discordant geo- and biochronological ages of the Vindhyan Supergroup, central India. Jour. Himalayan Geol. 29, 177–191.

Baird, G.C., and Brett, C.E., 1991. Submarine erosion on the anoxic seafloor: stratinomic,

paleoenvironmental, and temporal significance of reworked pyrite-bone deposits, in Tyson, R.V., and Pearson, T., eds., Modern and Ancient Continental Shelf Anoxia: Geological Society of America, Special Publication 58, 233–257.

Baird, G.C., and Lash, G.G., 1990. Devonian strata and environments: Chautauqua County region: New York State: New York State Geological Association, 62nd Annual Meeting Guidebook, Sat A1–A46.

Banerjee, S., Dutta, S., Paikaray, S and Mann, U., 2006. Stratigraphy, sedimentology and bulk organic geochemistry of black shales from the Proterozoic Vindhyan Supergroup (central India). Jour. Earth Syst. Sci. 115(1), 37–47.

Banerjee, P. K. and Prakash, O. 1975. Galena mineralisation in the Vindhyan rocks of Amjhore, Sahabad district, Bihar, India. Econ Geol 70, 399–404.

Bengtson, S., Belivanova, V., Rassmussen, B., Whitehouse, M.J., 2007. The Vindhyan enigma revisited. Geol. Soc. Am. Abstr. 39 (6), 331.

Bertine K. K., Koide M., and Goldberg E.D., 1996. Comparative marine chemistries of some trivalent metals-bismuth, rhodium and rare Earth elements. Mar. Chem. 53, 89–100.

Bose, P.K., Sarkar, S., Chakrabarty, S., Banerjee, S., 2001. Overview of the Meso- to Neoproterozoic evolution of the Vindhyan Basin, central India. Sed. Geol. 141, 395–419.

Bose P K and Chaudhuri A K 1990 Tide versus storm in epeiric coastal deposition: two Proterozoic sequences, India; Geological Journal 25 81–100.

Brasier, M.D., Lindsay, J.F., 1998. A billion years of environmental stability and the emergence of eukaryotes: new data from northern Australia. Geology 26, 555–558.

Chakraborty, C., 2006. Proterozoic intracontinental basin: The Vindhyan example. J. Earth Syst. Sci. 115 (1), 3–22

Chakraborty, C. and Karmakar, S., 1998. Structural architecture of Vindhyan strata in Son valley: implications for basin tectonics. Jour. Geol. Soc. India, 51, 377–382.

Chakraborty C 1995 Gutter casts from the Proterozoic Bijaygarh Shale Formation, India: their

implication for storm-induced circulation in shelf settings; Geological Journal 30, 69–78.

Chanda, S. K. and Bhattacharyya, A., 1982. Vindhyan sedimentation and paleogeography: post-Auden developments. In: Valdiya, K. S., Bhatia, S.B. & Gaur, V. K. (eds), Geology of Vindhyanchal. Hindustan Publ. Corp., New Delhi, 88–101.

Chaudhuri, A.K., Saha, D., Deb, G.K., Deb, S.P., Mukherjee, M.K., Ghosh, G., 2002. The Purana basins of southern cratonic province of India- A case for Mesoproterozoic fossil rifts. Gondwana Res. 5, 23–33.

Crawford, A.R., Compston, W., 1970. The age of the Vindhyan system of peninsular India. Q. Jour. Geol. Soc. Lond. 125, 351–371.

Crowe, S.A., Døssing, L.N., Beukes, N.J., Bau, M., Kruger, S.J., Frei, R., Canfield, D.E., 2013. Atmospheric oxygenation three billion years ago. Nature 501, 535–538.

Danyushevsky, L., Robinson, P., Gilbert, S., Norman, M., Large, R., McGoldrick, P., and Shelley, M., 2011. Routine quantitative multi-element analysis of sulphide minerals by laser ablation ICP-MS: Standard development and consideration of matrix effects. Geochemical Exploration Environment Analysis 11, 51–60.

Deb, M. and Pal, T., 2015. Mineral potential of Proterozoic intracratonic basins in India. In: Mazumder, R. & Eriksson, P. G. (eds), Precambrian Basins of India: Stratigraphic and Tectonic Context. Geol. Soc. London, Memoirs, 43: 309–325.

Deb, M., Thorpe, R., Krstic, D., 2002. Hindoli Group of rocks in the Eastern Fringe of theAravalli–Delhi Orogenic belt—Archean secondary greenstone belt or Proterozoicsupracrustals? Gondwana Res. 5, 879–883.

Formolo, M.J., and Lyons, T.W., 2007. Accumulation and Preservation of Reworked Marine Pyrite Beneath an Oxygen-Rich Devonian Atmosphere: Constraints from Sulfur Isotopes and Framboid Textures. Journal of Sedimentary Research 77, 623-633.

Gopalan, K., Kumar, A., Kumar, S., Vijayagopal, B., 2013. Depositional history of the Upper
Vindhyan succession, central India: time constraints from Pb–Pb isochron ages of its carbonate components. Precambrian Res. 233, 108–117.

Gordon, G.W., Lyons, T.W., Arnold, G.L., Roe, J., Sageman, B.B., Anbar, A.D., 2009. When do black shales tell molybdenum isotope tales? Geology 37, 535–538.

Gregory, L.C., Meert, J.G., Pradhan, V., Pandit, M.K., Tamrat, E., Malone, S.J., 2006. A paleomagnetic and geochronologic study of the Majhgawan kimberlite, India: Implications for the age of the Vindhyan Supergroup. Precambrian Res. 149, 65–75.

Guha, J., 1971. Sulfur isotope study of the pyrite deposit of Amjhore, Shahbad district, Bihar, India. Econ. Geol. 66: 326–330.

Jochum, K.P., Pfänder, J., Woodhead, J.D., Willbold, M., Stoll, B., Herwig, K., Amini, M., Abouchami, W. and Hofmann, A.W., 2005. MPI-DING glasses: New geological reference materials for in situ Pb isotope analysis. Geochemistry Geophysics Geosystems 6, 1525-2027.

Kumar, A., Gopalan, K., Rajagopalan, G., 2001. Age of the Lower Vindhyan sediments, central India. Curr. Sci. 81, 806–809.

Large, R.R., Halpin, J.A., Danyushevsky, L.V., Maslennikov, V.V., Bull, S.W., Long, J.A., Gregory, D.D., Lounejeva, E., Lyons, T.W., Sack, P.J., McGoldrick, P. and Calver, C.R., 2014. Trace element content of sedimentary pyrite as a new proxy for deep-time ocean- atmosphere evolution. Earth and Planet. Sci. Letters 389, 209-220.

Large R.R., Gregory, D.G., Steadman, J.A., Tomkins, A.G., Lounejeva, E., Danyushevsky, L.V., Halpin, J.A., Maslennikov, V.V., Sack, P.J., Mukherjee, I. and Hickman, A., 2015a. Gold in the oceans through time. Earth and Planetary Science Letters 428, 139-150.

Large, R.R, Halpin, J.A., Lounejeva, E., Danyushevsky, L.V., Maslennikov, V.V., Gregory, D., Sack, P.J., Haines, P.W., Long, J.A., Makoundi, C., Stepanov, A.S., 2015b. Cycles of nutrient trace elements in the Phanerozoic ocean, Gondwana Research 28 (4), 1282-1293.

Longerich, H.P., Jackson, S.E. and Günther, D., 1996. Laser ablation inductively coupled plasma mass spectrometric transient signal data acquisition and analyte concentration calculation. Journal of Analytical Atomic Spectrometry 11, 899-904.

Lyons, T.W., 1997. Sulfur isotopic trends and pathways of iron sulfide formation in upper Holocene sediments of the anoxic Black Sea: Geochimica et Cosmochimica Acta 61, 3367–3382.

Lyons, T.W., Reinhard, C.T., Planavsky, N.J., 2014. The rise of oxygen in Earth's early ocean and atmosphere. Nature 506, 307-315.

Malone, S.J., Meert, J.G., Banerjee, D.M., Pandit, M.K., Tamrat, E., Kamenov, G.D., Pradhan, V.R., Sohl, L.E., 2008. Paleomagnetism and detrital zircon geochronology of the Upper Vindhyansequence, Son Valley and Rajasthan, India: a ca. 1000 Ma closure age for the Purana Basins? Precambrian Research 164: 137–159

Mishra, M., and Sen, S. 2012. Provenance, tectonic setting and source-area weathering of Mesoproterozoic Kaimur Group, Vindhyan Supergroup, Central India. Geologica Acta 10 (3), 283-293.

Mondal, M.E.A., Goswami, J.N., Deomurari, M.P., Sharma, K.K., 2002. Ion microprobe$^{207}Pb/^{206}Pb$ ages of zircons from the Bundelkhand Massif, northern India: implications for crustal evolution of the Bundelkhand-Aravalli supercontinent. Precambrian Res. 117, 85–100.

Mukherjee, I., and Large, R., 2016. Pyrite trace element chemistry of the Velkerri Formation, Roper Group, McArthur Basin: Evidence for atmospheric oxygenation during the Boring Billion: Precambrian Res. 281, 13-26.

Mukherjee, I., and Large, R.R., 2017. Application of Pyrite Trace Element Chemistry to Exploration for SEDEX Style Zn-Pb Deposits: McArthur Basin, Northern Territory Australia: Ore Geol. Rev. 81, 1249–1270.

Nair, N., Ray, A., 1977. Syndepositional and diagenetic features in the pyrite ores of Amjhore, Bihar, India. Mineral. Deposita 12, 151–154.

Pandalai H. S., Chandra, D., 1986. Textural Studies on the ores of Amjhore pyrite deposit, Rohtas district, Bihar, India. Jour. Geol. Soc. India, 27(6), 527-530.

Pandalai, H.S., Changkakoti, A., Krouse, H.R., Gunalan, N. 1991. The relationship between Carbon, Sulfur and Pyritic Iron in the Amjhore Deposit, Bihar, India. Economic Geology (86), 862-869.

Partin, C.A., Bekker, A., Planavsky, N.J., Scott, C.T., Gill, B.C., Li, C., Podkovyrov, V., Maslov, A., Konhauser, K.O., Lalonde, S.V., Love, G.D., Poulton, S.W., Lyons, T.W., 2013. Large-scale fluctuations in Precambrian atmospheric and oceanic oxygen levels from the record of U in shales. Earth Planet. Sci. Lett. 369–370.

Planavsky, N.J., Reinhard, C.T., Wang, X., Thomson, D., McGoldrick, P., Rainbird, R.H., Johnson, T., Fischer, W.W., Lyons, T.W., 2014. Low Mid-Proterozoic atmospheric oxygen levels and the delayed rise of animals. Science, 346, 635-638.

Rasmussen, B., Bose, P.K., Sarkar, S., Banerjee, S., Fletcher, I.R., McNaughton, N.J., 2002. 1.6 Ga U–Pb zircon age for the Chorhat Sandstone, lower Vindhyan, India: possible implications for early evolution of animals. Geology 30, 103–106.

Ray, J.S., 2006. Age of the Vindhyan Supergroup: a review of recent findings. J. Earth Syst. Sci. 115, 149–160.

Ray, J.S., Veizer, J., Davis, W.J., 2003. C, O, Sr and Pb isotope systematics of carbonate sequences of the Vindhyan Supergroup, India: age, diagenesis, correlations and implications for global events. Precambrian Res. 121, 103–140.

Ray, J.S., Martin, M.W., Veizer, J., Bowring, S.A., 2002. U–Pb Zircon dating and Sr isotope systematics of the Vindhyan Supergroup, India. Geology 30, 131–134.

Rickard, D., 2012. Sulfidic sediments and sedimentary rocks. In: Van Loon, A.J. (Ed.), Developments in Sedimentology. Elsevier, p. 801.

Rickard, D., Mussmann, M., and Steadman, J.A., 2017. Sedimentary Sulfides. Elements 13, 117-122.

Reimann, C and de Caritat, P, 1998. Chemical Elements in the Environment, Fact Sheets for the Geochemist and Environmental Scientist: Springer-Verlag, Berlin, 397 p.

Sahoo, S.K., Planavsky, N.J., Kendall, B., Wang, X., Shi, X., Scott, C., Anbar, A.D., Lyons, T.W., Jiang, G., 2012. Ocean oxygenation in the wake of the Marinoan glaciation. Nature 489, 546–549.

Sarangi, S., Gopalan, K., Kumar, S., 2004. Pb–Pb age of the earliest megascopic, eukaryotic alga-bearing Rohtas Formation, Vindhyan Supergroup, India: implications for Precambrian atmospheric oxygen evolution. Precambrian Res. 121, 107–121.

Sarkar, A., Chakraborty, P. P., Mishra, B., Bera, M. K., Sanyal, P. and Paul, S., 2010. Mesoproterozoic sulphidic ocean, delayed oxygenation and evolution of early life: sulfur isotope clues from Indian Proterozoic basins. Geol. Mag. 147, 206–218.

Schieber, J., Sur, S., and Banerjee, S., 2007. Benthic microbial mats in black shale units from the Vindhyan Supergroup, Middle Proterozoic of India: the challenges of recognizing the genuine article. In Schieber, J., Bose, P.K., Eriksson, P.G., Banerjee, S., Sarkar, S. Altermann, W., and Catuneanu, O. (eds.) Atlas of Microbial Mat Features Preserved within the Siliciclastic Rock Record, Elsevier BV, Amsterdam, 189-197.

Schieber, J., and Baird, G., 2001. On the origin and significance of pyrite spheres in Devonian black shales of North America: Journal of Sedimentary Research 71, 155–166.

Schieber, J., 1998, Sedimentary features indicating erosion, condensation, and hiatuses in the Chattanooga Shale of central Tennessee: relevance for sedimentary and stratigraphic evolution, in Schieber, J., Zimmerle, W., and Sethi, P., eds., Mudstones and Shales 1: Basin Studies, Sedimentology and Paleontology: Stuttgart, Schweizerbartsch Verlagsbuchhandlung, 187–215.

Scott, C., Lyons, T.W., Bekker, A., Shen, Y., Poulton, S.W., Chu, X., Anbar, A.D., 2008. Tracing the stepwise oxygenation of the Proterozoic ocean. Nature 452, 456–459.

Singh, I., 1980. The Bijaigarh shale, Vindhyan system (Precambrian), India—an example of a lagoonal deposit. Sediment. Geol. 25, 83–103.

Soni, M. K., Chakraborty, S. and Jain, V. K., 1987. VindhyanSupergroup – a review. In: Radhakrishna, B. P. (ed.), Purana Basins of Peninsular India (Middle to Late Proterozoic). Geol.Soc. India, Memoir 6, 87–138.

Sur, S., Schieber, J. and Banerjee, S., 2006. Petrographic observations suggestive of microbial mats from Rampur shale and Bijaigarh shale, Vindhyan basin, India. Jour. Earth Sys. Sci., 115, 61-66.

Taylor, S.R., Mclennan, S.M., 1995. The geochemical evolution of the continental crust. Rev. Geophys. 33, 241–265.

Tripathy, G.R. and Singh, S.K., 2015. Re-Os depositional age for black shales from the Kaimur Group, Upper Vindhyan, India. Chem. Geol. 413, 63-72.

Wignall, P.B., and Newton, R., 1998, Pyrite framboid diameter as a measure of oxygen deficiency in ancient mudrocks: American Journal of Science 298, 537–552.

Wilkin, R.T., Barnes, H.L., and Brantley, S.L., 1996, The size distribution of framboidal pyrite in modern sediments: an indicator of redox conditions: Geochimica et Cosmochimica Acta 60, 3897–3912.

Valdiya, K.S., 2010. The making of India: geodynamic evolution. MacMillan Publ India Ltd, Delhi, 816 pp.

Chapter 6

The Boring Billion, a slingshot for Complex Life on Earth

Mukherjee, I., Large, R., Corkrey, R., Danyushevsky, L., 2018. Scientific Reports (4432)

Indrani Mukherjee[1], Ross R. Large[1], Ross Corkrey[2] and Leonid V Danyushevsky[1]

Centre of Excellence in Ore Deposits (CODES)[1] and Tasmanian Institute for Agricultural Research[2], University of Tasmania, Hobart, Australia

6.0 Abstract

The period 1800 to 800 Ma referred to as the "Boring Billion" is believed to mark a delay in evolution of complex life, primarily due to low levels of oxygen in the atmosphere. Earlier studies highlight the remarkably flat C, Cr isotope and low trace element trends during the so-called stasis, caused by prolonged nutrient, climatic, atmospheric and tectonic stability. In contrast to previous studies, we suggest a first-order variability of bio-essential trace element (trace element) availability in the oceans by combining systematic sampling of the Proterozoic rock record with sensitive geochemical analyses of marine pyrite by LA-ICP-MS technique. We also recall that several critical biological evolutionary events, such as, the appearance of eukaryotes, their cell organelles, the origin of multicellularity, the origin of sexual reproduction, the first major diversification of eukaryotes (crown group) occurred during this period. Therefore, it appears possible that the period of low nutrient trace element, between 2000 and 1400 Ma, caused evolutionary pressures which became an essential trigger for promoting biological innovations in the eukaryotic domain. Later periods of stress-free conditions with relatively high nutrient trace element concentration, on the other hand, facilitated diversification. We propose that the "Boring Billion" was a period of sequential stepwise evolution and possible diversification of complex eukaryotes, triggering evolutionary pathways that made the later rise of micro-metazoans and their macroscopic counterparts possible.

6.1 Introduction

The "Boring Billion" (period between 1800 and 800 Ma) in Earth's history, also referred to as the "dullest period in Earth's history" (Buick et al., 1995) is believed to represent a period of geobiological stasis (Brasier and Lindsay, 1998). The so-called stasis is manifested as a remarkably stable and flat carbon isotope trend due to prolonged nutrient supply, climatic and tectonic stability (Brasier and Lindsay, 1998). Other stable and undisturbed trends are depicted by S, Mo, Cr, Sr isotopes, and more particularly, by low values of trace element concentrations and P in marine black shales (Anbar and Knoll, 2002; Scott et al, 2008; Kendall et al., 2009; Partin et al., 2013; Large et al., 2014; Robbins et al., 2016; Reinhard et al., 2017). Outcomes of previous studies point towards a delay in the evolution of complex life primarily due to

lack of oxygen in the atmosphere (Lyons et al., 2014). It is believed it was not until the Neoproterozoic, a great diversity in complex life (both microscopic and macroscopic) developed. Absence of banded iron formations, evaporites, phosphorites, glaciation events and major ore deposits related to convergent plate margins (Orogenic Au, porphyry, VHMS and MVT deposits) also correlate with the period of stasis (Holland, 2006). Plate motions at that time, were also suppressed, owing to stagnant lid tectonics, with modern plate tectonics not operative until towards the end of the Neoproterozoic (Roberts et al., 2013; Piper, 2013). General consensus therefore is that the 1800-800 Ma period represents a billion years of geological standstill that stalled evolution of complex life.

Contrary to above, we have identified certain gaps in the understanding of the "Boring Billion" period. First, even though geochemical proxies indicate "stasis", certain key evolutionary breakthroughs occurred during this time span. These include appearance of eukaryotes (including its cell organelles) possibly via endosymbiosis, multicellularity and origin of sexual reproduction (Butterfield, 2015; Knoll, 2014; Katz, 2012; Porter, 2004; Bengston et al., 2017) and the evolution of precursors of metazoans (Urmetazoa) (Muller, 2001). Without these developments, any subsequent metazoan and macroevolution would be rather impossible. Second, we observe the first major diversification of eukaryotes (Crown group) (Javaux et al., 2003; 2004; 2017), appearance of metaphytes (Knoll, 2014; Bengston et al., 2017) and ~ 750 Ma metazoans (Knoll, 2014; Erwin et al., 2011), between the Great Oxidation Event (GOE) 1 and 2 indicating that oxygen may not have been the only driver of these developments. Experiments also support low oxygen requirements of modern analogues of primitive metazoans (Danovaro et al., 2010). The sudden appearance of macroscopic eukaryotes with no obvious prior evolutionary developments is hard to comprehend. That is because metazoan evolution requires multicellularity, development of scaled epithilea and extracellular digestion, a nervous system, mesoderm, bilaterity and establishment of a tubular gut (Nielson, 2008). Also, any one element (e.g. O) cannot account for the course of biologic evolution (Kobayashi and Ponnamperuma, 1985). A suite of bio-essential elements including H, C, N, O, P, S, Cl, Na, Mg, K, Ca, Fe, Al, Si (macro elements) and V, Cr, Mn, Co, Ni, Cu, Zn, Mo, B, F, As, Se (trace elements) are required for all kinds of life forms (Kobayashi and Ponnamperuma, 1985).

Interestingly, bio-essential trace element abundance unlike major elements does not necessarily signify its importance in an organism as it is utilized only if it has functional roles (Kobayashi and Ponnamperuma, 1985). Scarcity of an element plays an equal and important role as it encourages organisms to adapt to an alternative element that has similar functional roles. This results in selection of new protein molecules, with advanced roles (Ochiai, 1978 a, b). Thus, knowledge of multi-trace element variability in the ocean, particularly multi-trace element minima, is an essential aspect in understanding biologic evolution that has not been previously addressed. It has been noted by Sterner (2008) and Morel et al. (1991) that major elements have received far more attention than trace elements as potential limiting nutrients related to biological evolution.

The present study focuses on using a technique where trace element concentrations in sedimentary pyrite, determined using LA-ICP-MS, provide useful first order insights on trace element availability (abundance and scarcity) in the ocean with time (Large et al., 2014). Without undermining the role of macronutrients (such as P, N, O, C etc.) we aim to establish the link between trace element availability and biologic evolution through the Boring Billion period.

6.2 Method and materials

Our method involves measuring trace element concentrations in sedimentary pyrite in black shales using Laser Ablation- Inductively Coupled- Mass Spectrometry (LA-ICP-MS) as proxies for atmospheric oxygenation and their nutrient trace element availability (Large et al., 2014; Appendix Table A6.1). It is based on the premise that the availability of most trace elements in seawater is controlled by a combination of oxidative weathering on land and erosion/run-off to the ocean related to active tectonics. Subsequently, the trace elements become adsorbed into sedimentary pyrite forming in organic matter-bearing muds depositing in anoxic portions of the ocean. Sedimentary pyrite analyses are preferred to whole rock shale analyses as the method is more sensitive to trace element concentrations, and are preferentially partitioned into pyrite compared to whole rock (Mukherjee and Large, 2016; 2017). The validity of the technique has been the subject of several publications (Gregory et al., 2014; Large et al., 2014; Gregory et al., 2015; Gregory et al., 2017) which includes the proof of concept paper (Large et al., 2014) (See Appendix A6.1.1, 6.1.2, 6.1.3 for more information).

The study provides new analyses from the Riversleigh Siltstone in the Mt. Isa Basin in Australia and collates data from ~40 marine, least metamorphosed (lower greenschist and below), undeformed organic matter rich-sedimentary black shales from various sedimentary basins around the world (Appendix Table A6.1a, b) (Large et al., 2014; 2015; 2017). Samples were mainly collected in the form of drill cores in order to ensure the pyrite was well preserved and not oxidised. Polished laser mounts were prepared for petrological analysis using reflected light microscope followed by LA-ICP-MS pyrite analyses for trace elements at CODES, University of Tasmania (Large et al., 2014). Polished mounts were studied under reflected light in order to select samples that contain fine grained early-formed sedimentary pyrite and discard coarse, recrystallised and diagenetically altered pyrite. Most samples comprised sedimentary pyrite in the form of individual microcrystals (5-10 u), aggregates of microcrystals, framboids and nodular concretions in black shales. Samples containing coarser euhedral pyrites were discarded as trace element budget is affected due to recrystallization (Large et al., 2014; Gregory et al., 2015; Mukherjee and Large, 2016; 2017). Analyses were carried out using CompexPro 110 ArF Excimer laser microprobe equipped with S155 cell and coupled to an Agilent 7700 ICP-MS. A total of ~ 1400 robust analyses were obtained after exclusion of analyses that did not meet the criteria outlined for sedimentary pyrite (done on

the basis of trace element ratios such as Ni/Co>1 in pyrite; Gregory et al., 2015). Standards (or reference materials) were run at the start, ~ after every two samples (~every 1.5 hours) and at the end, in order to calculate the drift of the instrument (see Supplementary Information; Large et al., 2014). Signal from the mass spectrometer was generated in counts per second (cps) and was processed by CODES in-house software designed according to standard methods (Longerich et al., 1996), using Fe as the internal standard element (See Appendix A6.1.1, 6.1.2, 6.1.3 for more information).

Statistical methods: The trace element data were standardised by subtracting the mean and dividing by the standard deviation and then analysed using principal components analysis (PCA); (Appendix Table A6.2) (PCA; Johnson & Wichen, 1988). The standardisation was to ensure that the results were not influenced unduely by variables of large magnitude. The PCA was calculated using PROC PRINCOMP in the SAS System version 9.3. The scores from the first component of the PCA were used to construct boxplots that were plotted against the corresponding geologic age. The PCA scores of the first component against geologic age for all trace element data in Figure 6.1 and for selected variables such as Ni, Co, Se, Zn, Mo, Cd in Figure 6.2. In both figures, the scores are presented as box plots along with the median trend (solid line) and the overall median score (dashed line). The use of boxplots allowed the spread of scores at each age to be represented graphically. Boxplots were calculated using R version 3.3.3.

6.3 Results

The pyrite-LA-ICP-MS analyses for a suite of trace element (Co, Ni, Zn, Se, Mo, Cd, Cu, Mn, As, Ag, Sb, Tl and Pb) are presented in Table A6.1(Appendix). The data are a compilation from Large et al. (2014, 2015, 2017) along with additional new analyses from this study. The first component of the PCA accounted for 31% variation in the data using all trace element variables, and 38% when using the selected variables (Ni, Co, Se, Mo, Zn and Cd) (Table 6.1). The eigenvector for the first component of the PCA using all trace element variables had positive coefficients of similar magnitudes, except in the case of Pb, and when using selected variables, the coefficients were all positive (Table 6.1). While the first component's Pb coefficient was negative when using all variables, its value was very small and considered insignificant.

The interpretation of the first component is that it corresponds to a weighted average of the trace element variables. In other words, the first component of the PCAs provided a proxy for the trace element concentrations. In Figure 6.1, the trace element trend is mostly below the median value between 2500-1400 Ma (except at 2500, ~1900 and 1730 Ma). Between 1400-800 Ma, the trend is above the median value except at ~1260 Ma. In Figure 6.2, where only selected trace elements have been used to derive the principal component score, we observe a similar trend as Fig 6.1. The trace element trend is initially above the median value but drops below it and remains so until 1400 Ma (Fig 6.2). Between 1400-800 Ma

the trace element trend is above the median value.

During the period 2000–1400 Ma there were 4 biological innovations (Eukarya, organelles, multicellularity, sex) discussed below. We can calculate the probability of the 4 events occurring in this period by assuming that these 4 events could occur independently and with uniform probability anytime between 2000 and 800 Ma. Since the periods 2000–1400 Ma and 1400–800 Ma are equal length intervals and, by our assumption, the events could occur with the same probability in each, then the probability of them co-occurring only between 2000–1400 Ma would be $(1/2)^4 = 0.0625$.

Table 6.1 Shown are the PCA eigenvector coefficients and eigenvalues when using all variables or using the selected variables.

Analysis	Variable	Prin1	Prin2	Prin3
All variables	Co	0.087	0.560	0.015
	Ni	0.247	0.498	-0.037
	Zn	0.294	-0.202	0.396
	Se	0.304	0.056	-0.102
	Mo	0.330	-0.218	-0.045
	Cd	0.297	-0.146	0.235
	Cu	0.294	0.228	0.266
	Mn	0.209	0.008	0.495
	As	0.270	-0.063	-0.531
	Ag	0.371	-0.031	-0.073
	Sb	0.349	0.095	-0.394
	Tl	0.135	-0.505	-0.119
	Pb	0.273	-0.073	0.035
	Eigenvalue	4.07	1.94	1.53
	% explained	31	15	12
Selected variables	Co	0.070	0.702	0.388
	Ni	0.337	0.621	-0.131
	Zn	0.466	-0.227	0.569
	Se	0.466	0.039	-0.651
	Mo	0.451	-0.132	-0.152
	Cd	0.494	-0.227	0.250
	Eigenvalue	2.25	1.54	0.861
	% explained	38	26	14

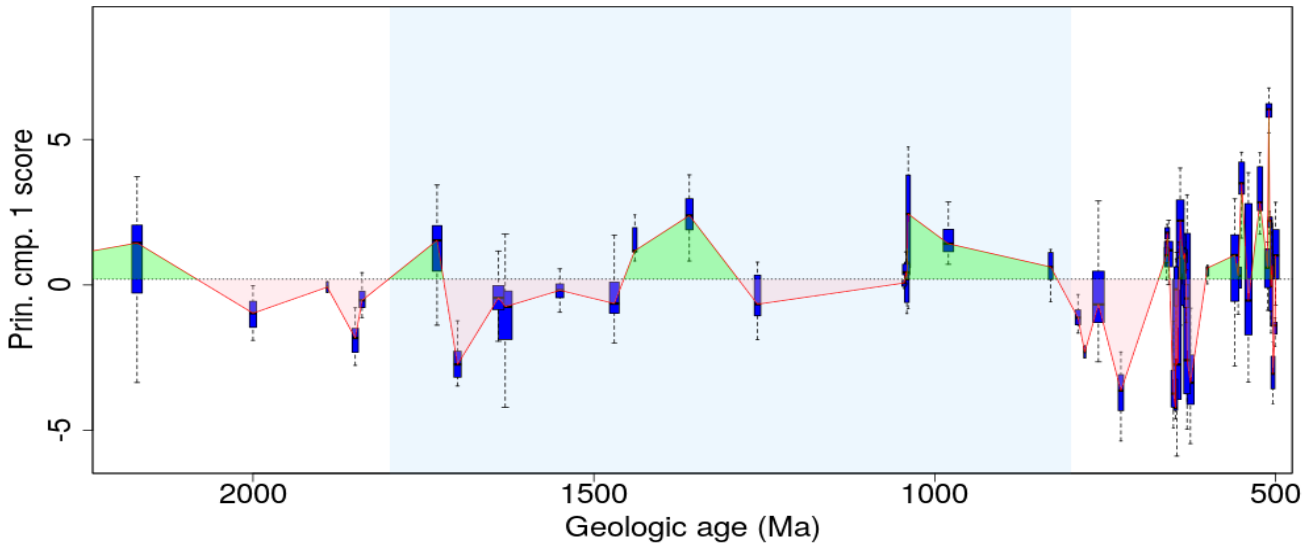

Fig 6.1 First principal component scores using all trace element variables against geologic age. Shown are the PCA scores for the first dimension as boxplots and also the median trend as a solid line. The overall median score is shown as a dotted line with areas above it coloured green and below coloured pink.

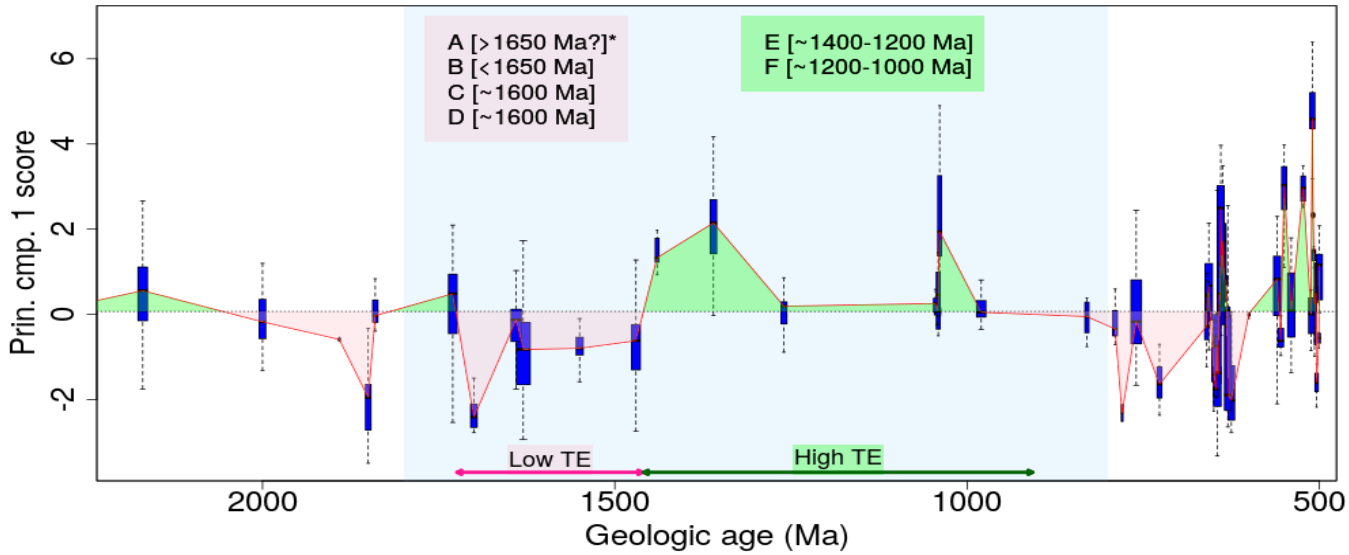

Fig 6.2 First principal component scores for selected trace element variables (Se, Ni, Co, Zn, Mo, Cd) against geologic age. Shown are the PCA scores of the first dimension as boxplots and also the median trend as a solid line. The overall median score is shown as a dotted line with areas above it coloured green and below coloured pink. (A: Endosymbiosis*(occurred prior to appearance of eukaryotes) B: First eukaryotes and its cell organelles[C: Multicellularity D: Sexual reproduction E: Diversification and radiation of eukaryotes F: Crown group eukaryotes)

6.4 Discussion

Here, we interpret the trace element trend in light of biologic evolution observed in the paleontological rock record in the Boring Billion period. Figures 6.1 and 6.2 demonstrate that trace element concentrations were mostly below the median value between 2000 and 1400 Ma. This is in agreement with previous research where low trace element concentrations have been proposed for this particular time span (Anbar and Knoll, 2002; Scott et al., 2008; Partin et al., 2013; Robbins et al., 2016). This can be attributed to the drop in oxygen levels after the GOE 1 event. As evident from various geochemical proxies in the rock record, the GOE 1 was transient in nature and oxygen dropped to lower levels at ~2000 Ma (Large et al., 2014; Lyons et al., 2014; Canfield, 1998). This is also evident from the Se/Co in pyrite trend through time in this study (Fig A6.1; Appendix 6.1.4). The decrease in critical/bio-essential trace element concentrations (Ni, Co, Se, Zn, Mo, Cd) is possibly due to a decreased trace element flux in the ocean as a result of decrease in oxidative weathering (Fig 6.1, 6.2). Coinciding with this drop in oxygen and trace element concentrations, a number of key evolutionary breakthroughs are believed to have occurred, including appearance of first eukaryotes, acquisition of certain cell organelles (or cell components such as plastids, mitochondria, nucleus, endoplasmic reticulum, cytoskeleton etc.) and multicellularity between 2000 and 1400 Ma (Butterfield, 2015; Knoll, 2014; Katz, 2012; Porter, 2004). Based on the paleontological record, the origin of sexual reproduction is also believed to have evolved between 2000-1400 Ma (Kabnick and Peattie, 1991; Bengston et al., 2017). The micro-paleontological record globally, confirms that the phenomena were global in nature as proposed by previous studies; for instance, in the Paleoproterozoic Changcheng and Ruyang Groups, China (Lamb et al., 2009; Xiao et al., 1997; Yin, 1997), Vindhyan Supergroup, India (Singh and Sharma, 2014), and Roper Group, Australia (Javaux et al., 2004), and Mesoproterozoic of Jixian Group (1.56 Ga), China (Zhu et al., 2016); Belt Group (1.5 Ga), USA (Adam et al, 2016); Kotuikan Fm (~1.5 Ga) Russia (Vorob'eva et al, 2015); Roper Group (1.5 Ga), Australia (Javaux & Knoll, 2017). Interestingly, most of the key biological innovations took place in a period where bio-essential trace element concentrations are consistently low between 2000 to 1400 Ma. These particular events were not all independent of each other in that Eukarya had to evolve before organelles (although some prokaryotes possess analogous structures (Diekmann, 2013). However, the 4 events, Eukarya, acquisition of organelles, sex, and multicellularity, could be considered plausibly to have happened in any order and time, although the latter two may not be independent (Porter, 2004). If they are independent then the likelihood of their co-occurrence during the low trace element period has been demonstrated to be quite small (~0.0625).

Unlike in past studies, the trace element trend observed in the total Boring Billion period is not entirely low and flat, but after 1400 Ma, is in fact, followed by a long period of relatively higher trace

element concentrations (1400-800 Ma) i.e., higher than the median value for the Proterozoic. We observe an increase in trace element concentrations at around 1400 Ma which also coincides with an oxygenation event recognized using independent geochemical proxies (pyrite redox-sensitive trace element chemistry in black shales (Mukherjee and Large, 2016), Mo isotopes in black shales (Zhang et al., 2016) and U isotopes (Yang et al., 2017). Interestingly, this event is coeval with a major diversification of eukaryotes (Javaux et al., 2003; 2004; 2017). Complex cellular morphological capacities (cytoskeletal architecture) were observed and eukaryote habitation spread to a wider range of environments (Javaux et al., 2003; 2004). Diversification of eukaryotes is also noted in the Kamo Gp (1.3 Ga) (Nagovitsin, 2009), Kaltasy Fm (1.4–1.45 Ga) (Sergeev et al., 2016); Sarda Fm (~1.3 Ga), India (Prasad and Asher, 2001); Arctic Canada (~1.3 Ga) (Butterfield et al, 2000; Loron et al, 2017); in the 1.1-0.9 Ga Mbuyi-Mayi Supergroup, DR Congo (Baludikay et al, 2016); in the 1.1 Ga Atar/El Mreiti Gp, Mauritania (Beghin et al. 2017). This was followed by the diversification of crown group eukaryotes between 1200-1100 Ma (Knoll, 2014) and the emergence of a gene (1000-800 Ma), recently identified, that is linked with emergence of protein kinases and choline kinases responsible for cell adhesion and transfer of signals within cells efficiently (Amoutzias et al., 2007; Lai et al., 2016). The period ended with the appearance of metazoans at ~750 Ma (Knoll, 2014; Erwin et al., 2011) and the origin of fungi between 760 and 1000 Ma (Lucking et al., 2009).

In summary, key biological innovations in eukaryotes seemed to have co-occurred during the low trace element period followed by a broad-scale diversification of eukaryotes, in the relatively high trace element period. We attribute this trend (from a prokaryotic community (>1800 Ma) to the formation of the first eukaryotes (1800-1500 Ma) and their diversification (1400-800 Ma) to nutrient trace element availability as shown in Figs 6.1 and 6.2. Of course, macronutrient availability too may have played a critical role. However, previous work suggests a low and stable P and N through most of Earth's history until towards the end of the Boring Billion (~800 Ma) (Reinhard et al., 2017). This further supports the putative role of trace elements in shaping the course of evolution.

We propose that co-limitation of nutrient trace element may have caused an environmental stress, a plausible driver of the biological innovations in the early part of the Boring Billion including endosymbiosis (Sagan, 1967), whereby unicellular prokaryotes are forced into a symbiotic relationship due to nutrient limitation, conceivably resulting in Eukarya. Hoffmann and Hercus (2000) have previously proposed environmental stress as a major driver for evolutionary changes (DNA/genotypic/phenotypic variations, adaptation capacities). A decrease in the population (clearing of the ecological space), as a result of stressful conditions, causes renewed predation and competition that promotes subsequent evolutionary radiations in the newly reconstructed ecological space (Hoffmann and Parsons, 1997; Hoffmann and Hercus, 2000). Another possible mechanism for

evolutionary change are major population bottleneck events, such as may be expected during low trace element stress periods, which were then fixed as a result of small population sizes (Diekmann, 2013). Experiments have demonstrated that stress can double rates of stress-induced genetic mutations in bacteria whereby new genes are created with different functions, in most cases with advanced functions (Rosenberg et al., 2012). We propose that a prolonged period of low nutrient trace element conditions may have contributed to an environmental stress that triggered the key biological innovations we observe in the rock record.

On the other hand, an increase in nutrient trace element (after a prolonged nutrient crisis) may have triggered/facilitated diversification of the eukaryotes between 1400 and 800 Ma. Of course, once the diversification process commenced, the eukaryotic community expanded in the marine realm. One could possibly question that if nutrient conditions did in fact improve, what delayed the rise of animals until ~750 Ma? It is quite possible that the evolution and expansion of complex eukaryotic communities played a significant role in fostering ocean oxygenation (as proposed by Lenton et al., 2014) and bring about major changes in P and N cycles making the conditions conducive for the subsequent evolution of metazoans and their macroscopic counterparts. Therefore, the Boring Billion period is a critical time in Earth's evolutionary history when the prerequisites for macroevolution were established.

6.5 Conclusions

Our primary conclusions lead to a paradigm shift in understanding evolution during the Proterozoic. Firstly, the Proterozoic ocean witnessed periods of both low and high trace element availability; trace element trends are not flat and uniform as previously assumed. Secondly, we emphasize that the low nutrient trace element periods, were possibly essential triggers in the course of evolution. Previous studies claim low concentrations of trace element may have stalled evolution (Anbar and Knoll, 2002). However, we argue that these periods of trace element crisis forced organisms to explore their options to adapt to stressful conditions and promote mechanisms to cope and evolve. On the upside of nutrient trace element cycles, when conditions improved in terms of high trace element availability from 1400 Ma to 800 Ma, organisms diversified. Thus, the need for both unfavorable and favorable nutrient conditions may have been required to generate the necessary evolutionary pressure and diversification respectively through time. Thirdly, we propose that the high and low trace element periods in the "Boring Billion" may have played a critical role in establishing the prerequisites for metazoan evolution. It is unlikely that metazoans appeared all at once without prior evolutionary achievements. Therefore, sequential stepwise evolution and diversification of complex eukaryotes was likely a result of fluctuating nutrient trace element

conditions (stress/stress-free) through the "Boring Billion".

6.6 Acknowledgements

The project was funded by the Australian Research Council (DP150102578). We would like to thank Prof. Malcolm Walter, Prof. Mihir Deb, Chris Large and Jacob Mulder for their comments and suggestions.

6.7 References

Adam, Z.R, Skidmore, M.L., and Mogk, D.W., 2016. Paleoenvironmental implications of an expanded microfossil assemblage from the Chamberlain Formation, Belt Supergroup, Montana: The Geological Society of America Special Paper 522, 20.

Amoutzias, G., Veron, A., Weiner, J., Robinson-Rechavi, M., Bornberg-Bauer, E., Oliver, S.G., and Robertson, D.L., 2007. One billion years of bZIP transcription factor evolution: conservation and change in dimerization and DNA- binding site specificity: Molecular Biology and Evolution 24, 827–835.

Anbar, A.D., and Knoll, A.H., 2002. Proterozoic ocean chemistry and evolution: a bioinorganic bridge? Science 297, 1137–1142.

Arnold, G.L., Anbar, A.D., Barling, J., Lyons, T.W., 2004. Molybdenum isotope evidence for widespread anoxia in Mid-Proterozoic ocean. Science 304, 87-90.

Baludikay, B.K., Storme, J.Y., François, C., Baudet, D., Javaux, E.J., 2016. A diverse and exquisitely preserved organic-walled microfossil assemblage from the Meso- Neoproterozoic Mbuji-MayiSupergroup (Democratic Republic of Congo) and implications for Proterozoic biostratigraphy. Precambrian Research 281, 166–184.

Beghin, J., Storme, J.-Y., Blanpied, C., Gueneli, N., Brocks, J.J., Poulton, S.W., Javaux, E.J., 2017. Microfossils from the late Mesoproterozoic – early Neoproterozoic Atar/El Mreïti Group, Taoudeni Basin, Mauritania, northwestern Africa. Precambrian Res. 291, 63–82.

Bengtson et al. 2017. Three-dimensional preservation of cellular and subcellular structures suggests 1.6 billion-year-old crown-group red algae. PLoSBiol 15 (3): e2000735; doi: 10.1371/journal.pbio.2000735

Brasier, M.D., and Lindsay, J.F., 1998. A billion years of environmental stability and the emergence of eukaryotes: new data from northern Australia: Geology 26, 555–558.

Buick, R., Des Marais, D.J., and Knoll, A.H., 1995, Stable isotopic compositions of carbonates from the Mesoproterozoic Bangemall Group, northwestern Australia: Chemical Geology 123 (1–4), 153–171.

Butterfield, N.J., 2015. Early evolution of the Eukaryota: Palaeontology 58, 5–17.

Butterfield, N.J., 2000. Bangiomorpha pubescens n. gen., n. sp.: implications for the evolution of sex, multicellularity and the Mesoproterozoic/Neoproterozoic radiation of eukaryotes. Paleobiology 26, 386–404.

Canfield, D.E., 1998. A new model for Proterozoic ocean chemistry: Nature 396, 450–453.

Danovaro, R., Dell'Anno, A., Pusceddu, A., Gambi, C., Heiner, I., and Reinhardt Møbjerg, K., 2010, The first metazoa living in permanently anoxic conditions: BioMed Central Biology, 8:30. doi: 10.1186/1741-7007-8-30.

Diekmann, Y., & Pereira-Leal, J.B., 2013. Evolution of intracellular compartmentalization Biochemical Journal 449, 319-331

Erwin, D.H., Laflamme, M., Tweedt, S.M., Sperling, E.A., Pisani, D., and Peterson, K.J., 2011. The Cambrian conundrum: early divergence and later ecological success in the early history of animals: Science 334, 1091–1097.

Gregory, D., Meffre, S., and Large, R., 2014. Comparison of metal enrichment in pyrite framboids from a metal-enriched and metal-poor estuary: American Mineralogist 99, 633-644.

Gregory, D.D., Large, R.R., Halpin, J.A., Lounejeva Baturina, E., Lyons, T.W., Wu, S., Sack, P.J., Chappaz, A., Maslennikov, V.V., Bull, S.W., Danyushevsky, L., 2015. Trace element content of sedimentary pyrite in black shales. Econ. Geol. 110, 1389–1410.

Gregory, D. D., Lyons, T. W., Large, R. R., Jiang, G., Stepanov, A. S., Diamond, C., Figueroa, M., and Olin, P., 2017. Whole rock and discrete pyrite geochemistry as complementary tracers of ancient ocean chemistry: An example from the Neoproterozoic Doushantuo Formation, China: Geochimica et Cosmochimica Acta. In press.

Hoffmann A.A., Parsons P.A., 1997. Extreme Environmental Change and Evolution. Cambridge (UK): Cambridge University Press.

Hoffmann, A.A., & Hercus, M.J., 2000. Environmental stress as an evolutionary force. BioScience 50: 217–226.

Holland. H.D., 2006. The oxygenation of the atmosphere and oceans Phil. Trans. R. Soc. 361.

Javaux, E., Knoll, A.H., and Walter, M.R., 2003. Recognizing and interpreting the fossils of early eukaryotes: Origins of Life and Evolution of the Biosphere 33, 75–94.

Javaux, E., Knoll, A.H., and Walter, M.R., 2004. TEM evidence for eukaryotic diversity in mid-Proterozoic oceans: Geobiology 2, 121–132.

Javaux, E.J., and Knoll, A.H., 2017, Micropaleontology of the lower Mesoprotero- zoic Roper Group, Australia, and implications for early eukaryotic evolution: Journal of Paleontology, doi:10.1017/jpa.2016.124

Johnson, R.A. & Wichern, D.W. 1988. "Applied Multivariate Statistical Analysis", 2nd Edition, Prentice-Hall: Englewood Cliffs.

Kabnick, K.S., and Peattie, D.A., 1991. Giardia: A Missing Link between Prokaryotes and Eukaryotes: American Scientist 79, 34.

Katz, L.A., 2012. Origin and diversification of eukaryotes: Annual Review of Microbiology 66, 411–427.

Kendall, B., Creaser, R.A., Gordon, G.W., Anbar, A.D., 2009. Re-Os and Mo isotope systematics of black shales from the Middle Proterozoic Velkerri and Wollogorang Formations, McArthur Basin, northern Australia. Geochim Cosmochim Acta 73, 2534-2558.

Knoll, A.H., 2014. Paleobiological perspectives on early eukaryotic evolution: Cold Spring Harbor Perspectives in Biology, doi: 10.1101/cshperspect.a01612.

Kobayashi, K., and Ponnamperuma, C., 1985, Trace elements in chemical evolution, I: Origins of Life and Evolution of the Biosphere 16(1), 41-55.

Lai, S., Safaei, J., and Pelech, S., 2016. Evolutionary ancestry of eukaryotic protein kinases and choline kinases: The Journal of Biological Chemistry 291, 5199–5205.

Lamb, D.M., Awramik, S.M., Chapman, D.J., and Zhu, S., 2009. Evidence for eukaryotic diversification in the similar to 1800 million-year-old Changzhougou Formation, North China: Precambrian Research 173, 93–104.

Large, R.R, Halpin, J.A., Lounejeva, E., Danyushevsky, L.V., Maslennikov, V.V., Gregory, D., Sack, P.J., Haines, P.W., Long, J.A., Makoundi, C., and Stepanov, A.S., 2015. Cycles of nutrient trace elements in the Phanerozoic ocean: Gondwana Research 28 (4), 1282-1293.

Large, R.R., Halpin, J.A., Danyushevsky, L.V., Maslennikov, V.V., Bull, S.W., Long, J.A., Gregory,

D.D., Lounejeva, E., Lyons, T.W., Sack, P.J., McGoldrick, P. and Calver, C.R., 2014. Trace element content of sedimentary pyrite as a new proxy for deep-time ocean- atmosphere evolution: Earth and Planetary Science Letters 389, 209-220.

Large R.R., Mukherjee, I., Gregory, D.G., Steadman, J.A., Maslennikov, V.V., and Meffre, S., 2017. Ocean and Atmosphere Geochemical Proxies Derived from Trace Elements in Marine Pyrite: Implications for Ore Genesis in Sedimentary Basins. Economic Geology 112(2), 423-450

Lenton, T.M., Boyle, R.A., Poulton, S.W., Shields-Zhou, G.A., and Butterfield, N.J., 2014. Co-evolution of eukaryotes and ocean oxygenation in the Neoproterozoic era: Nature Geoscience 7, 257–265.

Longerich, H.P., Jackson, S.E. and Günther, D., 1996. Laser ablation inductively coupled plasma mass spectrometric transient signal data acquisition and analyte concentration calculation. Journal of Analytical Atomic Spectrometry 11, 899-904.

Loron, C., and Moczydłowska., 2017. Tonian (Neoproterozoic) eukaryotic and prokaryotic organic-walled microfossils from the upper Visingsö Group, Sweden, Palynology, DOI: 10.1080/01916122.2017.1335656

Lücking, R., Huhndorf, S., Pfister, D.H., Plata, E.R., & Lumbsch, H.T., 2009. Fungi evolved right on track, Mycologia, 101(6), 810-822.

Lyons, T.W., Reinhard, C.T., and Planavsky, N.J., 2014, The rise of oxygen in Earth's early ocean and atmosphere: Nature, v. 506, p. 307-315.

Morel., M.M.F., Husdon, R., and Price, N.M. 1991. Limitation of productivity by trace metals in the sea. Limnol. Oceanogr., 36(8), 1742-1755

Mukherjee, I., and Large, R., 2016, Pyrite trace element chemistry of the Velkerri Formation, Roper Group, McArthur Basin: Evidence for atmospheric oxygenation during the Boring Billion: Precambrian Research 281, 13-26.

Mukherjee, I., and Large, R.R., 2017, Application of Pyrite Trace Element Chemistry to Exploration for SEDEX Style Zn-Pb Deposits: McArthur Basin, Northern Territory Australia: Ore Geology Reviews 81, 1249–1270.

Muller, W.E.G., 2001, How was metazoan threshold crossed: the hypothetical Urmetazoa: Comparative Biochemistry and Physiology- Part A 129, 433-460.

Nagovitsin, K., 2009, Tappania-bearing association of the Siberian platform: Biodiversity, stratigraphic position and geochronological constraints, Precambrian Research 173, 137–145.

Nielsen C., 2008, Six major steps in animal evolution: are we derived sponge larvae? Evolution and Development 10, 241–57.

Ochiai, E.I., 1978a. The evolution of the environment and its influence on the evolution of life: Origins Life 9, 81-91.

Ochiai, E.I., 1978b. Principles in the selection of inorganic elements by organisms -Application to molybdenum enzymes: BioSystems 10, 329-337.

Partin, C.A., Bekker, A., Planavsky, N.J., Scott, C.T., Gill, B.C., Li, C., Podkovyrov, V., Maslov, A., Konhauser, K.O., Lalonde, S.V., Love, G.D., Poulton, S.W., and Lyons, T.W., 2013. Large-scale fluctuations in Precambrian atmospheric and oceanic oxygen levels from the record of U in shales: Earth Planetary Science Letters, 369–370.

Planavsky, N.J., Reinhard, C.T., Wang, X., Thomson, D., McGoldrick, P., Rainbird, R.H., Johnson, T., Fischer, W.W., and Lyons, T.W., 2014. Low Mid-Proterozoic atmospheric oxygen levels and the delayed rise of animals: Science 346, 635-638.

Porter, S.M., 2004. The fossil record of early eukaryotic diversification: Paleontological Society Papers 10, 35-50.

Prasad, B., and Asher, R., 2001. Acritarch biostratigraphy and lithostratigraphic classification of Proterozoic and Lower Paleozoic sediments (Pre-unconformity sequence) of Ganga Basin, India. Precambrian Research 291, 63-82

Reinhard C. T., Planavsky N. J., Gill B. C., Ozaki K., Robbins L. J., Lyons T. W., et al. 2017. Evolution of the global phosphorus cycle. Nature 541, 386–389. 10.1038/nature20772

Robbins, L.J., et al., (14 more authors) 2016. Trace elements at the intersection of marine biological and geochemical evolution. Earth Science Reviews 163, 323-348.

Roberts, N.M.W., 2013. The boring billion? – Lid tectonics, continental growth and environmental change associated with the Columbia supercontinent. Geoscience Frontiers 4, 681-691.

Rosenberg, S.M., Shee, C., Frisch, R.L., and Hastings, P.J., 2012. Stress-induced mutation via DNA breaks in Escherichia coli: A molecular mechanism with implications for evolution and medicine: Bioessays., 34(10), 885-892.

Sagan, L., 1967, On the origin of mitosing cells: Journal of Theoretical Biology, v. 14, p. 225–274, doi:10.1016/0022-5193(67)90079-3.

Scott, C., Lyons, T.W., Bekker, A., Shen, Y., Poulton, S.W., Chu, X., and Anbar, A.D., 2008, Tracing the stepwise

oxygenation of the Proterozoic ocean: Nature, v. 452, p. 456–459.

Piper, J.S.A., 2013. A planetary perspective on Earth evolution: Lid Tectonics before Plate Tectonics. Tectonophysics 589, 44-56.

Sergeev, V.N., Knoll, A.H., Vorob'eva, N.G., and Sergeeva, N.D., 2016. Microfossils from the lower Mesoproterozoic Kaltasy Formation, East European Platform. Precambrian Research 278, 87-107

Singh, V.K., and Sharma, M., 2014. Morphologically complex organic-walled microfossils from the late Palaeoproterozoic–early Mesoproterozoic Chitrakut Formation, Vindhyan Supergroup, central India and their implications on the antiquity of eukaryotes: Palaeontological Society of India Journal 59, 89–102.

Sterner, R.W., 2008. On the Phosphorus Limitation Paradigm for Lakes. International Review of Hydrobiology 93, 433–445. doi:10.1002/iroh.200811068

Vorob'eva, N.G., Sergeev, V.N., and Yu, P., 2015. Kotuikan Formation assemblage: a diverse organic-walled microbiota in the Mesoproterozoic Anabar succession, northern Siberia: Precambrian Research 256, 201–222.

Wray, G.A., Levinton, J.S. and Shapiro, L.H., 1996. Molecular evidence for deep Precambrian divergences among metazoan phyla: Science, 568-573.

Xiao, S.H., Knoll, A.H., Kaufman, A.J., Yin, L.M., and Zhang, Y., 1997,Neoproterozoic fossils in Mesoproterozoic rocks? Chemostratigraphic resolution of a biostratigraphic conundrum from the North China Platform: Precambrian Research 84, 197–220.

Yang, S., Kendall, B., Lu, X., Zhang, F., and Zhang, W. 2017. Uranium isotope compositions of mid-Proterozoic black shales: Evidence for an episode of increased ocean oxygenation at 1.36 Ga and evaluation of the effect of post-depositional hydrothermal fluid flow. Precambrian Research 298, 187-201.

Yin, L.M., 1997. Acanthomorphicacritarchs from Meso-Neoproterozoic shales of the Ruyang Group, Shanxi, China: Review of Palaeobotany and Palynology 98, 15–25.

Zhang S, Wang, X., Wang, H., Bjerrum, C., Hammarlund, E.U., Costa, M.M., Connelly, J.N., Zhang, B., Su, J., and Canfield, D.E. 2016. Sufficient oxygen for animal respiration 1,400 million years ago. Proc Natl AcadSci USA 113(7), 1731–1736.

Zhu, S., Zhu, M., Knoll, A., Yin, Z., Zhao, F., Sun, S., Qu, Y., Shi, M., and Liu, H. 2016. Decimetre-scale multicellular eukaryotes from the 1.56-billion-year-old Gaoyuzhuang Formation in North

Chapter 7

Synthesis

7.0 Introduction

This synthesis summarises the findings and conclusions of this study and aims to answer the PhD research questions outlined in Chapter 1. These are the following:

1. How can we use trace element concentrations in sedimentary pyrite, and sulphur isotope compositions of sedimentary pyrite in black shales, to infer paleo-atmospheric ocean redox structure and nutrient-productivity cycles in the Boring Billion?

2. Does hydrothermal alteration affect sedimentary pyrite chemistry, and can this be used as a mineralisation vector?

3. How do trace element concentrations in pyrite reflect their availability in the oceans during the "Boring Billion"? What are the possible factors controlling their availability in the oceans?

4. What are the possible implications of trace element availability in the oceans on biologic evolution during the Boring Billion?

The following sections will elaborate on how each of these questions were addressed in the five chapters of my PhD research. Potential scope for future research is also discussed.

7.1 Paper 1: Pyrite trace element chemistry of the Velkerri Formation, Roper Group, McArthur Basin: Evidence for atmospheric oxygenation during the Boring Billion

(published in Precambrian Research)

This paper compared the conventional whole rock technique with the pyrite-LA-ICP-MS technique adopted for the PhD research to understand trace element geochemistry in the Roper Group, McArthur Basin in Northern Australia. Main findings were that the pyrite-LA-ICP-MS approach is more suitable for trace element analyses compared to whole rock as it provides better detection limits and is a more sensitive tool. Significant trace element variations were noted using the pyrite-LA-ICP-MS technique in the Roper Group black shales. These trends, in the same samples, were not identified through whole rock analyses, which confirmed the sensitivity issue mentioned above.

Results of the study demonstrate that trace elements in marine sedimentary pyrites can be used to track evolution of redox conditions of the atmosphere. An oxygenation event at ~1400 Ma was identified through pyrite-trace element geochemistry of the Velkerri Formation (Roper Group) that had not been previously recorded. This was determined on the basis of enriched trace elements (Se, Ni, Mo, Zn, U, V, Cr) in the pyrite and black shales of the Velkerri Formation. This paper partly addressed question 1.

7.2 Paper 2: Application of pyrite trace element chemistry to exploration for SEDEX style Zn-Pb deposits, McArthur Basin, Northern Territory, Australia

(published in Ore Geology Reviews)

This paper focused on the pyrite trace element geochemistry of the ~1640 Ma Barney Creek Formation (McArthur Basin) for two main reasons. First, to understand the redox state of the atmosphere during its deposition. Second, because the Barney Creek Formation hosts one of the world's largest SEDEX-Zn-Pb deposits (McArthur River), we analyzed shales from varying proximity to mineralization to measure variations in trace elements in sedimentary pyrites (if any). The main conclusions were that trace element content of sedimentary pyrites forming under the influence of hydrothermal exhalations impart different trace element characteristics compared to the pyrites forming without a hydrothermal influence. Certain trace elements (Zn, Pb, Tl) increased and some decreased (Mo, Ni, Co) in pyrite with respect to proximity to the ore body. These observations were then used to devise pyrite vector diagrams that would aid in future exploration of McArthur River-style deposits in the basin. The study also concluded that black shales known to host mineralization should be carefully sampled for interpreting past ocean chemistry. Only barren shales (and contained pyrite) that show no evidence of the effects of hydrothermal activity reflect genuine past seawater trace element concentrations. This paper addressed question 2.

7.3 Paper 3: Pyrite trace element and sulphur isotope geochemistry of Paleo-Mesoproterozoic black shales from the McArthur Basin, Northern Australia

(revision submitted to Geochimica et Cosmochimica Acta)

This paper aimed at providing a complete picture of the evolution of the atmosphere-ocean redox conditions from ~1730 Ma through till ~1360 Ma i.e., the early part of the Boring Billion. Two complimentary techniques, pyrite-LA-ICP-MS and pyrite-SHRIMP-SI, were adopted towards analyzing trace element concentrations and sulphur isotope compositions in marine sedimentary pyrites respectively. The study demonstrates that trace elements in pyrite (Se, Ni, Mo, Zn, Co, Bi) and their ratios (Se/Co, Ni/Co, Mo/Co, Zn/Co, Se/Bi, Ni/Bi, Mo/Bi, Zn/Bi) are robust indicators of

atmospheric oxygenation. Certain trace elements in the black shale matrix (Th, Cr, Ti and Zr) and their ratios were also used to identify potential provenance of the black shales to negate source rock influence on trace element compositions. Sulphur isotope compositions on the other hand provided useful insights on ocean redox conditions. A combination of these techniques helped identify an ocean oxygenation event at ~1360 and a rise in atmospheric oxygen levels from 1730 Ma till ~1360 Ma (confirming results of paper 1). This paper addressed questions 1 and 3.

7.4 Paper 4: Sedimentary Pyrites of Bijaigarh Shales, Vindhyan Basin, India: Textures, Trace Element Chemistry and their Implications

(to be submitted in Journal of Asian Earth Sciences)

This paper applied the pyrite-LA-ICP-MS technique to a ~1.2 Ga Proterozoic black shale formation (Bijaigarh Shale in the Vindhyan Supergroup, India). Detailed pyrite textural study was undertaken and a variety of textures were identified that were not previously reported. This was combined with pyrite trace element analyses that provided insights into the redox state of the Vindhyan Basin, India and were compared to pyrite analyses from different time spans (Phanerozoic, Proterozoic and Archean). Our data indicates suppressed oxidative weathering, in other words low atmospheric levels, during ~1.2 Ga compared to the Phanerozoic, on the basis of low trace element concentrations (and their ratios). However, O_2 levels were clearly higher than the Archean. The pyrite data from the Bijaigarh Shale is compatible with the Proterozoic pyrites previously reported by Large et al. (2017). This paper addressed question 1.

7.5 Paper 5: The Boring Billion, a slingshot for Complex Life on Earth

(published in Scientific Reports)

This paper collated data from various Proterozoic black shales undertaken for this PhD research with additional analyses from the ~1630 Ma Riversleigh Siltstone and ~1050 Ma Lilian Formation to provide an overall understanding of the Boring Billion. The main focus was to evaluate bio-essential trace element availability in the Proterozoic oceans and their profound impact on biologic evolution at the time. Several gaps in our knowledge, that were identified in previous work, were also addressed.

We observed that the bio-essential trace element availability declined after the Great Oxidation Event 1 and remained low until 1400 Ma. This is coeval with evolutionary innovations in microbial life such as the appearance of the first eukaryotes, multicellularity etc. From about 1400 Ma, we

saw a significant rise in nutrient trace element availability, which is also marked by major eukaryotic diversification events.

There were two main conclusions. First, trace element concentrations in the ocean vary significantly through the Boring Billion in contrast to the interpretation from previous studies that proposed a consistently low trace element period without any significant fluctuations. Second, we propose that the period of low trace element availability may have been a period of nutrient crisis. This caused an environmental stress that microorganisms had to cope with and adapt to, via evolutionary innovations. When conditions improved (increase in trace element availability), their diversification was facilitated. This conclusion is novel and provides a unique perspective on the time span. This paper addressed question 4.

7.6 Summary

The main focus of this PhD research was to evaluate atmosphere-ocean redox conditions, nutrient availability and their subsequent impact on biologic evolution in the Boring Billion using an unconventional technique (pyrite-LA-ICP-MS; Large et al., 2014). Chapters 2, 3, 4, 5 involved extensive pyrite trace element work, and in case of chapter 4, sulphur isotope analyses (a total of ~2000 analyses). This data aided in the technique validation and attesting to the lines of evidence presented in the proof of concept paper by Large et al. (2014). Furthermore, the data was used to construct a multi-trace element trend through the Boring Billion in order to investigate its implications on biologic evolution of life (Fig 7.1). This PhD research concludes by providing a novel explanation for the timing of the development of Earth's first complex cells in the early part of the Boring Billion (1800-1400) and their diversification in the latter part (1400-800 Ma).

There are several ways of explaining the bio-essential trace element trend between the 1800-800 Ma period. First, suppressed continental oxidative weathering prior to 1400 Ma may have caused a decreased supply of trace elements in the ocean. Second, source rock composition (felsic or mafic) may have been an important factor in controlling the type of trace element flux in to the oceans. This is because most bio-essential trace elements are generally enriched in mafic rocks than in felsic with the exception of Mo and Se (Riemann and Caritat, 1998). Molybdenum was slightly enriched in felsic rocks and Se concentrations were roughly the same in both mafic and felsic types. Overall, there was a decreased continental supply of these trace elements into the ocean via riverine flux. A combination of low oxidative weathering and erosion of dominantly felsic source rocks may have caused the low trace element period between 1800-1400 Ma. An increase

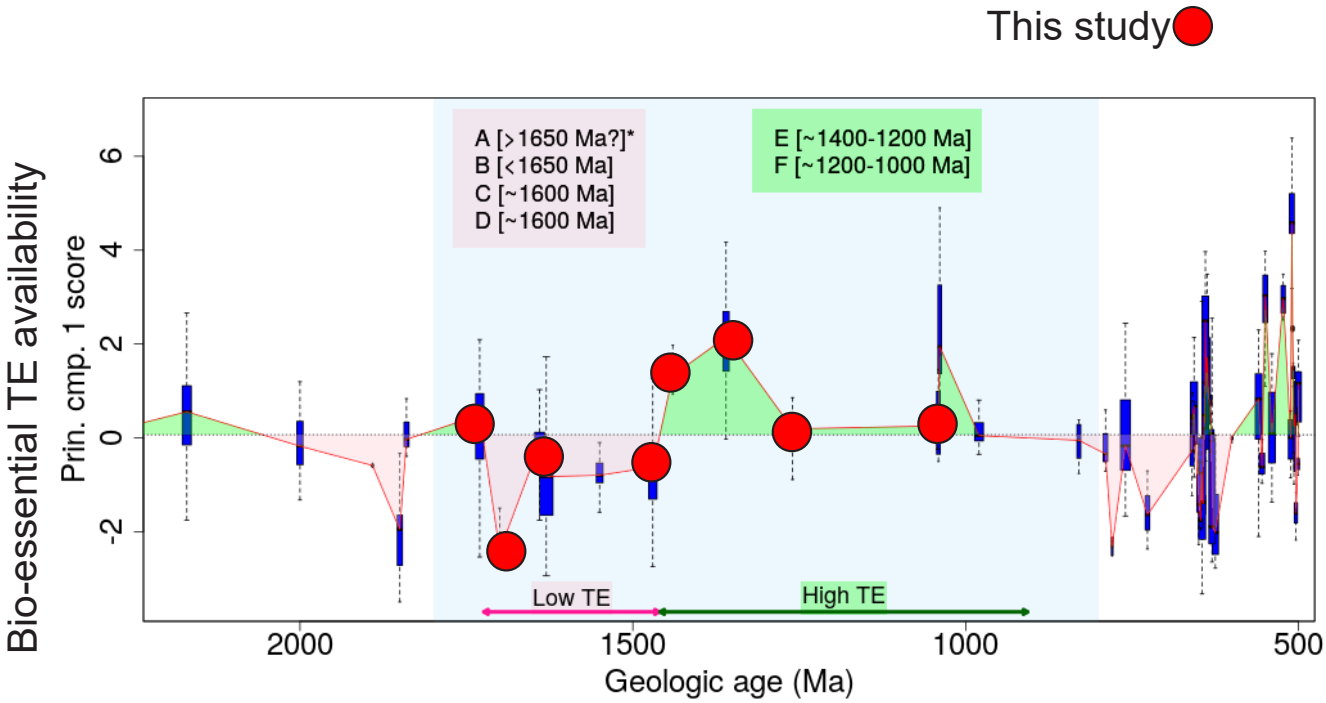

Fig 7.1 Bio-essential trace element availability through the Boring Billion period

in oxygen levels in the atmosphere-ocean system accompanied by a marked change in source rock composition may possibly explain the increase in trace element availability at ~1400 Ma.

7.7 Future research lines

While global events during the Proterozoic Eon have been the subject of many studies, including this PhD, certain aspects are yet to be fully understood. The following questions provide an excellent scope for further research.

- What were the causes for the step change in oxygen in the atmosphere during the GOE event (both rise and decline) and secular evolution of oxygen in the oceans?
- Was oxygenation the main driver of metazoan evolution?
- What were the geochemical conditions of ancient seawater in terms of actual concentration of bio-essential macro and trace elements, dissolved oxygen, pH, salinity and temperature?
- Were geochemical conditions in the Proterozoic a result of varying continental source rock composition and tectonic regimes?

- What role did these conditions play in the evolution of the first metazoans and their subsequent macroevolution?

The extensive pyrite database can also be used to compare multi-trace element trends in the ocean, to other sinks of trace elements like Banded Iron Formations, red shales etc. Trace elements in pyrite that are used as oxygenation proxies (Se, Co, Mo, Zn, Se/Co, Mo/Co, Zn/Co etc.) could be compared with other oxygenation proxies in the rock record such as the abundance and diversification of stromatolites through time. Overall, combining pyrite trace element chemistry with other geochemical proxies, a model for early life and its evolution could be developed, with wider applications such as the extraterrestrial search for life.

7.8 References

Large, R.R., Halpin, J.A., Danyushevsky, L.V., Maslennikov, V.V., Bull, S.W., Long, J.A., Gregory, D.D., Lounejeva, E., Lyons, T.W., Sack, P.J., McGoldrick, P. and Calver, C.R., 2014. Trace element content of sedimentary pyrite as a new proxy for deep-time ocean- atmosphere evolution. Earth and Planetary Science Letters 389, 209-220.

Large R.R., Mukherjee, I., Gregory, D.G., Steadman, J.A., Maslennikov, V.V., and Meffre, S., 2017. Ocean and Atmosphere Geochemical Proxies Derived from Trace Elements in Marine Pyrite: Implications for Ore Genesis in Sedimentary Basins. Economic Geology 112(2), 423-450

Reimann, C and de Caritat, P, 1998. Chemical Elements in the Environment, Fact Sheets for the Geochemist and Environmental Scientist: Springer-Verlag, Berlin, 397 p.

Appendix

Chapter 3

Table A3.1 Pyrite LA-ICP-MS data for drill hole MBXDD001 in ppm (see digital appendix)

Table A3.1 Pyrite LA-ICP-MS data for drill hole Leila Yard 1 in ppm (see digital appendix)

Table A3.3 Pyrite LA-ICP-MS data for Myrtle-4 in ppm (see digital appendix)

Table A3.4 Pyrite LA-ICP-MS data for two HYC samples in ppm (see digital appendix)

Chapter 4

A4.1 Provenance of sediments and tectonic setting

The Wollogorang Formation forms part of the middle package of the Tawallah Group. Studies by Rogers (1996), using detailed sedimentology, and Bull (1993), using paleocurrent measurements, indicate that the sediments of the Wollogorang Formation were derived from erosion of the basal package of the Tawallah Group, comprised of sandstones and mafic volcanics (Table A4.1). The sediments for the McArthur Group (including the Barney Creek Formation) were most likely derived from the underlying Tawallah Group as a result of uplift and erosion (Haines et al., 1993; 1994) (Table A4.1). The source rocks mainly comprised shallow water fluvial clastic sandstone, mudstones and dolostones along with bimodal volcanics (basalt and rhyolite) and higher level intrusives. Unlike the Wollogorang and Barney Creek Formations and their respective groups, the possible source rocks for the Roper Group are speculative (Table A4.1). Sediments for the Roper Group could have been derived from either the Helens Spring High (Gorter et al., 2012) or the Isan Orogen (Abbott and Sweet, 2000). Recent studies (U-Pb dating of zircons) suggest the Roper Group sediments were derived from the North Australian Craton composed of greywacke-siltstones, tuffs, BIFs and mafic-felsic volcanic rocks (Munsen et al., 2016). Both Tawallah and McArthur Groups are associated with rift to post rift related deposition (Rogers, 1996; Giles et al., 2002). The Roper Group was deposited in an intracratonic, siliciclastic ramp setting developed in response to tectonic and eustatic changes (Abbott and Sweet, 2000) (Table A4.1)

Formation (Age)	Group	Lithology	Depositional environment	Source rocks	Tectonic setting	Major Orogenies
Velkerri (~1400 Ma)	Roper	Grey and black mudstone and siltstone; minor glauconitic sandstone; ~**7-10 % TOC**	Most basinal facies	North Australian craton	subsidence-related	possibly Isan
Barney Creek (~1640 Ma)	McArthur	Dolomitic, carbonaceous and pyritic shale and siltstone, dololutite; **~10% TOC**	Basinal shale deposited in actively subsiding sub-basins	Tawallah Group	rift related	local uplift
Wollogorang (~1730 Ma)	Tawallah	Dolomitic, carbonaceous and pyritic shale; **~6-7% TOC**	Basinal shale	Basal Tawallah	rift related	local uplift

Table A4.1 Comparison of source rocks and tectonic setting between three black shale formations

Table A4.2, A4.3, A4.4 (see digital appendix)

A4.2 Evolution of Microorganisms in the McArthur Basin between 1730-1360Ma

It is interesting to note that the Wollogorang Formation has been known to only comprise unmineralised stromatolites and filamentous microfossils bearing resemblance to those in the HYC Pyritic Shale in the Barney Creek Formation, all of which are prokaryotic in origin (Muir, 1982). The Barney Creek Formation comprises mainly bacterial and algal microfossils. Nevertheless, the assemblage differs from most Precambrian biotas being dominated by filamentous bacteria that are mostly pyritized. Most algal fossils are prokaryotic in nature except two that could possibly be of eukaryotic origin (Oehler, 1977). Interestingly, the Velkerri Formation microfossils impart remarkable complexity i.e., cytoskeletal and ecological prerequisites for eukaryotic diversification, process-bearing microfossils confirming presence

of sophisticated organisms living in ecologically differentiated communities at the time (Javaux et al., 2001; 2004).

A4.3 Statistical tests on sedimentary pyrite analyses from McArthur Basin shales

Trace element concentrations of sedimentary pyrites from three different black shale formations were analysed using the Laser Ablation-Inductively Coupled Plasma-Mass Spectrometry. Means of trace element concentrations (e.g., Se, Mo, Zn etc.) in the three black shales were compared with one another. Considering the high variability in LA-ICP-MS analyses, certain statistical tests were performed to confirm the differences in the mean were significant. They included the following:

1. Normality tests
2. T-test for equal/unequal variances
3. Analyses of Variance (AOV's)

Normality tests were carried out in order to be able to apply parametric tests such as T tests. Both graphical and statistical tests (Q-Q plot and Shapiro-Wilk and Jarque-Bera tests) were performed to check for normality. Six elements (Se, Mo, Co, Ni, Bi, Zn) were included for the tests. The concentration (in ppm) was log transformed prior to normality tests. Results of the test indicate that all the elements in the Velkerri Formation impart normal distribution based on the Q-Q plot and the Shapiro-Wilk and Jarque-Bera tests. Elements in the Barney Creek Formation do not indicate a normal distribution according to the tests. In the Wollogorang Formation, Se, Ni, Bi, Co show a normal distribution whereas Zn, Mo do not. Please refer normality tests excel sheets for the three black shale formations.

Even though application for T-test is also not advisable with non-normal population it is usually not a major problem for when the sample size is >20. In this study, all three cases have sample size above 20. Please refer T tests excel sheet for the T test results.

The t-tests for six elements (Se, Ni, Mo, Zn, Bi, Co) are summarised below and in Table 4 in the manuscript:

Molybdenum: Mean Mo concentrations in the Velkerri Formation differ from both the Barney Creek and Wollogorang Formations. However, there is no significant difference between the mean Mo concentrations of the Barney Creek and Wollogorang Formations.

Selenium: Mean Se concentrations in the Velkerri Formation differ from both the Barney Creek and Wollogorang Formations. However, there is no significant difference between the mean Se concentrations of the Barney Creek and Wollogorang Formations.

Nickel: There is no significant differences of the mean in the three different formations

The CORR Procedure

Spearman Correlation Coefficients
Prob > |r| under H0: Rho=0
Number of Observations

	Co	Ni	Cu	Zn	As	Se	Mo	Ag	Tl	Pb	Bi
Age	0.54140	0.00943	0.39375	-0.16633	0.37540	-0.24914	0.24955	0.28389	0.35966	0.14187	0.40885
Age	<.0001	0.8904	<.0001	0.0144	<.0001	0.0002	0.0002	<.0001	<.0001	0.0381	<.0001
	216	216	216	216	216	216	216	211	216	214	216

The CORR Procedure

Spearman Correlation Coefficients, N = 216
Prob > |r| under H0: Rho=0

	Se_Co	Ni_Co	Zn_Co	Mo_Co	Se_Bi	Ni_Bi	Zn_Bi	Mo_Bi
Age	-0.66702	-0.75275	-0.48966	-0.14217	-0.47688	-0.40362	-0.46517	-0.06345
Age	<.0001	<.0001	<.0001	0.0368	<.0001	<.0001	<.0001	0.3534

Zinc: Mean Zn concentrations in the Velkerri Formation differ from both the Barney Creek and Wollogorang Formations. However, there is no significant difference between the mean Zn concentrations of the Barney Creek and Wollogorang Formations.

Cobalt: Mean Co concentrations differ significantly in all three formations.

Bismuth: Mean Bi concentrations differ significantly in all three formation

We show the Spearman correlations (generated by SASweave; Lenth and Højsgaard, 2007) of each variable with age (from 1400 Ma to 1700 Ma) below. This is a non-parametric measure, which means that using the logged data would give the same result. For each I show the correlation, the significance, and the sample size.

Results confirm that Co, Tl, Cu and Bi show positive correlation with increasing age (from 1400 Ma to 1700 Ma). Selenium and Zn show a negative correlation with increasing age. Molybdenum

shows a weak positive correlation with increasing age. All the ratios (Se/Co, Ni/Co, Zn/Co, Mo/Co, Se/Bi, Ni/Bi, Zn/Bi, Mo/Bi) show negative correlation with increasing age. On the basis of the significance values, we reject the hypotheses of unvarying trace element trends from 1400 Ma to 1700 Ma (except for Ni).

Please see A4.5_AOV's for more information in digital appendix.

A4.4 Sedimentary pyrite textures analysed for this study

Figure A4.1 represents some of the common pyrite textures observed in the three black shale formations. Pyrite usually occur as microcrystals disseminated in the black shale matrix with individual grain size ranging between 1-10 µ. Fine-grained pyrites in spherical and non-spherical aggregates (10-100 µ) and bedding-parallel layers were also observed. Sedimentary pyrite textures were similar in all three black shale formations. Importance of pyrite textural study prior to LA-ICP-MS analyses has been emphasized in Mukherjee and Large (2016, 2017) where TE concentrations were discussed in light of different textures. Both studies concluded that only sedimentary pyrites record sea water trace element chemistry and are most suitable for the LA-ICP-MS approach.

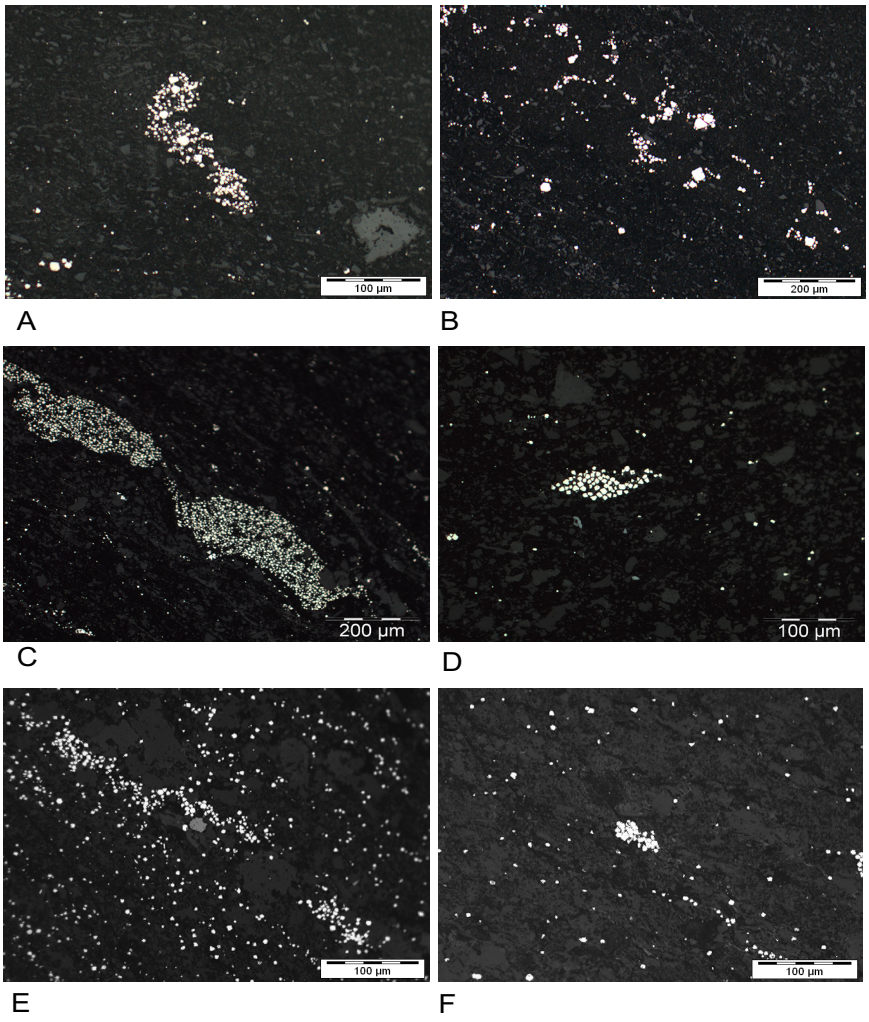

Figure A4.1 Pyrite textures observed in the three black shale formations (A, B: Velkerri Formation; C, D: Barney Creek Formation; E, F: Wollogorang Formation)

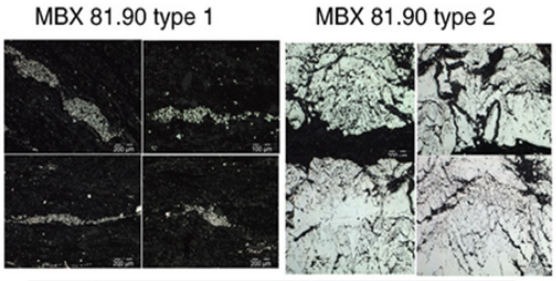

	MBX 81.90 type 1	MBX 81.90 type 2
Co	137	6
Ni	330	11
Cu	99	30
Zn	71	9
As	373	38
Se	6	5.07
Mo	214	4
Ag	2	0.08
Tl	7	39
Pb	409	37

Figure A2 Trace element concentrations of fine-grained sedimentary pyrite (type 1) and coarse grained pyrite (type 2) in the Barney Creek Formation (Mukherjee and Large, 2017).

Chapter 5

Table A5.1a (see digital appendix)

Table A5.1b (see digital appendix)

Chapter 6

Table A6.1 a and b (see digital appendix)

Table A6.2 (see digital appendix)

A6.1 Methods and materials

A6.1.1 Using sedimentary pyrite trace element

Certain redox-sensitive trace elements (Mo, U, Cr, V, Zn) in black shales have been used previously as paleoredox indicators of the water column (Algeo et al., 2006; Tribovillard et al., 2006; Algeo et al., 2009; Algeo et al., 2012; Meyer et al., 2008; Gordon et al., 2009; Sahoo et al., 2012; Sahoo et al., 2016). Also, they have been used to track atmospheric oxygenation through time (Scott et al., 2008; Partin et al., 2013; Lyons et al., 2014). Recently, Large et al. (2014) proposed that trace element concentrations in sedimentary pyrite formed in marine black shales could be used as proxies for ocean trace element chemistry and atmospheric oxygenation. This proxy relies on the fact that most redox-sensitive trace elements, in bottom waters and pore waters, are readily and efficiently adsorbed by sedimentary pyrites (Huerta-Diaz and Morse, 1992; Morse and Arakaki, 1993, Rickard et al., 2012; Gregory et al., 2014; Large et al., 2014; Gregory et al., 2015, 2016; Mukherjee and Large, 2016). The premise on which the technique is based, is that enhanced oxidative weathering on land causes an increase in the supply of redox-sensitive trace elements in the riverine flux (dominant source) in the ocean (Bertine et al., 1973; Taylor et al., 1995; Scott et al., 2008; Sahoo et al., 2012; Crowe et al., 2013). On encountering a redox-boundary, these become readily adsorbed by sedimentary pyrites forming in anoxic black shales. Hence, redox sensitive trace element concentrations in sedimentary pyrites act as an indirect proxy for atmospheric oxygenation events (Gregory et al., 2014; Large et al., 2014; Gregory et al., 2015a; Gregory et al., 2015; Mukherjee and Large, 2016) including the proof of concept paper (Large et al., 2014).

There are several advantages of using a marine pyrite trace element approach for understanding ocean chemistry. Firstly, the technique (LA-ICP-MS) is highly sensitive and allow in situ analysis of the pyrites. Better detection limits by LA-ICP-MS (particularly for elements like Se, Co and Mo) allow more robust trace element concentrations at lower levels. Secondly, both techniques offer high spatial resolution so measurements can be performed within a single grain domain, avoiding the problem of variation in composition of shales. Many TE, such as Mo, are partitioned between minerals in the shale (Tribovillard et al., 2006), and thus variation in mineral composition affects the bulk rock analyses. Thirdly and most importantly, the effects of diagenesis, metamorphism and hydrothermal activity, all of which affect trace element concentrations, can easily be detected by textural study of the pyrite before and after analyses. In case of trace elements, Large et al. (2009) demonstrated that the process of recrystallization of pyrite during diagenesis or metamorphism, releases most trace elements and results in a subhedral to euhedral form of pyrite with low trace element abundances. Hydrothermal pyrites, on the other hand, may be enriched/depleted in trace elements depending on the conditions of formation (temperature, salinity and proximity to vents).

These concentrations therefore do not reflect primary trace element concentrations of the sea water (Large et al., 2014; Mukherjee and Large, 2017).

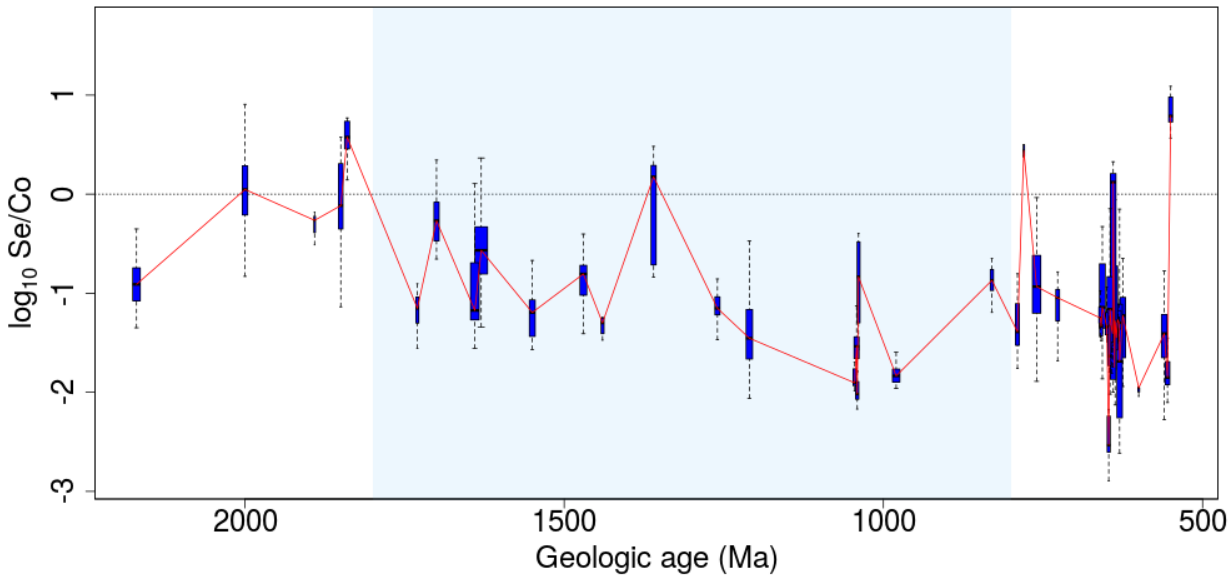

Fig A6.1 Plot of the log-ratio of Se to Co against geologic age. Shown are boxplots for each sample. The median trend is shown as a solid line.

A6.1.2 Sample details

Marine, least metamorphosed, undeformed organic matter rich-sedimentary black shales aged between 500-2500 Ma, were chosen for the study from various sedimentary basins around the world (Table A6.1 a, b). Samples were mainly collected in the form of drill cores in order to ensure the pyrite was well preserved and not oxidised. For all the drill holes, rock specimens were collected every ~10 m down-hole (approximately 20-30 samples per drill hole). From each interval of interest, rock specimens were set in 2.5 cm diameter epoxy molds and polished with 1-micron diamond paste. Polished laser mounts were prepared for petrological analysis using reflected light microscope followed by LA-ICP-MS pyrite analyses for trace elements at CODES, University of Tasmania.

Polished mounts were studied under reflected light in order to select samples that contain fine grained early-formed sedimentary pyrite and discard coarse, recrystallised and diagentically

altered pyrite. Most samples comprised sedimentary pyrite in the form of individual microcrystals, aggregates of microcrystals, framboids and nodular concretions in black shales. Coarser euhedral pyrites are present in some samples, that were not analysed as their TE budget is affected because of recrystallization (Large et al., 2014; Gregory et al., 2015; Mukherjee and Large, 2016).

A6.1.3 LA-ICP-MS analyses of pyrite data processing

Analyses were carried out using a New Wave Research UP-193ss laser microprobe coupled to an Agilent 7700s quadrupole ICP-MS for the following elements and their respective isotopes, ^{13}C, ^{23}Na, ^{24}Mg, ^{27}Al, ^{29}Si, ^{34}S, ^{39}K, ^{43}Ca, ^{49}Ti, ^{51}V, ^{53}Cr, ^{55}Mn, ^{57}Fe, ^{59}Co, ^{60}Ni, ^{65}Cu, ^{66}Zn, ^{75}As, ^{77}Se, ^{85}Rb, ^{88}Sr, ^{90}Zr, ^{95}Mo, ^{107}Ag, ^{111}Cd, ^{118}Sn, ^{121}Sb, ^{125}Te, ^{137}Ba, ^{157}Gd, ^{178}Hf, ^{181}Ta, ^{182}W, ^{195}Pt, ^{197}Au, ^{202}Hg, ^{205}Tl, ^{206}Pb, ^{207}Pb, ^{208}Pb, ^{209}Bi, ^{232}Th and ^{238}U. STGL2b2 (in-house standard for primary calibration; Danyushevsky et al., 2011), GSD-1G (USGS reference material; Jochum et al., 2005) and a pure stoichiometric pyrite crystal (Gilbert et al., 2014) were the three primary reference materials used for the analyses; viz. quantifying siderophile and chalcophile elements, lithophile elements and sulphur abundances, respectively. The standards were analysed before unknowns and thereafter every two samples (~every 1.5 hours) as well as at the end of each run, in order to measure any analytical drift. Backgrounds were analysed for 30-seconds before the signal from the ablated sample was acquired for 40-60 seconds. The laser instrument operated with ~3.5 J/cm^2 laser fluence and 5 Hz laser repetition rate. Samples were ablated in an atmosphere of pure He flowing at a rate of 0.8 l/min, immediately after which He carrier gas was mixed with Ar (0.85 l/min) for improved efficiency of aerosol transport within the cell.

Both ICP-MS instruments were optimized to maximize sensitivity on mid to high-mass isotopes (in the range 80– 240 amu) and production of molecular oxide species (i.e., $^{232}Th^{16}O^+/^{232}Th^+$) and doubly charged ion species (i.e., $^{140}Ce^{++}/^{140}Ce^+$) were maintained at levels below 0.2%. Dwell times on each mass varied between 5 and 30 msec, depending on the count rates and total sweep time (time required to measure all isotopes once) was 0.76 sec (similar to Large et al., 2014). A total of ~10 or more spot analyses, with spot size ranging from 15-35 mm, of sedimentary pyrites were performed on each sample. Also, 5 spot analyses of black shales (material surrounding the pyrites) on each sample were carried out to measure composition of silicate matrix in the black shales. Matrix analyses were also used in the data reduction process in order to account for matrix contamination during LA-ICP-MS analyses of pyrite grains.

The data were processed by data reduction software that uses a linear regression based algorithm for determining chalcophile and siderophile abundances relative to sulphur, for calculation of

sulfide composition. The conversion of raw data (counts per seconds) into concentrations in ppm involved splitting the integration curve (curve obtained from counts per second vs analysis time) into five segments of equal duration. Each of these segments was calculated using time-equivalent calibration standards. The data (in counts per seconds) were then converted to preliminary ppm values according to standard methods (Longerich et al., 1996), using Fe as the internal standard element. The method assumes a constant stoichiometric Fe content of pyrite for calculating preliminary compositions which are then normalized to a 100% total of siderophile, chalocophile and oxides of lithophile elements. To calculate the final concentrations, a linear regression equation using S content was employed such that the sum of the chalcophile and siderophile elements including S was 100%. Additionally, regression fits for individual analyses was visually inspected. The resulting compositions were close to major element composition of stoichiometric pyrite. The precision of the analyses was calculated using regression analysis. The errors vary from analysis to analysis, depending on quality of regression fit, concentration of element, abundance of measured isotope etc. Elements such as Se, As, Sb, Ni, Zn, Cu, Pb and Co at high concentrations, relative error is under 20% for 75% of analyses. However, uncertainty increases at lower concentrations. The analytical errors sourced from the uncertainty on composition of the reference materials is estimated under 5% (Danyushevsky et al., 2011). Considering that variations between grains in a sample typically is about 100% and concentration of an element can span 2-3 orders of magnitude different samples, we conclude that observed trends are outside of analytical uncertainty.

A6.1.4 Se and Se/Co in pyrite as oxygenation proxies

Trace elements such as Mo, Zn, Se, Pb, Co, Cu, Bi, As are known to be redox-sensitive (i.e. multiple valence states), and respond to changes in atmosphere-ocean redox conditions (Calvert and Pedersen, 1993; Jones and Manning, 1994; Wignall, 1994; Crusius et al., 1996; Dean et al., 1997, 1999; Yarincik et al., 2000; Morford et al., 2001; Pailler et al., 2002). Oxidative weathering results in the oxidized form of these trace elements, while reduced forms occur on encountering the redox boundary in the water column or sediment-water interface where they form complexes with organic acids and become incorporated into authigenic sulphides. Not all redox sensitive elements in pyrite can be used to infer atmospheric redox conditions because of partitioning into different phases (organic, detrital) other than pyrite. For instance, Ni and Cu may be adsorbed onto organic complexes and Fe-Mn oxides/hydroxides in the sedimentary process. Silver and Tl are not redox sensitive; however, Tl in pyrite is can be used to screen pyrites with hydrothermal effects (Mukherjee and Large, 2016). Some redox sensitive elements (Pb, As) in pyrites may not record any oxygenation trend solely due to their abundant supply in the water column (high source flux).

Arsenic is particularly problematic due it being relatively more mobile under reducing conditions than other redox sensitive TE (Smedley and Kinniburgh, 2002).

An increase in redox sensitive elements such as Se suggests a possible increased supply of these elements into the water column via oxidative weathering on land. Decrease in concentrations of elements such as Co and Bi can be used to support the oxidative weathering process on land because these elements tend to be retained by Fe-Mn hydroxides and oxides during oxidative weathering (Pickering, 1979; Jackson, 1998; Huang and Germida, 2002; Sparks, 2003; Violante et al., 2008). Cobalt, owing to its cationic speciation, is strongly retained by ferro-manganese hydroxides and more so by manganese oxides and its supply to the ocean is inhibited by oxidative processes on land (Pickering, 1979; Jackson, 1998; Huang and Germida, 2002; Sparks, 2003; Violante et al., 2008). Thermodynamic modelling of the concentration of Co in the oceans (Zerkle et al., 2005) as well Co in sedimentary pyrite (Large et al., 2015) and Co/Ti in iron formations (Swanner et al., 2014) confirm this behavior where a decrease in Co concentrations through time has been observed. The element Bi enters the marine realm via two main sources; atmospheric inputs i.e., eolian dust of volcanic origin (Lee et al., 1985; 1986) or river influx, both being comparable as source material (Bertine et al., 1996). Bismuth, owing to its extensive hydrolytic activity and strong particle reactivity, is also retained in oxyhydroxides, particularly manganese phases (Barnes, 1967; Fowler et al., 2010). Currently there is no thermodynamically modelled trend for Bi in the oceans through time. Nevertheless, Large et al. (2014) pointed out that Bi was one of the least abundant trace elements in the ocean today with a very short residence time (on the order of 20 years) and, like Co, likely decreased in concentration with increasing atmosphere oxygenation.

We propose that the use ratios of two elements that exhibit an antithetic behavior i.e., one element commonly increases in concentration with atmosphere oxidation (e.g., Se, Zn, Mo, Ni), and the other decreases in concentration (e.g., Co, Bi) is a more robust way to evaluate atmosphere oxygenation.

References

Abbott S. T. and Sweet I. P. (2000) Tectonic control on third-order sequences in a siliciclastic ramp-style basin: an example from the Roper Superbasin (Mesoproterozoic), northern Australia. Aust. J. Earth Sci. 47, 637–657.

Algeo T.J., Lyons T.W., 2006. Mo–total organic carbon covariation in modern anoxic marine environments: Implications for analysis of paleoredox and paleohydrographic conditions. Paleoceanography 21, 1- 23.

Algeo T.J., Rowe H., 2012. Paleoceanographic applications of trace-metal concentration data. Chemical Geology 324, 6–18.

Algeo T.J., Tribovillard N., 2009. Environmental analysis of paleoceanographic systems based on molybdenum-uranium covariation. Chemical Geology 268, 211–225.

Barnes S.S., 1967. Minor element composition of ferromanganese nodules. Science 157, 63-65.

Bertine K. K., Koide M., and Goldberg E.D., 1996. Comparative marine chemistries of some trivalent metals-bismuth, rhodium and rare Earth elements. Mar. Chem. 53, 89–100.

Bertine, K.K., Turekian, K.K., 1973. Molybdenum in marine deposits. Geochim. Cosmochim. Acta 37, 1415–1434.

Bull S. W. (1993) Progress report- sedimentology and volcanology of the southern McArthur Basin. AMIRA/ARC project P384 rep., 4: 33-53.

Calvert, S.E., Pedersen, T.F., 1993. Geochemistry of Recent oxic and anoxic marine sediments: implications for the geological record. Mar. Geol. 113, 67– 88.

Crowe, S.A., Døssing, L.N., Beukes, N.J., Bau, M., Kruger, S.J., Frei, R., Canfield, D.E., 2013. Atmospheric oxygenation three billion years ago. Nature 501, 535–538.

Crusius, J., Calvert, S., Pedersen, T., Sage, D., 1996. Rhenium and molybdenum enrichments in sediments as indicators of oxic, suboxic and sulfidic conditions of deposition. Earth Planet. Sci. Lett. 145, 65–78.

Danyushevsky, L., Robinson, P., Gilbert, S., Norman, M., Large, R., McGoldrick, P., Shelley, M., 2011. Routine quantitative multi-element analysis of sulphide minerals by laser ablation ICP-MS: Standard development and consideration of matrix effects. Geochem., Explor. Environ. Anal. 11, 51–60.

Dean, W.E., Gardner, J.V., Piper, D.Z., 1997. Inorganic geochemical indicators of glacial – interglacial changes in productivity and anoxia of the California continental margin. Geochim. Cosmochim. Acta 61, 4507– 4518.

Dean, W.E., Piper, D.Z., Peterson, L.C., 1999. Molybdenum accumulation in Cariaco basin sediment over the past 24 k.y.: a record of water-column anoxia and climate. Geology 27, 507– 510.

Fowler Scott W., Teyssie Jean-Louis, Church Thomas M., 2010. Scavenging and retention of bismuth by marine plankton and biogenic particles, Limnology and Oceanography 55, 1093–1104.

Gilbert S., Danyushevsky L., Goemann K. and Death D. (2014a) Fractionation of sulphur relative to iron during laser ablation-ICP-MS analyses of sulphide minerals: implications for quantification. J. Anal. At. Spectrom. 29, 1024–1033.

Giles D., Betts P. G. and Lister G. S. (2002) A continental back-arc setting for Early to Middle Proterozoic basins of northeastern Australia. Geology 30, 823–826.

Gordon, G.W., Lyons, T.W., Arnold, G.L., Roe, J., Sageman, B.B., Anbar, A.D., 2009. When do black shales tell molybdenum isotope tales? Geology 37, 535–538.

Gregory, D., Meffre, S., and Large, R., 2014, Comparison of metal enrichment in pyrite framboids from a metal-enriched and metal-poor estuary: American Mineralogist, v. 99, no. 4, p. 633-644.

Gregory, D.D., Large, R.R., Halpin, J.A., Lounejeva Baturina, E., Lyons, T.W., Wu, S., Sack, P.J., Chappaz, A., Maslennikov, V.V., Bull, S.W., Danyushevsky, L., 2015. Trace element content of sedimentary pyrite in black shales. Econ. Geol. 110, 1389–1410.

Haines P. W. (1994) The Balma and Habgood groups, northern McArthur Basin, Northern Territory; stratigraphy and correlations with the McArthur Group. In: 1994 AusIMM Annual Conference, Australian Mining Looks North; the Challenges and Choices, pp. 147-152. Australasian Institute of Mining and Metallurgy Publication Series 5/94.

Haines P. W., Pietsch B. A., Rawlings D. J. and Madigan T. L. (1993) Mount Young, Northern Territory; 1:250 000 Geological Map Series, sheet SD53-15. Northern Territory Geological Survey Explanatory Notes.

Huang, P.M., and Germida, J.J., 2002. Chemical and biochemical processes in the rhizosphere: metal pollutants. In Interactions Between Soil Particles and Microorganisms: Impact on the Terrestrial Ecosystem, ed. Huang, P. M., Bollag, J.M., and Senesi, N., Wiley, New York, 381–438.

Huerta-Diaz, M.A., Morse, J.W., 1992. Pyritization of trace metals in anoxic marine sediments. Geochim. Cosmochim. Acta 56, 2681–2702

Jackson, T.A., 1998. The biogeochemical and ecological significance of interactions between colloidal minerals and trace elements. In Environmental Interactions of Clays, ed. Parker, A., and Rae, J. E., Springer-Verlag, Berlin, 93–205.

Javaux E. J., Knoll A. H. and Walter M. R. (2001) Morphological and ecological complexity in early eukaryotic ecosystems. Nature 412, 66–69.

Javaux E., Knoll A. H. and Walter, M. R. (2004) TEM evidence for eukaryotic diversity in mid-Proterozoic oceans. Geobiology 2, 121–132.

Jochum, K.P., Pfänder, J., Woodhead, J.D., Willbold, M., Stoll, B., Herwig, K., Amini, M., Abouchami, W. and Hofmann, A.W., 2005. MPI-DING glasses: New geological reference materials for in situ Pb isotope analysis. Geochemistry Geophysics Geosystems 6, 1525-2027.

Jones, B., Manning, D.A.C., 1994. Comparison of geochemical indices used for the interpretation of palaeoredox conditions in ancient mudstones. Chem. Geol. 111, 111 – 129.

Large, R.R, Halpin, J.A., Lounejeva, E., Danyushevsky, L.V., Maslennikov, V.V., Gregory, D., Sack, P.J., Haines, P.W., Long, J.A., Makoundi, C., Stepanov, A.S., 2015. Cycles of nutrient trace elements in the Phanerozoic ocean, Gondwana Research 28 (4), 1282-1293.

Large, R.R., Danyushevsky, L., Hollit, C., Maslennikov, V., Meffre, S., Gilbert, S., Bull, S., Scott, R., Emsbo, P., Thomas, H., Singh, B., Foster, J., 2009. Gold and trace element zonation in pyrite using a laser imaging technique: Implications for the timing of gold in orogenic and carlin-style sediment-hosted deposits. Econ. Geol. 104, 635–668.

Large, R.R., Halpin, J.A., Danyushevsky, L.V., Maslennikov, V.V., Bull, S.W., Long, J.A., Gregory, D.D., Lounejeva, E., Lyons, T.W., Sack, P.J., McGoldrick, P. and Calver, C.R., 2014. Trace element

content of sedimentary pyrite as a new proxy for deep-time ocean- atmosphere evolution. Earth and Planetary Science Letters 389, 209-220.

Lee, D.S., Edmond, J.M., and Bruland, K.W., 1985/1986. Bismuth in the Atlantic and North Pacific Ocean: A natural analogue to plutonium and lead? Earth Planet. Sci. Lett. 76, 254–262.

Lenth, R. V. and Højsgaard, S. (2007). SASweave: Literate programming using SAS. Jour- nal of Statistical Software, 19(8). URL http://www.jstatsoft.org/.

Longerich, H.P., Jackson, S.E. and Günther, D., 1996. Laser ablation inductively coupled plasma mass spectrometric transient signal data acquisition and analyte concentration calculation. J. Anal. At. Spectrom. 11, 899-904.

Lyons, T.W., Reinhard, C.T., Planavsky, N.J., 2014. The rise of oxygen in Earth's early ocean and atmosphere. Nature 506, 307-315.

Meyer KM, Kump LR. 2008. Oceanic euxinia in Earth history: Causes and consequences. Annu. Rev. Earth Planet. Sci. 36, 251–88.

Morford, J.L., Russell, A.D., Emerson, S., 2001. Trace metal evidence for changes in the redox environment associated with the transition from terrigenous clay to diatomaceous sediment, Saanlich Inlet, BC. Mar. Geol. 174, 355– 369.

Morse, J.W., Arakaki, T., 1993. Adsorption and coprecipitation of divalent metals with mackinawite (FeS). Geochim. Cosmochim. Acta 57, 3635–3640

Muir M. D. (1982) A microfossil assemblage from the Wollogorang Formation, Tawallah Group, Middle Proterozoic, NT, Australia. Bureau of Mineral Resources, Geology and Geophysics record 1982/4.

Mukherjee I. and Large R. (2017) Application of pyrite trace element chemistry to exploration for SEDEX style Zn-Pb deposits: McArthur Basin, Northern Territory, Australia. Ore Geology Reviews 81, 1249-1270.

Mukherjee, I., and Large, R., 2016. Pyrite trace element chemistry of the Velkerri Formation, Roper Group, McArthur Basin: Evidence for atmospheric oxygenation during the Boring Billion:

Precambrian Res. 281, 13-26

Mukherjee, I., and Large, R., 2017. Application of pyrite trace element chemistry to exploration for SEDEX style Zn-Pb deposits: McArthur Basin, Northern Territory, Australia. Ore Geology Reviews 81, 1249-1270.

Munson T. J. (2016) Sedimentary characterisation and correlation of the Wilton package, greater McArthur Basin: in Annual Geoscience Exploration Seminar (AGES) presentations, Alice Springs, Northern Territory 15–16 March 2016. Northern Territory Geological Survey, Record 2016-001.

Oehler J. H. and Logan R. G. (1977) Microfossils, cherts and associated mineralization in the McArthur deposit, NT, Australia. Economic Geology 72, 393–409.

Pailler, D., Bard, E., Rostek, F., Zheng, Y., Mortlock, R., van Geen, A., 2002. Burial of redox-sensitive metals and organic matter in the equatorial Indian Ocean linked to precession. Geochim. Cosmochim. Acta 66, 849– 865.

Partin, C.A., Bekker, A., Planavsky, N.J., Scott, C.T., Gill, B.C., Li, C., Podkovyrov, V., Maslov, A., Konhauser, K.O., Lalonde, S.V., Love, G.D., Poulton, S.W., Lyons, T.W., 2013. Large-scale fluctuations in Precambrian atmospheric and oceanic oxygen levels from the record of U in shales. Earth Planet. Sci. Lett. 369–370.

Pickering, W., 1979. Copper retention by sediment/soil components. In Copper in the Environment Vol. I, Ecological Cycling, ed. Nriagu, J. O., Wiley, New York, 217–253

Rickard, D., 2012. Sulfidic sediments and sedimentary rocks. In: Van Loon, A.J. (Ed.), Developments in Sedimentology. Elsevier, p. 801.

Rogers J. (1996) Geology and tectonic setting of the Tawallah Group, southern McArthur Basin, Northern Territory. PhD thesis, University of Tasmania.

Sahoo, S. K., Planavsky, N. J., Jiang, G., Kendall, B., Owens, J. D., Wang, X., Shi, X., Anbar, A. D. and Lyons, T. W., 2016. Oceanic oxygenation events in the anoxic Ediacaran ocean. Geobiology 14, 457–468.

Sahoo, S.K., Planavsky, N.J., Kendall, B., Wang, X., Shi, X., Scott, C., Anbar, A.D., Lyons, T.W.,

Jiang, G., 2012. Ocean oxygenation in the wake of the Marinoan glaciation. Nature 489, 546–549.

Scott, C., Lyons, T.W., Bekker, A., Shen, Y., Poulton, S.W., Chu, X., Anbar, A.D., 2008. Tracing the stepwise oxygenation of the Proterozoic ocean. Nature 452, 456–459.

Smedley, P L, and Kinniburgh, D G. 2002. A review of the source, behaviour and distribution of arsenic in natural waters. Applied Geochemistry 17, 517–568

Sparks, D.L., 2003. Environmental Soil Chemistry, 2nd ed. Academic Press, San Diego, CA. pp.352

Swanner, E.D., Planavsky, N.J., Lalonde, S.V., Robbins, L.J., Bekker, A., Rouxel, O.J., et al., 2014. Cobalt and marine redox evolution. Earth Planet. Sci. Lett. 390, 253–263.

Taylor, S.R., Mclennan, S.M., 1995. The geochemical evolution of the continental crust. Rev. Geophys. 33, 241–265.

Tribovillard, N., Algeo, T.J., Lyons, T., Riboulleau, A., 2006. Trace metals as paleoredox and paleoproductivity proxies: an update. Chem. Geol. 232, 12–32.

Violante, A., Krishnamurti, G.S.R., Pigna, M. 2008. Mobility of Trace Elements in Soil Environments. In: A. Violante, P.M. Huang, G.M. Gadd (eds). Biophysico-Chemical Processes of Metals and Metalloids in Soil Environments. John Wiley and Sons, Hoboken, NJ, pp.169-213.

Wignall, P.B., 1994. Black Shales. Clarendon Press, Oxford. 127 pp.

Yarincik, K.M., Murray, R.W., Lyons, T.W., Peterson, L.C., Haug, G.H., 2000. Oxygenation history of bottom waters in the Cariaco Basin, Venezuela, over the past 578,000 years: results from redox-sensitive metals (Mo, V, Mn, and Fe). Paleoceanography 15, 593– 604

Zerkle, A.L., House, C.H., Brantley, S.L., 2005. Biogeochemical signatures through time as inferred from whole microbial genomes. Am. J. Sci. 305, 467–502.